Biologische Integration von Halbleiter-Nanostrukturen

Dissertation der Fakultät für Physik

der

Ludwig-Maximilians-Universität München

vorgelegt von

Christian Kirchner

aus Köln

München, den 06.10.2005

1. Gutachter: Prof. Dr. Hermann Gaub
2. Gutachter: Prof. Dr. Bianca Hermann

Datum der mündlichen Prüfung: 21.2.2006

Zusammenfassung

Die vorliegende Arbeit beschäftigte sich im ersten Teil mit der Entwicklung eines Oberflächenpotentialsensors für die Zell-Halbleiter-Kopplung. Im zweiten Teil ging es um die Konzeption eines Tests zur quantitativen Erfassung von Nebenwirkungen beim Einsatz von Halbleiter-Nanokristallen in biologischen Umgebungen. Als ein zentrales Problem bei der Realisierung solcher Bionano-Systeme wurde die Korrosionsbeständigkeit der Nano-dimensionierten Halbleiterbauteile in physiologischer Umgebung erkannt und eine systematische Untersuchung der Korrosion durchgeführt. Zur Lösung des Problems wurden Isolationsschichten aus Organosilikaten vorgeschlagen und ihre Wirksamkeit mit verschiedenen Methoden getestet.

Oberflächenpotentialsensoren können eine Schnittstelle des elektrischen Signalaustausch zwischen lebenden Nervenzellen (Gehirn) und künstlichen Sensoren (Computern) bilden. Der hier untersuchte Sensor realisiert die non-invasive Messung von Neuronen mit Feldeffekt-Transistoren (FETs), die an den Kreuzungspunkten von Gate-Elektroden aus Metall- und Feldeffekt-Kanälen aus Galliumarsenid-Heterostrukturen gebildet werden. Die Zellen wachsen dabei unmittelbar auf dem Halbleiter. Um dessen Korrosion und die Schädigung der Zellen durch Arsen-haltige Korrosionsprodukte zu verhindern, müssen geeignete Isolationsschichten eingesetzt werden. Dabei ist, wie beschrieben wird, für das Design der FETs eine minimale Halbleiter-Oxid-Schichtdicke entscheidend für die Messempfindlichkeit. Ohne angelegte elektrische Spannung erfüllen Schichten aus Organosilikaten von 20 nm Dicke diese Anforderungen, wie in Messungen mit „Atomic Force Microscopy“, „Atom Absorption Spectroscopy“ und Zellkultur-Techniken nachgewiesen wurde. Die Grenzen der elektrischen Belastbarkeit solcher Schichten wurden durch Messungen im Elektrolyt an lithographisch gefertigten Teststrukturen aus GaAs-Heterostrukturen und in Voltammetrie-Messungen an „Electrolyte-Insulator-Semiconductor“ Bauteilen aufgezeigt.

Die chemische Struktur der Schichtsysteme von Organosilikaten auf GaAs-Substraten wurde in Messungen mit Röntegenreflektivität unter streifendem Einfall untersucht. Neben einer Vereinfachung der Schicht-Synthese wurde gefunden, dass die (Rück-)Bildung einer amorphen Schicht des nativen GaAs-Oxids zwischen GaAs-Substrat und dem Polymer nicht

verhindert werden kann. Das native GaAs-Oxid gilt als die Ursache einer hohen Dichte von elektrischen „Oberflächenzuständen“, die bisher den Einsatz von GaAs in einer MOS-Technologie verbieten.

Fluoreszierende Halbleiter-Nanokristalle gelten in der Biologie als vielversprechende Alternative zu organischen Fluoreszenzmarkern, da sie über einzigartige optische Eigenschaften wie zum Beispiel eine hohe Stabilität gegenüber „Photobleichen“ und ein einfach einzustellendes Fluoreszenzspektrum verfügen. Im zweiten Teil der Arbeit wurden unterschiedlich funktionalisierte Halbleiter-Nanokristalle aus CdSe und CdTe auf ihre Biokompatibilität hin untersucht. In dieselbe Untersuchung wurde ein System aus Polyelektrolyt-Kapseln, befüllt mit fluoreszierenden CdTe-Nanokristallen, miteinbezogen. Eine mögliche Anwendung solcher Kapseln ist der gezielte Transport von Testsubstanzen und Pharmazeutika („targeted drug delivery“). Es wurde ein sensibler Test entwickelt, der auf dem Adhäsionsverhalten von Zellkulturen aus NRK-Fibroblasten beruht. Auf einer Oberfläche adhärente Zellen werden vor und nach Inkubation mit einer Testsubstanz, z.B. CdSe-Nanokristalle, über ein optisches Mikroskop mit einer CCD-Kamera fotografiert und anschließend mithilfe eines Bildanalyseverfahrens gezählt. Die Zahl der abgelösten Zellen wird so in Abhängigkeit von der Nanokristall-Konzentration erfasst und die Biokompatibilität auf diese Weise in einem automatisierten Messverfahren charakterisiert. Es konnte wie im Fall der planaren GaAs-Proben gezeigt werden, dass Organosilikate im Vergleich mit anderen Oberflächen-Funktionalisierungen eine optimale Schutzhülle für den Halbleiterkern mit sehr guter Biokompatibilität darstellen.

Einleitung und Motivation

Nanotechnologie wird als Schlüsseltechnologie des 21. Jahrhunderts bezeichnet [1]. Ihre Verschmelzung mit Biologie und Biotechnologie führte zu einem Boom von Forschungsaktivität und zum Begriff der Nanobiotechnologie. Das Gebiet gibt heute Forschern aus traditionellen Forschungsfeldern wie Biologie, Chemie, Materialwissenschaften und Physik ein animierendes Forum für erfolgreiche Kooperationen und fachübergreifende Projekte, was die vorliegende Arbeit einschließt. Kritiker mahnen, Wissensfusion durch interdisziplinäre Arbeit und eine konsequente Förderung erzeuge zwangsläufig Ideen und Innovationen, während eine wirkliche technische Revolution in der Nanotechnologie noch ausstehe [2]. An dieser Stelle muss klargestellt werden, dass die repräsentierten Forschungsgebiete nicht artifiziell sind wie die Begriffe selbst, sondern neu entwickelte Bereiche einer Wissenschaft, die in die „Nano"-Dimension vorgestoßen ist.

Angekündigt von Richard Feynman 1959 in seinem berühmten Vortrag „There's plenty of room at the bottom", wurde die Welt auf der Nanometerskala durch die Entwicklung des Rastertunnelmikroskops 1981 (Gerd Binnig, Nobelpreis 1986) und verwandte Rastersondentechniken sichtbar und manipulierbar gemacht. Das gilt insbesondere für die Biologie, deren wichtige Funktionsbausteine DNA, RNA und Proteine durch die neuen Analyseverfahren greifbar wurden [3]. Das Verstehen und Instrumentalisieren dieser Funktionsbausteine sowie biologischer Prinzipien und Prozesse ist ein Ziel der Biophysiker, die Biologie als „natürliche Nanotechnologie" betrachten. Verfolgt wird diese faszinierende Idee speziell in der Molekularen Biomimetik und allgemeiner, im sogenannten „bottom-up" Ansatz der Nanotechnologie [4]. Konsequent versucht dieser Zweig der Nanotechnologie, von der Natur inspiriert, komplexe Maschinen aus kleinsten Funktionseinheiten nach dem biologischen Prinzip der Selbstorganisation entstehen zu lassen [5, 6]. Ein direkterer Weg zu Nanotechnologie beruht auf dem „top-down" Ansatz, wo durch Miniaturisierung kleinste nanoskalige Strukturen geschaffen werden, um wie etwa in der Mikroelektronik zu einer leistungsfähigeren Nano- oder molekularen Elektronik zu gelangen, nanodünne Halbleiterschichten für die Optoelektronik oder Nanopartikel für „smarte Materialien" oder als Sonden zu erzeugen [7-9].

Während biomimetische „bottom-up“-Konzepte oft schon in biologischen Umgebungen entstehen, ist die Integration von „top-down“ Technologie in biologische Strukturen eine besondere Herausforderung für die Nanobiotechnologie, wie in dieser Arbeit gezeigt wird. Bei der Konstruktion eines „Bio/Nano“-Systems ist der Erhalt von sowohl technischen wie biologischen Funktionen über einen angemessenen Zeitraum entscheidend. Für Halbleiter ist eine physiologische Umgebung im Vergleich zu atmosphärischen Bedingungen äußerst problematisch, da Korrosionsvorgänge in wässriger Lösung, unter erhöhter Temperatur (37°C), hohen Salzkonzentrationen (140 mM NaCl) und hoher CO_2 Konzentration (5 vol%) gefördert werden. Halbleiter können zudem durch eindiffundierende Ionen kontaminiert werden. Dabei sind diese Vorgänge proportional zur Angriffsfläche, was bei dreidimensionalen nanoskaligen Strukturen mit einem großen Fläche/Volumen Verhältnis besonders relevant wird. Korrosionsprodukte können auf der anderen Seite toxisch wirken und biologische Funktionen beeinträchtigen. Zur Ausrichtung der „Zwangsheirat“ von Halbleiter und biologischem Material sind deshalb effektive Isolationsschichten gefordert.

Im Fokus der vorliegenden Arbeit stehen zwei Nano-Systeme, deren physikalische Eigenschaften durch Quantentopf-Strukturen geprägt werden. Der erste Teil widmet sich einem Oberflächenpotential-Sensor (FAPS, [10]) auf der Basis von Gallium Arsenid Heterostrukturen, dessen Zweck die extrazelluläre Messung elektrischer Potentiale von Neuronen ist. Im zweiten Teil geht es um Halbleiter-Nanokristalle aus Cadmium Selenid und Cadmium Telurid als Fluoreszenzmarker in lebenden Zellen. Die Elemente Arsen und Cadmium gehören zu den giftigsten überhaupt. Als Bestandteile von Materialien in biologischen Anwendungen erfordern sie eine sorgfältige Analyse der Halbleiter-Korrosion und der damit verbundenen Toxizität. Als besonders viel versprechende Gegenmaßnahme wird zudem eine Glas-artige Verkapselung der Halbleiterbausteine auf der Basis von Organosilikaten eingeführt und untersucht.

Die ersten 50 Seiten dieser „kumulativen“ Arbeit sollen als Einführung verstanden werden, die den Kontext für die wissenschaftlichen Publikationen aus dieser Dissertation bilden. Diese finden sich als Referenzen K1-K6 im Anhang der Arbeit.

I. Ein Oberflächenpotential-Sensor (FAPS, [10]), zur non-invasiven Messung elektrischer Potentiale von Neuronen, auf der Basis von Gallium Arsenid Heterostrukturen

1. Ziel

Ziel des Projekts war die Entwicklung eines hochauflösenden Oberflächenpotentialsensors zur non-invasiven Messung der Membranpotentiale von elektrisch aktiven Zellen. Das Prinzip des Sensors beruht auf Feldeffekttransistoren, die in einer Gitterstruktur an den Kreuzungspunkten von Gate-Elektroden aus Metall und Feldeffektkanälen auf Basis einer Galliumarsenid-Heterostruktur gebildet werden [10] [11].

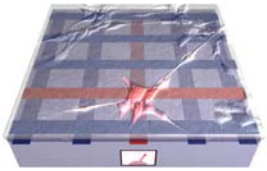

Abbildung 1 Der Feldeffekt-Adressierbare Potentiometer/Stimulator (FAPS)

2. Zusammenfassung der durchgeführten Arbeiten

Der Einsatz von GaAs in physiologischer Umgebung und unter elektrochemischer Belastung wurde im Rahmen dieser Arbeit erstmals systematisch untersucht. Dazu wurde an planaren GaAs-Substraten zunächst die Korrosion in Wasser quantifiziert. Als Messmethoden kamen AFM (atomic force microscopy), SEM (scanning electron microscopy), AAS (atom absorption spectroscopy), Ellipsometrie, Kontaktwinkelmessungen, Impedanzmessungen und Voltammetrie zur Verwendung. In einem nasschemischen Verfahren wurden eine Isolationsbeschichtung aus Organosilikaten in verschiedenen Varianten auf GaAs etabliert sowie chemische Strukturierungsmöglichkeiten untersucht. Die Effizienz der Isolation wurde neben den genannten Methoden auch unter elektrischer Belastung an lithographisch gefertigten Testkanälen aus GaAs-Heterostrukturen getestet. Als „Reporter“ der Biokompatibilität von beschichtetem GaAs wurden Zellkulturen von NRK-Fibroblasten auf den entsprechenden Substraten aufgewachsen, ihr Adhäsionsverhalten durch optische Mikroskopie beobachet und Schwellwerte der Arsenvergiftung über kommerzielle Life/Dead-

Tests ermittelt. In Patch-Clamp Messungen an elektrisch aktiven Zellen wurde der Erhalt von elektrophysiologischen Funktionen nachgewiesen.
Mikrostrukturanalysen durch Röntgenreflektivität unter streifendem Einfall wurden an Organosilikatschichten auf GaAs durchgeführt, um neben der chemischen Passivierung die Bedeutung des Schichtsystems zur Passivierung der elektrischen Oberflächenzustände des Halbleiters abzuschätzen.
Patch-Clamp Messungen und elektrische Charakterisierung wurden in Zusammenarbeit mit Michael George und Bernhard Stein durchgeführt, die SEM Bilder stammen von Armin Kriele. AAS Messungen waren ein Service des Instituts für Wassergüte, TU München. Messungen der Röntgenreflektivität unter streifendem Einfall entstanden in Zusammenarbeit mit den Arbeitsgruppen von Prof. U. Klemradt (RWTH Aachen) und Prof. T. Finlayson (Monash University, Australien).

3. Methoden zur Messung elektrischer Zellaktivität

Eine etablierte Möglichkeit zur Erfassung der elektrischen Aktivität einzelner Nervenzellen ist die „Patch-Clamp“ Methode. Sie misst direkt die Potentialdifferenz zwischen Zell-Innenraum und Aussenraum (Membranpotential), wobei eine mit Elektrolyt gefüllte Glaskapillare den elektrischen Kontakt zum Cytoplasma durch „Patch-Clamp“ herstellt [12] [13]. Eine Alternative ist die Verwendung Potential-sensibler Fluoreszenzfarbstoffe, mit denen die Potentialverteilung an einzelnen Zellen erfasst werden kann [14] [15]. Beide Methoden stellen einen physikalischen Eingriff in das Biosystem der Zelle dar, sie sind invasiv. Zudem sind sie für Langzeit-Beobachtungen von einzelnen Zellen oder Zellverbänden ungeeignet, bei Patch-Clamp aufgrund der empfindlichen Mechanik der Messanordnung, bei Fluoreszenzfarbstoffen aufgrund von Ausbleichen und Cytotoxizität. Der elegantere und non-invasive Ansatz zum Nachweis neuronaler Aktionspotentiale erfasst deren korrespondierende extrazelluläre Potentialschwankungen durch Oberflächenpotenzialmessung. Dabei liegt die besondere Herausforderung im Nachweis von Potentialschwankungen, die mit 25-100 µV im Betrag drei Größenordnungen kleiner sind als die Amplitude des verursachenden Aktionspotentials (z.B. 100 mV für Neuronen, ref E.Sackmannn Biophysikskript 1996). Feldeffekttransistoren (FET) können als solche Oberflächenpotentialsensoren verwendet werden, indem ihre Gate-Elektroden als Kontaktpunkte zu den Zellen arrangiert werden [16]**.** Eine angemessen dichte Anordnung

solcher FETs kann zu orts- und zeitaufgelösten Messung elektrischer Aktivität von einzelnen Zellen oder Zellverbänden genutzt werden [17]. In der Gruppe um Fromherz (in Zusammenarbeit mit INFINEON AG) verfolgt man dieses Ziel durch die Nutzung mikroelektronischer Fertigungsmethoden in Siliziumtechnologie ([18], Abb.2.a). Eine Alternative zu dicht gruppierten einzelnen FETs wurde mit dem „Field-effect adressable potentiometric sensor/stimulator“ vorgeschlagen (Abb 2.b, FAPS, [10])

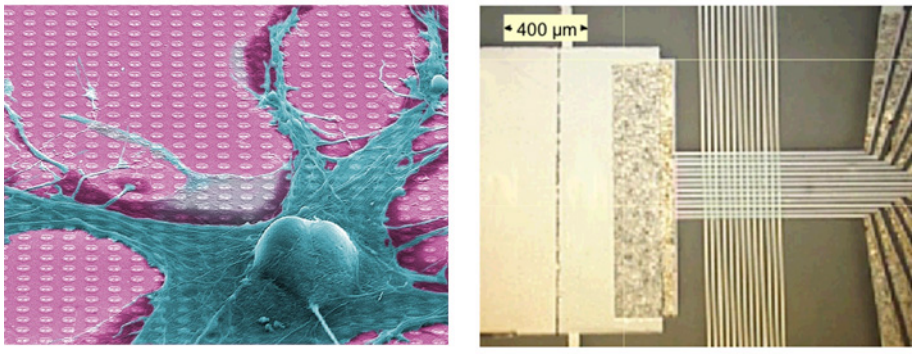

Abbildung 2. a) aus [18], Neuron auf Silizium-CMOS Chip mit einem Sensor (FET) – Abstand von 8 µm, SEM Aufnahme. b) FAPS Struktur [10, 11].

4. Prinzip des „Field-effect adressable potentiometric sensor/stimulator“ (FAPS)

Der Sensor beruht auf Feldeffekttransistoren, die in einer Gitterstruktur an den Kreuzungspunkten von Gate-Elektroden aus Metall und Feldeffektkanälen auf Basis einer Galliumarsenid-Heterostruktur gebildet werden (Abb 3.a) [10] (Referenz K2). Im Vergleich zu konventionellen FET-Anordnungen liegt sein Vorteil besonders darin, daß bei Aufbau eines $n^x n$ - Feldes die Zahl der nötigen Zuleitungen nur mit n und nicht mit n^2 skaliert.

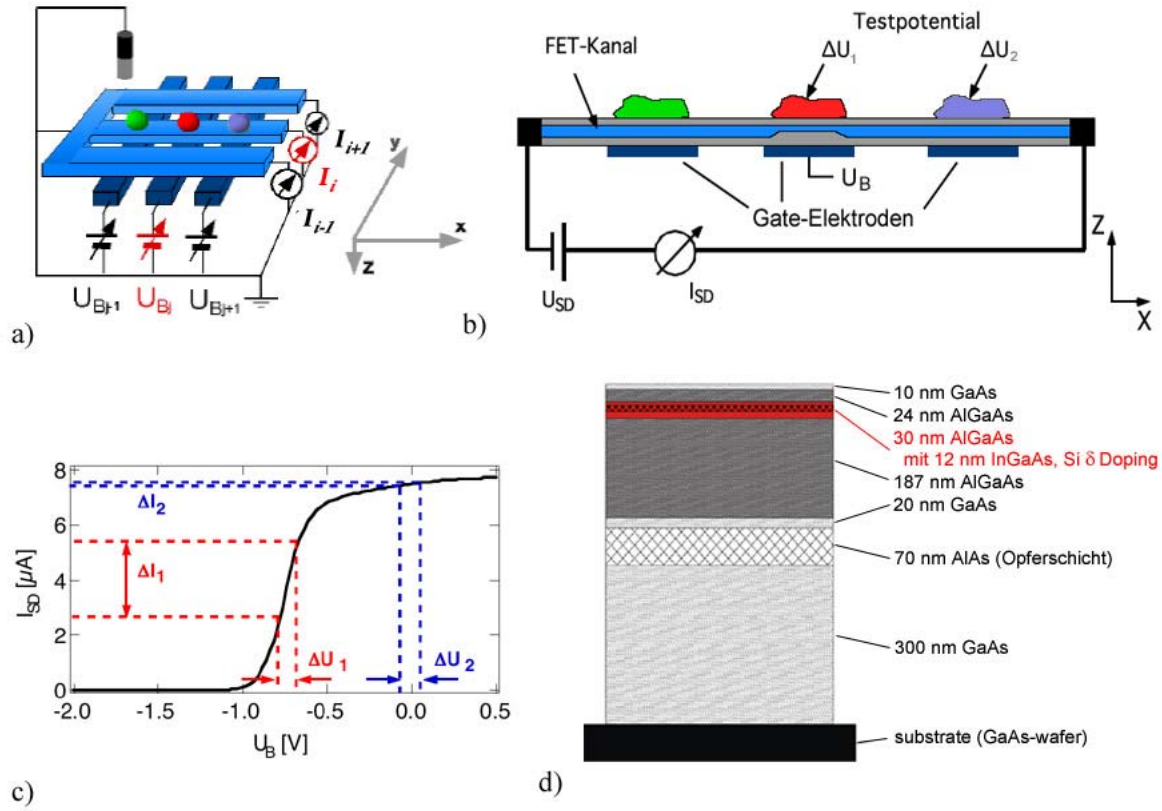

Abbildung 3 a) Schematischer Aufbau einer FAPS-Struktur. In y-Richtung sind die Rückelektroden dargestellt, an die eine Spannung U_B angelegt werden kann. In x-Richtung sind die FET-Kanäle gezeigt, an denen entweder der Widerstand R(t) oder der Strom I(t) gemessen wird. Durch Messung des Kanal-Stroms I_i und Anlegen einer Spannung U_{Bj} wird gezielt ein Messpunkt ausgewählt. b) Schematischer Querschnitt durch die Struktur. Die Verengung des FET-Kanals soll die Erhöhung des Kanalwiderstands unter Gate-Spannung U_B verdeutlichen. c) Kennlinie I_{SD} (U_B) für eine konstante Spannung U_{SD}. Kleine Testpotentiale ΔU_1 verursachen messbare große Stromänderungen ΔI_1 im aktiven FET-Kanal. d) Aufbau des FET Kanals als n-GaAs-Heterostruktur. Rot eingezeichnet ist der Bereich des Quanten-Topfs (Q2DEG), vgl. [19], S.117.

Die Heterostruktur der Feldeffekt-Kanäle besteht aus einem Schichtsystem von GaAs-Legierungen, die durch „Molecular Beam Epitaxy“ (MBE) auf einem GaAs-Substrat aufgetragen wurden ([19], S.117). Als wichtiger Schritt bei der Sensorherstellung lässt sich der obere Teil des Schichtsystems nach Ätzen der AlAs-Opferschicht (Abb. 3d) abheben und auf das Substrat mit den Gate-Elektroden verlegen („Epitaktischer Lift-off“, [20-22]). Der Zweck des komplexen Aufbaus des oberen Schichtsystems ist ein „band engineering“ der Halbleiterbandstruktur, deren Potentialprofil einen Quantentopf für Elektronen darstellt. Die Elektronen dieses „quasi 2-dimensionale Elektronengas“ (Q2DEG) werden von einer quasi-monoatomaren Schicht von Elektron-Donatoren (Si-δ-doping) unmittelbar vor den Potentialwällen der AlGaAs-Schichten hervorgerufen (Abb.3d). Die Ausdehnung des Quantentopfs in z-Richtung liegt in der Größenordnung der de Broglie-Wellenlänge

thermischer Elektronen, so dass die Ladungsträgerverteilung den Gesetzen der Quantenmechanik folgt und ihre Energie quantisiert ist. Die Dimensionen von Länge (z.B. 2 mm) und Breite (z.B. 20 μm) der FET-Kanäle liegen dagegen weit über dem Einsetzen quantenmechanischer Effekte, so dass die Elektronen in x- und y-Richtung gemäß der klassischen Elektrodynamik frei beweglich sind und man einen Feldeffekt-sensiblen Leitungskanal mit Elektronen erhält.

Die elektronischen Eigenschaften des Systems sind so gewählt, dass die FET-Kanäle bei einer Gatespannung $U_B = 0$ V leitend sind. Wird nun wie in Abb.4 an einer Stelle x_2 durch eine Gate-Elektrode eine negative Vorspannung U_{Bias} senkrecht zu dem Kanal angelegt, wird durch den resultierenden linearen Potentialgradient die potentielle Energie für freie Elektronen erhöht. Dadurch wird der Aufenthalt an der Stelle x_2 des Kanals für Elektronen energetisch ungünstig und sie wandern zu benachbarten, energetisch günstigeren Stellen x_1 und x_3 des Kanals. Somit sinkt an der Stelle der angelegten Vorspannung die Elektronendichte im Kanal und der lokale Widerstand wird größer. Stellt man die Vorspannung des aktiven FET-Kanals auf den Arbeitspunkt ein, der im Bereich maximaler Steigung von $I_{SD}(U_B)$ liegt, so bewirken minimale Testpotentiale ΔU_1 über dem adressierten Messpunkt maximale Stromdifferenzen ΔI_{SD}. Dagegen ist der Beitrag anderer Testpotentiale ΔU_2 vernächlässigbar, die zwar auf dem aktiven FET-Kanal, aber ausserhalb des aktiven Messpunktes liegen, siehe Abb. 3. b), c). Auf diese Weise können kleinste Oberflächenpotentialänderungen ortsaufgelöst gemessen werden.

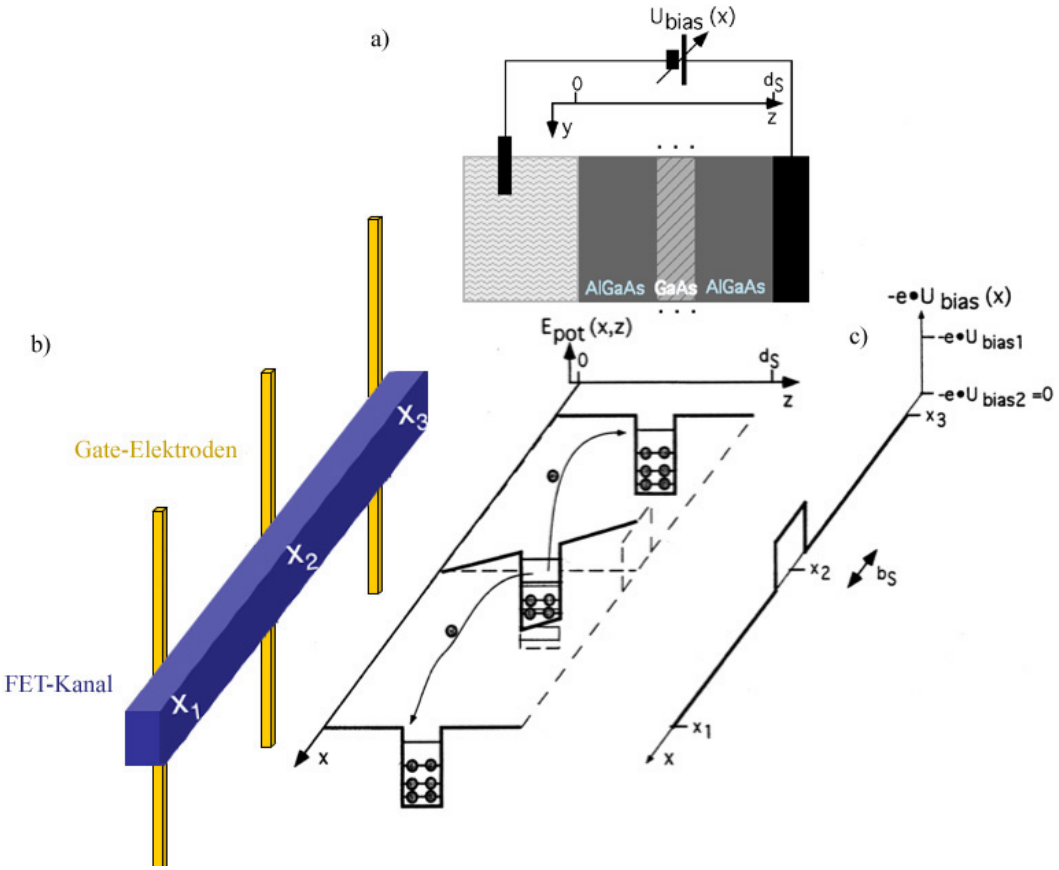

Abbildung 4: a) Um 90° gedrehtes Schema eines in Quantentopf-Bauweise erstellten leitfähigen Kanals. Durch die Beschaltung wirkt von der linken Seite auf den Kanal das Massepotential der Referenzelektrode im Elektrolyt, von der rechten Seite das über die angrenzende Gate-Elektrode angelegte Potential $U_{Bias}(x)$. b) Innerhalb der Quantentopfstruktur sind die freien Ladungsträger an die Schicht des Q2DEG gebunden, da dort die potentielle Energie am niedrigsten ist. In z-Richtung ist die Energie der Elektronen quantisiert, was in der Abbildung durch kugelförmige Teilchen auf diskreten Energieniveaus angedeutet ist. Durch Anlegen einer lokalen Vorspannung entlang einer Gate-Elektrode an der Stelle x2, vgl. c), wird die potentialle Energie der Elektronen erhöht. Die Wahrscheinlichkeit für Elektronenaufenthalt sinkt an dieser Stelle, die Elektronen „fliessen“ aus dem Quantentopf. Damit wird die Dichte der freien Elektronen am Kreuzungspunkt mit einer negativ vorgespannten Elektrode erniedrigt und der lokale Kanalwiderstand steigt.

Für diese Arbeit besonders relevant ist die Tatsache, dass im Sensorbetrieb die Q2DEG-Ebene ohne weitere Beschichtung nur durch ca. 34 nm GaAs vom Elektrolyt getrennt wird. Im Folgenden wird diskutiert, durch welche Parameter das Sensordesign optimiert werden kann.

5. Parameter für das Sensordesign

Die Bedeutung der Parameter bei der Sensorkonstruktion hängt von seiner Architektur ab. Eine besondere Schwierigkeit beim Herstellen einer FAPS-Struktur stellt der Epitaktische Lift-Off (ELO) dar [19], dessen mechanische Belastung die Halbleiterstrukturen oft zerstört. Verzichtet man auf ein Sensordesign mit ELO, kann man mit einer alternativen Architektur dennoch Materialparameter untersuchen, die auch für den FAPS gelten. Betreibt man die FET-Kanäle anstelle einer rückwärtigen Gate-Elektrode mit einer dem Elektrolyt zugewandten Gate-Elektrode, erhält man anstelle eines MOS-FET (Metal-Oxide-Semiconductor-FET) einen EOS-FET (Electrolyte-Oxide-Semiconductor-FET).

5.1 Der FAPS als MOSFET

Der FAPS bildet in seinen Messpunkten MOSFETs, bei denen der Quantentopf als eigentlicher FET-Kanal durch eine d≈200 nm dicke Isolationsschicht („Oxid“) aus GaAs und AlGaAs (vgl. Abb. 3.d) von der Gate-Elektrode aus Metall getrennt ist, siehe Abb. 5.a). Diese MOSFETs werden im Folgenden mit dem Standartmodell eines p-Kanal MOSFET verglichen, der in Inversion betrieben wird [23].

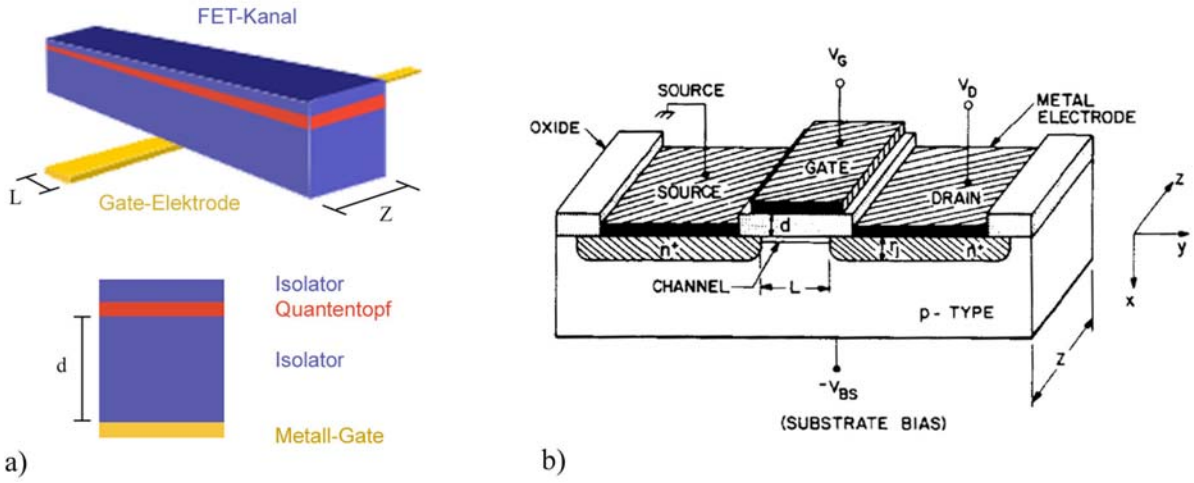

Abbildung 5: a) MOSFET am Kreuzungspunkt des FAPS. b) MOSFET mit p-Halbleiter Kanal, aus [23].

Der Strom durch den Leitungskanal eines in Inversion betriebenen p-Kanal MOSFET lässt sich annähernd beschreiben durch

$$I_{SD} \approx \left(\frac{Z}{L}\right)\mu_n C_i (V_G - V_T)\cdot V_D \quad für\, V_D << (V_G - V_T)$$

$$mit\ V_T = 2\Psi_B + \frac{\sqrt{2\varepsilon_S q N_A (2\Psi_B)}}{C_i}$$

Formel 1: Strom I_{SD} durch den Leitungskanal eines p-Kanal-MOSFET in Inversion (vgl. Abb. 5.b) für kleine Spannungen V_D am Leitungskanal [23]. μ_n ist die Elektronenbeweglichkeit, C_i die Kapazität der Isolatorschicht der Dicke d pro Einheitsfläche (vgl. Abb. 5.b), V_T die Schwellenspannung, die den Beginn des linear ansteigenden Bereichs von $I_{SD}(U_G)$ kennzeichnet. Ψ_B ist die Potentialdifferenz zwischen Fermilevel E_{Fp} des p-Halbleiters und seinem intrinsischem Fermilevel E_i an der Drain-Elektrode, siehe [23], ε_S ist die Dielektrizitätskonstante des p-Halbleiters, q die Elementarladung und N_A die Akzeptor-Dotierungs-Dichte.

Diese Näherung gilt für den linear ansteigenden Bereich der Kennlinie $I_{SD}(V_G)$ bei konstantem und kleinem V_D, vgl Abb. 3.c). Kleine Spannungsänderungen an der Gate-Elektrode können umso besser detektiert werden, desto steiler $I_{SD}(V_G)$ ist.

$$S \equiv \frac{\partial I_{SD}}{\partial V_G}\Big|_{V_D = const.} = \frac{Z}{L}\mu_n C_i V_D$$

Formel 2: Die Steigung S von $I_{SD}(V_G)$, für $V_D << (V_G - V_T)$.

Um S zu vergrößern, kann man aus Formel 2 für das FAPS-Design folgende Regeln ablesen.

1. Die Kanalbreite Z sollte groß sein.
2. Die Breite der Gate-Elektrode L sollte klein sein.
3. Die Elektronenbeweglichkeit μ_n sollte groß sein.
4. Die Isolator-Kapazität C_i sollte groß sein.

Die Gültigkeit der Regeln 1. und 2. wurde für den FAPS bereits gezeigt [19]. Die Elektronenbeweglichkeit in GaAs, dem Halbleitermaterial des FAPS, liegt bei einer Temperatur von 300K generell höher als in Silizium [23]. Bei sehr niedrigen Dotierungen mit

einer Donatoren-Konzentration von $10^{14}/cm^3$ erreicht man in Silizium eine Elektronenbeweglichkeit von maximal ca. $\mu_n = 1{,}7*10^3$ $cm^2/(Vs)$, die bei einer höheren Dotierung von $10^{17}/cm^3$ auf ca. $\mu_n = 0{,}8*10^3$ $cm^2/(Vs)$ abnimmt [23]. Für das Q2DEG der hier verwendeten GaAs-Heterostruktur ist eine Beweglichkeit von $\mu_n = (4{,}87\pm0{,}20)*10^3$ $cm^2/(Vs)$ bekannt [19], die somit um einen Faktor 3 höher liegt als bei Silizium MOSFETs. Die Kapazität des Isolators pro Einheitsfläche lässt sich schreiben als

$$C_i = \frac{\varepsilon_i}{d}.$$

Formel 3: Isolatorkapazität pro Einheitsfläche C_i, Dielektrizitätskonstante des Isolators ε_i, Isolatordicke d

Die hier verwendeten GaAs-Heterostrukturen haben die Werte
d = 200 nm (siehe Abb.3.d) sowie $\varepsilon_i = \varepsilon_{GaAs}*\varepsilon_0 = 13{,}1 * 8{,}854*10^{-14}$ F/cm [23]
und somit $C_i = 58$ nF/cm^2. Die Isolatordicke d wurde in dieser Probe nicht verkleinert, da das Schichtsystem bei der Sensorherstellung im ELO-Schritt diese Dicke zur mechanischen Stabilität benötigt. Zukünftige Proben könnten diese Stabilisatorschicht auf der dem Elektrolyt zugewandten Seite des Quantentopfs tragen, um sie nach dem ELO-Schritt durch Ätzen auf Minimaldicke zu reduzieren. Dies ist nötig, da die Dicke der Schichten an der Oberseite des Quantentopfs die Messempfindlichkeit mitsteuert, wie im Folgenden gezeigt wird.

5.2 Einfluss der Isolationsschicht auf der FET-Kanal-Oberfläche, EOSFET

An der Oberseite des FET-Kanals trennt zunächst eine Schicht von ca. 34 nm aus AlGaAs und GaAs das Q2DEG vom Elektrolyt. Diese elektrische Isolatorschicht dient teilweise als Potentialwall zur Quantentopfstruktur im FET-Kanal (vgl. [19] und Abb.3d) und hält einen Sicherheitsabstand zum Elektrolyt. Betrachtet man

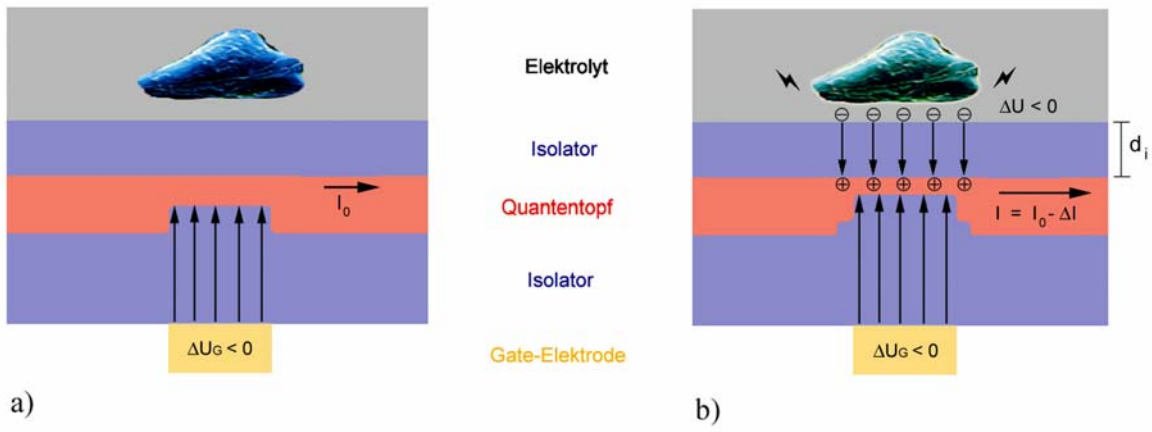

Abbildung 6: EIS auf MOSFET. Aktiver Messpunkt vor (a) bzw. während (b) eines Testpotentials. b) Ein negatives Testpotential ΔU polarisiert die Isolationsschicht der Dicke d_i und verarmt den Leitungskanal (Quantentopf) lokal an Elektronen, was hier schematisch durch eine Kanalverengung angedeutet ist. Der gemessene Strom sinkt aufgrund des erhöhten Widerstands, $I=I_0-\Delta I$.

einen FAPS-Messpunkt im Elektrolyt, erkennt man eine EIS-Struktur (Electrolyte-Insulator-Semiconductor) auf dem MOSFET. Elektrolyt- und Isolatorschicht beeinflussen im idealisierten Modellfall eines MOSFET (vgl. 4.1) nicht dessen $I_{SD}(U_G)$ Charakteristik. Dagegen wird eine Oberflächenpotentialschwankung an der Oberfläche des EIS-Isolators in diesem eine Polarisationsänderung bewirken, die zur Umladung seiner Grenzflächen führt, siehe Abb.6. Auf der Halbleiterseite ist diese Grenzfläche durch den Quantentopf definiert, dessen Leitungselektronen lokal verdrängt werden, wodurch der Kanalwiderstand dort erhöht wird, vgl. auch Abb.4.b. Aufgrund der konstanten Spannung U_{SD} über den FET-Kanal resultiert dies in einer Stromänderung ΔI_{SD}. Auf diese Weise wird das ursächliche Signal detektiert, was im Anwendungsfall ein neuronales Aktionspotential wäre. Wichtig an diesem simplen Bild der kapazitativen Signaleinkopplung ist, dass der Isolator des EIS-Systems einen Kondensator darstellt. Die induzierte Umladung ΔQ bei einem angelegten Testpotential ΔU ist

$$\Delta Q = C \cdot \Delta U = \frac{\varepsilon \cdot A \cdot \Delta U}{d_I}.$$

Formel 4: ΔQ ist die vom Testpotential ΔU induzierte Ladung an den Kondesatorplatten, C ist die Kapazität des Kondensators, ε die Dielektrizitätskonstante seines Isolators, A die Kondensator-Fläche und d_I die Isolatordicke des Kondensators.

Je größer die induzierte Umladung ΔQ ist, desto größer wird die Stromänderung ΔI_{SD} im MOSFET und desto empfindlicher wird der Sensor sein. Bei gegebener Kondensator-

(=Messpunkt-) Fläche wird ΔQ maximal, wenn folgende Regeln für das Sensordesign befolgt werden:

1. Die Dielektrizitätskonstante ε des Isolatormaterials sollte groß sein.
2. Die Dicke d_I der Isolationsschicht sollte gering sein.

Verglichen mit der DK von amorphem SiO_2 (ε=3.9 bei 300K) ist die des Isolators über dem Quantentopf hoch, wenn man hierfür ε=13.1 von GaAs ansetzt. Eine der größten DK bietet Hafnium-Oxid mit ε≈40 [24]. Solche „high-k" Materialien werden für die Mikroelektronik gesucht um bei fortschreitender Strukturverkleinerung Leckströme durch die Oxidschicht zu vermeiden, wenn diese reduziert wird. Wie weit kann man nun die Isolatordicke des FAPS verringern? Tatsächlich könnte man einen Teil der 34 nm GaAs/AlGaAs durch Ätzen entfernen, ohne die Struktur zu beeinträchtigen. Abb.7.b) zeigt einen GaAs-Heterostruktur-Testkanal, der als EIS-Struktur betrieben wird (Referenz K1).

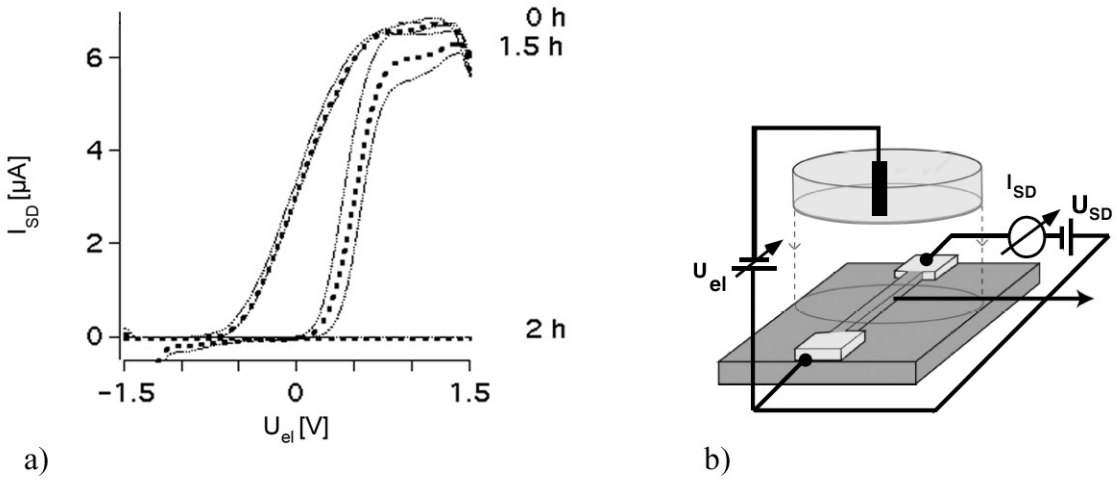

Abbildung 7: a) Kennlinien einer b) GaAs-Heterostruktur im EIS-Aufbau. Die Kanallänge beträgt 2,5 mm und die Kanalbreite 100 µm. U_{SD} = 140 mV war konstant, der Elektrolyt war 140 mM NaCl in Wasser (Millipore).

Aus Abb 7.a) kann man entnehmen, dass die Steigung S sich nach 1,5 Stunden im Elektrolyt etwa verdoppelt hat. Dies entspricht nach den Formeln 2) und 3) einer Halbierung der Isolatiosschichtdicke. Die Ätzrate des Elektrolyten von GaAs liegt bei etwa 8 nm/h (Referenz K1). Demnach liegt die Mindestdicke des Isolators über dem Q2DEG der Heterostruktur irgendwo zwischen 17 – 22 nm. In Abb. 7.a führt die abnehmende Isolatordicke über die Zunahme der Kapazität zu einem Rechts-„Shift" der Kennlinie, die sich mit der Abhängigkeit der Schwellenspannung U_T von der Kapazität C_i erklären lässt, vgl. Formel 1). Das Shiften

der Kennlinie stellt einen prinzipiellen Unterschied des FET-Kanal Betriebs im MOS und im EIS-Aufbau dar. Dennoch könnte man zu Testzwecken EIS-Strukturen aus GaAs-Heterostrukturen als Oberflächenpotentialsensor konstruieren [19]. Für beide Logiken, EOS und MOS-Aufbau, muss man mit einer Verschlechterung der Sensorkennlinien rechnen, wenn man die Sensoroberfläche längere Zeit im Zellmedium inkubiert, da Ablagerungen aus z.B. Serum- und Zellproteinen eine zusätzliche Isolationsschicht bilden können.

Für den FAPS gilt, dass die Dicke d_I seiner Isolationsschicht so gering wie möglich sein sollte. Dabei geht es nicht nur um die GaAs/AlGaAs-Isolation seiner Heterostruktur, sondern insbesondere um zusätzliche Isolationsschichten, mit denen das elektronische Bauteil im aggressiven Elektrolyt verkapselt werden muss.

6. Korrosion von GaAs

GaAs besitzt unter atmosphärischen Bedingungen eine native Oxidschicht von 3-4 nm Dicke, die aus einem amorphen Mix von Ga_2O_3, As_2O_3 und elementarem As besteht, wie man aus XPS-Messungen weiss [25]. Die Oxide sind wasserlöslich, so dass in wässriger Umgebung, pH-Wert abhängig, ein Abtransport stattfindet und die Neubildung dieser Oxide durch den Sauerstoff im Elektrolyten erfolgen kann, wodurch ein kontinuierlicher Ätzprozess entsteht.

6.1 Elektrochemie an der GaAs-Oberfläche

Die Ursache für die Bildung einer Oxidschicht liegt in den elektrischen Eigenschaften des Halbleiters [23]. An einer idealen Bruchfläche von n-GaAs (negativ dotiert) ist die periodische Zink-Blende Gitterstruktur plötzlich unterbrochen, so dass offene Bindungsstellen existieren, in denen unbesetzte Atomorbitale zusätzliche Elektronenzustände anbieten („intrinsische“ Oberflächenzustände). Die kontinuierliche Energieverteilung aller Oberflächenzustände (inklusive „extrinsischer“ Oberflächenzustände) deckt die verbotene Zone im Halbleiter-Band-Diagramm an seiner Oberfläche ab. Die Dichte dieser Zustände liegt, abhängig vom Energielevel, in einer ähnlichen Größenordnung wie die der Oberflächenatome (10^{12}-10^{14} $cm^{-2}eV^{-1}$, siehe [26]) und hat unter Angleichung von Halbleiter- und Oberflächen- Fermilevel eine Verbiegung der Bandstruktur des Halbleiters zur Folge,

siehe Abb. 8.a. Geht man im Modell vom Vakuum in den Elektrolyt, hat man eine Situation ähnlich einer Metall-n-Halbleiter Kontaktstelle (Schottky-Kontakt), vgl. Abb 8.b und etwas detaillierter, Abb.10.a.

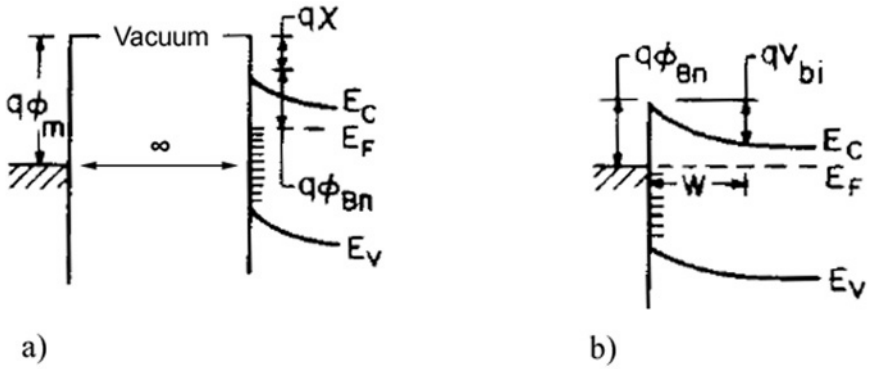

Abbildung 8: Band-Diagramme eines n-Halbleiters mit Oberflächen-Zuständen a) im Vakuum in grosser Distanz zu einer Metallfläche und b) im direkten Kontakt mit einer Metallfläche (Schottky-Kontakt). Aus [23].

Im atomaren Bild werden Akzeptor-Oberflächenzustände unterhalb des Fermilevels von den Majoritätsladungsträgern (also Elektronen für n-GaAs) aufgefüllt und durch die so gefangene Ladung eine negativ geladene Oberfläche erzeugt, als würde man von außen eine negative Spannung anlegen.* Diese wiederum erzeugt ein elektrisches Feld, das den Halbleiter bis zu einer bestimmten Tiefe W an Elektronen verarmt. Für die Oxidbildung ist nun wichtig, dass in diesem Feld Löcher h^+ an die Halbleiteroberfläche diffundieren können und den Startpunkt für eine komplexe Oberflächenoxidation darstellen, die in ihrer Mechanik komplexer ist als es folgende Reaktionsgleichungen beschreiben:

$$GaAs + 6\,h^+ \rightarrow Ga^{3+} + As^{3+},$$

$$4\,Ga^{3+} + 3\,O_2 \rightarrow 2\,Ga_2O_3,$$

$$4\,As^{3+} + 3\,O_2 \rightarrow 2\,As_2O_3,$$

oder

$$GaAs + 3\,H_2O + 6h^+ \rightarrow \tfrac{1}{2}\,Ga_2O_3 + \tfrac{1}{2}\,As_2O_3 + 6H^+ \quad [27]$$

Zum Beispiel ist die Bildung von Ga_2O_3 thermodynamisch favorisiert, was unter Entstehung von elementarem Arsen in

$$As_2O_3 + 2GaAs \rightarrow Ga_2O_3 + 4As$$

resultiert [25]. Der zeitliche Verlauf der Bildung sowie die laterale und vertikale Verteilung der Produkte ist inhomogen und nicht komplett aufgeklärt [25, 28]. Das elementare Arsen gilt als weitere wichtige Ursache für Oberflächenzustände (extrinsischer Natur) welche die GaAs-Oberfläche elektrisch dominieren [25, 26, 29]).

* Donatoren-Oberflächenzustände erzeugen ebenfalls lokalisierte negative Oberflächenladung

Klar ist, dass durch eine verstärkte Lochbildungsrate die Oxidwachstumsgeschwindigkeit erhöht wird. Dies erreicht man z.B. durch anodische Schaltung des Halbleiters und durch Bestrahlung mit Licht, das eine größere Energie $E=h\cdot\nu$ haben muss, als der Breite der Bandlücke E_g entspricht, vgl. Abb.9.a [30] E_g=1,42 eV für GaAs bei einer Temperatur von 300K.

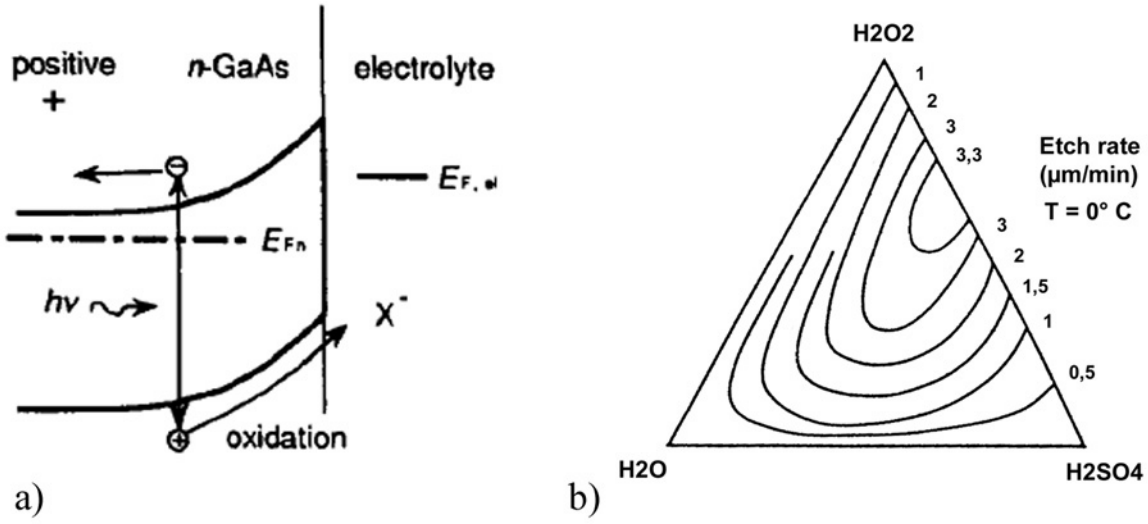

Abbildung 9: a) Elektrochemische Reaktion von anodisch gepoltem n-GaAs. Licht-generierte Löcher an der Oberfläche sind für die Oberflächenoxidation verantwortlich. Aus [30]. b) Ätzraten von $H_2O/H_2O_2/H_2SO_4$ auf GaAs(100). Aus [31].

Wären die Oxide von GaAs nicht wasserlöslich, würde die Oxidschicht wie im Fall von Silizium und vielen Metallen eine natürliche Passivierungsschicht bilden, und der Korrosionsprozess würde zum erliegen kommen. Sauerstoffgehalt und pH-Wert des Elektrolyt beeinflussen den Korrosionsprozess in seiner Geschwindigkeit. Die Variation dieser Größen wird genützt beim Ätzen mit dem $H_2O/H_2O_2/H_2SO_4$-System [31], dessen Ätzraten auf diese Weise genau eingestellt werden können, siehe Abb. 9.b.

6.2 Konsequenzen der GaAs-Elektrochemie für den FAPS

Für GaAs-Strukturen in Wasser bei 37 °C und 5 % CO_2-Atmosphäre (Zellkulturbedingungen) ergaben sich Ätzraten von ca. 4 nm/h (Referenz K1). Bei physiologischem Kochsalzgehalt von 140 mM NaCl ist diese Rate nochmals verdoppelt. Kohlendioxid senkt in Wasser als Säure den pH-Wert, gemäß $CO_2 + H_2O \rightarrow H_2CO_3$ und könnte so verstärkend zur Korrosion beitragen. Der Betrieb von FAPS-Strukturen oder FET-Kanälen aus GaAs-Heterostrukturen erfolgt unter variablen Gleichspannungen. Gerät man in den Spannungsbereich, der das GaAs-Material gegenüber dem Zellmedium/Elektrolyt anodisch polt, fördert man wie oben beschrieben die elektrochemische Korrosion und zerstört die Strukturen dauerhaft, was aus den in (Referenz K1) durchgeführten elektrischen Messungen (z.B. Voltammetrie) deutlich wird. Da auch unter kathodischer Polung von GaAs eine irreversible Oberflächenchemie induziert [30], somit das Oberflächenpotential modifiziert wird und zudem Na^+-Ionen in den Halbleiter gezogen werden, zeichnen sich schwierigste Bedingungen bei der Messung von Oberflächenpotentialschwankungen mit dem FAPS ab.

An den Kreuzungspunkten von Gate-Elektroden und FET-Kanal am FAPS findet man eine weitere kritische Situation. n-GaAs und Metall, z.B. ein NiCr-Leitungsbahn wie in Abb. 10.b, bilden hier einen Schottky-Kontakt, siehe Abb 10.a, in dem Elektronen vom GaAs in das Metall fliessen, und so im Halbleiter eine Raumladungszone entstehen lassen, die wiederum die Loch-Diffusion an die Halbleiteroberfläche fördern, wo anodische Oxidation stattfindet, siehe Paragraph 5.1. Offenbar sind diese Kreuzungspunkte sichere Keimstellen für Korrosion.

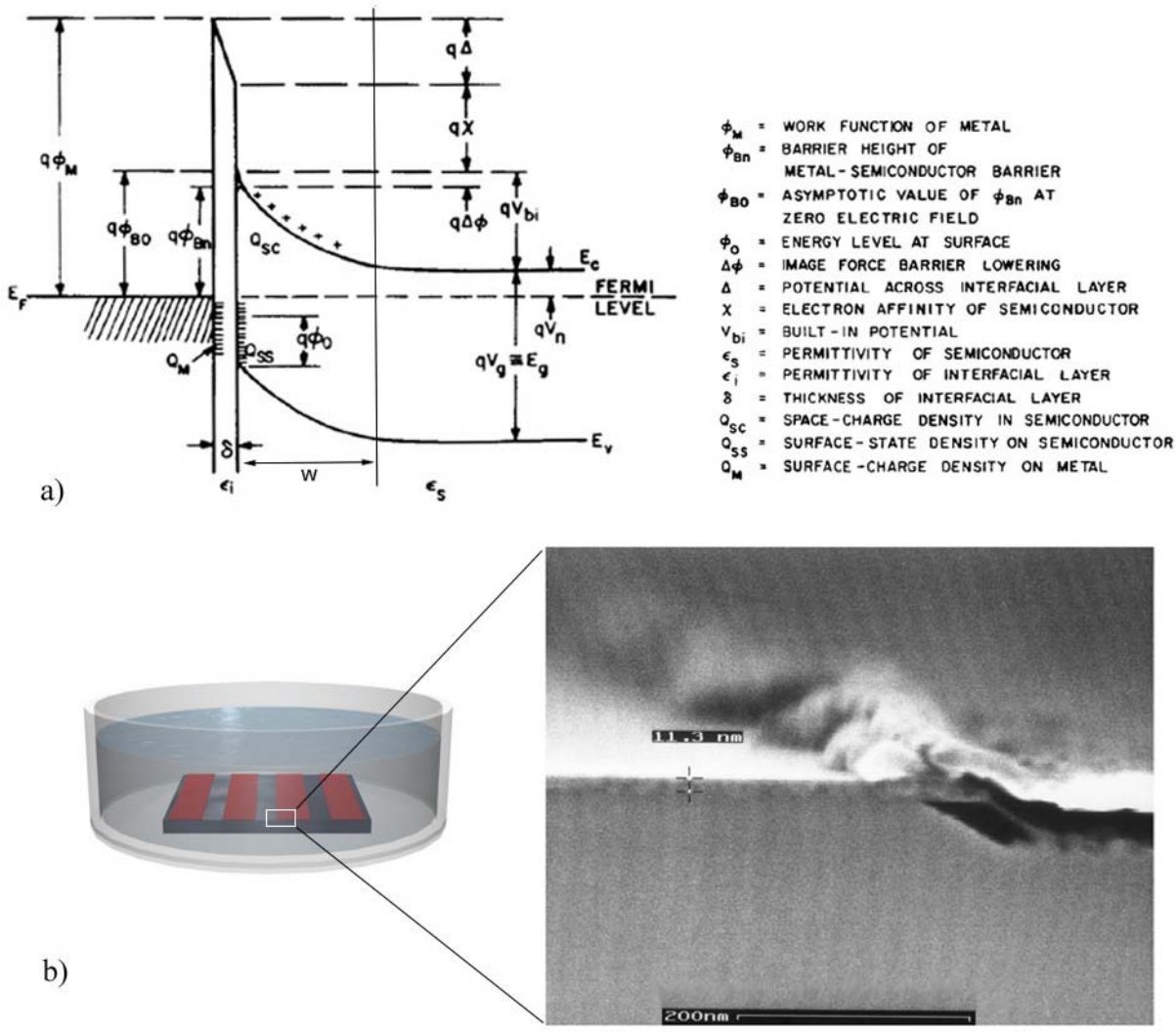

Abbildung 10: a) Detailliertes Energie Band-Diagramm einer Metall-n-Halbleiter Kontaktstelle (Schottky-Kontakt) mit einer atomaren Zwischenschicht. Aus [23]. b) Cartoon (links) und SEM-Aufnahme (rechts) der Bruchstelle eines n-GaAs Substrates nach 12 h bei 37 °C in Wasser (Millipore). Das Substrat war lithographisch mit 10 nm dicken und 10 µm breiten NiCr-Streifen versehen und danach mit einer 11 nm dicke Organosilikat-Beschichtung verkapselt worden. Man erkennt links in der Aufnahme die markierte Organosilikatschicht, die bis unter den Rand des NiCr-Streifens reicht und das GaAs-Substrat offenbar perfekt vor Korrosion schützt. Dagegen ist der Metall-Halbleiter-Kontaktbereich im rechten Bereich der Aufnahme stark unterhöhlt, was auf einen anodischen Oxidationsprozess zurückgeführt werden kann, siehe Text.

6.3 Konsequenzen der Korrosion für die lebenden Zellen

Die Verwendung von Materialien aus Verbindungen der giftigsten Schwermetalle in der Biologie birgt einen entscheidenden Nachteil. Die löslichen Korrosionsprodukte (hier: As_2O_3) sind meist ebenfalls sehr giftig und beeinträchtigen so schon in geringsten Konzentrationen die biologischen Funktionen, siehe Abb.10.

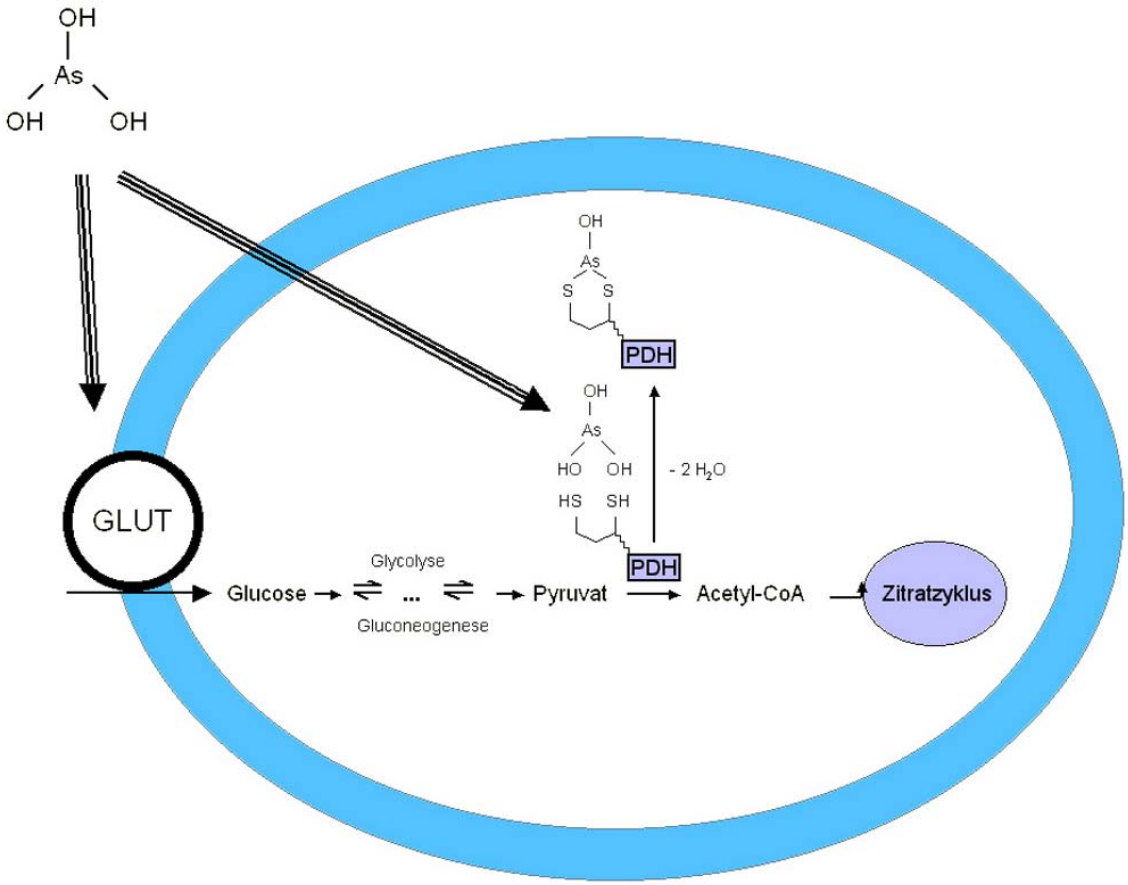

Abbildung 11: Arsen[III], im Bild als Arsenige Säure präsent, blockiert die Glukose-Transporter über die Zellmembran (GLUT) und blockiert den mitochondrialen Glukose-Metabolismus in Zellen, indem es einen stabilen 6-Ring mit den α,γ-dithiol-Gruppen von Proteinen ausbildet. Nach [32].

Toxische Erscheinungen treten erst bei bestimmten Dosierungen des Giftes auf. In dieser Arbeit werden die Grenzwerte der Vergiftung von NRK-Fibroblasten durch As(III) ermittelt und mit den Konzentrationen von As(III) verglichen, die im Korrosionsfall freigesetzt werden. Anders betrachtet, die Zellen sind in der Lage, quasi als Reporter der Korrosion, die Zersetzung ihres Substrates quantitativ nachzuweisen.

6.4 Antikorrosive Beschichtungen

GaAs-Elektronik und lebende Zellen funktionieren jeweils nur unter sehr unterschiedlichen Bedingungen. Die Konstruktion eines Zell-GaAs-Hybriden erfordert eine effektive Isolationsschicht zwischen den zwei Bereichen, die zur optimalen Kopplung möglichst dünn sein soll (vgl. 4.2) sowie im Betrieb die eigenen und auch die elektronischen Eigenschaften der GaAs-Oberfläche konstant hält, indem es unter anderem eine Rückbildung von GaAs-Oxid verhindert.

7. Organosilikate als Isolationsschichten

Für die Sensorentwicklung wurden von Beginn an geeignete Isolationsschichten benötigt, um mit Teststrukturen auf GaAs-Basis im Elektrolyt arbeiten zu können. Parallel zur Entwicklung eines nass-chemischen Verfahrens wurde eine Bedampfungsmethode eingesetzt, die zunächst diskutiert werden soll.

7.1 Alternative: PECVD Beschichtung

„Plasma-Enhanced Chemical Vapor Deposition“ (PECVD, Plasmalab 80 Plus, Oxford Instruments) von Siliziumdioxid (SiO_2) oder Siliziumnitrid (Si_3N_4) ermöglicht die Beschichtung von Halbleiteroberflächen und Strukturen, wobei die besten Schichtqualitäten mit Mehrschichtsystemen erzielt werden können, die bei Temperaturen zwischen 400 °C und 800 °C ausgeheizt werden. Gerade für die Isolation in physiologischer Umgebung ist Si_3N_4 besser geeignet, da Natrium-Ionen Na^+ aus dem Elektrolyt zur Diffusion in SiO_2-Schichten neigen, insbesondere wenn diese kathodisch geschaltet sind [33, 34]. Doppelschichtsysteme aus SiO_2 und Si_3N_4 wurden für die Zell-Halbleiter-Kopplung bereits erfolgreich verwendet [35-38]. Bei der PECVD-Beschichtung von Halbleiter-Heterostrukturen muss beachtet werden, dass um 300 °C und noch stärker bei höheren Temperaturen, Metallatome aus den Gate-Elektroden in den Halbleiter eindiffundieren und einen „ohmschen Kontakt“ herstellen, also einen irreversiblen Kurzschluss verursachen. Niedrigere Aufdampftemperaturen wiederum erzeugen stöchiometrisch nicht exakte Si_3N_4 Schichten. Der Kompromiss liegt bei der Erzeugung von Si_3N_4 Schichten von maximal 400 nm Dicke bei 300 °C für maximal 20 Minuten [19]. Von ultradünnen Schichten für den optimalen Sensorbetrieb ist man mit dieser Strategie weit entfernt, zumal Si_3N_4 zusätzlich mit Polyelektrolyten oder Peptiden (z.B. Poly-L-lysin, Fibronektin) beschichtet werden muss, um eine ausreichende Zelladhäsion zu ermöglichen. Offensichtlich haben die zelleigenen Markierungs- und Anker-Proteine, die Zelladhäsion vermitteln, nur eine geringe Affinität zu Si_3N_4 (vgl Abb. 8.a,b).

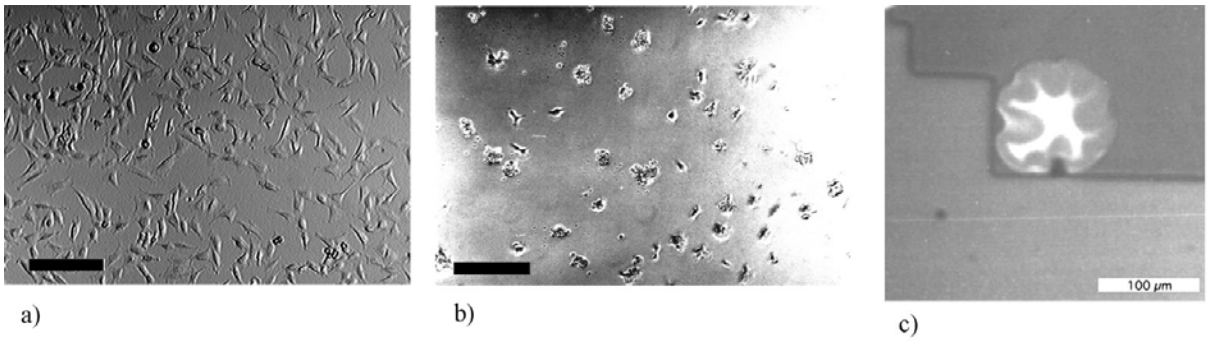

Abbildung 12: a), b) NRK-Fibroblasten nach 2 Tagen Zellkultur auf Si_3N_4 beschichteten Substraten, a) mit adhäsionsförderender Beschichtung, b) ohne Beschichtung. Länge des Skalierungsbalken: 200 µm. c) Beschichtungsdefekt (Blase) in einer 400 nm dicken Si_3N_4-Schicht über GaAs (aus [19]).

Der letztlich entscheidende Nachteil von Si_3N_4 ist dessen mangelhafte Haftung auf GaAs. Aufgrund der starren molekularen Struktur von CVD Beschichtungen (SiO_2, Si_3N_4) genügen Defektstellen oder Ränder, um großflächige Film-Ablösung zu verursachen [34], siehe Abb.7.c). Dieser Effekt wird bewirkt durch intrinsischen mechanischen Stress oder temperaturinduziertem Stress in den Schichten, elektrostatische Aufladung oder die Anwendung auf heterogenen Oberflächen, wie etwa strukturiertem GaAs-Substraten [39].

7.2 Organosilikate auf GaAs: Glas auf GaAs

Im Elektrolyt demonstriert die Natur mit den Lipid-Doppelschichten von Zellmembranen eindrucksvolle elektrische Isolatoren, die das negative Zellinnere gegen den Elektrolyt abschirmen und so die Basis für komplexe Abläufe wie die elektrische Signalverarbeitung und spezifische Transportvorgänge legen. Selbstorganisation (Self-assembly) und Strukturbildung aufgrund entropischer Effekte sind die Basis dieser stabilen und selbst-heilenden Interfaces in einer hoch dynamischen und von stochastischen Prozessen geprägten Umgebung [40]. Künstliche Membranen bzw. Halb-Membranen (Lipid-Monolayer) wurden deshalb mit der Verfügbarkeit geeigneter Techniken wie dem Langmuir-Blodgett Übertrag [40] auf ihre technische Verwertbarkeit in elektrischen Interfaces von Halbleiterstrukturen getestet. Monolayer aus Cadmium-Arachidat, einem amphiphilen Molekül, wurden so durch die aufwändige LB-Technik auf GaAs-Substrate übertragen [41]. Lipid-Schichten ähnlich, aber durch kovalente Bindungen mit dem Substrat verbunden, sind sogenannte „Self-assembled monolayer“ (SAM) von langkettigen Molekülen mit Ankergruppen für die chemische Funktionalisierung und Passivierung verschiedenster Substrate [42].

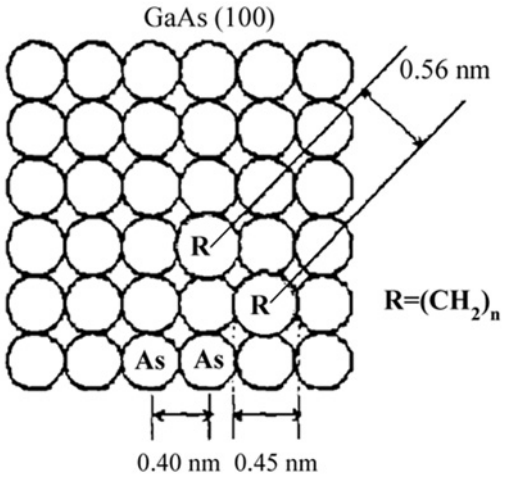

Abbildung 13: Modell eines Octadecylthiol Monolayer auf GaAs(100). Es wurde eine mittlere Stöchiometrie von einer Alkankette für jedes zweite Oberflächen-Arsenatom errechnet [41, 43].

Aufgrund ihrer, im Vergleich zu Lipidmonolayern, höheren Stabilität bilden sie ein vielversprechendes System [44] [45], das allerdings von der Beschaffenheit des Substrats abhängt. Im Fall von Alkanthiol-SAMs auf dem Halbleiter GaAs, erfordert dessen ca. 4 nm dicke native Oxidschicht ein zusätzliches Ätzen der Oberfläche vor dem chemischen Funktionalisieren. Dennoch führt die chemische Reaktivität der Oberfläche mit der Zeit zur Korrosion der defektreichen SAM-Schicht, weswegen diese Passivierungsmethode speziell in wässriger Umgebung unzureichend ist (Referenz K1).

Als Erweiterung des Konzepts von SAMs auf GaAs wurden in dieser Arbeit Schichten auf Basis von Mercaptopropyltrimethoxysilan (MPT) entwickelt, die durch Polymerisation vernetzt werden können und so eine hohe Stabilität auch in wässriger Umgebung aufweisen (Abb.10, Referenz K1). Wurzelnd auf der „Stöber-Synthese“ [46], ähnelt diese Beschichtungsmethode der daraus entwickelten Sol-Gel-Chemie (Abb. 11, [47, 48]), indem sich die Reaktionen nur in der Konzentration der beteiligten Substanzen unterscheiden. Dass hier verwendete Verfahren beruht auf einer stark verdünnten Sol-gel-Chemie (solution sol-gel process), die das Entstehen sehr dünner Glas-artiger Schichten von großer Homogenität und Dichte fördert (Referenz K1), ohne dass eine Ausheizen wie im Fall dickerer Schichten nötig wäre [48].

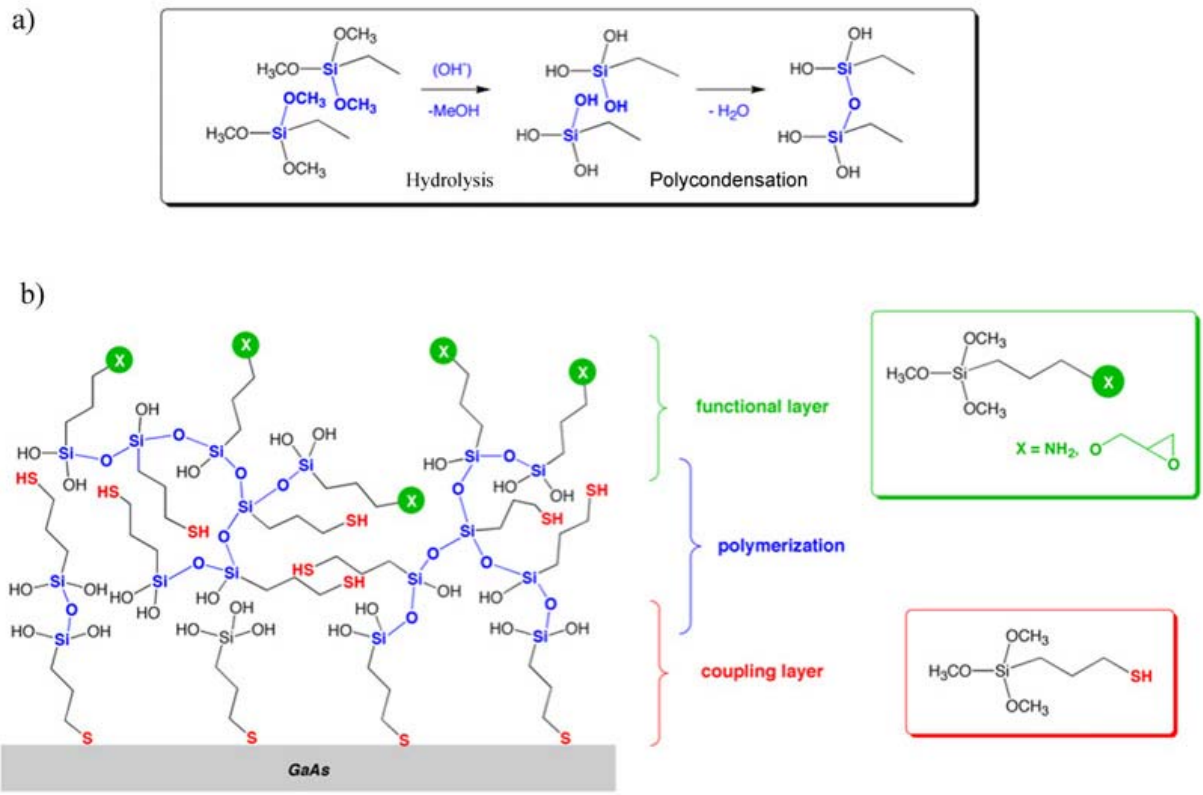

Abbildung 14: a) Polymerisation von Trimethoxy-silanen durch Hydrolyse der Methoxy-Gruppen und nachfolgender Kondensation der Silanol-Gruppen. b) Konzept zur Verwendung von Organosilikatschichten auf GaAs als ultradünne Passivierungsschichten in wässriger Umgebung. Ein Monolayer aus Mercaptopropyltrimethoxysilan (MPT) bindet als Kopplungsschicht das vernetzte Silan an das GaAs-Substrat. Nach aussen bietet eine abschliessende Silanschicht die Möglichkeit weiterer Oberflächenfunktionalisierung, z.B. durch Amino- oder Epoxy-Gruppen.

Das Konzept der Organosilikatschichten (siehe Abb.10) auf GaAs verwendet eine Kopplungsschicht aus einem MPT-monolayer, die über die Thiol-Gruppe eine kovalente Verbindung der Schicht mit dem Substrat herstellt. Gleichzeitig dient diese Schicht der elektrischen Passivierung des Substrats [25]. Dieselben Organosilikatschichten konnten auch auf Si_3N_4- und SiO_2- Oberflächen hergestellt werden, wo sie über die Methoxygruppen durch Hydrolyse und anschließende Kondensation mit Oberflächen-Silanol-Gruppen (-Si-OH) anbinden. In Abb.8.a wurde eine solche Beschichtung verwendet, um die Zell-Adhäsion auf Si_3N_4 zu verbessern.

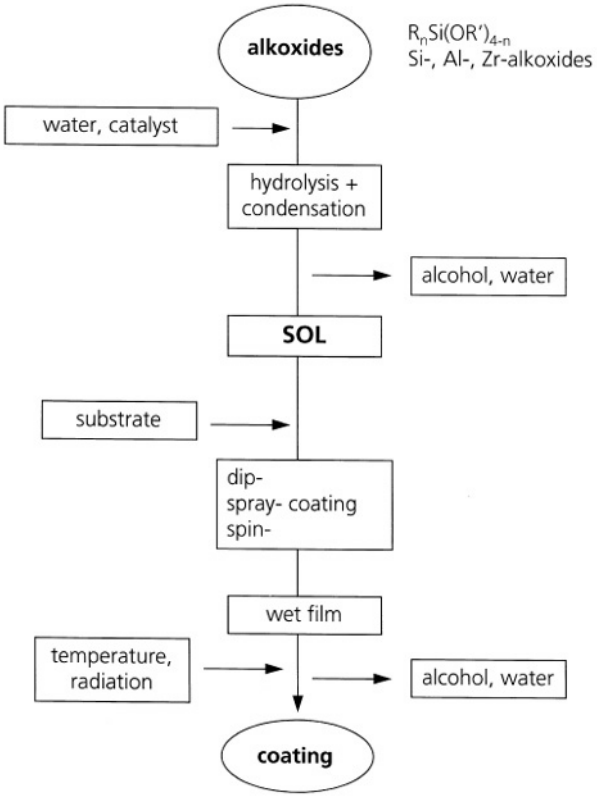

Abbildung 15: Sol-gel Chemie, aus [48].

Entscheidend ist hierbei die chemische Struktur der Oberfläche, die auf Organosilikaten durch die ganze Breite der Silan-Oberflächenchemie variiert werden kann [42]. Die Variabilität des Sol-gel Chemie durch Einbau unterschiedlicher funktioneller Gruppen [48] bei der Schichtsynthese könnte man auch für die hier untersuchten Organosilikate nützen, um z.B. durch Einbau von Metall-Alkoxiden (z.B. Zirkonium-Alkoxide) den Brechungsindex und die Dielektrizitätskonstante der Filme zu erhöhen [48]. Mit einem relativ hohen Alkan-Anteil sind die hier erzeugten Glas-ähnlichen „Organo"-Schichten relativ flexibel. Eine Erhöhung der Vernetzungsknoten-Dichte durch kurze anorganische Monomere wie z.B. TEOS (Tetraethoxysilan) senkt die Elastizität der Filme und erhöht die Wahrscheinlichkeit einer Film-Ablösung unter Belastung, ähnlich dem Fall von Si_3N_4. Als Beispiel für die Erzeugung unterschiedlicher Schichteigenschaften durch Variation des Monomers wurde n-Trifluoropropyltrimethoxysilan (FPT) verwendet, um die Zelladhäsion auf den Organosilikaten zu steuern. Fluor-Gruppen (-F) erzeugen deutlich inertere Oberflächen als Mercapto-Gruppen (-SH), vgl. Abb.12.

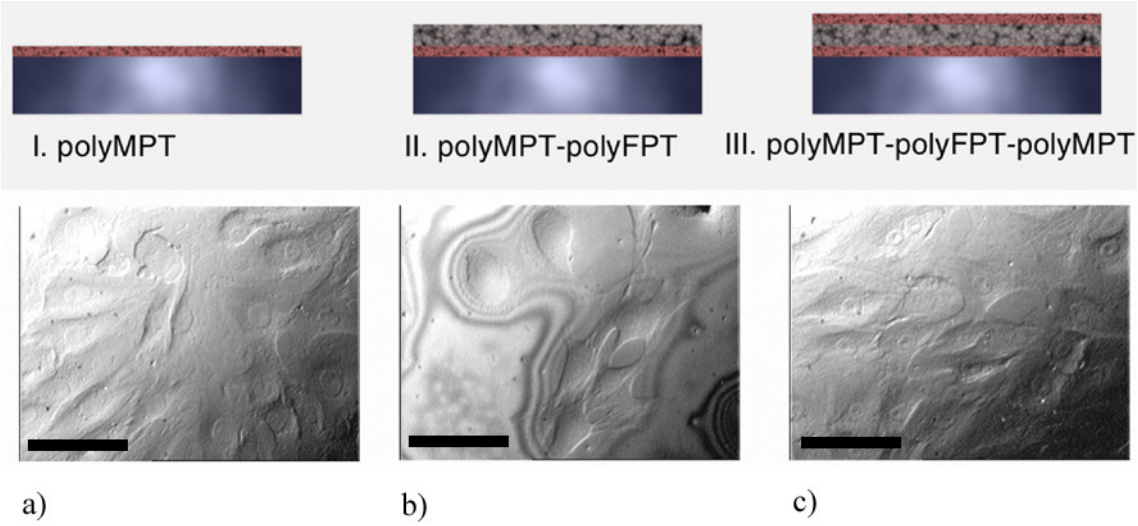

Abbildung 16: NRK-Fibroblasten nach 2 Tagen in Zellkultur, auf GaAs-Substraten mit verschiedenen Organosilikatschichten in Sandwichaufbau. Skalierungsbalken 100 µm. a) MPT als Monomer (polyMPT), Schichtdicke d=0,6 nm b) FPT als Monomer (polyFPT), d=1,8 nm. Die Schicht zeigt eine verminderte Zelldichte. c) MPT als Monomer, d=2,7 nm. Die Schichtdicken wurden ellipsometrisch bei variablem Brechungsindex ermittelt.

Die Eignung der Organosilikate als Korrosionsschutz wird in dieser Arbeit intensiv untersucht (Referenz K1). Als ungiftige und billige Alternative zu den effektiven Chromat-basierenden Beschichtungen (chromat conversion coatings) sind Korrosionsschutzschichten auf Sol-Gel Basis zur Zeit auf vielen Substraten Gegenstand der Forschung [49, 50].

8. Mikrostrukturanalyse von Organosilikaten auf GaAs mittels Röntgenreflektivitätsmessungen unter streifendem Einfall

Nach der Einführung eines neuen Passivierungskonzepts (vgl. Abb. 17) für GaAs interessiert besonders dessen Leistungsfähigkeit im Vergleich mit bekannten Passivierungsstrategien. Bis zu diesem Punkt ist vor allem klar, dass Organosilikate als Interface zwischen korrosiver biologischer Welt und toxischen Halbleiter-Nanostrukturen eine gute Barriere darstellen, die aber unter elektrischer Dauerbelastung nach wenigen Stunden zusammenbricht (Referenz K1).

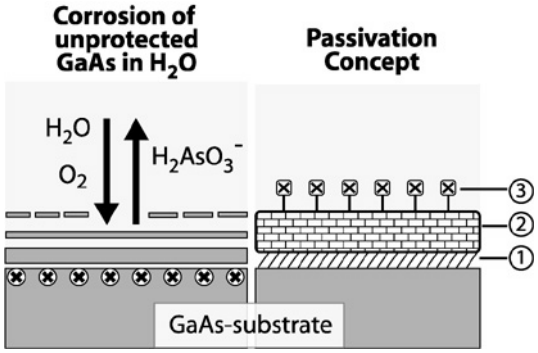

Abbildung 17: Links: Modell des technischen Problems. GaAs mit einer hohen Dichte an Oberflächenzuständen (Kreuzsymbole) korrodiert in Wasser und setzt dabei toxisches Arsen frei. Rechts: Passivierungskonzept für GaAs in Wasser. Die elektrisch/chemische Passivierungsschicht (1) der Oberfläche reduziert die Oberflächenzustände und koppelt die Diffusionsbarriere (2) ans Substrat. Die Glas-artige Struktur der langzeit-stabilen Isolationsschicht ermöglicht die einfache chemische Funktionalisierung der Oberfläche (3).

Unter atmosphärischen Bedingungen bleibt zu prüfen, ob die GaAs/Isolator-Grenzschicht hinreichend passiviert ist. Folgt man dem molekularen Bild aus § 5.1, wäre für eine perfekte elektrische Passivierung einer GaAs-Grenzfläche die Absättigung aller ungesättigten Bindungen aus der unterbrochenen Kristallstruktur nötig. Das ist mit Alkanthiolen aus sterischen Gründen nicht möglich (siehe § 6.2), was eine „perfekte“ elektrische Passivierung ausschliesst, da freie Bindungsstellen an der Kristalloberfläche und potentielle Gitterfehler als Ursache für intrinsische Oberflächenzustände gelten [41, 43]. Dies würde auch bedeuten, dass eine nachträgliche Oberflächenoxidation und damit wiederum eine Zunahme extrinsischer Oberflächenzustände ausgeschlossen wäre.

Zusammengefasst erwartet man von einer optimalen Passivierung auf Basis von Alkanthiolen

- die Eliminierung der extrinsischen Oberflächenzustände unter Verdrängung ihres verursachendem Mediums (GaAs-Oxid) durch ein wohl definiertes Material ohne solche Zustände, und
- die Unterbindung von Re-Oxidation und anderen Nachfolge-Reaktionen, die zu Oberflächenzuständen führen, also ein thermodynamisch stabiles System.

8.1 Passivierungsstrategien für GaAs

GaAs wurde in den 1960er Jahren in den SIEMENS Laboratorien synthetisiert, um einen direkten Halbleiter mit einer 5 mal höheren Elektronenbeweglichkeit im Vergleich zu Silizium zu entwickeln [51]. Für die Anwendung in digitaler Schaltungslogik war das Ziel eine MOS-Technologie auf Basis von GaAs, die eine effektive Passivierung der hohen Oberflächenzustandsdichte erfordert, wie sie im Fall von Silizium durch dessen Oxid SiO_2 relativ leicht erreichbar ist [23]. Mangels eines durchschlagenden Erfolges, aber getrieben von potentiellem ökonomischen Gewinn wurden immer wieder alternative Strategien zur Passivierung untersucht.

Alle Ansätze, insbesondere die nass-chemischen Verfahren auf Basis von anorganischen Sulfiden, organischen Thiolen oder anderen Adsorbaten scheiterten vor den Anforderungen nach einer leistungsfähigen, zuverlässigen und rentablen Oxid-Technologie [28, 45, 52, 53]. Speziell die Oxidrückbildung im Fall von monomolekularen Adsorptionsschichten (monolayer) stellt ein Problem dar [53]. Die derzeit erfolgreichste Strategie zur Oxidbildung auf GaAs verwendet eine monokristalline Schicht von $Ga_2O_3(Gd_2O_3)$, die mittels MBE (molecular beam epitaxy) aufgebracht wird. Der resultierende Oxid-Kristall ist thermodynamisch stabil und vermag die Oberflächenzustandsdichte in der Mitte der Bandlücke von GaAs (um 0,7 eV) auf ca. 10^{11} $cm^{-2}eV^{-1}$ zu senken, obwohl die Gitterkonstante des Oxids ungefähr doppelt so groß ist wie die von GaAs (5,65 Å bei 300 K) [54] [55]. „Depletion-mode“ MOSFETs auf der Basis von n-GaAs/Gadoliniumoxid sind bereits realisiert, während die Optimierung des Herstellungsprozess noch Gegenstand aktueller Forschung ist [55].

8.2 XRGI als Methode zur Untersuchung der Oxidbildung auf GaAs

Kann eine Passivierungsschicht von Organosilikaten auf GaAs das Oxid entfernen und die Rückbildung verhindern? Sind die Schichten auf diese Weise an Luft und Wasser stabil? Welche Prozessparameter bei der Organosilikatsynthese beeinflussen deren Leistungsfähigkeit? Zur Klärung dieser Fragen wurde in dieser Arbeit XRGI (X-ray reflectivity under grazing incidence) mit 9,5 keV-Synchrotron Strahlung (DESY, Hasylab, Hamburg) herangezogen, als Methode zur zerstörungsfreien Ermittlung von Materialeigenschaften wie Schichtdicke (in Angström-Auflösung), Interface-Rauhigkeit

sowie Elektronendichte, Materialdichte und Stöchiometrie der Schichten, vgl Abb.18. Für Details zur Methode siehe (Referenzen K3, K4).

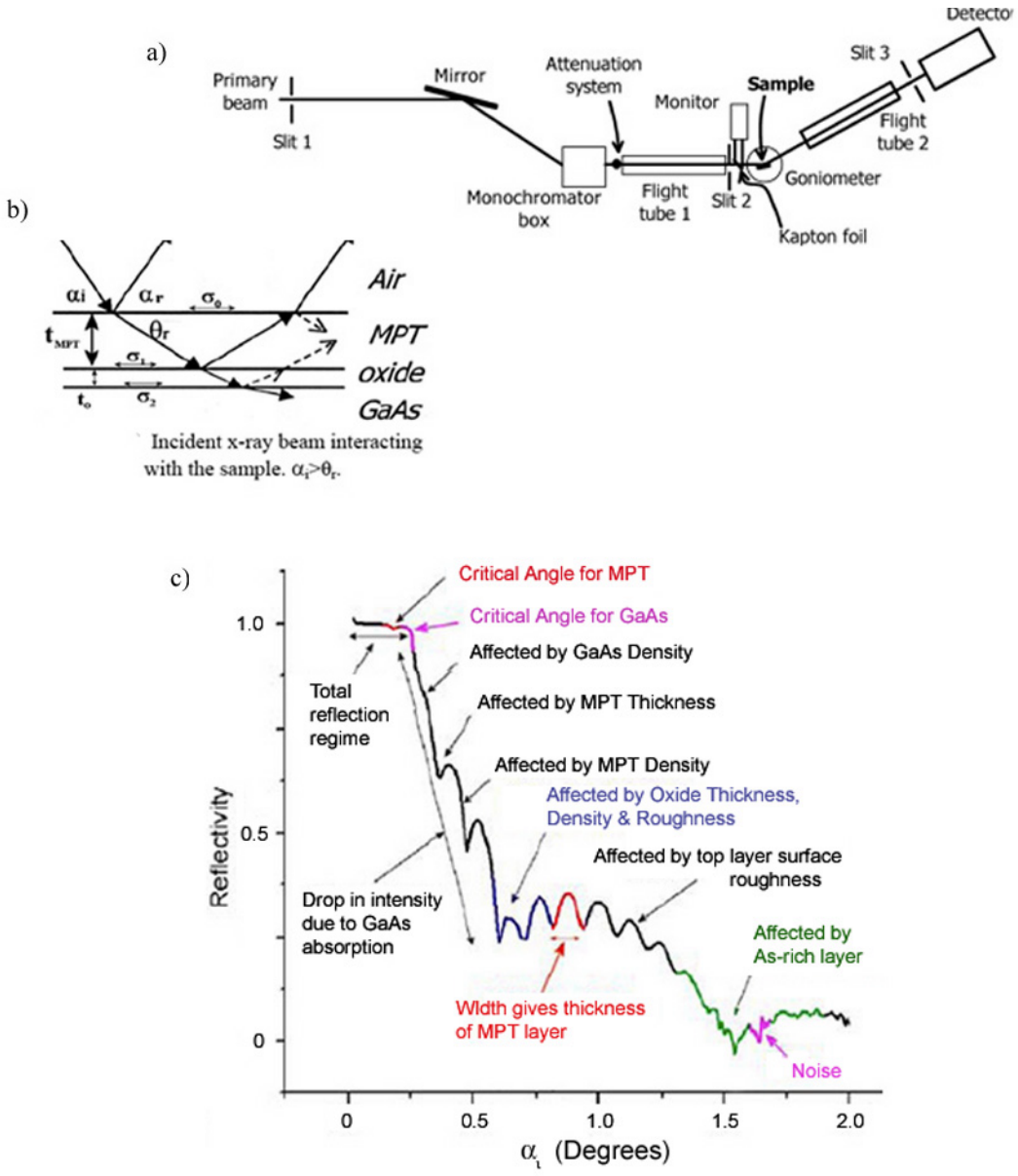

Abbildung 18: Röntgenreflektivitätsmessungen unter streifendem Einfall. a) Aufbau des Messplatzes Beamline E2, Hasylab, DESY, Hamburg b) Röntgenstrahlreflektion an mehrschichtiger Probe c) Interferenzbild der Röntgenreflektivität an der mehrschichtigen Probe.

8.3 Ergebnis (Referenzen K3, K4)

Die nasschemische Schichtherstellung führt zu teilweise inhomogenen Beschichtungen, was aus den unterschiedlichen XRGI-Kurven von ein und demselben Substrat deutlich wird, die sich unterscheiden. Zudem scheint die Methode im Fall der Organosilikate keineswegs völlig zerstörungsfrei zu sein, da bei den Wasser-exponierten Proben teilweise mit bloßem Auge eine Strukturveränderung erkennbar war, die sich in einer Verfärbung entlang des

einfallenden Röntgenstrahls ergab. Die Folge ist ein Messfehler, der Aussagen zur Wirkung von variierten Prozessparametern schwierig macht. Klar ist, dass sich eine Oxidschicht zwischen 8-37 Å Dicke nicht vermeiden lässt. Ein Ätzen der GaAs-Oberfläche zur Oxidentfernung scheint keinen Einfluss zu haben, vielmehr scheint sogar schon die Ausbildung eines MPT-Monolayer die Oberfläche zu ätzen. Eine leichte Zunahme der Oxidschichten unter einer Organosilikatschutzschicht um ca. 15% war nach 2-monatiger Alterung der Schichten festzustellen. Dies könnte man einer Sauerstoffdiffusion durch die Isolationsschicht zuschreiben oder alternativ langsamen Umformungsreaktionen unterhalb einer O_2-dichten Isolationsschicht. Es ist also nicht völlig klar, ob die Oxidschicht nie völlig entfernt war, durch O_2-Kontamination der Reagenzien entstand oder durch spätere Re-Oxidation aufgrund einer Gas-undichten Beschichtung generiert wurde. In jedem Fall scheint die Alkanthiolschicht die Oxidschicht nicht komplett verdrängen zu können. Diese Beobachtung deckt sich mit Literaturergebnissen aus XPS-Messungen [25] [56]. Die Organosilikatschicht selbst ändert ihre Eigenschaften unter Langzeit-Lagerung und Wasser-Exponierung nicht auffällig. Ein Ausheizen der Organosilikate bei 120 – 150 °C, um etwa noch nicht vollzogene Kondensationsreaktionen zur Vernetzung zu komplettieren, zeigte keinerlei Effekt.

In einer Schlussfolgerung könnte man planen, bei zukünftigen Proben auf das Ätzen mit O_2-haltigen Lösungen zu verzichten und mit völlig entgasten, O_2-freien Lösungsmitteln sowie Reagenzien und unter Argon-Atmosphäre zu arbeiten, um die Re-Oxidation beurteilen zu können. Zudem erfordert die Inhomogenität der Probenbeschichtungen einen statistischen Ansatz der Messungen. Die Organosilikatschichten erscheinen thermodynamisch stabil.

II. Cytotoxizität von CdSe und CdTe Nanokristallen

1. Überleitung

In Teil I dieser Arbeit wurden Quantentopf-Kanäle vorgestellt, die auf einer GaAs-Heterostruktur mit einem 2-dimensionalem Elektronengas (2DEG) beruhen. Die Elektronenzustände sind in diesem Kanal in z-Richtung quantisiert.

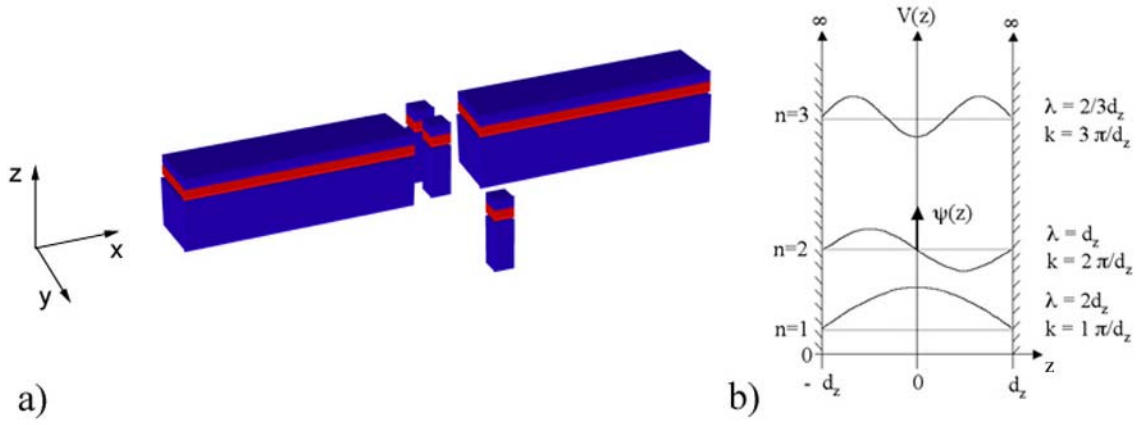

Abbildung II. 1: a) Vom Quantentopf-Kanal zum Quantenpunkt, realisierbar z.B. durch lithographisches Ätzen einer GaAs-Heterostruktur. b) Künstliche Atome: Die Lösungen der Schrödingergleichung, hier für den Fall eines Teilchens im rechteckigen Potentialtopfes mit unendlich hohem Potentialwall in einer Dimension z, zeigen diskrete Energieabstände. Die Eigenfunktionen Ψ sind stehende Wellen, ihre Betragsquadrate entsprechen den Aufenthaltswahrscheinlichkeiten der Elektronen.

Reduziert man die Kanaldimension auch in x und y-Richtung lithographisch auf bis zu 10 nm, erhält einen durch Potentialwälle begrenzten Bereich aus einigen 1000 bis 10000 Atomen, den man Quantenpunkt nennt [57]. Es gibt neben der lithographischen Methode (siehe Abb.II.1.a) einige weitere Strategien, um Quantenpunkte durch räumliche Strukturbildung zu definieren [58] [59] [60]. Von besonderer Bedeutung und im Mittelpunkt dieses Kapitels sind in Lösung synthetisierte Nanokristalle, auch bezeichnet als Kolloidale Quantenpunkte.

2. Überblick: Nanopartikel für die Biologie

Metall- und Halbleiter-Nanopartikel haben eine Größe im Bereich weniger Nanometer und bestehen mitunter nur aus einigen zehn bis hundert Atomen. Die unterschiedlichsten Morphologien sind bekannt (amorph, kristallin, rund, länglich, Tetrapod) mit oft noch

unbekannten elektrischen, magnetischen und optischen Eigenschaften, abhängig vom Material (Au, Ag, Co, $CoPt_3$, CdTe, CdSe, CdS, CdSe/ZnS, PbSe,Fe_2O_3, Al_2O_3, TiO_2) bzw. dem Materialmix im Fall von Heterostrukturen, siehe Abb.II.2. Hier wird anorganisches Material in den Größenbereich von Makromolekülen herunterskaliert und trifft damit die Dimension wichtiger biologischer Bausteine wie DNA, RNA und Proteine. Kombinationen von beiden sind Bio/Nano-Systeme mit bedeutendem Potential für die Anwendung in medizinischer Diagnostik, gezielter Therapie, molekularer Biologie oder Zellbiologie.

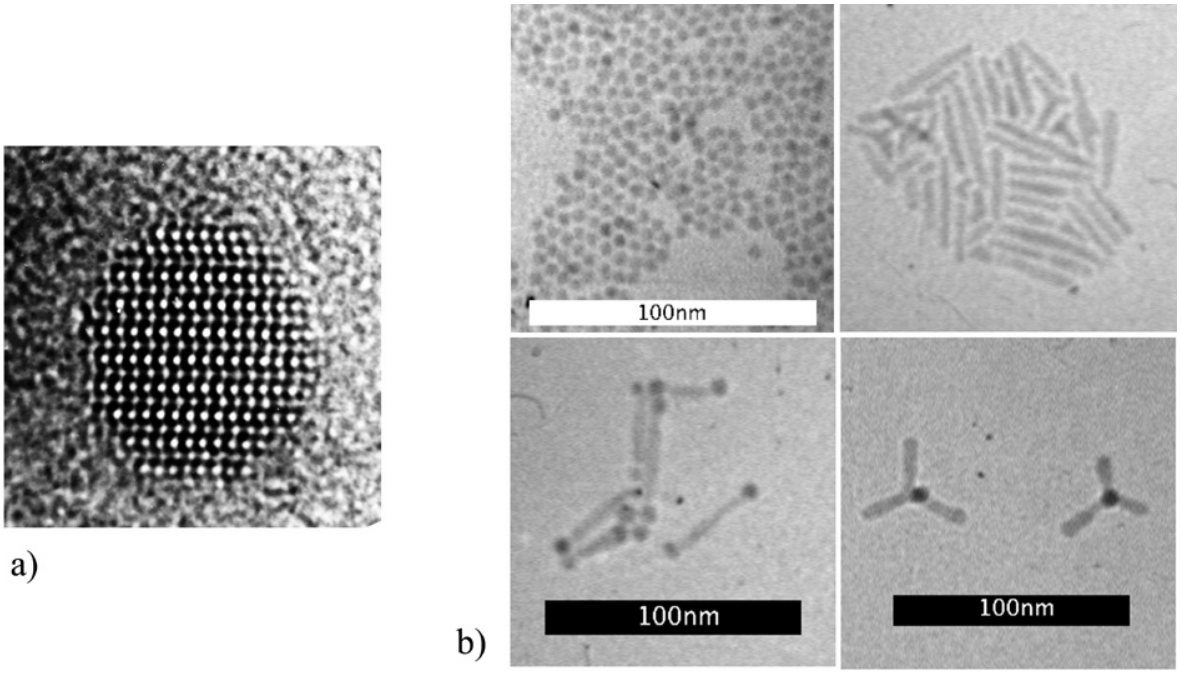

Abbildung II. 2: a) TEM-Aufnahme eines CdSe-Nanokristalls. Deutlich zu sehen ist das atomare Gitter des Einkristalls. b) TEM-Aufnahmen unterschiedlicher Morphologien von Monokristallen und Heterostrukturen, hier z.B. sphärische CdSe-Nanokristalle, Stäbchen-Strukturen aus CdS, Hantel-Strukturen aus CdS mit PbSe an den Endpunkten und CdTe-Tetrapods (TEM-Aufnahmen von Stefan Kudera).

Im Fokus des Interesses in dieser Arbeit stehen Halbleiter-Nanokristalle (NC), kristalline Cluster aus einigen hundert bis tausend Atomen. Auf dieser Größenskala zeigt Materie häufig ein Mischverhalten aus makroskopischen und atomaren bzw. molekularen Eigenschaften. Direkte Halbleiter ermöglichen die Erzeugung von Photonen aus der Rekombination von Elektron-Loch-Paaren, den Exzitonen. Die Wellenlänge λ des so emittierten Lichts entspricht dem Übergang der Halbleiter-Bandlücke

$$h \cdot \nu = E_c - E_v \quad \text{und} \quad \lambda = c_0/(n \cdot \nu),$$

wobei h das Plancksche Wirkungsquantum ist, n der Brechungsindex des Halbleiters für das Licht der Frequenz ν ist und c_0 die Lichtgeschwindigkeit im Vakuum. Reduziert man nun die räumliche Ausdehnung des Halbleiters in den Größenbereich der de Broglie Wellenlänge der

freien Ladungsträger von wenigen Nanometern, werden quantenmechanische Effekte relevant, weshalb man solche Halbleiter-Nanokristalle auch Quantenpunkte nennt. Die Energielevel und damit die möglichen Übergänge lassen sich durch die Lösung der Schrödingergleichung für Teilchen in einem eindimensionalen Potentialtopf abschätzen. Eine wichtige Eigenschaft ist die Abhängigkeit der so quantisierten Energielevel von der Ausdehnung d des Kristalls, vgl. Abb.II.1.b.

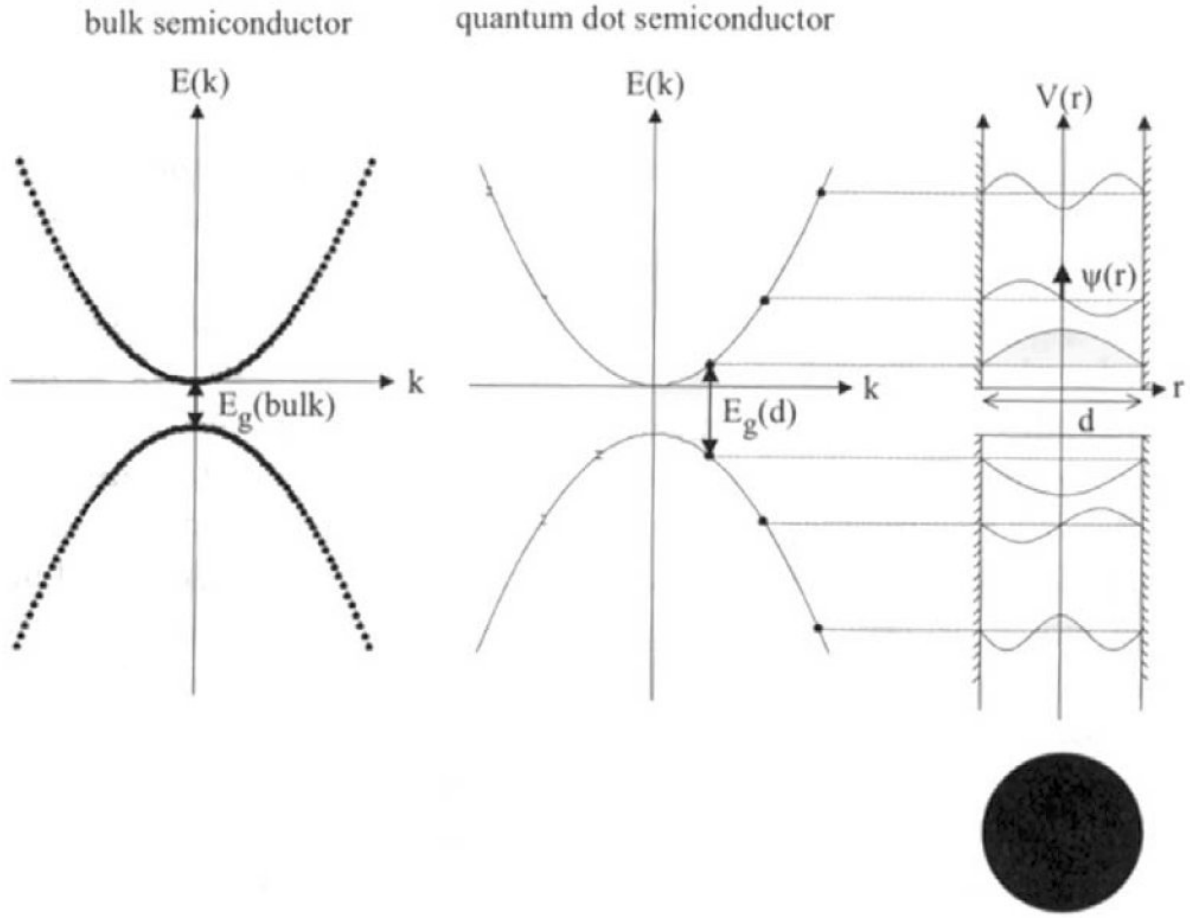

Abbildung II. 3: Energiezustände E(k) im Halbleiter. Die Bandlücke E_g ist im Halbleiter-Nanokristall von dessen Durchmesser, d.h., der Breite des Potentialtopfs d abhängig und wird durch die Grundzustände von Elektronen und Löchern bestimmt, siehe auch Abb.II.1.b.

Neben Halbleitern zeigen auch Nanopartikel aus anderen Materialien größenabhängige Eigenschaften. Metall-Nanopartikel, wie die in dieser Arbeit verwendeten Goldpartikel, weisen optische Absorptionsspektren auf, ähnlich denen von Halbleiter NCs. Hier allerdings resultiert die Absorption nicht von Übergängen zwischen erlaubten Energiezuständen, sondern durch Anregung von Oberflächen-Plasmonen, den kollektiven Schwingungen der Leitungselektronen und deren Moden an der Metalloberfläche. Als Konsequenz ist die Größenabhängigkeit der Plasmon-Frequenzen der Metalle im Nanometerbereich relativ klein,

für Goldpartikel ist das im Bereich zwischen 5 und 30 nm, bei einer Plasmonen-Resonanz Frequenz im Bereich von 530 nm.

Eine weitere wichtige Klasse sind magnetische Nanopartikel, wo das Trägermaterial durch die Dimensionierung ebenfalls neue Eigenschaften erhält. Ab einem bestimmten Punkt der räumlichen Eingrenzung können sich magnetische Bereiche wie einzelne magnetische Domänen verhalten, in denen alle Spins zusammen ein riesiges magnetisches Moment erzeugen. In einem Partikel sind bei hinreichend grossen Temperaturen die magnetischen Momente zunächst zufallsverteilt (super-paramagnetisch), jenseits einer kritischen Korngröße steigt die magnetische Koerzitivität drastisch (ferromagnetisch). Für Eisenoxid liegt die Grenze bei 25 nm. Funktionalisierte Eisenpartikel spielen die tragende Rolle in der Hyperthemie. Bei diesem therapeutischen Verfahren zur Bekämpfung einiger gefährlicher Tumorarten wird das kanzerogene Gewebe zunächst gezielt durch die ferromagnetischen Partikel markiert und diese anschließend durch Anlegen eines äußeren magnetischen Wechselfeldes thermisch angeregt. Dabei wird auf die Tumorzellen Wärme übertragen (ca. 45 °C) und sie sterben, während die Partikel sich auflösen und vom Körper ungeschadet resorbiert werden. Das Verfahren wird hier besonders erwähnt, weil es eine der ersten spektakulären Erfolge von Bionanotechnologie darstellt. Es befindet sich derzeit bereits in einer klinischen Erprobungsphase [61] [62] [63] [64].

Man kann zusammenfassend feststellen, dass sich nanostrukturierte Materialien von ihrem makroskopischen Trägermaterial in physikalischen und chemischen Eigenschaften unterscheiden, z.B. in optischer Absorption oder Fluoreszenz, Schmelzpunkt, katalytischer Aktivität, Magnetismus, elektrischer und thermischer Leitfähigkeit etc..

3. Halbleiter-Nanokristalle als Fluoreszenzmarker

Halbleiter-Nanokristalle fluoreszieren aufgrund der emittierenden Rekombination von angeregten Elektron-Loch Paaren, speziell CdSe oder CdTe emittieren Licht im sichtbaren Bereich des Spektrums.

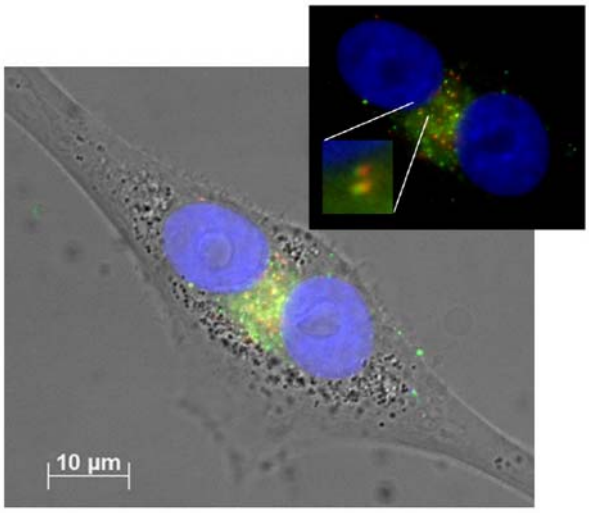

Abbildung II. 4: Unspezifische Aufnahme von CdSe-Nanokristallen.

Fluoreszenzbild von einer sich teilenden Brustkrebszelle vom Typ MDA-MB-235s. Blau markiert: Zellkerne, mit organischem Fluoreszenzmarker DAPI angefärbt. Rote Spots: CdSe-NC mit einer Fluoreszenz-Wellenlänge von 599 nm. Grüne Spots: CdSe-NC mit einer Fluoreszenz-Wellenlänge von 521 nm. Rote und grüne Farbspots werden Ansammlungen von NC zugeordnet, die durch Endocytose über Vesikeln in die Zelle gelangt sind [65].

Dabei sind die Fluoreszenzspektren symmetrisch und relativ schmal (30-40 nm Halbwertsbreite, „fwhm“), siehe Abb.II.4, die Lage ihrer Maxima entspricht der Bandlücke des Halbleiters, die wiederum vom Durchmesser des NC abhängt, siehe Abb.II.3. Durch die Größe des NC kann man folglich mit Präzision die Farbe des emittierten Lichts einstellen, was zahlreiche optische Detektionsverfahren mithilfe dieser Kristalle ermöglicht. Kleine CdSe-NC (ca. 2 nm) beispielsweise fluoreszieren grün, größere (ca. 5 nm) fluoreszieren rot. Durch den - im Vergleich zu organischen Fluorophoren - geringen Überlapp der Fluoreszenzspektren kann man parallel mehrere Farben detektieren [66] bis hin zu einem Signal-„Multiplexing“, in dem Millionen Marker durch ihren Farbcode unterschieden werden können [67] [68]. Das Absorptionsspektrum der NC wiederum ist kontinuierlich breit, wodurch mit einer einzigen Anregungswellenlänge alle NC zur Fluoreszenz angeregt werden können, was einen weiteren Vorteil gegenüber organischen Fluorophoren darstellt.

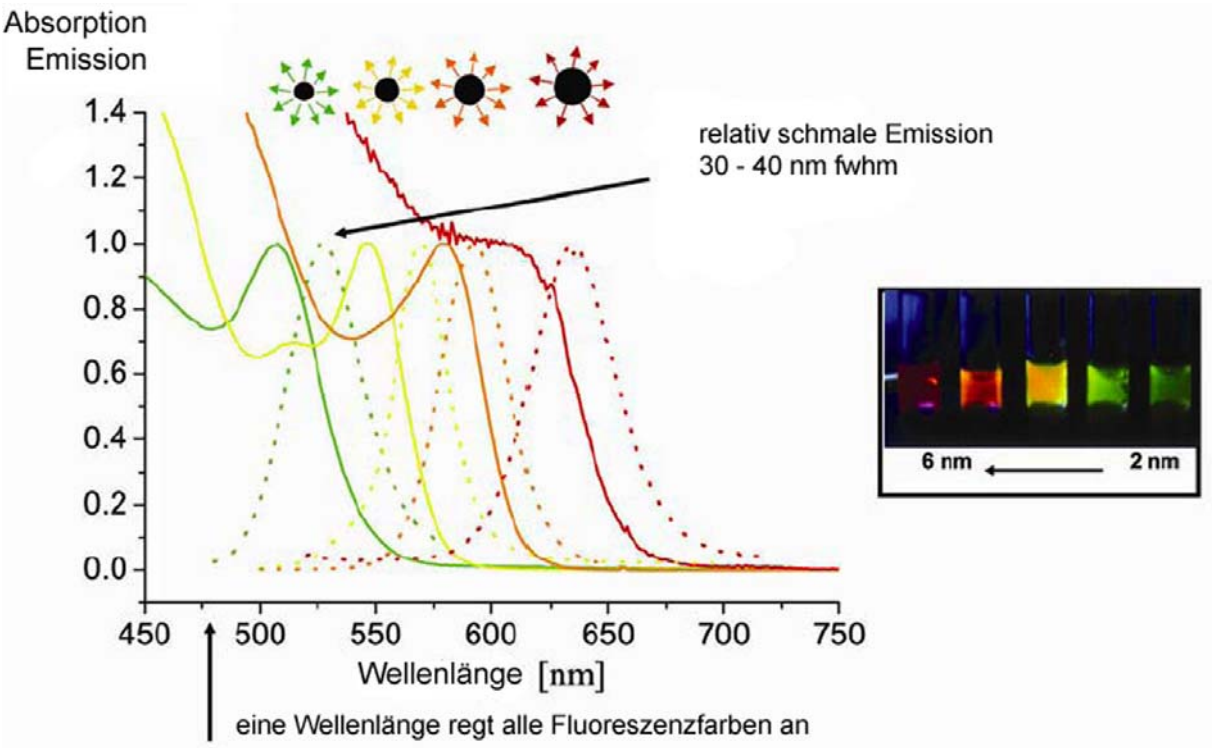

Abbildung II. 5: Absorptionsspektren (solide Linien) und Emissionsspektren (gepunktete Linien) von CdSe-Nanokristallen mit zunehmendem Durchmesser/Emissionswellenlänge [69].

Der größte Vorteil der NC gegenüber organischen Fluoreszenzmarkern liegt in ihrer Resistenz gegenüber Photobleichen, siehe Abb.II.5 und [69].Organische Marker können unter optischer Anregung irreversible Konformationsänderungen vollziehen, aus denen sie strahlungslos relaxieren, ohne fluoreszierende Emission. Aufgrund ihrer anorganischen Natur leiden NC kaum unter diesem Mechanismus, was sie zu idealen Markern für Langzeitexperimente macht. Beispielsweise wurde die Embryogenese von Fröschen auf diese Weise mitverfolgt [70].

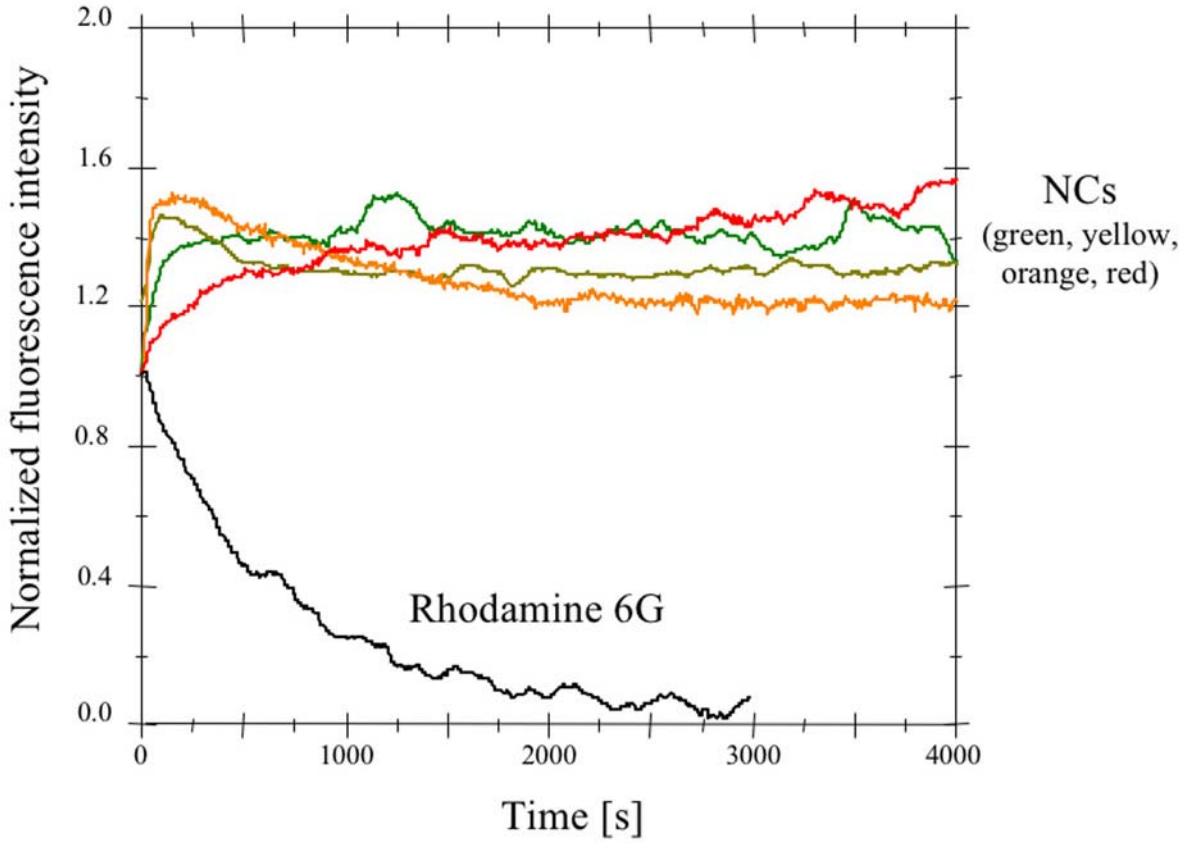

Abbildung II. 6: Reduziertes Photobleichen von NC mit verschiedenen Fluoreszenzfarben, gegenüber dem organischen Farbstoff Rhodamin 6G. Aus [71].

4. Oberflächenmodifizierung von Halbleiter-Nanokristallen

Die Synthese eines Halbleiter-Nanokristalls ergibt einen reinen Einkristall, der nur durch ein Benetzungsmittel umhüllt wird. Ähnlich wie bei GaAs (siehe Teil I. der Arbeit) finden sich elektrische Oberflächenzustände auf den Halbleiterkugeln. Diese stellen Oberflächen-nahe Elektronenzustände in der Bandlücke des Halbleiters zu Verfügung, über die nun strahlungslose Rekombinationen von angeregten Exzitonen stattfinden können. Dadurch wird die Quantenausbeute der Fluoreszenz gemindert. Aus diesem Grund passiviert man die Halbleiteroberfläche durch zusätzliche Synthese einer kristallinen ZnS-Hülle. Entsprechende NC heißen „core-shell“ Nanokristalle [72] [73].

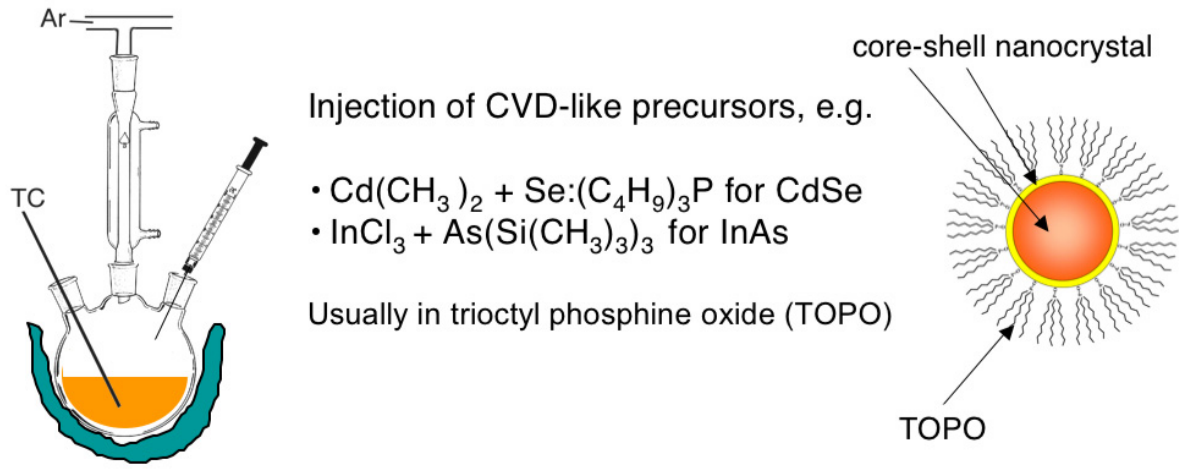

Abbildung II. 7: Synthese von Halbleiternanokristallen. Ähnlich wie in CVD-Verfahren, werden Precursors aus den Zielmaterialien verwendet, die in einer unpolaren Lösung mit (unter anderem) TOPO in einer Sauerstoff- und Wasser-freien Umgebung bei hohen Temperaturen um 270°C kristallisieren. Auch ZnS-Hüllen werden in unpolarem Lösungsmittel synthetisiert. Das Endresultat sind Nanokristallkugeln mit einer monomolekularen Hülle des hydrophoben TOPO. Details siehe Referenz K5.

Halbleiter-Nanokristalle werden in unpolaren organischen Lösungsmitteln synthetisiert. Um sie als Fluoreszenzmarker in physiologischen Umgebungen einsetzen zu können, muss ein Phasentransfer von unpolarem in das polare Lösungsmittel (Wasser) durchgeführt werden.
Dazu muss die Nanokristalloberfläche, die in der unpolaren Phase mit einem hydrophoben Surfaktant (Trioktylphosphin Oxid, TOPO) benetzt ist, durch einen Liganden mit hydrophilen chemischen Gruppen funktionalisiert werden. Zum Nanokristall kann ein solcher Ligand entweder durch eine kovalente Bindung über eine Thiol- oder Pyridin-Gruppe ankoppeln. Alternativ zu einer chemischen Bindung kann man unter Ausnutzung des hydrophoben Effektes eine Hülle von amphiphilen Molekülen um den hydrophoben Kristall bilden, die man durch Quervernetzung stabilisiert, siehe AbbII.7-rechts unten.

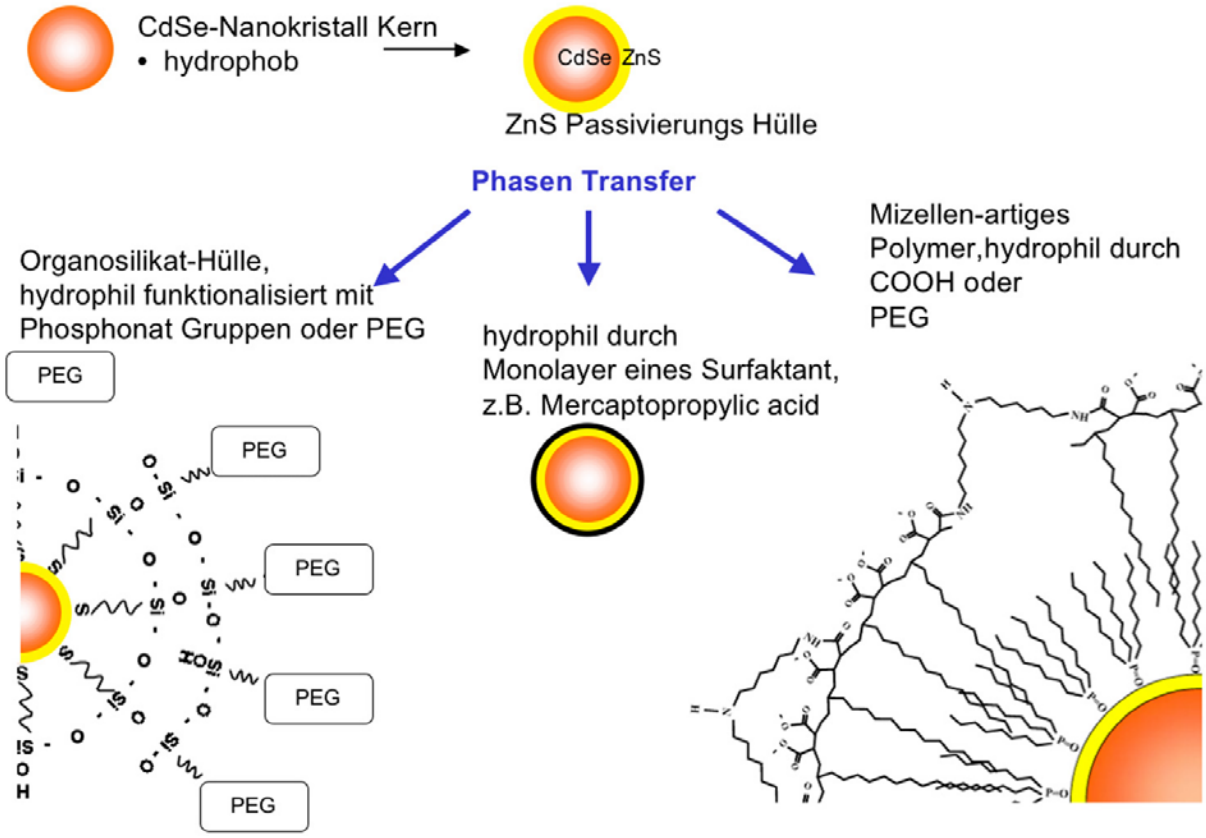

Abbildung II. 8: Strategien zum Phasentransfer hydrophober NC in wässrige Lösungen

Dies ähnelt einer Mizellenbildung durch Phospholipide, die in der Literatur für den Phasentransfer von NC auch bereits beschrieben wurde [70]. Als hydrophile Gruppen nach außen bieten sich polare chemische Gruppen an, z.B. die Carboxy- oder Phosphonat-Gruppe, die zu ihrer Polarität noch eine statische Ladung mitbringen, die in Lösung das Aggregieren von Kristallen vermindern können. In salzigen Lösungsmitteln wie einem Zellmedium werden diese geladenen Oberflächen durch eine Schicht von Gegenionen abgeschirmt (Helmholtzschicht), wodurch die abstossende Wirkung verringert wird. Die Aggregation von Nanokristallen stellt ein sehr konkretes praktisches Problem in der Anwendung von Nanokristallen dar, das klare Versuchsbedingungen und somit präzise Aussagen über Experimente erschwert (Referenz K5). Eine Alternative zur Kluster-Vermeidung ist die Methode der sterischen Abstossung von Kristallen durch Polymerkissen aus Polyethylenglykol (PEG), die z.B. über Veresterung an den Kristall angebunden werden können (Referenz K5). Interessant ist PEG auch deswegen, weil es eine chemisch inerte Oberfläche ergibt, mit einer geringen Neigung zur Bindung oder Adsorption von Proteinen, was wiederum die Adhäsion zu Zellmembran und damit die Aufnahme des funktionalisierten NC in das Zellinnere verhindern könnte (Referenz K5).

Eine weitere etablierte Methode für den Phasentransfer von hydrophoben NC in wässrige Lösungsmittel beruht auf der Bildung einer Glas-artigen Hülle um den hydrophoben Kern (oder core-shell), siehe Abb.II.7-links unten. Dazu wird Mercaptopropyltrimethoxysilan verwendet, das an den Kristall über die Schwefelgruppe anbindet und über die Methoxygruppen in einem Prozess von Hydrolyse und Kondensation quervernetzen kann [71]. In einem zweiten Schritt werden über Methoxysilane funktionelle Gruppen wie Phosphonat oder PEG angebunden, um die Aggregation durch die oben beschriebenen Mechanismen zu hemmen und die reaktiven Si-OH Gruppen an der Außenseite der „Glas"-Hülle zu quenchen, die ebenfalls zu einer kovalenten Aggregation der NC führen würden. Das Konzept der Silanisierung war eine Parallelentwicklung zu den in Teil 1.6. dieser Arbeit entwickelten Organosilikaten. So sind die beiden Syntheseverfahren im Prinzip gleich und unterscheiden sich nur in Details, was aber dennoch zu einer anderen Schichtbeschaffenheit führen kann, wie die komplexe Sol-gel Chemie zeigt (vgl. § I.6.2).

Unklar war, wie effizient solche Organosilikatschichten als Isolationshüllen den toxischen Nanokristall-Kern gegen das Zellmedium abschirmen und umgekehrt, die Korrosion des Kerns durch das Medium verhindern.

5. Die Toxizität von Cadmium

Cadmium* wird zu den 10 gefährlichsten Substanzen für die menschliche Gesundheit gerechnet [74], und z.B. in Zigaretten sowie der metallverarbeitenden Industrie aufgefunden [75]. Wie für Schwermetalle typisch, wird es im menschlichen Körper in der Leber irreversibel akkumuliert und wirkt bei hohen Dosen dort auch als erstes toxisch [76]. Leberzellen (Hepatozyten) sind spezialisiert auf das Binden von schädlichen Metallen, die oft mit essentiellen Spurenelementen biochemisch konkurrieren. Andere bekannte Mechanismen im Zusammenhang mit der toxischen Wirkung von Cadmium sind passive Diffusion, Träger-gebundene Diffusion, Kopplung an Rezeptor getriggerte Ca^{2+}-Kanäle, die Verwendung von Temperatur unabhängigen Ionen-Poren, Kopplung an Plasma-seitige Liganden der Zellmembran und intrazelluläre Bindungen über Thiolgruppen von diversen Biomolekülen, ähnlich dem Fall von Arsen (vgl. §I.5.3) [77]. Das Binden von Arsen entspricht auch dem Filter-Mechanismus der Leberzellen, die auf diese Weise Schwermetalle über Proteine wie Metallothionein aus dem Blutkreislauf entfernen und darüber hinaus über diese natürlichen

* wie auch Arsen

Antidote selber größere Schwermetallmengen tolerieren, während andere Zelltypen wesentlich empfindlicher reagieren. Neuronale Schäden sind hierbei besonders zu erwähnen und häufig dokumentiert [78], da Cadmium die Blut-Hirn Schranke durchdringt und dort z.B. an Neuronen oxidativen Proteinschaden induziert [79].

Letztendlich verursacht Cadmium den Zelltod, für den zwei Haupt-Mechanismen bekannt sind: Apoptose und Nekrose. Apoptose, oder programmierter Zelltod, ist ein wichtiger aktiver Regulierungsmechanismus für das Wachstum und die Proliferation von Zellen. Diese reagieren auf bestimmte biochemische Signale mit der Initiierung eines intrazellulären Prozesses, an dessen Ende der Verlust der Zellmembranintegrität, Zellschrumpfung und der Zelltod stehen. Beispielsweise erzeugt Serum-Mangel in Zellkulturen Apoptose [80]. Bei der Nekrose wird die Selbstregulation der Zelle übergangen, Toxine zerstören die Plasmamembran, die Zelle schwillt an und platzt. Prinzipiell scheint es so zu sein, dass Apoptose und Nekrose nur die Extremfälle einer großen Spanne möglicher morphologischer und biochemischer Todesarten darstellen [81]. Für diese Arbeit besonders interessant ist die Beobachtung, dass ein und derselbe Stimulus beide Todesarten hervorrufen kann und dass die Toxinkonzentration eine Schwelle beschreibt, an der die Mechanismen sich ablösen. Speziell im Fall von Cadmium erzeugen niedrige Konzentrationen Apoptose und hohe Konzentrationen Nekrose. Dies wurde von Lopez et al. anhand der Cadmium Chlorid-Toxizität für kortikale Ratten-Neuronen detailliert untersucht und ergab dort einen Schwellwert von 1 μM [78].

6. Die Toxizität von Nanokristallen

Toxizität und Risiken von Nanomaterial sind zur Zeit aktuelle Themen des öffentlichen Interesses und werden in staatlich geförderten Forschungsprogrammen untersucht [1] [82]. Bei der Risikoeinschätzung stehen besonders Aerosole wie Russpartikel oder Platinpartikel aus Auto- und Industrieabgasen im Zentrum der Aufmerksamkeit [1, 83, 84], während scheinbar abgeschlossene Systeme aus biologischen Anwendungen von Nanomaterial und dessen Rückstände als weniger relevant eingeschätzt werden.

Für den Anwender von Halbleiter-Nanokristallen in biologischen Experimenten sollte die Frage nach unerwünschten Nebenwirkungen von zentralem Interesse sein.

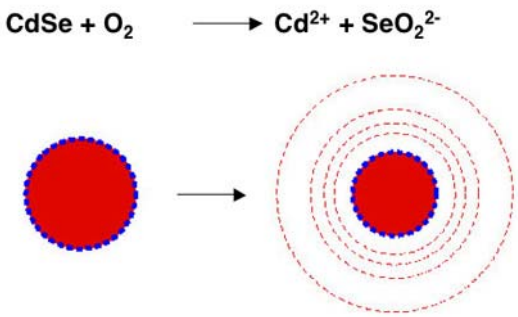

Abbildung II. 9: Korrosion von CdSe als Folge von Oxidation.

Aus den Untersuchungen der Korrosion von GaAs in wässrigen Elektrolyten (vgl. Teil I der Arbeit) erwartet man auch von Nanokristallen aus CdSe und CdTe nichts anderes, als dass sie sich in Wasser ebenfalls unter Korrosion auflösen, dieses mit Cd^{2+}-Ionen anreichern und so zu einer toxischen Wirkung der Nanokristalle führen. Durch das größere Verhältnis von Fläche/Volumen im Fall der Nanokristalle ist dieses Risiko besonders schwerwiegend einzuschätzen. Aber auch andere toxische Mechanismen sind denkbar. So könnten auch völlig inerte Materialien allein durch eine Nano-Dimensionierung schädlich werden, indem die im Vergleich zu makro-skaligem planarem Material höhere Oberflächenenergie chemische Oberflächenreaktionen ermöglicht, die sonst kinetisch oder thermodynamisch blockiert sind [85]. Dies ist z.B. für Gold der Fall, das ab einer bestimmten Partikelgröße reaktiv wird [86]. Allein die makromolekulare Größe von Partikeln könnte auch zum Interferieren mit biologischen Mechanismen führen, beispielsweise indem sie unspezifisch von Zellen aufgenommen werden und sich intrazellulär anreichern [87-90]. Falls eine Größenabhängigkeit der Toxizität existiert, würde die Aggregatbildung eine Rolle spielen, indem sich aus Nanopartikeln als kleinsten Bestandteilen mit erhöhter Wahrscheinlichkeit auch eine Partikel-Spezies in toxischer Größe bildet. Von Aerosolen weiß man, dass nur bestimmte Größen von Makrophagen in der Lunge erkannt und „bekämpft“ werden, was sich in Entzündungsreaktionen äußert [83, 84, 91]. Auch die Behinderung von Transportprozessen an und über die Membranen der Zelle scheinen nicht ausgeschlossen, nachdem Nanopartikel dazu tendieren, sich an Zellmembranen anzulagern [88, 92]. Ein weiterer Faktor für die Toxizität von Nano-Objekten ist ihre Form. Carbon-Nanotubes z.B. können eine Zelle beeinträchtigen, indem sie die Zellmembran wie Nadeln durchstechen [93, 94].

7. Quantitative Bestimmung der Cadmium Toxizität

Cytotoxische Effekte von CdSe/CdTe Nanokristallen in Abhängigkeit von der Oberflächenfunktionalisierung sind bislang nie quantitativ beschrieben worden. Bekannt ist, dass sich diese Kristalle in wässriger Lösung unter Freisetzung von Cd^{2+} auflösen, welches man cytotoxischen Effekten zugeordnet hat. Durch UV-Bestrahlung ließ sich dieser Korrosionsprozess beschleunigen und durch Verkapselung der CdSe-Kerne mit ZnS oder organischen Hüllen verzögern [95]. Eine widersprüchliche Feststellung wurde an anderer Stelle getroffen, wo man die cytotoxischen Effekte allein der Oberflächenchemie der CdSe-NC zuordnete [96]. In der vorliegenden Arbeit wurde ein sensibler Cytotoxizitätstest entwickelt. Er beruht auf der Computer-gestützten Auswertung automatischer Fotoserien von Zellkulturen und ermöglicht eine quantitative Beschreibung der Cytotoxizität. Adhärente Zellen vom Typ NRK-Fibroblasten in Serum-freien Medium werden 48 Stunden vor und nach Inkubation mit der Probesubstanz auf der Kulturgefäß-Oberfläche gezählt, der Quotient der Werte wird gegen die Probesubstanz-Konzentration aufgetragen (Referenz K5), siehe Abb.II.10. Im Ergebnis werden die toxischen Effekte auf die Kristallkorrosion zurückgeführt und vergleichende Zahlenwerte für toxische Grenzwerte in Abhängigkeit von der Oberflächenfunktionalisierung des NC ermittelt. Der Schwellwert der Cd^{2+}-Toxizität für NRK-Fibroblasten kann zu (1,5±0,5) μM angegeben werden und stimmt somit überein mit dem Wert für kortikale Ratten-Neuronen von ca. 1 μM [78], vgl. auch §II.5.

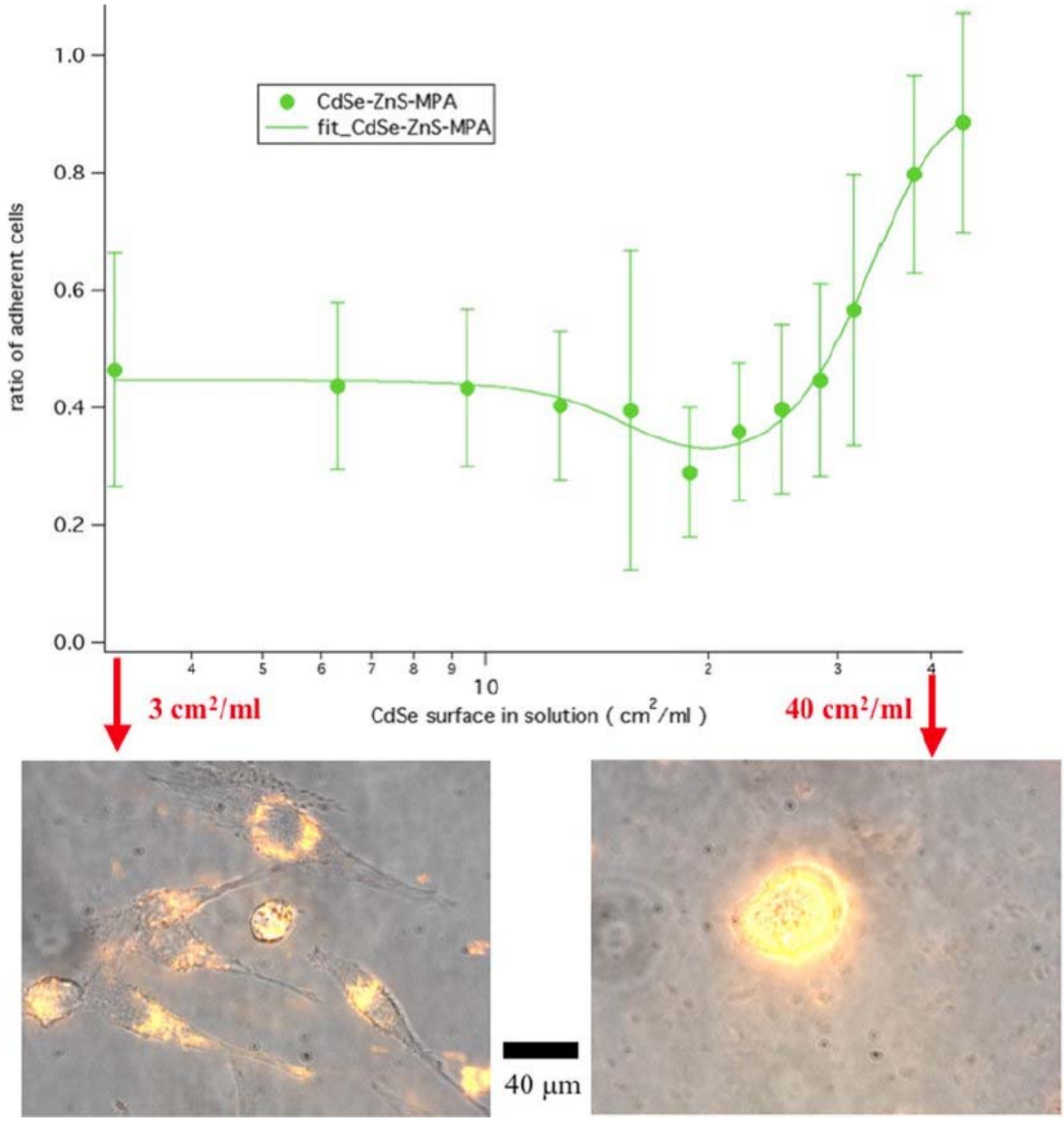

Abbildung II. 10: Cytotoxizitätskurve für NRK-Fibroblasten, inkubiert mit CdSe-ZnS-MPA. Die Daten wurden angenähert durch eine Doppelt-Sigmoide Funktion. Diese ist die Superposition zweier Sigmoid-Kurven und wird interpretiert als Zelltodkurve, die durch Überlagerung eines apoptotischen mit einem nekrotischen Mechanismus zustande kommt (Referenz K5). Die Fluoreszenzfotos zeigen die Zellen im Konzentrationsbereich der Apoptose (3 cm^2/ml) und Nekrose (40 cm^2/ml) nach 48 Stunden Inkubationszeit. Im rechten Bild sieht man die hohe Anreicherung von NC im Zellinneren der toten Kugel-förmigen Zelle.

8. Drug-Delivery : Cytotoxizität von CdTe-Nanokristallen in Polyelektrolyt-Kapseln (Referenz K6)

„Drug-Delivery“ bedeutet den gezielten Transport von Pharmazeutika in bestimmte Geweberegionen eines Organismus, um nach lokaler Freisetzung ausschließlich dort und

nicht im Nachbargewebe zu wirken [97] [98] [99]. Zahlreiche Trägersysteme für Drug-Delivery wurden bereits entwickelt und getestet. Solche Konzepte verwenden Hohlkapseln aus Lipidvesikeln [100] oder Polymeren [99] [101]. Diese Verkapselung schützt den Inhalt vor verfrühter Verteilung außerhalb des Zielgewebes. Dieses wird erst im Zielgebiet durch die Öffnung der Kapseln freigegeben.

In dieser Arbeit wurden Kapseln aus Polyelektrolyt-Multilayern, bestehend aus 8 Hüllen von alternierend Polystyrensulfonat und Polyallylamin Hydrochlorid [102-104], angereichert mit toxischen CdTe-Nanokristallen, auf ihre Giftigkeit untersucht (Referenz K6). Dazu wurde der in §II.7 vorgestellte Cytotoxizitätstest verwendet und die Kapselaufnahme durch die NRK-Fibroblasten mit Phasenkontrast- und Fluoreszenzmikroskopie sichtbar gemacht, siehe Abb.II.11.

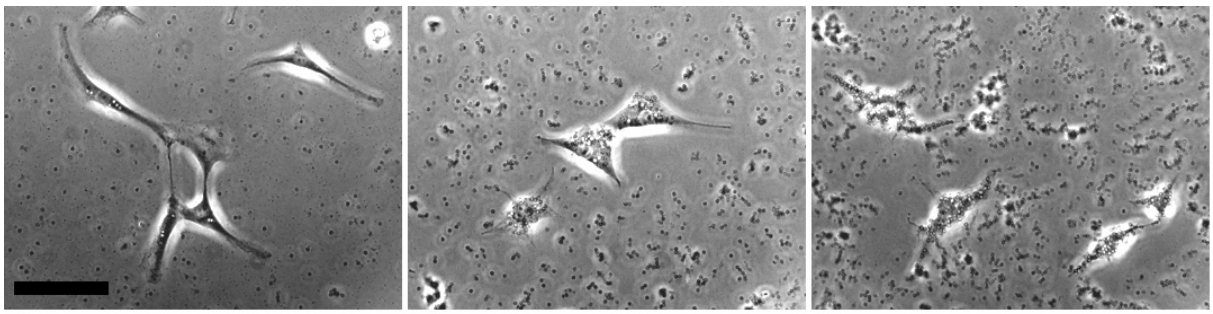

Abbildung II. 11: Phasenkontrastbilder Bilder von adhärenten NRK-Fibroblasten, 48h nach Inkubation mit leeren Polyelektrolyt-Kapseln in verschiedenen Konzentrationen. a) $50 \cdot 10^3$ Kapseln/ml b) $250 \cdot 10^3$ Kapseln/ml c) $500 \cdot 10^3$ Kapseln/ml. Die quantitative Auswertung ergibt, dass bereits leere Kapseln in hohen Konzentrationen ab $250 \cdot 10^3$ Kapseln/ml cytotoxisch wirken.

III. Fazit

Ziel der vorliegenden Arbeit war es, nanostrukturierte Biosensoren aus Halbleitermaterialien in eine physiologische Umgebung zu integrieren und dort zu betreiben. Dabei handelte es sich erstens um einen Biosensor mit empfindlichen FET-Messpunkten auf GaAs-Basis zur Messung extrazellulärer Potentiale von elektrisch aktiven biologischen Zellen. Das zweite Sensorsystem bestand aus Halbleiternanokristallen auf der Basis von CdSe und CdTe, die durch ihre stabilen und steuerbaren Fluoreszenzeigenschaften besonders in Langzeitexperimenten als optische Sensoren zur Markierung und Beobachtung von biologischen Funktionseinheiten und Funktionsabläufen verwendbar sind.

Bei den genannten Halbleitermaterialien wurde eine Korrosionsanfälligkeit festgestellt, die nicht nur zur Beeinträchtigung oder Zerstörung der Sensorstruktur führt, sondern die sich auf eine biologische Umgebung, insbesondere auf Zellen, toxisch auswirkt.

Um diesem Problem entgegenzuwirken, wurden verschiedene Beschichtungsstrategien angewandt und getestet.

Auf planaren GaAs-Substraten sowie auf GaAs-Heterostrukturen wurde ein Verfahren zur Beschichtung mit Organosilikaten entwickelt, das im Wesentlichen auf einer katalysierten Oberflächenpolymerisation von Organo-tri(tetra)-(m)ethoxy-silanen in organischer Lösung beruht. Durch die hohe Affinität von Sulfidgruppen (-SH) zu GaAs konnten die genannten Organosilikatschichten kovalent auf solchen Substraten angebunden werden, wenn eine Kopplungsschicht aus Mercaptotrimethoxysilan verwendet wurde. Da die Sulfidgruppe und die beim Verfahren auftretende Silanolgruppe (Si-OH) darüber hinaus eine hohe Affinität zu einer Vielzahl von weiteren Substraten (Metalle, Halbleiter, Silikate) aufweisen und da zudem andere Organo-tri-(m)ethoxy-silanen, z. B. mit Carboxy- (-COOH) oder Aminogruppen (-NH2) kommerziell verfügbar sind, kann das hier entwickelte Beschichtungsverfahren breit eingesetzt werden.

Das Verfahren eignet sich zudem besonders für nicht-planare Strukturen, da anders als z. B. bei Sol-Gel-Verfahren üblich, die Polymerisation nicht nach einem „Spin-Coating“-Schritt sondern durch „Dip-coating“ erfolgt.

Unter elektroneutralen Bedingungen wurde auf GaAs eine ausgezeichnete Langzeitstabilität der Organosilikat-Schichten in physiologischer Umgebung nachgewiesen. Dagegen wurden unter elektrischer Belastung mittels Voltammetrie und Impedanzspektroskopie Grenzwerte der Belastbarkeit ermittelt. In Mikrostrukturanalysen mittels Synchrotron-Strahlung wurde die Korrosion von beschichteten GaAs-Substraten verfolgt und die Tendenz von GaAs zur Oxidbildung als mögliche Ursache der Korrosionsprobleme bestätigt.

Schichten aus Organosilikaten kamen auch zur Verkapselung von CdSe/CdTe-Nanokristallen zum Einsatz. Im Zusammenhang mit der Bestimmung der Effektivität der Verkapselung, insbesondere auch im Vergleich mit anderen chemischen Verkapselungsmethoden, wurde ein hochsensibles Verfahren zur Messung der Wirkung von toxischen Ionen, die von den korrodierenden Halbleitermaterialien freigesetzt werden, auf die Adhäsion von einzelnen Zellen lebender Zellkulturen entwickelt. Das Verfahren kann auch als Reportersystem zur Bestimmung von Korrosion aus dem Adhäsionsverhalten lebender Zellen verstanden werden. Es beruht auf einer computergestützten Partikelzählung an Oberflächen mittels Bildverarbeitung.

Durch dieses Verfahren konnte u. a. die Abhängigkeit der Toxizität und damit die Abhängigkeit des Korrosionsschutzes der CdSe/CdTe-Nanokristalle von der Verkapselungsmethode gezeigt werden. Insbesondere konnte die langzeitstabile Verkapselung der Kristalle durch Organosilikate in physiologischer Umgebung nachgewiesen werden.

Ferner wurde durch das Verfahren ein charakteristischer Zusammenhang zwischen der Anzahl adhärenter Zellen (Fibroblasten) und der Arsen- bzw. Cadmiumkonzentration im Nährmedium ermittelt, der einer doppelt-sigmoiden Funktion folgt. Dies wurde als Koexistenz zweier verschiedener Arten des Zelltods, Apoptose und Nekrose, interpretiert.

Das Verfahren wurde zudem bei unterschiedlich beschichteten Gold-Nanopartikeln sowie bei der Ermittlung der Toxizität von Polyelektrolyt-Mikrokapseln verwendet, die derzeit als Kandidaten zum zielgerichteten Applizieren von Medikamenten („targeted drug-delivery“) erprobt werden.

Die Ergebnisse zeigen, dass das vorliegend entwickelte Verfahren zur Messung der Zelladhäsion ein sensibles Werkzeug ist, um die Störung eines biologischen Systems durch

Schadstoffe, wie z. B. Arsen- oder Cadmiumionen, zu quantifizieren. In einer Weiterentwicklung dieses Verfahrens bestände zudem die Möglichkeit, neben der Anzahl der adhärenten Zellen auch andere statistische Größen, wie z. B. die mittlere Zellfläche, den mittleren Zellumfang oder die mittlere Form (Zirkularität) in Abhängigkeit von der Konzentration der Testsubstanz festzuhalten. Da diese Größen möglicherweise noch sensibler von der Konzentration abhängen, bietet das Verfahren reichlich Potenzial, um mit verbesserter Genauigkeit weitere Effekte bei der biologischen Integration von Halbleiter-Nanostrukturen zu erforschen.

Literaturverzeichnis

[1] W. Luther, *Industrial application of nanomaterials - chances and risks*, vol. 54: VDI-Technologiezentrum, 2004.

[2] [Anon], "Nanotechnology: Don't forget the big picture," *NATURE MATERIALS*, vol. 2, pp. 127-127, 2003.

[3] V. T. Moy, E.-L. Florin, and H. E. Gaub, "Intermolecular Forces and Energies Between Ligands and Receptors," *Science*, vol. 265, pp. 257 - 259, 1994.

[4] M. SARIKAYA, C. TAMERLER, A. K.-Y. JEN, K. SCHULTEN, and F. BANEYX, "Molecular biomimetics: nanotechnology through biology," *Nature Materials*, vol. 2, pp. 577-585, 2003.

[5] N. Seeman and A. Belcher, "Emulating biology: Building nanostructures from the bottom up," *PROCEEDINGS OF THE NATIONAL ACADEMY OF SCIENCES OF THE UNITED STATES OF AMERICA*, vol. 99, pp. 6451-6455, 2002.

[6] B. Parviz, D. Ryan, and G. Whitesides, "Using self-assembly for the fabrication of nano-scale electronic and photonic devices," *IEEE TRANSACTIONS ON ADVANCED PACKAGING*, vol. 26, pp. 233-241, 2003.

[7] B. Muller, "Natural formation of nanostructures: From fundamentals in metal heteroepitaxy to applications in optics and biomaterials science," *SURFACE REVIEW AND LETTERS*, vol. 8, pp. 169-228, 2001.

[8] X. Michalet, F. Pinaud, L. Bentolila, J. Tsay, S. Doose, J. Li, G. Sundaresan, A. Wu, S. Gambhir, and S. Weiss, "Quantum dots for live cells, in vivo imaging, and diagnostics," *SCIENCE*, vol. 307, pp. 538-544, 2005.

[9] N. Rudraiah and C. Ng, "A model for manufacture of nano-sized smart materials free from impurities," *CURRENT SCIENCE*, vol. 86, pp. 1076-1091, 2004.

[10] W. J. Parak, M. George, H. E. Gaub, S. Böhm, and A. Lorke, "The Field-Effect-Addressable Potentiometric Sensor / Stimulator (FAPS) - A new concept for a surface potential sensor and stimulator with spatial resolution," *Sensors and Actuators B*, vol. 58, pp. 497-504, 1999.

[11] A. Lorke, S. Böhm, J. P. Kotthaus, W. J. Parak, and M. George, "Ortsaufgelöster Potential-Sensor und -Stimulator auf Halbleiterbasis," in *Patentschrift DE 19840157 C2, Deutsches Patant- und Markenamt*. Germany: A. Lorke, 1998.

[12] E. Neher and B. Sakmann, "Single-channel currents recorded from membrane of denervated frog muscle fibres," *Nature*, vol. 260, pp. 799 - 802, 1976.

[13] B. Sakmann and E. Neher, *Single-Channel Recording*, 2 ed. New York: Plenum Press, 1995.

[14] R. E. Meyer, C. O. Müller, and P. Fromherz, "Cable Properties of Dendrites in Hippocampal Neurons of the Rat Mapped by a Voltage-sensitive Dye," *European Journal of Neuroscience*, vol. 9, pp. 778-785, 1997.

[15] L. B. Cohen and B. M. Salzberg, "Optical Measurement of Membrane Potential," *Rev. Physiol. Biochem. Pharmacol*, vol. 83, pp. 34 - 88, 1978.

[16] P. Fromherz, A. Offenhäusser, T. Vetter, and J. Weis, "A Neuron-Silicon Junction: A Retzius Cell of the Leech on an Insulated-Gate Filed-Effect Transistor," *Science*, vol. 252, pp. 1290 - 1293, 1991.
[17] C. Sprössler, D. Richter, M. Denyer, and A. Offenhäusser, "Long-term recording system based on field-effect transistor arrays for monitoring electrogenic cells in culture," *Biosensors & Bioelectronics*, vol. 13, pp. 613-618, 1998.
[18] A. Lambacher, M. Jenkner, B. Eversmann, M. Merz, A. Kaul, F. Hofmann, R. Thewes, and P. Fromherz, "Electrical imaging of neuronal activity with CMOS chip at 8 micrometer resolution," *BIOPHYSICAL JOURNAL*, vol. 86, pp. 270A-271A, 2004.
[19] B. Stein, "Entwicklung von Potentialsensoren für die Zell-Halbleiter-Kopplung," in *Center for Nanoscience*. München: Ludwig Maximilians Universität, 2003.
[20] E. Yablonovitch, T. Gmitter, J. P. Harbison, and R. Bhat, "Extreme selectivity in the lift-off of epitaxial GaAs films," *Applied Physics Letters*, vol. 51, pp. 2222-2224, 1987.
[21] P. Demeester, I. Pollentier, P. DeDobbelaere, C. Brys, and P. VanDaele, "Epitaxial lift-off and its applications," *Semicond. Sci. Technol.*, vol. 8, pp. 1124-1135, 1993.
[22] E. Yablonovitch, D. M. Hwang, T. J. Gmitter, l. T. Florez, and J. P. Harbison, "Van der Waals bonding of GaAs epitaxial lift-off films onto arbitrary substrates," *Applied Physics Letters*, vol. 56, pp. 2419-2421, 1990.
[23] S. M. Sze, *Physics of Semiconductor Devices*, 2 ed. New York: John Wiley & Sons, 1981.
[24] C. Yang, Y. Fang, C. Chen, W. Wang, T. Lin, M. Wang, T. Hou, J. Cheng, L. Yao, S. Chen, C. Yu, and M. Liang, "Dramatic reduction of gate leakage current in 1.61 nm HfO2 high-k dielectric poly-silicon gate with AI(2)O(3) capping layer," *ELECTRONICS LETTERS*, vol. 38, pp. 1223-1225, 2002.
[25] T. Hou, M. Greenlief, S. Keller, L. Nelen, and J. Kauffman, "Passivation of GaAs (100) with an adhesion promoting self-assembled monolayer," *CHEMISTRY OF MATERIALS*, vol. 9, pp. 3181-3186, 1997.
[26] C. J. Sandroff, R. N. Nottenburg, J. C. Bischoff, and R. Bhat, "Dramatic enhancement in the gain of a GaAs/AlGaAs heterostructure bipolar transistor by surface chemical passivation," *Appl. Phys. Lett.*, vol. 51, pp. 33-35, 1987.
[27] Y. Okada, Y. Iuchi, and M. Kawabe, "Scanning probe microscope tip-induced oxidation of GaAs using modulated tip bias," *JOURNAL OF APPLIED PHYSICS*, vol. 87, pp. 8754-8758, 2000.
[28] F. Seker, K. Meeker, T. Kuech, and A. Ellis, "Surface chemistry of prototypical bulk II-VI and III-V semiconductors and implications for chemical sensing," *CHEMICAL REVIEWS*, vol. 100, pp. 2505-2536, 2000.
[29] A. M. Green and W. E. Spicer, "Do we need a new methodology for GaAs passivation," *J. Vac. Sci. Technol. A*, vol. 11, pp. 1061-1069, 1993.
[30] T. Okumura and C. Kaneshiro, "Ideal GaAs Schottky Contacts Fabricated by in Situ Photoelectrochemical Etching and Electrodeposition," *Electronics and Communications in Japan 2*, vol. 82, pp. 690-697, 1999.
[31] R. E. Williams, *Gallium Arsenide (GaAs) Processing Technologies*. Dedham, MA: Artech House, 1984.
[32] H. V. Aposhian, "Biochemical toxicology of arsenic," in *Reviews in biochemical toxicology*, vol. 10, E. Hodgson, J. R. Bend, and R. M. Philpot, Eds. Amsterdam: Elsevier, 1989, pp. 265-299.
[33] S. Böhm, "Der epitaktische Lift-off als Methode, elektrische- und optische Eigenschaften
an III-V-Halbleiter-Strukturen zu beeinflussen," in *Center for Nanoscience*. München: Ludwig Maximilians Universität, 2002.

[34] G. Schmitt, J. Schultze, F. Fassbender, G. Buss, H. Luth, and M. Schoning, "Passivation and corrosion of microelectrode arrays," *ELECTROCHIMICA ACTA*, vol. 44, pp. 3865-3883, 1999.

[35] H. M. McConnell, J. C. Owicki, J. W. Parce, D. L. Miller, G. T. Baxter, H. G. Wada, and S. Pitchford, "The Cytosensor Microphysiometer: Biological Applications of Silicon Technology," *Science*, vol. 257, pp. 1906 - 1912, 1992.

[36] J. W. Parce, J. C. Owicki, K. M. Kercso, G. B. Sigal, H. G. Wada, V. C. Muir, L. Bousse, K. L. Ross, B. I. Sikic, and H. M. McConnell, "Detection of Cell-Affecting Agents with a Silicon Biosensor," *Science*, vol. 246, pp. 243 - 247, 1989.

[37] J. C. Owicki, L. Bousse, D. Hafeman, G. L. Kirk, J. D. Olson, H. G. Wada, and J. W. Parce, "The Light-Addressable Potentiometric Sensor: Principles and Biological Applications," *Annual Review of Biophysics and Biomolecular Structure*, vol. 23, pp. 87 - 113, 1994.

[38] H. Tanaka, T. Yoshinobu, and H. Iwasaki, "Application of the chemical imaging sensor to electrophysiological measurement of a neural cell," *Sensors and Actuators B*, vol. 59, pp. 21-25, 1999.

[39] W. CLAASSEN, W. VALKENBURG, M. WILLEMSEN, and W. VANDERWIJGERT, "INFLUENCE OF DEPOSITION TEMPERATURE, GAS-PRESSURE, GAS-PHASE COMPOSITION, AND RF FREQUENCY ON COMPOSITION AND MECHANICAL-STRESS OF PLASMA SILICON-NITRIDE LAYERS," *JOURNAL OF THE ELECTROCHEMICAL SOCIETY*, vol. 132, pp. 893-898, 1985.

[40] E. Sackmann, "Vorlesungsskript Biophysik (4.Auflage)," Technische Universität, München 1996.

[41] D. L. Allara and S. Ashok, "Modification of semiconductor surface properties with chemically bound molecular films," The Pennsylvania State University ARO 27770-CH;DAAL03-92-G-1015, Feb 1994 1994.

[42] A. Ulman, "Formation and structure of self-assembled monolayers," *CHEMICAL REVIEWS*, vol. 96, pp. 1533-1554, 1996.

[43] C. BAIN, "A NEW CLASS OF SELF-ASSEMBLED MONOLAYERS - ORGANIC THIOLS ON GALLIUM-ARSENIDE," *ADVANCED MATERIALS*, vol. 4, pp. 591-594, 1992.

[44] O. NAKAGAWA, S. ASHOK, C. SHEEN, J. MARTENSSON, and D. ALLARA, "GAAS INTERFACES WITH OCTADECYL THIOL SELF-ASSEMBLED MONOLAYER - STRUCTURAL AND ELECTRICAL-PROPERTIES," *JAPANESE JOURNAL OF APPLIED PHYSICS PART 1-REGULAR PAPERS SHORT NOTES & REVIEW PAPERS*, vol. 30, pp. 3759-3762, 1991.

[45] S. LUNT, P. SANTANGELO, and N. LEWIS, "PASSIVATION OF GAAS SURFACE RECOMBINATION WITH ORGANIC THIOLS," *JOURNAL OF VACUUM SCIENCE & TECHNOLOGY B*, vol. 9, pp. 2333-2336, 1991.

[46] W. STOBER, A. FINK, and E. BOHN, "CONTROLLED GROWTH OF MONODISPERSE SILICA SPHERES IN MICRON SIZE RANGE," *JOURNAL OF COLLOID AND INTERFACE SCIENCE*, vol. 26, pp. 62-&, 1968.

[47] C. J. Brinker, A. J. Hurd, P. R. Schunk, G. C. Frye, and C. S. Ashley, "Review of Sol Gel Thin Film Formation," *Journal of Non-Crystalline Solids*, vol. 147, pp. 424-436, 1992.

[48] K. Haas, S. Amberg-Schwab, K. Rose, and G. Schottner, "Functionalized coatings based on inorganic-organic polymers (ORMOCER (R) s) and their combination with vapor deposited inorganic thin films," *SURFACE & COATINGS TECHNOLOGY*, vol. 111, pp. 72-79, 1999.

[49] T. Chou, C. Chandrasekaran, and G. Cao, "Sol-gel-derived hybrid coatings for corrosion protection," *JOURNAL OF SOL-GEL SCIENCE AND TECHNOLOGY*, vol. 26, pp. 321-327, 2003.
[50] M. Khobaib, L. Reynolds, and M. Donley, "A comparative evaluation of corrosion protection of sol-gel based coatings systems," *SURFACE & COATINGS TECHNOLOGY*, vol. 140, pp. 16-23, 2001.
[51] M. H. Brodsky, "Fortschritte in der Galliumarsenid-Technologie," *Spektrum der Wissenschaft*, vol. Sonderheft 11, pp. 18-27, 1991.
[52] C. J. Sandroff, M. S. Hegde, and C. C. Chang, "Structure and stability of passivating arsenic sulfide phases on GaAs surfaces," *J. Vac. Sci. technol. B*, vol. 7, pp. 841-844, 1989.
[53] A. M. Green and W. E. Spicer, "Do we need a new methodology for GaAs passivation?" *J. Vac. Sci. Technol. A*, vol. 11, pp. 1061-1069, 1993.
[54] M. Hong, J. Kwo, A. Kortan, J. Mannaerts, and A. Sergent, "Epitaxial cubic gadolinium oxide as a dielectric for gallium arsenide passivation," *SCIENCE*, vol. 283, pp. 1897-1900, 1999.
[55] B. Yang, P. Ye, J. Kwo, M. Frei, H. Gossmann, J. Mannaerts, M. Sergent, M. Hong, and K. Bude, "Impact of metal/oxide interface on DC and RF performance of depletion-mode GaAs MOSFET employing MBE grown Ga2O3(Gd2O3) as gate dielectric," *JOURNAL OF CRYSTAL GROWTH*, vol. 251, pp. 837-842, 2003.
[56] H. OHNO, M. MOTOMATSU, W. MIZUTANI, and H. TOKUMOTO, "AFM OBSERVATION OF SELF-ASSEMBLED MONOLAYER FILMS ON GAAS(110)," *JAPANESE JOURNAL OF APPLIED PHYSICS PART 1-REGULAR PAPERS SHORT NOTES & REVIEW PAPERS*, vol. 34, pp. 1381-1386, 1995.
[57] A. P. Alivisatos, "Semiconductor Clusters, Nanocrystals, and Quantum Dots," *Science*, vol. 271, pp. 933-937, 1996.
[58] J. M. Garcia, G. Medeiros-Ribeiro, K. Schmidt, T. Ngo, J. L. Feng, A. Lorke, J. Kotthaus, and P. M. Petroff, "Intermixing and shape changes during the formation of InAs self-assembled quantum dots," *Appl. Phys. Lett.*, vol. 71, pp. 2014-2016, 1997.
[59] D. J. Paul, "Silicon-germanium strained layer materials in microelectronics," *Advanced Materials*, vol. 11, pp. 191-? 1999.
[60] W. J. Parak, L. Manna, F. C. Simmel, D. Gerion, and P. Alivisatos, "Quantum Dots," in *Nanoparticles - From Theory to Application*, G. Schmid, Ed., 1 ed. Weinheim: Wiley-VCH, 2004, pp. 4-49.
[61] A. JORDAN, P. WUST, H. FAHLING, W. JOHN, A. HINZ, and R. FELIX, "INDUCTIVE HEATING OF FERRIMAGNETIC PARTICLES AND MAGNETIC FLUIDS - PHYSICAL EVALUATION OF THEIR POTENTIAL FOR HYPERTHERMIA," *INTERNATIONAL JOURNAL OF HYPERTHERMIA*, vol. 9, pp. 51-68, 1993.
[62] A. Jordan, P. Wust, R. Scholz, B. Tesche, H. Fahling, T. Mitrovics, T. Vogl, J. CervosNavarro, and R. Felix, "Cellular uptake of magnetic fluid particles and their effects on human adenocarcinoma cells exposed to AC magnetic fields in vitro," *INTERNATIONAL JOURNAL OF HYPERTHERMIA*, vol. 12, pp. 705-722, 1996.
[63] A. Feussner, J. Gellermann, A. Jordan, R. Scholz, U. Gneveckow, K. Maier-Hauff, R. Urichl, P. Wust, and R. Felix, "Magnetic fluid hyperthermia combined with percutaneous radiotherapy as a new treatment option for malignant gliomas," *STRAHLENTHERAPIE UND ONKOLOGIE*, vol. 180, pp. 19-19, 2004.
[64] U. Gneveckow, A. Jordan, R. Scholz, N. Waldofner, J. Gellermann, M. Seebass, A. Feussner, K. Maier-Hauff, P. Wust, and R. Felix, "Computation of temperature distributions and comparison for preliminary clinical measurement data in magnetic

fluid hyperthermia," *STRAHLENTHERAPIE UND ONKOLOGIE*, vol. 180, pp. 20-20, 2004.
[65] T. Liedl, "Biologische Anwendung von Nanokristallen," in *Lehrstuhl für Angewandte Physik*. München: Ludwig-Maximilians Universität, 2004.
[66] X. Wu, H. Liu, J. Liu, K. Haley, J. Treadway, J. Larson, N. Ge, F. Peale, and M. Bruchez, "Immunofluorescent labeling of cancer marker Her2 and other cellular targets with semiconductor quantum dots," *NATURE BIOTECHNOLOGY*, vol. 21, pp. 41-46, 2003.
[67] S. J. Rosenthal, "Bar-coding biomolecules with fluorescent nanocrystals," *Nature Biotechnology*, vol. 19, pp. 621-622, 2001.
[68] M. Han, X. Gao, J. Z. Su, and S. Nie, "Quantum-dot-tagged microbeads for multiplexed optical coding of biomolecules," *Nature Biotechnology*, vol. 19, pp. 631-635, 2001.
[69] W. J. Parak and T. Pellegrino, "Labeling of cells with quantum dots," 2004.
[70] B. Dubertret, P. Skourides, D. J. Norris, V. Noireaux, A. H. Brivanlou, and A. Libchaber, "In Vivo Imaging of Quantum Dots Encapsulated in Phospholipid Micelles," *Science*, vol. 298, pp. 1759-1762, 2002.
[71] D. Gerion, F. Pinaud, S. C. Williams, W. J. Parak, D. Zanchet, S. Weiss, and A. P. Alivisatos, "Synthesis and Properties of Biocompatible Water-Soluble Silica-Coated CdSe/ZnS Semiconductor Quantum Dots," *Journal of Physical Chemistry B*, vol. 105, pp. 8861-8871, 2001.
[72] B. O. Dabbousi, J. Rodriguez-Viejo, F. V. Mikulec, J. R. Heine, H. Mattoussi, R. Ober, K. F. Jensen, and M. G. Bawendi, "(CdSe)ZnS Core-Shell Quantum Dots: Synthesis and Characterization of a Size Series of Highly Luminescent Nanocrystallites," *Journal of Physical Chemistry B*, vol. 101, pp. 9463-9475, 1997.
[73] D. V. Talapin, A. L. Rogach, A. Kornowski, M. Haase, and H. Weller, "Highly Luminescent Monodisperse CdSe and CdSe/ZnS Nanocrystals Synthesized in a Hexadecylamine-Trioctylphosphine Oxide-Trioctylphospine Mixture," *NanoLetters*, vol. 1, pp. 207-211, 2001.
[74] D. Bae, C. Gennings, W. Carter, R. Yang, and J. Campain, "Toxicological interactions among arsenic, cadmium, chromium, and lead in human keratinocytes," *TOXICOLOGICAL SCIENCES*, vol. 63, pp. 132-142, 2001.
[75] M. WAALKES, T. COOGAN, and R. BARTER, "TOXICOLOGICAL PRINCIPLES OF METAL CARCINOGENESIS WITH SPECIAL EMPHASIS ON CADMIUM," *CRITICAL REVIEWS IN TOXICOLOGY*, vol. 22, pp. 175-201, 1992.
[76] M. NORDBERG, "GENERAL-ASPECTS OF CADMIUM - TRANSPORT, UPTAKE AND METABOLISM BY THE KIDNEY," *ENVIRONMENTAL HEALTH PERSPECTIVES*, vol. 54, pp. 13-20, 1984.
[77] T. Baker, H. VanVooren, W. Smith, and M. Carfagna, "Involvement of calcium channels in the sexual dimorphism of cadmium-induced hepatotoxicity," *TOXICOLOGY LETTERS*, vol. 137, pp. 185-192, 2003.
[78] E. Lopez, S. Figueroa, M. Oset-Gasque, and M. Gonzalez, "Apoptosis and necrosis: two distinct events induced by cadmium in cortical neurons in culture," *BRITISH JOURNAL OF PHARMACOLOGY*, vol. 138, pp. 901-911, 2003.
[79] G. SHUKLA, T. HUSSAIN, and S. CHANDRA, "POSSIBLE ROLE OF REGIONAL SUPEROXIDE-DISMUTASE ACTIVITY AND LIPID PEROXIDE LEVELS IN CADMIUM NEUROTOXICITY - INVIVO AND INVITRO STUDIES IN GROWING-RATS," *LIFE SCIENCES*, vol. 41, pp. 2215-2221, 1987.
[80] A. Caccamo, M. Scaltriti, A. Caporali, D. D'Arca, F. Scorcioni, S. Astancolle, M. Mangiola, and S. Bettuzzi, "Cell detachment and apoptosis induction of immortalized human prostate epithelial cells are associated with early accumulation of a 45 kDa

nuclear isoform of clusterin," *BIOCHEMICAL JOURNAL*, vol. 382, pp. 157-168, 2004.

[81] P. Nicotera, M. Leist, and E. Ferrando-May, "Apoptosis and necrosis: different execution of the same death," *MITOCHONDRIA AND CELL DEATH*, pp. 69-73, 1999.

[82] BMBF-Studie, "Nanotechnologie pro Gesundheit:Chancen und Risiken," BMBF, Aachen Förderkennzeichen 16 / 1502, 2004.

[83] S. Artelt, O. Creutzenberg, H. Kock, K. Levsen, D. Nachtigall, U. Heinrich, T. Ruhle, and R. Schlogl, "Bioavailability of fine dispersed platinum as emitted from automotive catalytic converters: a model study," *SCIENCE OF THE TOTAL ENVIRONMENT*, vol. 228, pp. 219-242, 1999.

[84] K. Kanitsar, G. Koellensperger, S. Hann, A. Limbeck, H. Puxbaum, and G. Stingeder, "Determination of Pt, Pd and Rh by inductively coupled plasma sector field mass spectrometry (ICP-SFMS) in size-classified urban aerosol samples," *JOURNAL OF ANALYTICAL ATOMIC SPECTROMETRY*, vol. 18, pp. 239-246, 2003.

[85] D. Jefferson, "The surface activity of ultrafine particles," *PHILOSOPHICAL TRANSACTIONS OF THE ROYAL SOCIETY OF LONDON SERIES A-MATHEMATICAL PHYSICAL AND ENGINEERING SCIENCES*, vol. 358, pp. 2683-2692, 2000.

[86] A. Haruta, "When gold is not noble: Catalysis by nanoparticles," *CHEMICAL RECORD*, vol. 3, pp. 75-87, 2003.

[87] W. Parak, R. Boudreau, M. Le Gros, D. Gerion, D. Zanchet, C. Micheel, S. Williams, A. Alivisatos, and C. Larabell, "Cell motility and metastatic potential studies based on quantum dot imaging of phagokinetic tracks," *ADVANCED MATERIALS*, vol. 14, pp. 882-885, 2002.

[88] A. Jordan, R. Scholz, P. Wust, H. Schirra, T. Schiestel, H. Schmidt, and R. Felix, "Endocytosis of dextran and silan-coated magnetite nanoparticles and the effect of intracellular hyperthermia on human mammary carcinoma cells in vitro," *JOURNAL OF MAGNETISM AND MAGNETIC MATERIALS*, vol. 194, pp. 185-196, 1999.

[89] C. Wilhelm, C.Billotey, J.Roger, J.N.Pons, J.-C.Bacri, and F.Gazeau, "Intracellular uptake of anionic superparamagnetic nanoparticles
as a function of their surface coating," *Biomaterials*, vol. 24, pp. 1001-1011, 2003.

[90] J. A. Kloepfer, R. E. Mielke, M. S. Wong, K. H. Nealson, G. Stucky, and J. L. Nedeau, "Quantum Dots as Strain- and Metabolism-Specific Microbiological Lables," *Applied and Environmental Microbiology*, vol. 69, pp. 4205-4213, 2003.

[91] M. A. Videira, M. F. Botelho, A. C. Santos, L. F. Gouveia, J. J. P. d. Lima, and A. J. Almeida, "Lymphatic uptake of pulmonary delivered radiolabelled solid lipid nanoparticles," *JOURNAL OF DRUG TARGETING*, vol. 10, pp. 607-613, 2002.

[92] L. Ghitescu and A. Fixman, "Surface charge distribution on the endothelial cell of liver sinusoids," *J. Cell Biol.*, vol. 99, pp. 639-647, 1984.

[93] C.-W. Lam, J. T. James, R. McCluskey, and R. L. Hunter, "Pulmonary Toxicity of Single-Wall Carbon Nanotubes in Mice 7 and 90 Days After Intratracheal Instillation," *TOXICOLOGICAL SCIENCES*, vol. 77, pp. 126-134, 2004.

[94] D. B. Warheit, B. R. Laurence, K. L. Reed, D. H. Roach, G. A. M. Reynolds, and T. R. Webb, "Comparative Pulmonary Toxicity Assessment of Single-wall Carbon Nanotubes in Rats," *TOXICOLOGICAL SCIENCES*, vol. 77, pp. 117-125, 2004.

[95] A. M. Derfus, W. C. W. Chan, and S. N. Bhatia, "Probing the Cytotoxicity of Semiconductor Quantum Dots," *NanoLetters*, vol. 4, pp. 11-18, 2004.

[96] A. Shiohara, A. Hoshino, K. Hanaki, K. Suzuki, and K. Yamamoto, "On the cyto-toxicity caused by quantum dots," *MICROBIOLOGY AND IMMUNOLOGY*, vol. 48, pp. 669-675, 2004.

[97] M. C. Garnett, "Targeted drug conjugates: principles and progress," *Advanced Drug Delivery Reviews*, vol. 53, pp. 171-216, 2001.
[98] T. M. Allen and P. R. Cullis, "Drug Delivery Systems: Entering the Mainstream," *Science*, vol. 303, pp. 1818-1822, 2004.
[99] R. S. Tu and M. Tirrell, "Bottom-up design of biomimetic assemblies," *Advanced Drug Delivery Reviews*, vol. 56, pp. 1537-1563, 2004.
[100] A. N. Lukyanov and V. P. Torchilin, "Micelles from lipid derivatives of water-soluble polymers as delivery systems for poorly soluble drugs," *Advanced Drug Delivery Reviews*, vol. 56, pp. 1273-1289, 2004.
[101] A. Lavasanifar, J. Samuel, and G. S. Kwon, "Poly(ethylene oxide)-block-poly(L-amino acid) micelles for drug delivery," *Advanced Drug Delivery Reviews*, vol. 54, pp. 169-190, 2002.
[102] E. Donath, G. B. Sukhorukov, F. Caruso, S. A. Davis, and H. Möhwald, "Novel Hollow Polymer Shells by Colloid-Templated Assembly of Polyelectrolytes," *Angewandte Chemie International Edition*, vol. 37, pp. 2201-2205, 1998.
[103] G. B. Sukhorukov, E. Donath, S. Davis, H. Lichtenfeld, F. Caruso, V. I. Popov, and H. Möhwald, "Stepwise polyelectrolyte assembly on particle surfaces: a novel approach to colloid design," *Polymers for Advanced Technologies*, vol. 9, pp. 759-767, 1998.
[104] D. G. Shchukin, G. B. Sukhorukov, and H. Möhwald, "Smart inorganic/organic nanocomposite hollow microcapsules," *ANGEWANDTE CHEMIE-INTERNATIONAL EDITION*, vol. 42, pp. 4472-4475, 2003.

Anhang

K1

"Corrosion protection and long-term chemical functionalization of gallium arsenide in aqueous environment"

C. Kirchner, M. George, B. Stein, W. J. Parak, H. E. Gaub, and M. Seitz, *Advanced Functional Materials*, vol. 12, pp. 266-276, 2002.

ADVANCED FUNCTIONAL MATERIALS

Corrosion Protection and Long-Term Chemical Functionalization of Gallium Arsenide in an Aqueous Environment**

By *Christian Kirchner, Michael George, Bernhard Stein, Wolfgang J. Parak, Hermann E. Gaub,* and *Markus Seitz**

The chemical instability of the gallium arsenide surface poses a serious limitation to its use under ambient conditions, such as in air or aqueous solution. It is shown that both bare GaAs and GaAs coated with self-assembled monolayers of organic alkanethiols are continuously etched in aqueous environments, which limits their use as biosensor devices in physiological environments. A corrosion protection material having long-term stability ("chemical passivation") and biocompatibility ("biological passivation") with the GaAs surface was found to be interfacial layers of polymerized organic mercaptosilanes a few tens of nanometers thick. The mercaptosilanes not only provided a nearly perfect corrosion protection of GaAs in water, but they also have the potential to introduce chemical groups that allow easy, further surface functionalization. Characterization of the interfacial polymer layer and its protective role was done by atomic force microscopy (AFM), ellipsometry, contact angle measurements, and atomic absorption spectroscopy (AAS). The interfacial polymer layers fully suppressed the release of arsenic into the electrolyte buffer and also provided an adhesion-promoting interface, which allowed the cultivation of electrically excitable cells, normal rat kidney (NRK) fibroblasts, on GaAs. The electrical performance of GaAs and GaAs/InGaAs heterostructures in water was monitored via cyclic voltammetry and the *IU* characteristics of field-effect channels. GaAs was significantly stabilized by the insulating polymeric surface coatings, even under moderate electrochemical loads. These findings are promising for, e.g., the implementation of GaAs technology in future cell–semiconductor hybrids.

1. Introduction

Gallium arsenide is a semiconductor that has several advantages over silicon. In addition to its useful optoelectrical properties, it offers a higher electron mobility, which results in faster electronic circuits and switching times, as well as a lower energy dissipation at comparable powers and, therefore, a lower noise level.[1] Moreover, alloys of GaAs with other elements of comparable atomic size, such as aluminum or indium, may be used to control electronic excitation energies, and to design heterostructures of various geometries with sophisticated electronic properties, i.e., two-dimensional electron gases and quantum wells.[1,2] Although GaAs has found practical uses in many applications, such as in semiconductor lasers, photodetectors, and solar cells, the chemical instability of its surface under ambient conditions has prevented a wider range of implementations, including practicable GaAs-based metal-oxide–semiconductor (MOS) technology.

One implication of the native GaAs oxide layer is that it causes a substantial Fermi level pinning and an increase in band-bending of the electronic surface states, therefore impairing the performance of the practical device.[3–5] Moreover, when GaAs is transferred to an aqueous environment, the oxide layer dissolves rapidly. As a result, the substrate is continuously etched, which not only complicates the definition of stable electronic surface states, but also contaminates the aqueous solution with highly toxic arsenic acid (or the arsenite anion, AsO_3^{3-}), which is generated by oxide layer hydrolysis. Arsenic(III) compounds are known to be toxic to living cells, both in vivo and in vitro,[6,7] e.g., by blocking mitochondrial glucose metabolism. This poses another serious problem when GaAs is to be deployed in biological environments, e.g., in biosensors or nanocrystalline semiconductor fluorescence probes. GaAs therefore needs to be coated with protective layers that provide biocompatible interfaces. These should act as diffusion barriers for small ions and molecules, in order to prevent etching and contamination of the semiconductor and, in turn, to suppress the release of toxic arsenite into the buffer solution (Fig. 1).

The electronic and chemical "passivation" of the GaAs surface has been intensely discussed in the literature.[3–5,8] Inorganic sulfur compounds have frequently been used to lower the surface recombination rate of charge carriers in GaAs,[5,8–10] and passivation effects such as an increased photoluminescence intensity have also been reported when organic thiols were used.[11,12] The self-assembly of alkane thiol monolayers, a process well studied on gold,[13] has also, therefore, become an obvious strategy for the realization of ultra-thin surface coatings

[*] Dr. M. Seitz, C. Kirchner, M. George, B. Stein, Dr. W. J. Parak, Prof. H. E. Gaub
Lehrstuhl für Angewandte Physik & Center for NanoScience
Ludwig-Maximilians Universität
Amalienstrasse 54, D-80799 München (Germany)
E-mail: markus.seitz@physik.uni-muenchen.de

[**] The authors thank Dr. Brigitte Helmreich and Dr. Christoph Greil (Institut für Wassergüte und Abfallwirtschaft, TU München) for atomic absorption spectroscopy measurements. GaAs/InGaAs heterostructures were provided by Dr. H. Riechert (Infineon Corporate Research, München, Germany). The work was supported by the Deutsche Forschungsgemeinschaft (DFG) through SFB 486. Also, financial support by the Fonds der Chemischen Industrie is gratefully acknowledged.

  1616-301X/02/0404-0266 $ 17.50+.50/0

ADVANCED FUNCTIONAL MATERIALS A 3

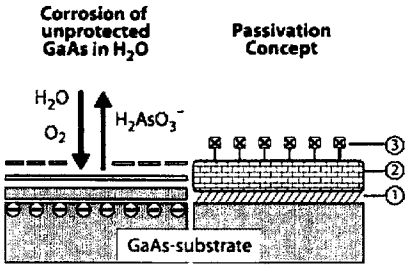

Fig. 1. Corrosion protection and chemical functionalization of gallium arsenide substrates under ambient conditions: Left: Corrosion of GaAs takes place in an aqueous environment by permanent formation and dissolution of an interfacial oxide layer. The formation of the oxide layer is responsible for surface states at the GaAs–electrolyte interface, and the dissolution of the oxide layer causes contamination of the electrolyte by arsenic ions. Right: Electrical passivation of the GaAs surface is provided by an organic thiol monolayer (1); a polymerized silane layer adds long-term corrosion protection (chemical and biological passivation) (2), and introduces functionalities for further surface reactions (3).

on GaAs,[14] e.g., octadecylthiol (ODT) adsorption layers were employed as resist masks on GaAs for lithographic purposes.[15] Also, as on gold, alkane thiols were used to introduce surface functionalities present at the ω-end of the mercaptoalkyl chain,[12,16] such as the carboxy group in 16-mercaptohexadecanoic acid (MHDA).[12,16] However, whereas oxide regrowth is remarkably inhibited at the thiol/GaAs interface,[17] surface coverage is often incomplete,[16,18] and the monolayer films are gradually disrupted over the course of hours to days unless they are stored in an inert atmosphere.[15] To improve thiol binding to the GaAs surface, in-situ etching methods have been introduced to avoid oxide regrowth on freshly etched substrates,[19,20] which would otherwise occur immediately upon exposure to air.[21] It was recently suggested that ODT surfaces, assembled with a photochemical etching method, keep impedance spectra stable for several hours in an aqueous electrolyte solution under conditions of zero-current potential.[22] Further, as a promising alternative to the surface passivation of gallium arsenide with organic monolayers, benzoic and dicarboxylic acid derivatives have been introduced.[23–25] Their chemisorption to GaAs has been shown to control the work function of the semiconductor,[23] and the compatibility of the resulting interface with at least some biological environments has recently led to the development of the first GaAs-based biosensor for the direct detection of micromolar levels of nitric oxide under physiological conditions.[26,27]

Chemical crosslinking provides an additional means for improving the stability of GaAs surface coatings. In particular, an adsorption layer of (3-mercaptopropyl)trimethoxysilane (MPT) provides a trimethoxy-silyl terminated surface that can be polymerized by subsequent exposure to a weak acid. The significant initial improvement of the photoluminescence intensity was found to decay only over the course of several days to weeks, in a controlled argon atmosphere, and MPT polymerization further increased the observed degradation times by about one order of magnitude.[28] However, whereas deterioration of the GaAs surface was generally avoided more effectively when the polymerized overlayer rather than non-polymerized MPT was used, the difference was not as pronounced under ambient conditions (i.e., in humid air).

This work reports on an effective chemical passivation and functionalization of the GaAs surface by polymerization and deposition of silane precursors in a solution sol–gel process,[29–31] which results in interfacial organosilicate layers that are about an order of magnitude thicker than self-assembled monolayers. So far, there has been no investigation on the stability of polymerized MPT coatings on GaAs in aqueous environments, and in particular on their behavior under permanent electrochemical stress. As the thickness and crosslink density of the interfacial polymer layer is increased, degradation of the GaAs substrate should also be prevented with increasing efficiency. However, it is intended that the thickness of the insulating coating atop the semiconductor substrate should be no more than a few tens of nanometers (i.e., less than that which could be achieved with spin-coated polymers). This approach is somewhat related to current efforts towards the stabilization and chemical functionalization of quantum dots and semiconductor nanocrystals by polysilane (i.e., silica) encapsulation.[32–34]

Atomic force microscopy (AFM), ellipsometry, and atomic absorption spectroscopy (AAS) were employed to investigate the durability of monomolecular and polymerized organic thiol adsorption layers on GaAs in an aqueous environment, with a view to their use as biocompatible surface coatings for the cultivation of living cells on gallium arsenide. Finally, the substrate protection was monitored by examining the electrical characteristics of poly(MPT)-coated GaAs wafers (and of quantum-well heterostructures) in a physiological buffer, which provided an additional criterion for the quality and stability of the interfacial layer.

2. Results

2.1. Corrosion of Bare Gallium Arsenide Surfaces in an Aqueous Environment

First, the corroding effect of water and aqueous 140 mM NaCl solution on a bare, cleaned gallium arsenide surface was determined. Figure 2a shows a 45 × 45 μm^2 section of such a gallium arsenide substrate, partially covered with a protecting stripe mask of photoresist, upon exposure to water at 37 °C for 24 h. After removal of the photoresist, by rinsing with acetone, the previously protected areas appeared bright, whereas the dark regions correspond to the deeper, etched channels. The depth of the etched channels was estimated from the corresponding height profile of a horizontal cross section as ~100 nm (Fig. 2b), i.e., the etching rate of gallium arsenide in pure water under incubating conditions (37 °C, 5 vol.-% atmospheric CO_2) can be given as ~100 nm/day. From the crystal structure of GaAs, which is of the sphalerite-type (zinc blende) with a lattice constant, d = 5.56 Å,[35] we can estimate the number of arsenic atoms released from the substrate. Four atoms of

  1616-301X/02/0404-0267 $ 17.50+.50/0

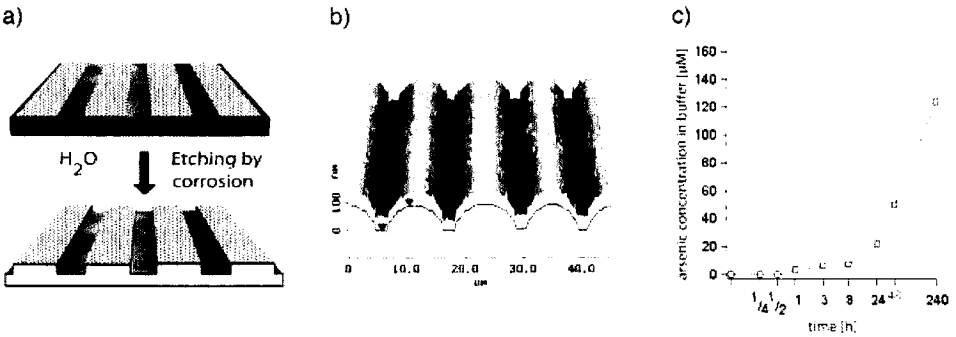

Fig. 2. Etching of bare GaAs substrates in water. a) For the determination of etching rates, the GaAs sample was partially covered by a stripe mask of photoresist during water exposure for 24 h, and imaged after removal of the photoresist. b) An AFM image from which the etching depth was evaluated from the averaged cross section profile. c) The time-dependent increase of arsenite concentration (as determined by AAS) in water over a bare, uncoated GaAs wafer. Note the logarithmic timescale.

each element are present per unit cell, i.e., per ~170 Å^3, so that an etching depth of 100 nm over an area of 1 mm^2 corresponds to a volume of 10^{-13} m^3, i.e., 5.8×10^{14} unit cells. This is equivalent to 2.3×10^{15} arsenic atoms, which corresponds to an arsenic release of ~4 nmol (mm^2 day)$^{-1}$ from the GaAs wafer.

The etching rate approximately doubled in a 140 mM NaCl solution, that is, ~200 nm/day (or ~8 nm/h). Apparently, higher temperatures as well as the presence of salt and CO_2 (or a combination of them) lead to faster corrosion of gallium arsenide in water, but even in pure water at room temperature the etching of the substrate proceeds at a rate of at least ~0.7 nm/h (i.e., an arsenic release rate of 0.7 nmol (mm^2 day)$^{-1}$). The root mean square (rms) surface roughness values of a freshly cleaned and an etched GaAs surface (i.e., after 0 and 24 h of water exposure) were found to be 0.8 and 1.0 nm, respectively. Additionally, the actual amount of arsenic present in the aqueous solution over an untreated GaAs surface was determined by atomic absorption spectroscopy. Figure 2c shows the arsenite concentration increase over the course of two days, again under incubating conditions. The arsenic concentration of 22 µM, which was found in the buffer after one day, is approximately a magnitude lower than the actual amount of arsenic released from the substrate as estimated from the above AFM data. For full hydrolysis and complete solubility of the released arsenic ions, a concentration of 75 mm^2 × 4 nmol mm^{-2} in 1 mL water, i.e., 300 µM, would be expected. This suggests that the material removed from the GaAs wafer is not fully hydrolyzed and remains insoluble to a great extent.[36]

2.2. Gallium Arsenide Substrates Covered with Self-Assembling Alkanethiol Monolayers

Figure 3a shows an AFM image of a GaAs wafer coated with a self-assembled monolayer of octadecylthiol (ODT) prepared from an ethanolic solution. The surface appears uniform, but grainy, with a surface roughness of 1.3 ± 0.1 nm (rms value). The film thickness of the freshly prepared interfacial layer was determined by ellipsometry to be 1.7 nm, which correlates well with a thiol monolayer in which the alkyl chains are slightly tilted with respect to the surface normal.[37] Contact angle measurements further indicated the successful deposition of the hydrophobic alkane thiol. The values measured for the advancing and receding contact angles of a water droplet on the ODT-covered GaAs surface were $\theta_a = 97°$ and $\theta_r = 62°$ (the contact angles on GaAs were found to be pH dependent, i.e., $\theta_a = 63°$ and $\theta_r = 32°$ at pH 5, and $\theta_a = 36°$ and $\theta_r = 9°$ at pH 11). Figure 3b shows the AFM image of the same ODT monolayer-coated GaAs surface after exposure to water at 37 °C for one day: the surface had become significantly rougher. The corresponding rms surface roughness values were 16.8 ± 1.3 nm for a sample etched in pure water (shown), and 13.0 ± 1.0 nm for a second sample etched in 140 mM NaCl solution. The AFM image of the latter surface is not shown here, as it revealed a surface topography resembling the water-etched sample shown in Figure 3b.

Similar results were also found for MHDA treated surfaces. The contact angles of water droplets on freshly prepared

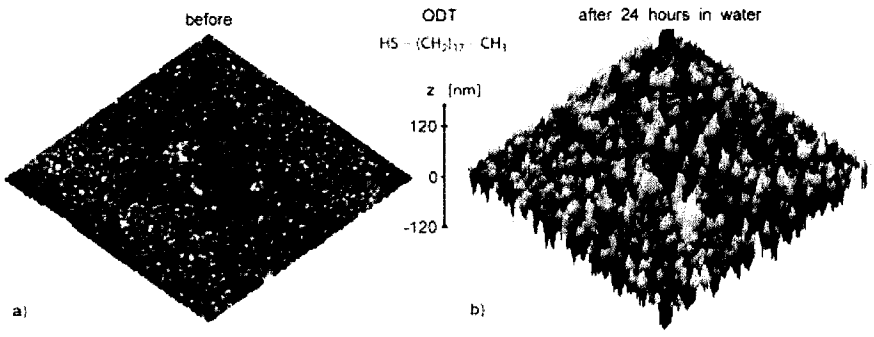

Fig. 3. AFM images (2 µm × 2 µm) of ODT-coated GaAs wafers a) before and b) after 24 h exposure to water at 37 °C.

  1616-301X/02/0404-0268 $ 17.50+.50/0

MHDA-coated GaAs wafers were θ_a = 81° and θ_r = 42° at pH 5; and θ_a = 77° and θ_r = 4° at pH 11. The topographic AFM images of the surfaces before and after exposure to water were comparable to those observed for the ODT-covered GaAs wafers. Note that the rms value of 16 nm, observed for monolayer-coated substrates after exposure to water for 24 h corresponds to an average peak–valley distance of ~45 nm. This is an order of magnitude greater than the thickness of the ODT or MHDA monolayer, but comparable to the etching depths found on bare GaAs. This significant increase in surface roughness can be seen as evidence of the significant etching of the GaAs substrate, even in the presence of the thiol monolayers, indicating that the interfacial thiol monolayers must have been at least partially destroyed upon exposure of the samples to water. The mere ineffectiveness of alkanethiol monolayers to protect gallium arsenide from corrosion in an aqueous environment was further revealed by AAS measurements. The arsenic concentrations and release rates found in the buffer solution over MHDA- and ODT-coated GaAs samples did not differ significantly from those found for uncoated GaAs substrates (see Fig. 5 below). These data further indicate a great deal of surface damage to the ODT coated GaAs surfaces after 24 h, the extent of which is comparable to that of completely unprotected GaAs.

2.3. Gallium Arsenide Substrates Coated with Adsorption Layers of Polymerizable Thiol

It was suggested that self-assembled MPT monolayers may be used as a coupling layer between GaAs and a corrosion protection layer, as the MPT would provide stable thiol binding to the substrate as well as reactive alkoxysilane units for the attachment of a polymerized silica or siloxane layer.[28] The polymerization reaction for the coating of GaAs surfaces with a multilayer of polymerized MPT is sketched in Figure 4a. Following this approach, we prepared poly(MPT) layers with thicknesses between 10 and 50 nm. Representative of these layers, Figures 4b and 4c show AFM images of a poly(MPT)-coated wafer before and after exposure to water at 37 °C for one day, respectively. Although the interfacial roughness becomes somewhat more pronounced as the rms value increases from 1.3 to 2.6 nm, from before to after water treatment (or 3.8 nm after exposure to 140 mM NaCl solution), the ellipsometrical data indicate good corrosion stability of the interfacial layer in an aqueous environment. The ellipsometrically determined thicknesses, d, of the interfacial polymer layers of two different samples, before and after 24 h of storage in pure water (d_o = 40.6 nm, d_{24h} = 41.2 nm), or in 140 mM NaCl solution (d_o = 39.3 nm, d_{24h} = 39.2 nm), are, within experimental error, the same. This was confirmed by the observation that polymerized MPT layers on GaAs completely prevented the release of arsenic into the bulk. As shown in Figure 5, practically no arsenite was detected (over the course of 10 days) in the aqueous solution in which a GaAs substrate coated with a 20 nm thick layer of poly(MPT) was stored.

2.4. Toxicity of Sodium Arsenite to Normal Rat Kidney Fibroblasts

Normal rat kidney (NRK) fibroblasts are a fast growing and robust cell line that, in contrast to other fibroblasts, form an electrically excitable tissue.[38,39] They were found to be sensitive

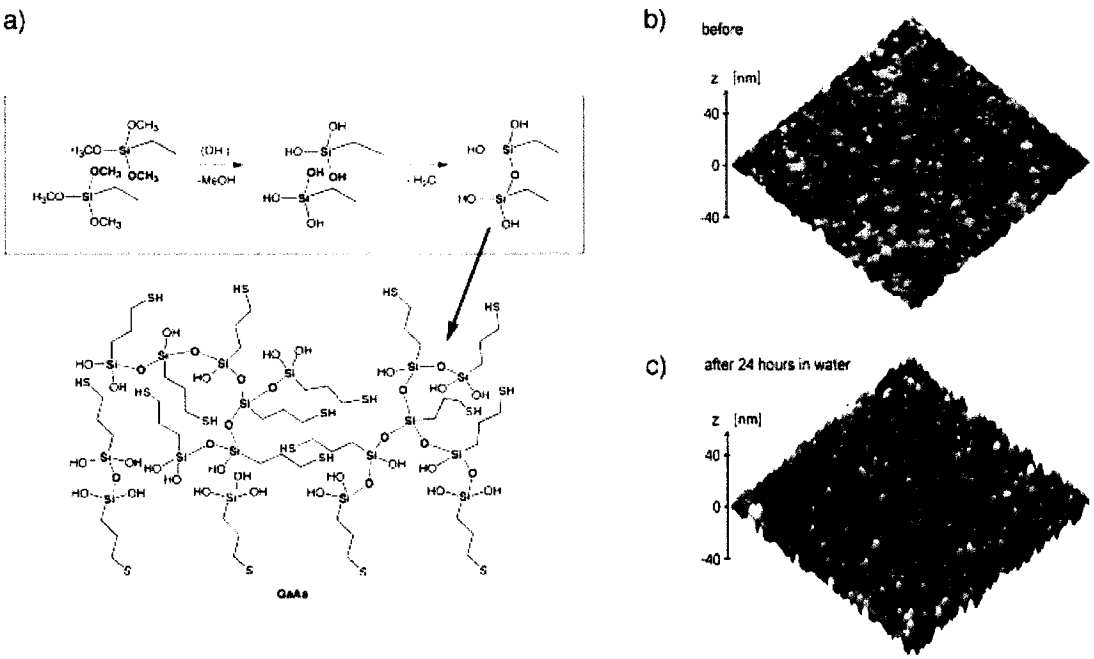

Fig. 4. a) Preparation of polymerized interfacial layers on GaAs from 3-mercaptopropyltrimethoxysilane (MPT). b,c) AFM images (2 μm × 2 μm) of poly(MPT)-coated GaAs wafers before (b) and after (c) exposure to water for 24 h, at 37 °C.

  1616-301X/02/0404-0269 $ 17.50+.50/0

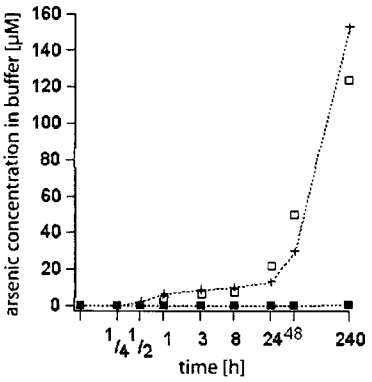

Fig. 5. Concentration of arsenite released from the GaAs wafers in an aqueous solution vs. a logarithmic timescale as determined by AAS. Bare GaAs (□); ODT-coated GaAs (+), poly(MPT)-coated GaAs (■).

to the presence of arsenite in the buffer medium, and may thus serve as reporters of the surface corrosion of GaAs substrates. Toxic effects of arsenite ions on NRK fibroblast cultures grown in petri dishes were observed upon addition of sodium arsenite to the buffer solution. Although AsO_3^{3-} up to concentrations of 40 μM had little effect on cells already adhering to the petri dish substrate, even a fully confluent cell layer was found to be detached from the substrate one day after the addition of 50 μM sodium arsenite. The toxic effect was even more pronounced when arsenite was already present at the beginning of fibroblast cultivation: cell adhesion was strongly altered above an arsenite concentration of 8 μM, and completely suppressed at 10 μM AsO_3^{3-}. Although in general there may be several factors limiting fibroblast adhesion and growth on gallium arsenide, it was concluded that the efficient blocking of arsenite release from the substrate below a threshold concentration of approximately 8 μM is mandatory in order to achieve NRK cultivation, particularly in the early stages of cell layer proliferation.

2.5. Cultivation of NRK Fibroblasts on GaAs Substrates

As a first test for biocompatibility, the cultivation of NRK fibroblast cells on various surface coatings on gallium arsenide was attempted. When fibroblasts were spread on GaAs, they did not adhere to the surfaces at any time. However, trypan blue tests proved that cell death did not occur until 1–2 days after seeding the cells. Coating GaAs surfaces with self-assembled monolayers of ODT, MHDA, or MPT was found to significantly promote fibroblast adhesion. During the first eight hours, cell proliferation proceeded as in petri dishes, but, after longer times, the cells no longer proliferated and they began to detach from the surfaces, until after 24 h nearly no cells remained adhered, as shown for MHDA-coated substrates in Figure 6a. On GaAs covered with a 20 nm thick layer of poly(MPT) the cultivation of NRK fibroblasts was possible, without any signs of arsenite toxicity, during the entire life cycle from seeding to the apoptosis of the confluent cell layer after 7 days. Figure 6b shows the optical microscopy image obtained after four days in culture. Therefore, in addition to meeting the primary condition of completely preventing the release of toxic ions from GaAs, poly(MPT)-coated surfaces promote the adhesion of NRK fibroblasts, such that cultures of living cells could be grown for days only a few nanometers away from the toxic semiconductor substrate.

2.6. Electrical Characterization of GaAs in an Aqueous Environment

Although in the above it was shown that polymeric surface coatings on GaAs effectively block the release of arsenic from GaAs in aqueous solution, and thus prevent contamination of the buffer, the interfacial corrosion itself can be monitored by studying the electronic characteristics of the semiconductor substrate. Figure 7 shows the cyclic voltammograms of uncoated and poly(MPT)-coated GaAs substrates immediately after exposure to a 140 mM NaCl solution. Over the potential range from –1 to +0.5 V, the poly(MPT)-coated sample showed low oxidation and reduction currents $I < 200$ nA cm^{-2}, whereas $I > 250$ μA cm^{-2} was found for freshly etched n-GaAs, which is comparable to values reported for bare GaAs after photochemical etching treatment.[22] The poly(MPT)-coated sample was then continuously measured for 40 h in an electrolyte solution over the voltage range from –1.5 to +1.5 V, and it was observed that, with time, the threshold voltage U_{th} decreased, while the maximum current, I_{max}, increased. This indicates slow degradation of the interfacial polysiloxane coating under constant electrical stress. However, as can be seen from the inset (Fig. 7) showing a magnification of the IU curve taken after 24 h, the current over the range from –1 to +0.5 V remained at low values throughout the entire measurement.

The poly(MPT) coatings on GaAs are currently being characterized by impedance measurements. A detailed description of these studies will be published later; however, it should be noted here that the interfacial capacitance of the coated semi-

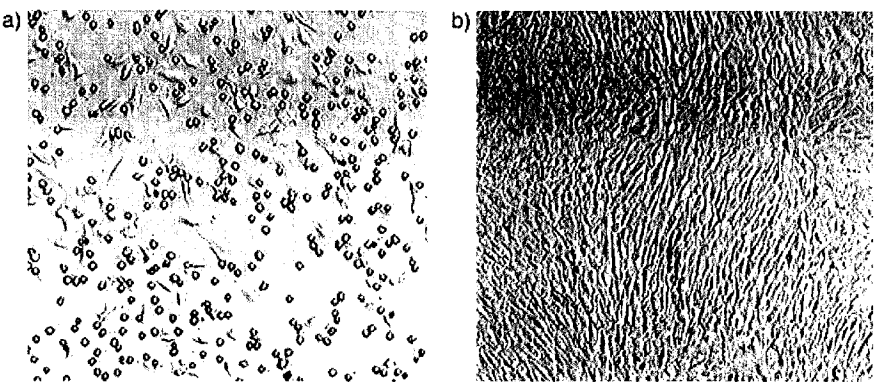

Fig. 6. Optical microscopy images (600 μm × 600 μm) of NRK fibroblast cultures on a) MHDA-coated GaAs wafers, taken after 15 h, and b) poly(MPT)-coated GaAs wafers, taken after 4 days.

  1616-301X/02/0404-0270 $ 17.50+.50/0

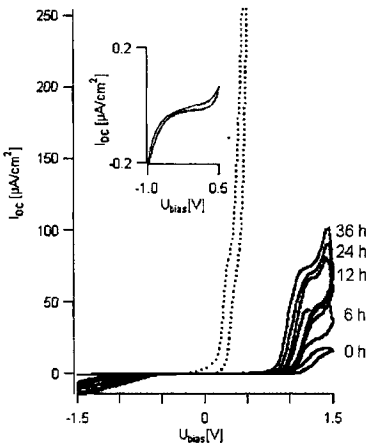

Fig. 7. Cyclic voltammograms of the uncoated, freshly etched GaAs (dotted line, potential range from –1 to +0.5 V), and of the poly(MPT)-coated sample (solid line, potential range from –1.5 to +1.5 V) in 140 mM NaCl solution, at room temperature. For bare GaAs, only the curve taken immediately after exposure to the electrolyte is shown. The curves for poly(MPT)-coated GaAs are taken from a set of continuous recordings of cyclic voltammograms, immediately after exposure to the electrolyte solution, and after 4, 8, 12, 24, and 36 h of continuous measurement. The inset shows a magnification of the recording after 24 h, over the range from –1 to +0.5 V.

conductor substrate, as obtained from a simplified circuit model, is dominated by the capacitance of the polymer layer. It amounts to $C \approx 110$ nF cm^{-2}, whereas $C \approx 1$–2 μF cm^{-2} has been reported for freshly etched GaAs substrates of comparable doping densities.[22]

To study the passivation effect of poly(MPT) coatings on field-effect channels, which are candidates for future biosensor applications,[40,41] the $I_{SD}U_{el}$ characteristics of GaAs/InGaAs quantum-well heterostructures were recorded in a 140 mM NaCl electrolyte solution at room temperature (Fig. 8d). The source–drain current, I_{SD}, was recorded over the potential range $U_{el} = -1.5$ to +1.5 V for uncoated and poly(MPT)-coated test channels (Figs. 8a and b, respectively).

In the beginning, the uncoated samples (Fig. 8a) showed typical $I_{SD}U_{el}$ curves for n-type channels,[35] with a constant high conductivity for positive electrode potentials and low conductivity for negative potentials, i.e., showing a depletion of the majority of the charge carriers (electrons). For positive potentials, $U_{el} > +1.5$ V, the conductance was found to decrease due to gate leakage (note that similar curves can be obtained when the electrolyte is replaced by a metallic top-gate). With time, the characteristics of the uncoated channels shifted to more positive values and became steeper, indicating an increase of the gate capacitance C_g, which in this case is the capacitance between the electrolyte and the field-effect channel. This most likely corresponds to a reduction in the thickness of the cap-layer between the field-effect channels and the electrolyte solution due to etching of GaAs in the aqueous environment, which was found to occur at a comparable rate. Moreover, the maximum channel conductivity drastically decreased after 1.5 h, and, after 2 h the channel resistance was found to be infinitely high. This observation may be explained by a decreased breakthrough voltage of the gate as a result of the reduction of the cap thickness. Furthermore, an increased density of surface states may act as recombination centers for electrons. In order to illustrate this time-dependent degradation of the $I_{SD}U_{el}$ characteristics, the maximum channel conductivity (g_{max}) for positive potentials of the electrolyte solution was plotted versus time and this is shown in Figure 8c.

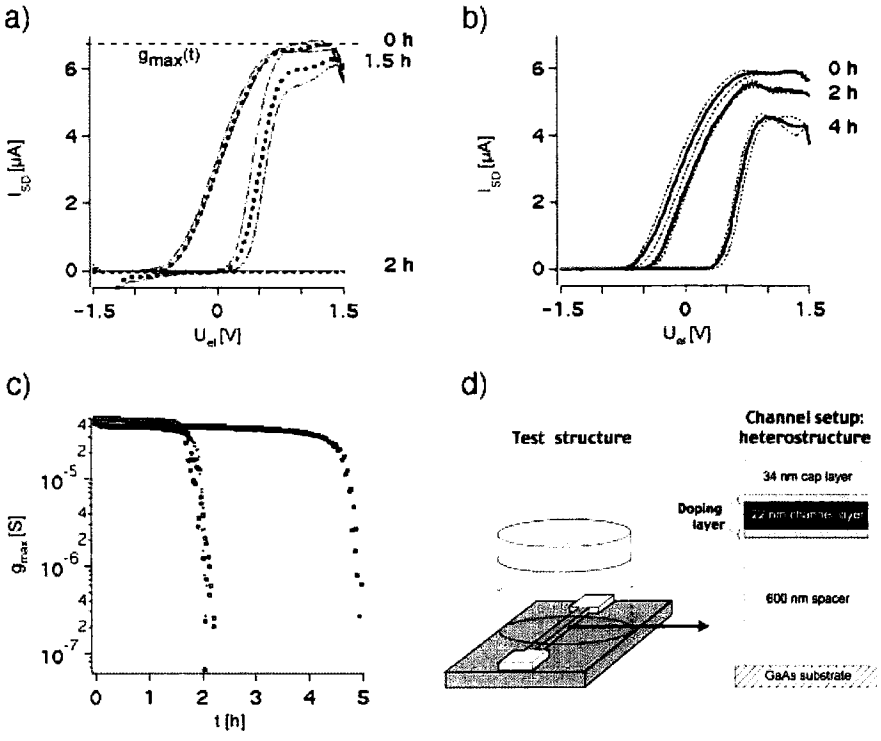

Fig. 8. Stability of a GaAs heterostructure (shown in d) under an electrical load: a) Channel current I_C of an uncoated sample versus the electrolyte potential U_{el} at 140 mV source–drain voltage, U_{SD}, after 0, 1.5, and 2 h of continuous recording of the I_C–U_{el} characteristics. The bold lines are the mean values of the trace and retrace curves (thin lines, recorded from –1.5 to +1.5 V). b) The corresponding curves of poly(MPT)-coated channels (ellipsometrically determined layer thickness $d \approx 10$ nm) after 0, 2, and 4 h of continuous measurement. c) Maximum channel conductance, g_{max}, for uncoated (□) and coated (■) samples plotted versus time. d) A field-effect channel (length: 2.5 mm, width 100 μm) was prepared from a GaAs heterostructure by lithographic etching, and placed in a sealed Teflon chamber containing electrolyte solution (140 mM NaCl). The source–drain voltage, U_{SD}, was applied via ohmic gold contacts on the outside of the test chamber, while the gate voltage was applied via a Ag/AgCl electrode in the electrolyte. The field-effect channel was built as a GaAs/InGaAs quantum-well heterostructure located 34 nm below the sample surface. Charge carriers were provided by surrounding doping layers (details are given in the Experimental section).

1616-301X/02/0404-0271 $ 17.50+.50/0

Compared to the uncoated samples, the slope of the $I_{SD}U_{el}$ curves of poly(MPT)-coated channels is slightly reduced (shown here for a 10 nm surface coating), which can be assigned to a decreased gate capacitance. Again, the curves are shifted to more positive potentials upon exposure to an electrolyte solution, but the degradation is significantly decelerated during the first 2.5 h. As can be seen in Figure 8c, the lifetime of the channel was extended by a factor of ~2.5 compared to the uncoated samples. Thicker poly(MPT) coatings further prolong the lifetime of the field-effect channels, but the shape of the characteristics may be affected as the polymer layer becomes thicker, and thus increasingly inhomogeneous. Also, it was found that the stability of the field-effect channels was dramatically affected by the continuous electrochemical stress during the measurements. A second, non-contacted channel, which was immersed in the same electrolyte solution during the measurement of a parallel, active channel, showed the typical, original shape of the $I_{SD}U_{el}$ characteristics, even after 24 h contact with the electrolyte solution. In contrast, the uncoated channels did not show any conductance after that time, as the cap layer and the field-effect channels were fully removed by etching in the NaCl solution. Therefore, poly(MPT) coatings efficiently preserve the electronic properties of the GaAs heterostructures in an aqueous environment, as long as the electrochemical potential is held below a certain positive threshold value.

3. Discussion

The chemical composition of the native GaAs oxide layer has been described in many previous publications.[28,42] It is known that it contains elemental As, as well Ga_2O_3 and As_2O_3, the latter of which is readily hydrolyzed and is soluble in water. It was further reported that GaAs degradation in water depends on the concentration of oxygen in the water,[42] so that the observed corrosion of gallium arsenide can be understood as a two-step process consisting of GaAs oxidation followed by dissolution of the oxide. There appears to be a further dependence of the GaAs etching rate on temperature, salt concentration, and the presence of carbon dioxide, as the etching rate was highest in a 140 mM NaCl solution in an incubator with an atmosphere containing 5 % CO_2 at 37 °C (which corresponds to near physiological conditions during cell cultivation).[43]

Most passivation strategies found in the literature employ inorganic or organic thiols, where sulfur is intended to bind covalently to the GaAs surface, but the stability of the adsorbed monolayers is often limited, in part due to their defective structure.[18,44] Our observations on self-assembled monolayers (SAMs) of ODT and MHDA are in accordance with earlier findings.[15,16,18,37] The ellipsometrically obtained thicknesses of ~1.5 nm point to a tilted arrangement of the alkyl chains with respect to the surface normal, as has been previously reported.[37,45] Further, the surface topography after SAM formation was confirmed to have an island-like character for both compounds.[16,18] The wetting behavior of these surfaces by deionized water further points to their poor quality. Although the increase of the advancing contact angle after thiol adsorption formation corresponds to the successful deposition of a layer of hydrophobic alkyl chains on GaAs, the measured values deviate from those of the same SAMs on gold surfaces, i.e., 97° instead of 109–112° for ODT, and 81° instead of 60–65° for MHDA.[46] The pH dependence of the receding contact angle on MHDA-coated GaAs indicates the existence of COOH groups on the surface, although the expected decrease of the advancing contact angle θ_a from 60–65° at pH 5.8 to 48–52° at pH 11.0 of MHDA on gold[46] was not found here. The observed contact angle hysteresis ($\theta_a - \theta_r$) may have been caused by surface roughness as well as chemical heterogeneity,[47] and—in anticipation of the following—by any non-equilibrium process in which the surface is altered during wetting.

For GaAs wafers prepared by standard wet-etching methods, irreversible changes to the interfacial structure and composition certainly occur upon long-time exposure of the monolayer-coated wafers to water, during which significant etching is observed, accompanied by an increase in surface roughness. Most critically, AAS measurements revealed that the GaAs substrate is not efficiently protected by a thiol monolayer. The time-dependent increase of the arsenic concentration in the buffer above the monolayer-coated samples does not indicate any significant change in ion permeability from that of an uncoated substrate. It appears that the "islands" of self-assembled thiols in the grainy monolayer structure may only initially act as a "mask" for the etchant until the anisotropy of the etching process ensures that lateral corrosion of the covered GaAs substrate also occurs, after which the thiols are removed. Such a delayed corrosion of the thiol-protected areas in the early stages of the etching process would explain the observed surface roughness increase after exposure to water (which would otherwise leave a rather smooth surface).

Consequently, the corrosion protection provided by self-assembled thiol monolayers in an aqueous environment is rather limited. Hou et al. have suggested that two-dimensional crosslinking of the adsorbed MPT's silane groups stabilizes the interfacial monolayer.[28] Apparently, increasing the thickness and crosslink density of the interfacial polymer layer should assist this process with increasing efficiency, as was found for poly(MPT) coatings a few tens of nanometers thick. The thickness range of interest lies between "ultra-thin" thiol monolayers and spin-coated polymer (e.g., poly(methylmethacrylate)—PMMA) films, which were found to provide an improved biocompatibility,[40] but only above a certain thickness (>80 nm). A particular advantage of the approach is its potential for the subsequent introduction of surface functionalities, which would allow, e.g., the decoration of GaAs with biomolecules, such as adhesion-promoting peptides, employing standard surface chemistry. The first step in this approach is the adsorption of an MPT monolayer, which serves as a reactive silane interface for the subsequent covalent coupling and continuous polymerization of further silane monomers (see Fig. 4).[28] In principle, any alkoxyalkylsilane carrying functional end groups on the alkyl chain may be used to modify the surface of the interfacial polymer layer (i.e., the interfacial –SH in Fig. 1 may be replaced by $-NH_2$, –epoxy, etc.).

1616-301X/02/0404-0272 $ 17.50+.50/0

The preparation of "pure" poly(MPT) layers, which has been investigated here as a first step, could be achieved in one step by the hydrolysis and precipitation of MPT monomers from an alkaline ethanolic solution.[30,32,33] The reaction mechanism has not been further investigated here, but, as indicated, the reaction most likely proceeds via the formation of oligomeric aggregates in solution by a polycondensation reaction of the silanol units (see Fig. 4a), which may continue after their deposition onto the substrate. The reaction can be driven further to completion (i.e., to a higher crosslink density) by baking the coated substrates at elevated temperatures (~80 °C) for several hours. Although not systematically studied, the thickness of the resulting polysiloxane layer could easily be adjusted in our preparations, simply by varying the monomer concentration and exposure times of the GaAs samples to the ethanolic monomer solutions. Here, we investigated samples with approximate thicknesses of 10, 20, and 40 nm. These coatings, which are about an order of magnitude thicker than self-assembled thiol monolayers, showed a remarkably high stability in aqueous environments. They did not deteriorate when exposed to water, and ellipsometry did not detect any significant differences between the thickness of the coating before and after water treatment.[48]

One of the most exciting applications of field-effect devices in physiological environments is, of course, the development of cell–semiconductor hybrids, as it has been shown that extracellular potentials of single electrically excitable cells can be monitored by silicon-based sensors.[49] The excellent electronic properties of GaAs promise an improved sensitivity of the biosensors, and should allow the construction of surface potential detectors with a high spatial resolution and a large number of addressable points, for example, the so-called field-effect-addressable potentiometric sensor (FAPS).[40,41,50,51] Next to the demonstrated suppression of toxic effects due to arsenic release, the cultivation of adherent cells on a semiconductor surface is a second obvious and fundamental requirement of the biosensor.

It is interesting to note that, despite their permeability to arsenic, both ODT- and MHDA-coated surfaces provided an adhesion-promoting surface on GaAs within the first 8 h of cultivation before the cells started to detach. The loss of the anchor points on the substrate may have been caused either by the deterioration of the interfacial monolayer, or by the toxic effects of arsenite. It has been shown that fibroblast cells are separated from supporting substrates by a cleft of approximately 50 nm.[52] The intervening space is known to be filled by an extracellular matrix produced by the settled fibroblasts, containing, e.g., hyaluronic acid or fibronectin.[53] Moreover, it was recently found that biomacromolecules may strongly and selectively bind to semiconductor surfaces, including gallium arsenide.[54] One should therefore assume that our fibroblast layers are supported by an adhesion-promoting network of macromolecules stabilizing anchoring of the cell layer to the substrate. In this context, our separate toxicity studies of sodium arsenite on NRK fibroblasts grown in petri dishes revealed that an arsenite concentration of 8–10 μM hinders the development of a young cell layer, whereas an already grown confluent cell layer tolerates arsenite concentrations up to 50 μM. The adhesion-promoting extracellular matrix may thus improve anchoring of the fibroblast to the substrate, but it is not sufficient to suppress the release, and toxic effects of, arsenite fully, and eventually the cell layer detaches. The delayed cell detachment from alkanethiol-coated substrates after the initial adhesion is thus assumed to be caused primarily by the presence of arsenite toxin. This assumption is supported by the fact that the critical arsenite concentration in the buffer solution above the alkanethiol monolayer-coated GaAs is reached after approximately 8 h (see Fig. 5), as a result of substrate corrosion.[55]

Despite their potential to provide an initially biocompatible and adhesion-promoting interface, it is the instability of self-assembled monolayers that renders these systems practically useless under physiological conditions. Although it was noticed that the homogeneity and stability of self-assembled monolayers was significantly improved when arsenic-rich GaAs surfaces were prepared in a photochemical etching step prior to thiol adsorption,[22] the long-term cultivation of living cells on these substrates remains to be proven. On the other hand, there was no arsenic release into the aqueous medium from the underlying GaAs substrate through the thicker interfacial poly(MPT) layer within the detection limit of AAS over a period of 10 days. In addition to this excellent durability, poly(MPT) provides an adhesion-promoting surface for both NRK fibroblasts and chicken cardiomyocytes (results not shown here). This successful cultivation of electrically excitable cells makes it a highly promising material for the future development of cell–semiconductor hybrids based on GaAs technology.

A final, most demanding condition for the successful implementation of GaAs technology in the life sciences is the conservation of the electrical properties of the GaAs substrate itself, under electrochemical loads and in physiological environments (the protection of the semiconductor under these conditions may thus be termed "biological" passivation). The long-term evaluation of the electrical characteristics of GaAs devices directly monitors the stability of the semiconductor surface, and serves as a sensitive criterion for the protection of the substrate by poly(MPT) coatings. Cyclic voltammograms of poly(MPT)-coated GaAs indicate a significant shift of the breakthrough voltage to positive potentials, compared to bare GaAs. Practically no oxidation or reduction current was observed in the range between –0.5 and +0.5 V, and it is only the applied electrochemical stress resulting from continuously sweeping the potential between –1.5 and +1.5 V that induces deterioration of the interface with time. Electrochemical stress was also found to significantly impair the performance of GaAs/InGaAs heterostructures. This occurs much faster than for bulk GaAs, as induced point defects appear to have much more drastic consequences on the characteristics of a field-effect channel than on the characteristics of the bulk material. Local destruction of the heterostructure cap and doping layers finally results in an infinite resistance over the entire voltage range. Again, degradation occurs fastest during the application of positive gate potentials, but it has to be stressed that this is a

1616-301X/02/0404-0273 $ 17.50+.50/0

general problem when semiconductor devices are deployed in aqueous environments, and is not limited to GaAs devices. For instance, it is known that for SiO_2 gate isolation layers, hydration and diffusion of alkali ions may strongly alter the electrical properties of the field oxide layer, resulting in hysteresis effects and a destabilization of the interfacial layer, and, therefore, the fast aging of the device. Especially for positive gate voltages, electrical currents are measured through the SiO_2 layer, if a sufficiently high number of positive ions is present in the field oxide layer.[56,57] It is thus important to note that poly(MPT) fully protects the otherwise unstable GaAs substrate in an aqueous environment in the absence of any electrochemical potential. The present work shows that poly(MPT) shields GaAs-based field-effect channels from corrosion, as the *IU* characteristics remain practically unaltered after 24 h under physiological conditions.

Generally, poly(MPT) improves the long-term stability of GaAs in aqueous environments, even under continuous electrochemical loads, and a more thorough analysis of the voltage range over which the field-effect channels can be operated steadily is currently under investigation: this is a necessary requirement for their use in future biosensor devices. Cyclic voltammetry may indicate a potential for the stable implementation of poly(MPT)-coated GaAs surfaces, if the gate voltage is kept below +0.5 V (note that the *IU* characteristics of the investigated heterostructures are steepest in the range around 0 V, so that they may be operated in this working range).

Finally, passivation of GaAs by interfacial coatings is often monitored by photoluminescence measurements,[28,58] since this mirrors the reduction in the effective surface recombination velocity of charge carriers at traps of surface impurities responsible for midgap states. Although the work presented here has merely focussed on the chemical stability of the interface, it is expected that the improved long-term stability provided by the polymerization of the MPT layer should also improve the long-term electrical passivation of the GaAs device. This will be addressed in future work.

4. Conclusion

The long-term stable chemical and biological passivation of the GaAs surface with interfacial organic polymer layers a few tens of nanometers thick provides an efficient compromise between ultrathin (but too labile) thiol monolayers and stable (but too thick) spin-coated polymer films. They not only provide near-perfect corrosion protection for the GaAs substrate in air and water, but they also have the potential to introduce chemical groups for easy, further surface functionalization. In air, the improvement of the chemical stability and the electrical insulation of the GaAs surface might allow the development of metal–insulator–semiconductor (MIS) technology based on GaAs. In water, or, more generally, in electrolyte buffers, it may allow the implementation of GaAs technology in biosensors and, possibly, even cell–semiconductor hybrids. The cultivation of NRK fibroblasts on GaAs surfaces, together with the conservation of the performance of polymer-coated GaAs electrical devices under physiological conditions are the first important steps in that direction, and have established the basis for future investigations of the electrical coupling between electrically excitable cells and GaAs-based field-effect transistor devices.

5. Experimental

Ultrapure water (MilliQ-grade) was used in all experiments. *n*-octadecylthiol (ODT, $HS(CH_2)_{17}CH_3$), 16-mercapto(hexadecanoic) acid (MHDA, $HS(CH_2)_{15}COOH$), and 3-(trimethoxy)mercaptopropylsilane (MPT, $HS(CH_2)_3Si(OCH_3)_3$) were purchased from Aldrich. Acetone (99 %), HPLC-grade ethanol (99 %), concentrated H_2SO_4, and 30 % H_2O_2 were purchased from Fluka. NaCl and Na_3AsO_3 (1 M solution) were obtained from Merck. PBS (phosphate buffer saline), HBSS (Hanks' balanced salt solution) buffer, Penstrep solution (containing 10 000 units/mL of penicillin and 10 mg/mL of streptomycin sulfate, and 0.9 % NaCl), and trypsin were purchased from Sigma. Dulbecco Modified Eagle Medium (DMEM) and Trypan Blue, 0.5 % (w/v) in physiological saline for cell culture investigations were purchased from Biochrom KG (Berlin, Germany). All chemicals were used as received.

Gallium arsenide substrates were obtained from Freiberger (Freiberg, Germany) as 3′ GaAs (100) wafers, n-type, with a carrier concentration of 1–6 × 10^{17} cm^{-3} (Te). From these wafers, 0.5 × 0.5 cm^2 pieces were cut and cleaned in acetone by ultrasonication for 5 min, rinsed with ethanol, and dried under a stream of nitrogen. Quantum-well heterostructures used for the determination of the $I_{SD}U_{el}$ characteristics of the GaAs field-effect channels were obtained from Siemens (München, Germany). The multilayered heterostructure (see schematic sketch in Fig. 8d) consists in detail, from top to bottom, of a cap layer of 10 nm GaAs (charge carrier concentration n = 2.35 × 10^{18} cm^{-3}) and 24 nm $Al_{0.2}Ga_{0.8}As$, the field-effect channel consisting of 0.8 nm GaAs, Si–delta doping, δ = 4 × 10^{12} cm^{-2}, 0.8 nm GaAs, 5.8 nm $Al_{0.2}Ga_{0.8}As$, 12 nm $In_{0.2}Ga_{0.8}As$, 4 nm $Al_{0.2}Ga_{0.8}As$, and a final doping layer of 7 nm $Al_{0.2}Ga_{0.8}As$ (n = 1.9 × 10^{18} cm^{-3}), followed by a spacing layer of 187 nm $Al_{0.2}Ga_{0.8}As$, 20 nm GaAs, 70 nm AlAs, 300 nm GaAs between the field-effect channel and the substrate.

For the preparation of thiol adsorption layers, cleaned GaAs samples were etched in $H_2O/H_2SO_4/H_2O_2$ (400:20:1) for 10 s, rinsed with deionized water (Milli-Q), treated in a second etching step in concentrated HCl (35–37 %) for 1 min, and finally rinsed in Milli-Q water and ethanol. The samples were then immediately immersed in a 5 mM ethanolic solution of the thiol (ODT, MHDA, or MPT) at 50 °C for 4 h. Polymerization of MPT was initiated by adding 3 vol.-% of NH_4OH (25 %), after which the solution was kept at 50 °C for at least 24 h. The samples were then rinsed with ethanol, dried under a stream of nitrogen, and used immediately.

For the determination of etching rates in aqueous solution, stripe masks of SHIPLEY photoresist Microposit S1805 on cleaned gallium arsenide substrates with 2 μm wide channels and 8 μm spacings between the channels were prepared by standard lithographic techniques. The photoresist was deposited by spin-coating at 7000 rpm and then baked at 90 °C for 10 min. The samples were kept in pure Milli-Q water, or 140 mM aqueous NaCl solution, under constant conditions (room temperature, 21 °C; or incubator atmosphere, 37 °C, 5 vol.-% CO_2), each for a period of 24 h. The samples were then rinsed in water, followed by treatment with acetone and ethanol to remove the photoresist, and finally dried in a nitrogen stream.

Film thickness measurements were done with a Plasmos SD2300 photometric ellipsometer. A He–Ne laser (632.8 nm) light source was used at a 70° angle of incidence. Each sample was measured at five different spots, and, for each spot, the layer thickness was individually calculated using the Plasmos software, and then averaged. The refractive indices, n, and the extinction coefficients, k, of the GaAs substrate, the native GaAs oxide, as well as of the self-assembled monolayers of ODT, MHDA, and MPT were taken from the literature as follows: n_{GaAs} = 3.856, k_{GaAs} = 0.196; $n_{GaAs\,oxide}$ = 1.8, $k_{GaAs\,oxide}$ = 0; n_{MPT} = 1.5, k_{MPT} = 0 [28]; $n_{ODT} = n_{MHDA}$ = 1.45, $k_{ODT} = k_{MHDA}$ = 0 [59]. The values for polymerized MPT layers have not yet been reported in the literature. The best fits to our experimental data were obtained for $n_{poly(MPT)}$ = 1.6–1.8 and $k_{poly(MPT)}$ = 0.

AFM topography measurements were performed within 24 h after sample preparation, in tapping mode (air) with a Digital Instruments Nanoscope IIIa. Silicon tips type TESP (DI) with a spring constant of 10 N/m were used at driving frequencies of 230–250 kHz. The z-calibration of the AFM piezo for height measurements was confirmed by comparing the channel depth analyses of the respective AFM and SEM images. The depths of the etched channels were obtained from the cross section profiles, as acquired by the Nanoscope IIIa software. At least three values for the height difference of neighboring plateaus and channels were averaged (see Fig. 2b). Further, averaged surface roughness data were obtained from AFM images of 2 × 2 μm^2 with a 512 × 512 pixels lateral and 16 bit z-resolution, using the rms algorithm of the Nanoscope software.

  1616-301X/02/0404-0274 $ 17.50+.50/0

For the determination of arsenite release from bare and thiol-coated gallium arsenide substrates, home-built cylindrical Teflon chambers (diameter: 1 cm) were mounted over a GaAs surface area of 75 mm^2, sealed from the outside with a two-phase gel (KWIK SIL, World Precision Instruments), and filled with 1 mL Milli-Q water. A fresh GaAs substrate sample was used for each release time investigated. Before determining the arsenite concentration of the contaminated buffer solutions, the 1 mL solutions were diluted to 5 mL by adding water to yield a sufficient probe volume for the atomic absorption spectroscopy (AAS) measurements (see below). The arsenic concentration in the solution was measured within three weeks of the experiment, i.e., after completion of a full set of different exposure times between 5 min and 10 days. To prevent precipitation of arsenic hydroxides upon storage, the solutions were acidified to pH 2 with nitric acid. Note that under the given experimental conditions, the oxidation of As^{III} to As^{V} can be neglected, as the standard oxidation potential is E° = –0.559 V, and reduction is further favored at low pH [36]. The determination of arsenic concentrations in contaminated buffer solutions was performed at the "Institut für Wassergüte und Abfallwirtschaft" at the Technical University of Munich, Germany, employing atomic absorption spectroscopy. The arsenic detection limit of the used instrument was 5 $\mu g\,L^{-1}$.

For the investigation of cell cultures, bare and coated GaAs substrates were fixed under Teflon chambers, the dimensions of which were in this case suitable for optical microscopy (i.e., height = 0.3 cm), and sterilized with 70 % ethanol in sterile water. Then, NRK fibroblasts [39,60] in a DMEM medium containing 1 vol.-% Penstrep solution were settled at 37 °C following standard protocols [61], and observed at time intervals of 3 h under a light microscope (ZEISS, AXIOPLAN). Images were taken with a CCD camera connected to a Macintosh PowerPC with a video card. For vitality tests, the medium was removed and the cells were harvested by the addition of 40 µL of a trypsin stock solution (0.25 % in HBSS) to the cell layer. After 5 min, 300 µL of cell medium was added, and the resulting cell suspension was treated with 30 µL of Trypan Blue solution. Dead cells were identified by their blue color under a light microscope, and counted.

For cyclic voltammetry, ohmic contacts were established at the backside of the cleaned and etched GaAs wafers by electron beam evaporation of 5.6 nm Ni and 40 nm AuGe (88:12) followed by a subsequent thermal diffusion process (3 min at 150 °C, 3 min at 350 °C). The samples were then mounted under a cylindrical Teflon chamber with a diameter of 10 mm, so that approximately 0.8 cm^2 of the substrate surface was in contact with electrolyte solution (in a geometry comparable to that shown in Fig. 8d).

Cyclic voltammograms were obtained in three-electrode measurements in deionized (Millipore) water containing 140 mM NaCl, in which a 1.5 cm^2 Pt plate and an Ag/AgCl electrode served as the counter and reference electrodes, respectively. A constant medium flow was supplied to the measurement chamber to minimize electrode contamination and screening effects [22]. For impedance measurements, an additional AC potential was added to the DC bias potential. After pre-amplification (DLCPA200, Femto), the AC component of the current was phase-sensitive measured with a lock-in-amplifier (SR830DSP, Stanford Research Systems), while the DC component was low-pass filtered (f_{LP} = 30 Hz) and further amplified by a low-noise voltage preamplifier (SR 560, Stanford Research Systems). To test the coating properties under harsh conditions, cyclic voltammograms were continuously recorded over the voltage range from –1.5 to 1.5 V for several hours, with a sweep velocity of 50 $mV\,s^{-1}$.

For the investigation of the $I_{SD}U_{el}$ characteristics, isolated field-effect channels (width: 100 µm, length: 2.5 mm) were prepared from GaAs/InGaAs heterostructures by standard lithographic methods. The etching procedure prior to coating the resulting channels with MPT was slightly modified. The native oxide layer (natural thickness: ~2–4 nm) was removed by etching in $H_2O_2/H_2SO_4/H_2O_2$ (400:20:1) for 1 s and subsequently rinsing in Milli-Q water; this reduced the thickness of the primary GaAs cap layer from the nominal 10 nm to ~5 nm. After coating with poly(MPT) from ethanolic solution (see above), the samples were then placed under cylindrical Teflon chambers.

In the $I_{SD}U_{el}$ measurements on quantum-well heterostructures, an Ag/AgCl electrode was used to steer the electrolyte (140 mM NaCl solution) potential over the range from –1.5 to +1.5 V, while a constant source–drain voltage of U_{SD} = 140 mV was supplied to the field-effect channel via two ohmic contacts outside the measurement chamber (see Fig. 8d). The channel current, I_{SD}, was recorded after pre-amplification (DLCPA200, Femto) in traces and re-traces with a sweep velocity of 50 $mV\,s^{-1}$ every 4 min, so that after a sampling time of 2 min, the gate electrode was disconnected during the interval between subsequent recordings for 4 min.

Received: August 13, 2001
Final version: December 27, 2001

[1] M. H. Brodsky, *Sci. Am.* **1990**, *262*, 68.
[2] C. Weisbuch, B. Vinter, *Quantum Semiconductor Structures*, Academic Press, San Diego, CA **1991**.
[3] J. M. Woodall, J. L. Freeouf, *J. Vac. Sci. Technol.* **1981**, *19*, 794.
[4] A. M. Green, W. E. Spicer, *J. Vac. Sci. Technol. A* **1993**, *11*, 1061.
[5] F. Seker, K. Meeker, T. F. Kuech, A. B. Ellis, *Chem. Rev.* **2000**, *100*, 2505.
[6] B. Liebl, *Habilitationsschrift*, Ludwig-Maximilians-Universität, Munich **1997**.
[7] B. Liebl, H. Mueckter, P. T. Nguyen, E. Doklea, S. Islambouli, B. Fichtl, W. Forth, *Appl. Organomet. Chem.* **1995**, *9*, 531.
[8] C. J. Sandroff, R. N. Nottenburg, J. C. Bischoff, R. Bhat, *Appl. Phys. Lett.* **1987**, *51*, 33.
[9] M. S. Carpenter, M. R. Melloch, M. S. Lundstrom, *Appl. Phys. Lett.* **1988**, *52*, 2157.
[10] V. N. Bessolov, M. V. Lebedev, N. Minh Binh, M. Friedrich, D. R. T. Zahn, *Semicond. Sci. Technol.* **1998**, *13*, 611.
[11] S. R. Lunt, P. G. Santangelo, N. S. Lewis, *J. Vac. Sci. Technol. B* **1991**, *9*, 2333.
[12] S. R. Lunt, G. N. Ryba, P. G. Santangelo, N. S. Lewis, *J. Appl. Phys.* **1991**, *70*, 7449.
[13] A. Ulman, *Chem. Rev.* **1996**, *96*, 1533.
[14] O. S. Nakagawa, S. Ashok, C. W. Sheen, J. Martenson, D. J. Allara, *Jpn. J. Appl. Phys. Part 1* **1991**, *30*, 3759.
[15] R. C. Tiberio, H. G. Craighead, M. Lercel, T. Lau, C. W. Sheen, D. L. Allara, *Appl. Phys. Lett.* **1993**, *62*, 476.
[16] H. Ohno, L. A. Nagahara, W. Mizutani, J. Takagi, H. Tokumoto, *Jpn. J. Appl. Phys.* **1999**, *38*, 180.
[17] C. W. Sheen, J. X. Shi, J. Martenson, A. N. Prikh, D. J. Allara, *J. Am. Chem. Soc.* **1992**, *114*, 1514.
[18] H. Ohno, M. Motomatsu, W. Mizutani, H. Tokumoto, *Jpn. J. Appl. Phys.* **1995**, *34*, 1381.
[19] T. Baum, S. Ye, K. Uosaki, *Langmuir* **1999**, *15*, 8577.
[20] T. Okumura, C. Kaneshiro, *Electron. Commun. Jpn. 2* **1999**, *82*, 690.
[21] J. Massies, J. P. Contour, *J. Appl. Phys.* **1985**, *58*, 806.
[22] K. Adlkofer, M. Tanaka, H. Hillebrandt, G. Wiegand, E. Sackmann, T. Bolom, R. Deutschmann, G. Abstreiter, *Appl. Phys. Lett.* **2000**, *76*, 3313.
[23] S. Bastide, R. Butruille, D. Cahen, A. Dutta, J. Libman, A. Shanzer, L. Sun, A. Vilan, *J. Phys. Chem. B* **1997**, *101*, 2678.
[24] A. Vilan, R. Ussyshkin, K. Gartsman, D. Cahen, R. Naaman, A. Shanzer, *J. Phys. Chem. B* **1998**, *102*, 3307.
[25] R. Cohen, L. Kronik, A. Vilan, A. Shanzer, D. Cahen, *Adv. Mater.* **2000**, *12*, 33.
[26] D. G. Wu, G. Ashkenasy, D. Shvarts, R. V. Ussyshkin, R. Naaman, A. Shanzer, D. Cahen, *Angew. Chem. Int. Ed.* **2000**, *39*, 4496.
[27] D. G. Wu, D. Cahen, P. Graf, R. Naaman, A. Nitzan, D. Shvarts, *Chem. Eur. J.* **2001**, *7*, 1743.
[28] T. Hou, M. Greenlief, S. W. Keller, L. Nelen, J. F. Kauffman, *Chem. Mater.* **1997**, *9*, 3181.
[29] C. J. Brinker, A. J. Hurd, P. R. Schunk, G. C. Frye, C. S. Ashley, *J. Non-Cryst. Solids* **1992**, *147*, 424.
[30] M. W. Daniels, J. Sefcik, L. F. Francis, A. V. McCormick, *J. Colloid Interface Sci.* **1999**, *219*, 351.
[31] K. H. Haas, S. Amberg-Schwab, K. Rose, G. Schottner, *Surf. Coat. Technol.* **1999**, *111*, 72.
[32] A. P. Alivisatos, *J. Phys. Chem. B* **1996**, *100*, 13 226.
[33] M. A. Correa-Duarte, M. Giersig, L. M. Liz-Marzan, *Chem. Phys. Lett.* **1998**, *286*, 497.
[34] D. Gerion, F. Pinaud, S. C. Williams, W. J. Parak, D. Zanchet, S. Weiss, A. P. Alivisatos, *J. Phys. Chem. B* **2001**, *105*, 8861.
[35] S. M. Sze, *Semiconductor Devices—Physics and Technology*, Wiley, New York **1985**.
[36] The resulting arsenic concentrations in the electrolyte solution may differ significantly from the actual amount of arsenic atoms that are removed from the GaAs wafer by etching. This is because only the fully soluble fraction, such as the arsenic fully hydrolyzed to arsenite, is probed. Whereas precipitation upon storage could be efficiently avoided at low pH, we could not control flocculation and the possible adsorption of mixed, partially hydrolyzed GaAs hydroxides onto the walls of the cultivation dishes. The values given may therefore include a systematic error due to the geometry of our experimental set-up. The arsenic concentrations given are nevertheless good indicators for the actual pollution of the buffer solutions (or their effective shielding from the toxic ions by the respective surface coatings), but they are less useful for the quantification of arsenic release from the substrates. The latter can be estimated from the etching depths acquired in the AFM experiments, as discussed.
[37] C. D. Bain, *Adv. Mater.* **1992**, *4*, 591.
[38] A. D. G. deRoos, P. H. G. M. Willems, P. H. J. Peters, E. J. J. V. Zoelen, A. P. R. Theuvenet, *Cell Calcium* **1997**, *22*, 195.
[39] W. J. Parak, J. Domke, M. George, A. Kardinal, M. Radmacher, H. E. Gaub, A. D. G. deRoos, A. P. R. Theuvenet, G. Wiegand, E. Sackmann, J. C. Behrends, *Biophys. J.* **1999**, *76*, 1659.
[40] W. J. Parak, M. George, H. E. Gaub, S. Böhm, A. Lorke, *Sens. Actuators B* **1999**, *58*, 497.

  1616-301X/02/0404-0275 $ 17.50+.50/0

[41] S. Böhm, W. J. Parak, M. George, H. E. Gaub, A. Lorke, *Sens. Actuators B* **2000**, *68*, 266.
[42] N. A. Ives, G. W. Stupian, M. S. Leung, *Appl. Phys. Lett.* **1987**, *50*, 256.
[43] Note that although we are not aware of a systematic study on the influence of CO_2 on GaAs oxidation, we believe that the effect of CO_2 is unlikely to be negligible. This significant corrosion calls for an effective protection layer, if GaAs devices are to be applied in aqueous, namely biological, environments. Surface coatings for GaAs by wet chemical methods are frequently employed in semiconductor physics, where it is desired to assimilate the electronic properties of the ill-conditioned GaAs surface to the favored properties of the bulk GaAs by reducing the amount of surface states (see [4,5]). In semiconductor physics, the term "passivation" typically stands for a (chemical) surface treatment intending to reduce the surface state density and to unpin the Fermi level from the midgap in the energy band of the semiconductor's surface (see [4,5]). In our context, "passivation" is used in a more chemical sense, and therefore generally refers to surface treatment with the goal of preventing surface degradation by shielding the unstable GaAs surface against oxidizing agents and water, which is a fundamental requirement for its long-term function under an ambient atmosphere.
[44] K. Remashan, K. N. Bhat, *Thin Solid Films* **1999**, *342*, 20.
[45] K. Adlkofer, M. Tanaka, *Langmuir* **2001**, *17*, 4267.
[46] J. Drelich, J. L. Wilbur, J. D. Miller, G. M. Whitesides, *Langmuir* **1996**, *12*, 1913.
[47] L. W. Schwartz, S. Garoff, *Langmuir* **1985**, *1*, 219.
[48] The slight increase in surface roughness and the increase in domain size observed after storing poly(MPT)-coated wafers in water may point to a partial structural rearrangement within the polymer layers, possibly caused by microphase separation in the hydrophilic (SiO-rich) and hydrophobic (alkyl-rich) domains that could be induced upon contact with water. Although the effect appears to be reduced for polymer layers treated by prolonged baking, an (ongoing) detailed structural investigation by X-ray reflectivity should help to elucidate this observation.
[49] A. Offenhäusser, C. Sprössler, M. Matsuzawa, W. Knoll, *Biosens. Bioelectron.* **1997**, *12*, 819.
[50] A. Lorke, S. Böhm, J. Kotthaus, W. Parak, M. George, *German Patent DE19840157A*, **1999**.
[51] W. J. Parak, M. George, M. Kudera, H. E. Gaub, J. C. Behrends, *Eur. Biophys. J.* **2001**, 29, 607.
[52] Y. Iwanaga, D. Braun, P. Fromherz, *Eur. Biophys. J. Biophys.* **2001**, *30*, 17.
[53] B. Alberts, D. Bray, J. Lewis, M. Raff, K. Roberts, J. D. Watson, *Molecular Biology of the Cell*, Garland Publishing, New York **1995**.
[54] S. R. Whaley, D. S. English, E. L. Hu, P. F. Barbara, A. M. Belcher, *Nature* **2000**, *405*, 665.
[55] The adhesion promoting effect of the extracellular matrix layer on GaAs is supported by an additional experiment, in which fibroblasts were settled in a petri dish in the presence of a bare GaAs piece, small enough to keep the arsenic concentration in the buffer below the critical level, at any time. After four days in culture, a confluent cell layer had developed in the petri dish. In addition, several fibroblasts were found adhering on top of the edges of the GaAs piece. Since fibroblast adhesion was not observed on untreated GaAs alone, this points to the presence of an adhesion-promoting coating at the edges, which was released by the surrounding confluent cell layer in the petri dish.
[56] M. J. Madou, S. R. Morrison, *Chemical Sensing with Solid State Devices*, Academic Press, London **1988**.
[57] S. R. Morrison, M. J. Madou, K. W. Frese, Jr., *Appl. Surf. Sci.* **1980**, *6*, 138.
[58] J. F. Kauffman, G. L. Richmond, *Appl. Phys. Lett.* **1991**, *59*, 561.
[59] L. Yan, C. Marzolin, A. Terfort, G. M. Whitesides, *Langmuir* **1997**, *13*, 6704.
[60] A. D. G. deRoos, *Ph.D. Thesis*, Katholische Universität Nijmegen, The Netherlands **1997**.
[61] R. I. Freshney, *Animal Cell Culture*, 2nd ed., IRL Press/Oxford University Press, Oxford **1992**.

  1616-301X/02/0404-0276 $ 17.50+.50/0

K2

„ Entwicklung und Charakterisierung von Potentialsensoren für die Zell-Halbleiter Kopplung“

B. Stein, M. George, C. Kirchner, M. Seitz. W. J. Parak, H. E. Gaub, *Dresdner Beiträge zur Sensorik*, Band 16, pp 41-44, 2002, ISBN 3-935712-71-5

Entwicklung und Charakterisierung von Potentialsensoren für die Zell-Halbleiter Kopplung

Bernhard Stein, Michael George, Christian Kirchner, Markus Seitz, Wolfgang J. Parak, Hermann E. Gaub

Lehrstuhl für Angewandte Physik
Sektion Physik and Center for Nano Science, Ludwig-Maximilians Universität
Amalienstr. 54 D-80799 München

Zusammenfassung

In dieser Arbeit wurden zwei verschiedene Sensorsysteme zur nicht invasiven Messung extrazellulärer Membranpotentiale entwickelt, der Licht-adressierbare-potentiometrische Sensor (LAPS) und der Feld-Effekt-addressierbare-potentiometrische Sensor (FAPS). Dabei wurde insbesondere beim LAPS die Potential- und Ortsauflösung genau untersucht. Es konnte eine Ortsauflösung von ca. 10µm und eine Potentialauflösung von ca. 70µVrms nachgewiesen werden. Beim Feld-Effekt-adressierbaren-potentiometrischen Sensor konnte eine ausreichende Potentialauflösung an Luft von ca. 30µV erreicht werden. Zudem wurden auf der Basis von organischen Polymeren Passivierungsschichten entwickelt die zum einen eine Korrosion des Halbleitermaterials und zum anderen die toxische Wirkung des Halbleiters auf die Zellen unterbinden.

Einleitung

Die noninvasive Kontaktierung elektrisch aktiver oder erregbarer Zellen ist für die Untersuchung der Informationsverarbeitung in neuronalen Netzwerken [1, 2, 3], für Neuroprothesen und für Biosensoren [4], die auf zellulärer Ebene arbeiten von großer Bedeutung. Messungen an Zellkulturen geringer Dichte, wie etwa an neuronalen Netzwerken, erfordern dabei eine hohe Dichte aktiver Meßpunkte oder die freie Adressierbarkeit der gesamten Messfläche, um zu gewährleisten, daß eine ausreichende Anzahl von Zellen erreicht werden kann. Die Größe der einzelnen Messpunkte (bzw. die Ortsauflösung bei freier Adressierbarkeit) muß auf die Größe der einzelnen Zellen (ca. 10µm) abgestimmt sein. Zur Aufzeichnung einzelner Aktionspotentiale wird des weiteren eine Zeitauflösung von 3kHz und eine Potentialauflösung von ca. 10µV benötigt. Hierfür wurden zwei Sensorsysteme, der Licht-adressierbare-potentiometrische Sensor (LAPS) [5] und der Feld-Effekt-adressierbare-potentiometrische Sensor (FAPS) [6] entwickelt.

1 Der Licht-addressierbare-potentiometrische Sensor (LAPS)

Im Gegensatz zu anderen potentialempfindlichen Sensoren ist der LAPS lateral nicht strukturiert (Bild 1a)). Er besteht aus einem EIS-Schichtsystem (elektrolyte-insulator-semiconductor), bei dem jeder Punkt der Oberfläche durch gepulstes Beleuchten mit einem Lichtzeiger adressiert werden kann. Photogenerierte Elektron-Lochpaare werden in der Raumladungszone an der Isolator-Halbleiter Grenzschicht getrennt und erzeugen so einen AC-Photostrom, dessen Amplitude von der Bandverbiegung im Halbleiter und somit vom Oberflächenpotential abhängt. Im Wesentlichen arbeitet der LAPS damit nach dem Prinzip einer ortsaufgelösten CV-Messung. Bild 1b) zeigt ein Beispiel für eine C-V Messung im konstant beleuchteten und im dunklen Fall. Der potentialabhängige Photostrom ist proportional zur Differenz dieser beiden Kapazitäten. Somit kann der LAPS dazu benutzt werden das extrazelluläre Potential von adhärenten Zellen zu messen, in dem der Sensor unter einer einzelnen Zelle beleuchtet wird. Dabei ist eine Ortsauflösung

gefordert, die kleiner ist als die zu beobachtenden Zellen, die einen Durchmesser zwischen 10µm bis 100µm aufweisen [8]. Um eine Zeitauflösung von 3 kHz zu erreichen, sollte aufgrund der verwendeten Lock-in technik die Modulationsfrequenz des Lichtzeigers mindesten das 10- fache (also 30 kHz) betragen, ohne das sich dabei die Potentialauflösung verschlechtert [9].

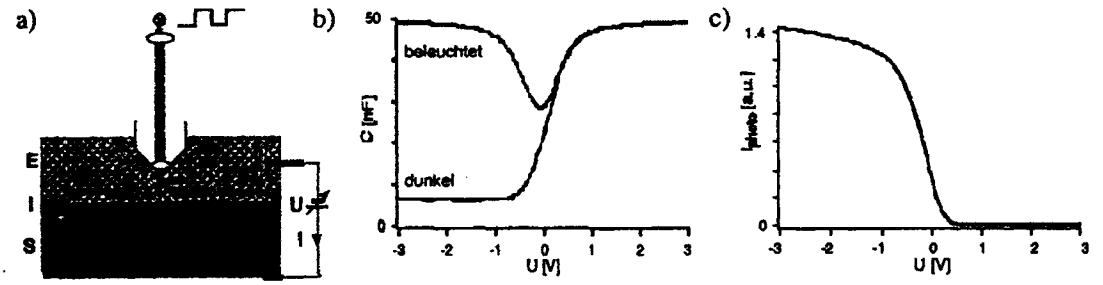

Bild 1 a) Prinzipieller Meßaufbau b) C-V Charakteristiken beleuchtet und unbeleuchtet c) Photostrom bei gepulster Beleuchtung mit 10kHz

Die geforderte Ortsauflösung, die nicht nur durch die Größe des Lichtzeigers, sondern vor allem durch die laterale Diffusion der Ladungsträger begrenzt ist, konnte durch den Einsatz dünner Schichtsubstrate erreicht werden [7, 8]. Die erforderliche Potentialauflösung (10µV bei 3kHz) wurde dagegen noch nicht erzielt. Daher wurde eine gezielte theoretische und experimentelle Rauschanalyse auf Basis einer äquivalenten MOS-Kapazität durchgeführt. Die Ergebnisse zeigen, daß neben einer sehr stabilen Lichtquelle (Amplitude/Rauschen ≥ 10e5) eine Verringerung der Chipgröße auf 100µm x 100µm nötig wird, um Streukapazitäten und somit das Rauschen im Photostrom ausreichend stark zu unterdrücken, und damit typische Aktionspotentiale von Zellen messen zu können.

2.1 Der Feld-Effekt-addressierbare-potentiometrische Sensor (FAPS)

Der FAPS arbeitet nach dem Prinzip von Feld-Effekt-Transistoren. Er unterscheidet sich jedoch durch sein Adressierungsprinzip, das eine wesentlich höhere Dichte an aktiven Meßpunkten ermöglicht als dies bei einem Array aus Feld-Effekt-Transistoren möglich wäre. Dies wird durch eine gitterartige Anordnung von Feld-Effekt-Kanälen und darunterliegenden Gate-Elektroden erreicht (Bild 2 a), Bild 3a)).

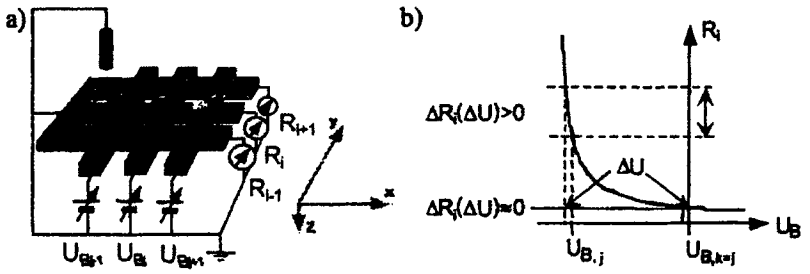

Bild 2 a) Feld-Effekt-Kanäle mit darunter liegenden Gate-Elektroden b) R-V Kennlinie eines Kanals

Durch Anlegen einer Spannung an eine Gate-Elektrode werden die Ladungsträger in einem Feld-Effekt-Kanal lokal verarmt. Dadurch steigt der Kanalwiderstand und dieser wird sensitiv für Potentialänderungen ober- und unterhalb des so adressierten Meßpunktes (Bild 2 b)). Potentialänderungen über dem adressierten Meßpunkt, die durch eine adhärente Zelle verursacht werden, können dann durch eine Änderung des Kanalwiderstandes nachgewiesen werden. Bei diesem Adressierungsprinzip skaliert die Zahl der Zuleitungen nur mit $\sqrt{N}$, wobei N die Anzahl der aktiven Meßpunkte ist, und nicht mit N wie bei herkömmlichen Feld-Effekt-Transistor Arrays. Dies hat den Vorteil, daß die aktiven Punkte sehr dicht angeordnet werden können, ohne daß es Konflikte mit Zuleitungen gibt. Derzeit hergestellte Strukturen weisen aktive Meßpunkte mit einer Größe von 15µm x 15µm auf (Bild 3a)). Einer Reduzierung auf 5µm x 5µm sollte aber technisch

möglich sein. Eine Möglichkeit, halbleitende Feld-Effekt-Kanäle kreuzweise auf metallische Gate-Elektroden anzuordnen, ist der so genannte epitaktische Lift-off (ELO), bei dem GaAs/AlGaAs-Heterostrukturen auf nahezu jedes Substrat transferiert werden können [10, 11]. Verwendet werden Heterostrukturen die, wie in Bild 3b) dargestellt, aufgebaut sind und mittels „molecular-beam-epitaxy" auf GaAs Substrate und darüber befindlicher Opferschicht aufgewachsen werden. Mit dem ELO-Verfahren ist es möglich, durch selektives Ätzen der AlAs Opferschicht, die GaAs/AlGaAs- Heterostruktur zu trennen und auf das vorgesehene Substrat zu übertragen. Diese Schicht hat eine typische Dicke < 500 nm und adhäriert durch Van der Waals Wechselwirkung auf dem strukturierten Substrat [12]. Bild 3a) zeigt eine realisierte Struktur und Bild 2a) eine schematische Zeichnung. Der genaue Herstellungsprozeß dieser Strukturen ist in [6] detailliert beschrieben. Es wurden grundlegende Untersuchungen zur Potentialauflösung durchgeführt wobei u.a. auf das Übersprechen mehrerer Meßpunkte auf einem Feld-Effekt Kanal eingegangen wurde, welches zu einer Verringerung der Empfindlichkeit führt. Eine Änderung der Potentialempfindlichkeit war bei einer symmetrischen Verkleinerung der aktiven Punkte nicht zu beobachten. Versuche mit Proben an Luft legen die Vermutung nahe, dass die Potentialauflösung, die mit dem FAPS erreicht werden kann, für die Zwecke der Zell-Halbleiter-Kopplung ausreichen.

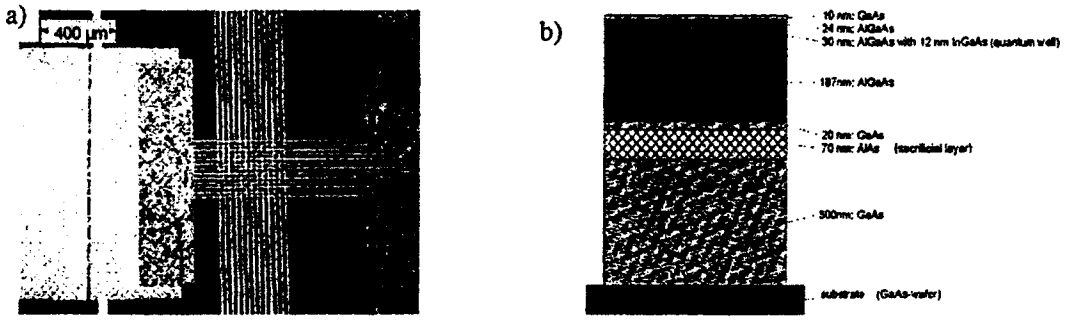

Bild 3 a) FAPS-Struktur mit 13 • 13 Meßpunkten b) GaAs/AlGaAs Heterostruktur.

Um ELO-Filme aus GaAs als Biosensoren einsetzen zu können, müssen drei grundlegende Probleme gelöst werden. Zum einen tendieren ELO-Filme, z.B. auf Glassubstraten, dazu sich von diesen abzulösen, wenn sich diese für mehrere Tage im Brutschrank in elektrolytischen Lösungen befinden, wie sie für das Überleben von Zellen nötig sind. Zum anderen gehen, ohne geeignete Beschichtung der GaAs-Filme, Arsen Ionen in Lösung und vergiften das Nährmedium. Weiterhin werden die GaAs-Filme im Nährmedium (z.B. 140mM NaCl) geätzt, so daß sich ihre elektronischen Eigenschaften stark verändern. Diese Effekte erfordern die Entwicklung dünner Schutzschichten, die einerseits die GaAs-Filme stabilisieren und andererseits eine elektrische Kopplung zwischen Zellen und den Halbleiterkanälen zulassen.

2.2 Beschichtungen

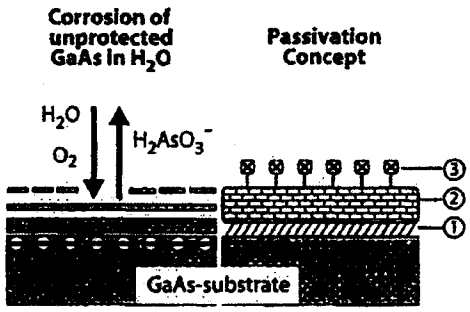

Bild 3. Passivierung von GaAs in wässriger Umgebung
Links: GaAs lost sich in Wasser unter Freigabe von toxischem Arsenit auf. Rechts: Eine Thiolmonoschicht passiviert die GaAs-Oberfläche elektronisch (1) und koppelt die Korrosionsschutzschicht aus Polysiloxan (2) kovalent ans Substrat. Funktionalitäten (3) in dieser Schicht optimieren die Biokompatibilität der Oberfläche

Neben anorganischen Schutzschichten für GaAs in Wasser aus Si_3N_4 wurden organische Schutzschichten aus Alkanthiolen untersucht [13], die als SAMs (Self Assembled Monolayers) auf GaAs für ihre elektrisch

passivierende Wirkung bekannt sind (Bild 3). Atomabsorptions-Spektroskopie und Zellkulturexperimente zeigen, dass solche Monolayer keinen ausreichenden Korrosionsschutz bieten. Wirksamen Korrosionsschutz erhält man erst durch den Einsatz einer zusätzlichen 15-20 nm dicken Sol-Gel-Schicht (Bild 3 (2)). Zunächst wird eine Thiolmonoschicht aus Mercaptopropyltrimethoxysilan (MPT) aufgebracht, die als Kopplungsschicht für das anschließend aufgebrachte Polysiloxan dient. Unter basischen Bedingungen polymerisiert die Trimethoxygruppe von MPT durch Hydrolyse und Polykondensation („Stöber Synthese") zu poly(MPT). Funktionalitäten zur Optimierung der Biokompatibilität können durch bekannte chemische Verfahren einfach implementiert werden (Bild 3 (3)). Atomadsorptionsmessungen und Zellkulturexperimente bescheinigen diesem System gute Effizienz beim Verhindern von Korrosion, als Diffusionsbarriere gegen das Austreten von giftigen Arseniten sowie als biokompatible Schicht für die Kultur von NRK-Fibroblasten und Cardiomyocyten.

Literatur

[1] G. Zeck, P. Fromherz: Noninvasive neuroelectronic interfacing with synaptically connected snail neurons immobilized on a semiconductor chip. P NATL ACAD SCI USA 98 (2001) 18, S. 10457 – 10462.

[2] M. Jenker, B. Müller, et al: Interfacing a silicon chip to pairs of snail neurons connected by electrical synapses. Biological Cybernetics 84 (2001), S. 239 - 249.

[3] G.W. Gross, E. Rieske, et al: A new fexed-array multi-microelectrode system designed for long-term monitoring of extracellular single unit neuronal activity in vitro. Neuroscience Letters 6 (1977) S. 101 – 105.

[4] A.Offenhäuser, W. Knoll: Cell-transistor hybrid systems and their potential applications. Trends of Biotechnology 19 (2001) 2, S. 62 – 66.

[5] D.G. Hafeman et al. : Light-Addressable Potentiometric Sensor for Biochemical Systems. Science (1988) 240, S. 1182 – 1185.

[6] WJ Parak, M George, et al.: The Field-Effect-Addressable Potentiometric Sensor / Stimulator (FAPS) - A new concept for a surface potential sensor and stimulator with spatial resolution. Sensors and Actuators B 58 (1999), S. 497-504.

[7] WJ Parak, UG Hofmann, et al.: Lateral Resolution of Light Addressable Potentiometric Sensors: An Experimental and Theoretical Investigation. Sensors and Actuators A 63 (1997) S.47-57

[8] M. George, W.J. Parak, et al.: Inverstigation of the spatial resolution of the light-adressable-potentiometric sensor. Sensors and Actuators A 86 (2000) S. 187 – 196.

[9] M. George, et al.: Investigation of different semiconductor substrates for an optimized light-addressable potentiometric sensor (LAPS). In: Roger de Reus und Siebe Bouwstra: Eurosensors XIV. Copenhagen, Denmark 2000. S.433 - 434

[10] P. Demeester, I. Pollentier et al.: Epitaxial Lift-Off and its applications. Semiconductor Science and Technology 8 (1993) 6. S. 1124 – 1135.

[11] E. Yablonovitch, T. Gmitter et al.: Extreme selectivity in the lift-off of epitaxial GaAs films. Appl Phys. Lett. 51 (1987) 6. S. 2222 – 2224.

[12] E. Yablonovitch, D.M. Hwang et al.: Van der Waals bonding in the lift-off of epitaxial GaAs films. Appl Phys. Lett. 56 (1990) 6. S. 2419 – 2421.

[13] C. Kirchner, M. George et al: Corrosion protection and long-term chemical functionalization of gallium arsenide in aqueous environment. Adv. Funct. Mat., accepted

K3

"Microstructural study of a passivation layer on GaAs: An application of X-ray reflectivity under grazing angles using a synchrotron source"

K. E. Crompton, T. R. Finlayson, C. Kirchner, and e. al., *Surface Review and Letters*, vol. 10, pp. 373-379, 2003

Surface Review and Letters, Vol. 10, Nos. 2 & 3 (2003) 373–379

World Scientific
www.worldscientific.com

MICROSTRUCTURAL STUDY OF A PASSIVATION LAYER ON GaAs: AN APPLICATION OF X-RAY REFLECTIVITY UNDER GRAZING ANGLES USING A SYNCHROTRON SOURCE

K. E. CROMPTON and T. R. FINLAYSON
School of Physics and Materials Engineering? Monash University, Clayton, 3800 Australia

C. KIRCHNER, M. SEITZ and U. KLEMRADT*
Sektion Physik and Center for NanoScience, Ludwig-Maximilians University, 80539 Munich, Germany

X-ray specular reflectivities of GaAs samples passivated with a thin film of (3-mercaptopropyl)-trimethoxysilane (MPT) have been studied using bending-magnet synchrotron radiation. Various preparation procedures covering etching the GaAs, MPT deposition and its baking have been investigated. An oxide film is always observed between the GaAs and MPT films. The microstructural parameters, such as film thickness, density and interfacial roughness (including the external surface), have been determined from appropriate modeling of the reflectivity. The surface roughness has been compared with a direct measurement using tapping-mode atomic force microscopy. The results are discussed with reference to the potential applications of GaAs as a biosensor.

1. Introduction

The potential for gallium arsenide (GaAs) use in chemical and biological sensors[1–3] has sparked new interest in the surface properties of the material. One most prominent advantage is the high mobility of charge carriers in GaAs compared to, say, silicon. The material is therefore efficient at reacting to high-frequency changes in electric field, and is able to do so with a low noise level. Further, the Fermi level of GaAs can be easily tuned by controlling the dopant concentration, which is another important advantage for the engineering of materials to applications.

However, the implementation of GaAs in an ambient medium, namely air or water, is complicated by the notorious chemical instability and heterogeneity of its native oxide layer. This allows a high concentration of surface defect states to form, effectively pinning the Fermi level near the mid-gap.[1,4,5] To optimize the electronic properties? it was suggested to reduce surface-state defect concentration by interfacial passivation layers of organic thiol compounds.[4,6] Moreover, when GaAs is transferred into an aqueous environment, the oxide layer dissolves rapidly. As a result, the bare semiconductor substrate is continuously etched by oxidation and hydrolysis, which not only complicates the definition of stable electronic surface states, but also contaminates the aqueous solution with highly toxic arsenic acid (specifically its anion arsenite, AsO_3^{3-}) generated by oxide layer hydrolysis. This poses another serious problem when GaAs is to be deployed in biological environments, namely when living cells are to be cultivated on the surface of this material. GaAs therefore needs to be coated with protective layers providing biocompatible interfaces. These should prevent etching of the substrate and suppress the release of toxic arsenite into the buffer solution.

The purpose of the present research is to examine the effectiveness of a specific surface coating based on polymerized (3-mercaptopropyl)trimethoxysilane (MPT), in preventing oxide buildup on the surface of GaAs, under various conditions such as apply

*Present address: II Physik. Institut, RWTH-Aachen, D-52066, Germany.

during its use as a biosensor. This polymer was chosen because it has been shown to prevent loss of As and AsO_3^{3-} from the heterostructure into the culture solution, to promote cell adhesion and to preserve the electronic characteristics of a GaAs heterostructure under buffered, physiological conditions.'

2. The Materials

2.1. *GaAs and its native oxide*

The native oxide is usually an amorphous mix of Ga_2O_3, As_2O_3 and elemental As.[8] Hou et *al.*[4] have suggested that in laboratory conditions both As_2O_3 and Ga_2O_3 form, but that the latter is thermodynamically favored. Both Hou et al. and Green and Spicer[5] agree that the reaction undergone is

$$As_2O_3 + 2GaAs \rightarrow Ga_2O_3 + 4As. \qquad (1)$$

Therefore, there is very little elemental Ga, but much more As due to the oxidation of a GaAs (100) surface as used in the present experiments.

2.2. *(3-mercaptopropyl)trimethoxysilane (MPT)*

MPT is a functionalized silane, where the functional group is a mercaptan. The molecule is 12 Å in length. The silane is able to cross-link with itself, so the layer can polymerize, increasing chemical stability. The sulfur in the mercaptan group is known to bond covalently to both Ga and As,[6,9,10] and hence forms a chemically stable layer. There is some evidence that the sulfur favors bonds with As.[11]

The electrical passivation of GaAs with both monomeric and polymerized MPT has been studied by a number of groups using photoluminescence[4,6,9] which provides an indirect measure of the surface density of states of GaAs, as mid-gap electronic states of the surface quench photoluminescence. The studies concentrate on self-assembled munolayers (SAM's) of only about 20 Å thickness. However, under aqueous environments, SAM's are not effective as a protective layer against corrosion, since they allow continuous etching of the GaAs substrate.[7] For this reason, the thin films of MPT used here are of the order of tens of nanometers, significantly thicker than a SAM.

There is evidence from polymerization of similarly structured polymers[12–14] that cross-linking of monomeric material in the sol could lead to the formation of aggregates, which may bond into the surface of the film.

Kirchner et *al.*[7] have studied the biocompatibility of MPT with normal rat kidney fibroblasts and showed that MPT promotes adhesion of the cells. As part of the same study, an examination of AsO_3^{3-} concentration in the aqueous medium surrounding a sample was conducted over time in solution. Because there was almost no change in concentration over a period of 10 days, it was concluded that MPT layers of approximate thickness 400 Å prevent leakage of toxic AsO_3^{3-} from the GaAs substrate. Thus MPT fulfils two of the most important criteria for a passivation layer on a biosensor using GaAs.

However, although it would appear that MPT is an efficient barrier to AsO_3^{3-} diffusion, it has not yet been demonstrated that it is also an efficient barrier to molecules that would cause oxide buildup and dampen the electrical sensitivity of the GaAs substrate.

3. Experimental Details

3.1. *Sample preparation*

The samples were prepared from n-type GaAs (100) wafers supplied by Freiberger (Freiberg, Germany}, with carrier concentrations between 1×10^{17} and 6×10^{17} cm^{-3} Te-doped.[7] The wafers were cleaned, etched (using five different procedures, as summarized below), and MPT, supplied by Aldrich, was applied using various deposition methods. Finally, for some samples, a baking procedure of variable temperature and time was followed. These preparation details have been encapsulated into a nomenclature, as follows.

3.1.1. *Etching methods*

E_S = standard etch comprising firstly, 5 s in a 1:20:400 solution of H_2O_2:H_2SO_4:H_2O, and secondly, 60 s in 37% HCl.

E_1 = as for E_S but 2 s for first step rather than 5 s.

E_2 = only first step of E_S fur just 2 s.

E_3 = only first step of E_S but for 10 s.

E_4 = in H_2O of pH 2 for 60 s, and under a 300 W Xe arc lamp.

[Following all of the above, the specimen was rinsed with H_2O (ultrapure, MilliQ-grade).]
E_5 = in 1:1 H_2O:HCl solution for 60 s, and under a 300 W Xe arc lamp, followed by rinsing with pH 2 H_2O and ethanol.

3.1.2. *MPT deposition methods*

D_S = Immersion in 10 mM solution of MPT in ethanol for 2 h at 50°C. Polymerization initiated through addition of 3 vol% of 25% NH_4OH and solution then maintained at 50°C for 24 h.
D_1 = Immersion in 5 mM solution of MPT in ethanol for 4 h at 50°C. Rest of procedure as for D_S.
D_2 = Immersion in 11 mM solution of MPT in ethanol for 3 h at 50°C. Polymerization initiated through addition of 3 vol% of 25% NH_4OH and solution then maintained at 50°C for 24 h. Immersion in fresh 11 mM solution of MPT in ethanol for 3 h at 50Å° and same polymerization repeated.

3.1.3. *Baking treatments*

$B_{90/3}$ = baking at 90°C for 3 h.
$B_{90/3.5}$ = baking at 90°C for 3.5 h.
$B_{120/3.5}$ = baking at 120°C for 3.5 h.

Samples having the same preparations are numbered sequentially for identification. Thus, a typical sample, following the above nomenclature, is $1E_3D_1B_{90/3}$, and where a particular letter is not used, this treatment was not applied in the sample preparation.

3.2. *Atomic force microscopy (AFM)*

Samples $1E_SD_S$, $2E_SD_S$, $1E_1D_1$, $2E_1D_1$, $1E_2D_1$, $2E_2D_1$, $1E_1D_1B_{90/3}$, and $2E_1D_1B_{90/3}$ were examined using tapping-mode atomic force microscopy (TM-AFM) in air, on a Digital Instruments Nanoscope IIIa. An extended multimode unit was used with a scanner (Type ex mm-J2, Make 2564 J). The silicon cantilevers had spring constants in the range 32–57 Nm^{-1}, frequencies 319–383 kHz, length 125 μm, widths 25–27 μm and thicknesses 3.9–4.6 μm. The drive frequency used was 287.057 kHz: the data type was "height," and both "trace" and "retrace" images were created. The z-range used in each measurement was 15 nm, chosen to provide favorable contrast. Each image was created with 512 × 512 pixels, at a scan rate of 0.984–1 Hz (to prevent smearing of the image). Most scans were taken of a 5 pm x 5 pm region. All values of the root mean square roughness (σ) were computed after plane fitting.

3.3. *X-ray reflectivity*

X-ray scattering techniques under grazing angles are suitable for the characterization of thin films and nanostructures. The most simple of these techniques is specular reflection, as is familiar for the optical characterization of thin films. However, for X-rays the reflectivity can still be calculated from the Fresnel formula, R_F [see Eq. (1) in Ref. 16], by taking into account that the index of refraction, n, is less than one. This gives rise to a total reflection regime up to a critical angle, α_c, above which the X-ray beam penetrates the film, or films, in the case of a multilayer sample. (See Fig. 1.)

As can be seen in the inset, the measured intensity results from the superposition of reflections from more than one interface. Hence, interference occurs, and, depending on the thicknesses and refractive indices of the media, can be either constructive or destructive.[**] The interference effects are seen in a reflectivity curve as oscillations in intensity, known as Kiessig fringes.

All of the above assumes perfectly smooth interfaces. Of course, no interface is perfectly smooth. and as Klemradt *et al.* showed in their analysis of the roughness of interfaces in a GaAs heterostructure,[16] there are no abrupt interfaces even for highly perfect, epitaxial layers. The roughness they found was of the order of a couple of atomic layers.

The deviations, σ, from the average surface height, mathematically designated $z = 0$, can be described using a Gaussian smoothing function:[17]

$$G(z) = \frac{1}{(2\pi)^{1/2}\sigma} \exp\left(\frac{-z^2}{2\sigma^2}\right). \qquad (2)$$

σ is the root mean square (RMS) roughness of the surface or interface. The effect of roughness is a modified Fresnel reflectivity:[17]

$$R = R_F \exp(-Q_z Q_z^t \sigma^2), \qquad (3)$$

where the Q's are the moduli of the wave vectors on either side of the interface. Thus, interface roughness will "wash out" sharp interference conditions. This

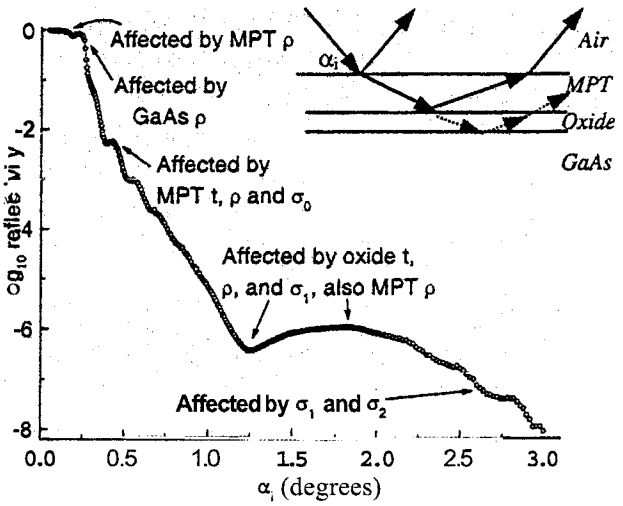

Fig. 1. Dominant effects of electron density, p, layer thickness, t, and interface roughness, σ, on the refectivity curve for MPT and oxide layers on a GaAs substrate (inset).

shows that reflectivity is very sensitive to the deviation in the surface height, especially for large wave vector (or small-wavelength radiation). When examining the roughness of a buried interface, any reflection from the first interface will also be detected.

The experiments were conducted at the Hasylab beamline D4 of DESY, Hamburg) which is a bending-magnet source. The diffractometer is a triple-axis type, with a Huber goniometer. The detector used was a Cyberstar (Oxford Instruments) plus absorber foils to keep dead times below 5%.

The reflectivity curves were fitted using the program PCTRF.[18] The parameters varied during fitting were MPT thickness (t) and density (p), oxide t and p, roughness above the MPT (σ_0), and above and below the oxide layer (σ_1 and σ_2). A typical curve is shown in Fig. 1, in which the features predominantly influenced by these model parameters are indicated.

4. Results and Discussion

4.1. *TM-AFM*

A typical image (Fig. 2) shows an even distribution of peaks of uniform diameter. The spacing of neighboring peaks is, on average?0.7 pm. There are troughs as well as peaks represented, and the entire height range) from 0 to 15 Å above the lowest point in the surface, is used. However) the majority of the

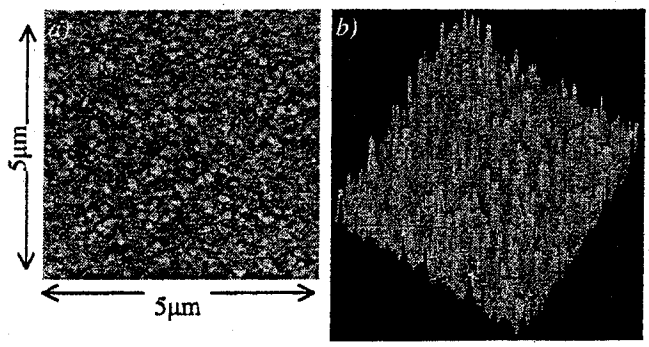

Fig. 2. $2E_1D_1B_{90/3}$. (a) Vertical view and (b) three-dimensional view.

Table 1. Data from samples, taken by TM-AFM (column 2) and X-ray reflectivity (all other columns). The data have been averaged over the samples of each preparation type. The data have been averaged over the samples of each preparation type. The uncertainties presented measure variations for multiple scans (for AFM) and variations between each of the two specimens (for X-ray results).

Sample	AFM σ (Å)	σ_0 (Å)	MPT t (Å)	MPT ρ (gcm^{-3})	σ_1 (Å)	Oxide t (Å)	Oxide p (gcm^{-3})	σ_2 (Å)
E_sD_s	26 ± *3*	18 ± 2	186 ± 77	1.50 ± 0.04	3.2 ± 0.3	15.4 ± 0.1	3.4 ± 0.3	5 ± 1
E_1D_1	42 ± 8	29 ± 5	243 ± 11	1.6 ± 0.3	9.1 ± 0.3	16.4 ± 1	4.70 ± 0.06	2.3 ± 0.1
E_2D_1	51 ± 7	24 ± 3	218 ± 34	1.5 ± 0.2	10.9 ± 0.3	16.4 ± 0.4	5.01 ± 0.04	2.7 ± 0.6
$E_1D_1B_{90/3}$	51 ± 2	41 ± 3	277 ± 46	1.52 ± 0.07	9.3 ± 0.2	12.8 ± 0.8	5.07 ± 0.02	0.4 ± 0.4
$E_3D_1B_{90/3}$		18 ± 1	26 ± 5	1.9 ± 0.2	1.8 ± 1.8	15.4 ± 0.2	2.92 ± 0.06	3.1 k0.2
$D_1B_{90/3}$		24.5	85.0	2.1258	5.1 ± 0.1	10.4 ± 0.1	4.38 ± 0.02	0
$E_4D_1B_{90/3}$		26 ± 7	218 ± 127	1.5 ± 0.2	12 ± 1	18 ± 2	5.2 ± 0.1	4 ± 2
$E_5D_1B_{90/3}$		38 ± 13	161 ± 61	1.6 ± 0.1	8.2 ± 0.1	12 ± 2	4.4 ± 0.3	3.8 ± 0.5
E_5D_2		23.8	129.2	1.777	3.2	13.8	3.375	5.7
$E_5D_2B_{90/3.5}$		28.8	128.3	1.912	3.7	13.3	3.579	5.3
$E_5D_2B_{120/3.5}$		**34** ± *3*	148 ± 11	1.86 ± 0.07	4.5 k0.9	13.4 ± 0.6	3.7 ± 0.2	5.5 ± 0.6

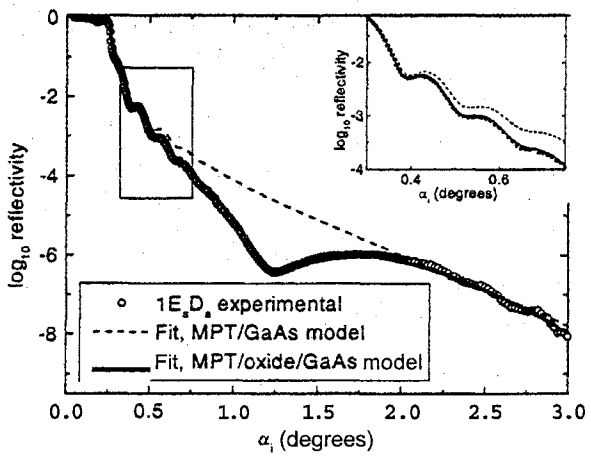

Fig, 3. Best fit using different models, sample $1E_sD_s$. Inset is from 0.35 to 0.75°, as indicated by the box.

surface is between 7 and 11 Å above the lowest point. TM-AFM provides the RMS roughness for the sample surface and these results for the samples measured are given in Table 1.

For some samples the peaks were less uniform than those in Fig. 2 and in others the peaks themselves were nonsymmetrical, implying coalescence of peaks of different heights. The uniformity of the peak heights suggests a common cause for their existence. From other studies, it is known that polymerized agglomerates form within a solution of a comparable polymer in an alkaline solution of ethanol[13,14] and that these bond to the polymer layer forming on the substrate. If this were also the case here, the agglomerates would form nodules on the surface of relatively uniform diameter and height, just as is seen in the majority of the images.

4.2. *X-ray reflectivity*

The reflectivity curve for sample $1E_SD_S$ and model fits are shown in Fig. 3. Initially, models based on an MPT single film on GaAs were tried, as indicated in the inset to Fig. 3. However, the only satisfactory fit was for a model that contains a second layer between the GaAs and MPT (solid line in Fig. 3).

The reflectivity curves for 21 samples, in various microstructural states involving different combinations of the preparation routes, have been measured. The parameters from the best fits to all of these data are summarized in Table 1. The oxide film is present in all samples, regardless of the etching procedure, and its modeled density varies widely amongst the samples, ranging from 2.86 gcm^{-3} to 5.26 gcm^{-3}. This range of densities implies a range of growth rates and conditions. This could well have occurred because the samples were not prepared under sufficiently controlled conditions, and variations in temperature and/or humidity might influence oxide growth. The densities for bulk As_2O_3, α-Ga_2O_3 and β-Ga_2O_3 are 3.738, 6.44 and 5.88 gcm^{-3}, respectively.[19] These bulk values are in contrast to the varied oxide densities found here, which, while within the same range as the bulk values, indicate that the layer is not a single oxide but a mix of possible molecules. The relatively low density is indicative of a loosely packed, possibly amorphous, layer, to be expected following reaction with the atmosphere, as has been found previously for oxide films growing on GaAs.[20]

4.2.1. *Surface roughness*

The values measured using the two different methods do not agree. The RMS roughness measured from TM-AFM is consistently higher than that from the X-ray reflectivity fits by around 30% (with the exception of samples $2E_2D_1$ and $1E_1D_1B_{90/3}$, which were believed to have been damaged prior to the AFM measurements).

The most likely explanation for this difference is that the physical model used for fitting was not strictly correct. If the surface were made of a graded layer, the electron density would alter. Since the layers were treated as having uniform density, any variation in electron density is assigned to the roughness. Thus, the roughnesses determined from the two techniques really measure different things. While TM-AFM directly measures the local surface roughness, X-ray reflectivity gives an average over the macroscopic surface. From the AFM images (e.g. Fig. 2), it is apparent that the "surface" is composed of a distribution of peaks on an otherwise relatively smooth surface. These peaks are most likely aggregates of polymer material that formed in solution before bonding to the surface. Depending on the chemistry and kinetics of the polymerization reaction, the aggregates may be more completely crosslinked and, therefore, denser. This increased density in the peaks would offset the lack of material at the highest points of the sample, so the average electron density at this level would be larger?leading to a reduced roughness parameter.

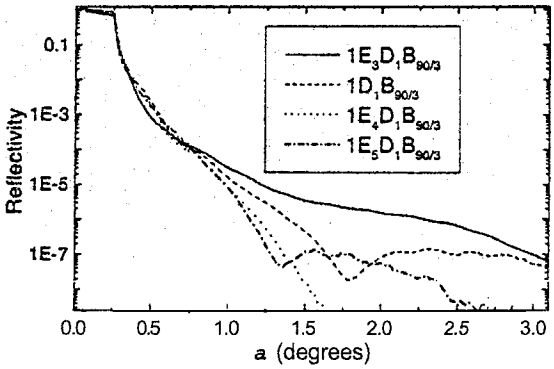

Fig. 4. Reflectivity of samples comparing etch methods.

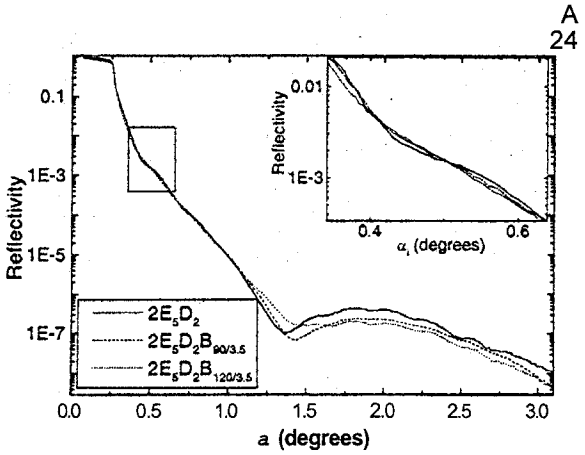

Fig. 5. Reflectivity of samples comparing baking treatments. Inset shows an enlargement of the area in the box.

4.2.2. *Etch methods*

Four different etch methods, E_3, E_4 and E_5 and "no etch," were applied to pairs of samples, the pairs being used to check reproducibility. Very large differences were found amongst the curves from different etch methods. (See Fig. 4 for a selection of the curves.) The amplitudes of MPT oscillations were similar, although the periods of the oscillations varied widely. Only one oxide oscillation was visible for samples $D_1B_{90/3}$ and $E_5D_1B_{90/3}$, and the angle at which the first minimum was located, varied between the two $E_5D_1B_{90/3}$ samples. Both angles for $E_5D_1B_{90/3}$ were much lower than those for $D_1B_{90/3}$, implying that the oxide layers for $D_1B_{90/3}$ were much thinner than those for the $E_5D_1B_{90/3}$ samples, a surprising result considering samples $D_1B_{90/3}$ were not etched. This is evidence of regrowth of the oxide layer.

The levels of intensity of this series of curves also varied widely. Samples $E_3D_1B_{90/3}$ produced scans of the highest level of intensity, then $D_1B_{90/3}$, $E_5D_1B_{90/3}$ and $E_4D_1B_{90/3}$. This would imply that the order of roughness on either side of the oxide layer also follows this hierarchy amongst samples, from lowest to highest. However, because samples $E_3D_1B_{90/3}$ have no clear oxide trough, they must have a higher roughness above the oxide than those for samples $D_1B_{90/3}$ or $E_5D_1B_{90/3}$.

4.2.3. *Baking treatments*

Data comparing the effects of different baking treatments are shown in Fig. 5. The curves are remarkably similar with regard to shape, level of scattering and basic features. The troughs from the oxide layer are all located around 1.4' to within ±0.1°, so the thickness of the oxide is uniform amongst these samples. There are some differences in MPT thickness, density and roughness (see Table 1), but the level of scattering is similar in this region of the curves (inset to Fig. 5), implying that despite these differences in the MPT structure, the surfaces are comparable. Note that the MPT oscillations of samples $2E_5D_2$ and $2E_5D_2B_{90/3.5}$ are quite similar, while those of the two $E_5D_2B_{120/3.5}$ samples are similar to each other but different to the other two. The variations in tail shapes of these curves can be attributed to differences in buried interfacial roughnesses, and differences in the shapes of the troughs can be attributed to variations in oxide densities.

The process of baking the samples under moderate conditions ($\sim 120°C$) did not appear to enhance polymerization, which is evidenced by the MPT density increasing from the unpolymerized value of 1.039 to 1.5–1.8 gcm^{-3} for baked and unbaked samples alike.

5. Conclusions

This study has shown that all GaAs samples coated with layers of polymerized MPT have an oxide layer present between the semiconductor substrate and the polymer coating. The layer has a thickness of, on average, 15 Å. Its density varies amongst the samples, but in every case is less than the density of bulk gallium arsenide oxide, suggesting that it may be mixed oxide and possibly amorphous. It was observed regardless of (i) variations in the etching protocol prior to polymer deposition, (ii) the polymerization conditions, and (iii) thermal treatment (baking) of the polymer coatings.

The photochemical etch (E_5) resulted in the thinnest oxide layer, 12 Å. However, this is most probably a result of other effects on the surface, rather than an improved efficiency of the method. The unetched samples showed the thinnest oxide layer, for which there is currently no sound explanation.

The microstructural stability of the interfacial layers in water remains to be studied.

Acknowledgments

We acknowledge the support of a DESY project grant which provided access to the Hasylab beamline. K. E. C. is grateful for support from Monash University (via Monash Abroad, SPME and the J. L. William Bequest) and from Sektion Physik, LMU. Financial support from the Australian AMRF scheme (Exp. 01/02-S-04) is also acknowledged, along with the Deutsche Forschungsgemeinschaft (DFG) through SFB 486.

References

1. F. Seker, K. Meeker, T. F. Kuech and A. B. Ellis, *Chem. Rev.* 100, 2505 (2000).
2. S. Bohm, W. J. Parak, M. George, H. E. Gaub and A. Lorke, *Sensors and Actuators* B68, 266 (2000).
3. W. J. Parak, M. George, H. E. Gaub, S. Bohm and A. Lorke, *Sensors and Actuators* B58, 497 (1999).
4. T. Hou, C. M. Greenlief, S. W. Keller, L. Nelen and J. F. Kauffman, *Chem. Mater.* Q, 3181 (1997).
5. A. M. Green and W. E. Spicer, J. *Vac. Sci. Technol.* A11, 1061 (1993).
6. S. R. Lunt, *G.* N. Ryba, P. G. Santangelo and N. S. Lewis, *J. Appl. Phys.* 70, 7449 (1991).
7. C. Kirchner, M. George, B. Stein, W. J. Parak, H. E. Gaub and M. Seitz, *Adv. Funct. Mater. 12,* 266 (2002).
8. M. R. Brozel and G. E. Stillman, eds., *Properties* of *GaAs*, 3rd edn. (INSPEC, London, 1996), pp. 9, 36, 151, 335, 447, 449, 451, 463–7.
9. S. R. Lunt, P. *G.* Santangelo and N. S. Lewis, J. *Vac. Sci. Technol.* **B9**, 2333 (1991).
10. J. F. Dorsten, J. E. Maslar and P. W. Bohn, *Appl. Phys. Lett.* 66, 1755 (1995).
11. K. Adlkofer and M. Tanaka, *Langmuir* 17, 4266 (2001).
12. M. W. Daniels, J. Sefcik, L. F. Francis and A. V. McCormick, J. *Colloid Interface Sci.* 219, *351* (1999).
13. W. Stöber, A. Fink and E. Bohn, J. *Colloid Interface Sci. 26,* 62 (1968).
14. P. A. Buining, L. M. Liz-Marzán and A. P. Philipse, *J. Colloid Interface Sci. 179,* 318 (1996).
15. K. Kago, H. Endo, H. Matsuoka, H. Yamaoka, N. Hamaya, M. Tanaka and T. Mori, *J. Synchrotr.* 5, 1304 (1998).
16. U. Klemradt, M. Funke, M. Fromm, B. Lengeler, J. Peisl and A. Förster, *Physica* **B221**, 27 (1996).
17. T. P. Russell, *Mater. Sci. Rep. 5,* 171 (1990).
18. U. Klemradt, PCTRF Multilayer Reflectivity Fitting Program (available on request).
19. D. R. Lide, ed., *CRC Handbook* of *Chemistry and Physics,* 72nd edn. (Chemical Rubber Company Press, Boca Raton, 1991), pp. B69 and B92.
20. A. Plech, U. Klemradt, H. Metzger and J. Peisl, *J. Phys. Condens. Matter 10, 971* (1998).

K4

"An Application of Synchrotron radiation to study the microstructure of passivation layers on GaAs"

J. D. Smith, T. R. Finlayson, U. Klemradt, C. Kirchner, M. Seitz, and J. Sutter, *Materials Forum*, vol. 27, pp. 21-27, 2004

MATERIALS FORUM VOL. 27 (2004) 21 - 27

AN APPLICATION OF SYNCHROTRON RADIATION TO STUDY THE MICROSTRUCTURE OF PASSIVATION LAYERS ON GaAs

J.D. Smith,[1] T.R. Finlayson,[1] C. Kirchner,[2] U. Klemradt,[3] M. Seitz[2] and J.P. Sutter[4*]

[1]School of Physics and Materials Engineering, Monash University, Clayton, Vic. 3800, Australia.
[2]Centre for NanoScience, Ludwig-Maximilians University, 80539 Munich, Germany.
[3]II. Physik. Inst., RWTH Aachen, D-52066, Germany.
[4]Hamburger Synchrotronstrahlungslabor HASYLAB at Deutsches Elektronen-Synchrotron DESY, D-22607 Hamburg, Germany.
[*]Spring-8/JASRI, 1-1-1 Kuoto, Mikazuki-cho, Sayo-gun, Hyogo 679 5198, Japan

ABSTRACT

Some of the background to the application of GaAs as a field-effect, addressable, potentiometric sensor/stimulator (FAPS) is reviewed and the need for the passivation of this material prior to its use in this application is outlined. (3-mercaptopropyl)trimethoxysilane (MPT) was deposited on a GaAs surface to provide passivation against corrosion by oxygen and to prevent AsO_3^{3-} escape into the surrounding environment. X-ray reflectivity was used to probe the surface to obtain an electron density depth profile that could then be fitted to a computer model revealing the number of layers and their corresponding thicknesses, densities and roughnesses, respectively. Since GaAs surfaces are highly reactive due to dangling bond formation it was hoped that the thiol (SH) group in the MPT overlayer could effectively stick to the surface and block the thermodynamic path for Ga_2O_3 and As_2O_3 formation via oxidation. However, it was found from the models fitted that all samples had buried oxide layers due to either inadequate cleanliness during preparation or subsequent surface corrosion occurring after sample preparation. Further study is required regarding the effectiveness of thiol overlayers against arsenic and oxygen diffusion and perturbation of the electronic states of GaAs.

1. INTRODUCTION

GaAs has long been used in the semiconductor industry due to its higher electron mobility, radiation resistance, lower noise levels during device operation and lower power dissipation[1-4]. Recently, however, its potential as a substrate material for extracellular detection of biological cells on its surface has been realized[5,6]. The low noise level obtained from GaAs has unique advantages for noise reduction and sensitivity enhancement for potentiometric sensor types[1].

However GaAs is well known to complicate the semiconductor/biological interface due to corrosion of its surface in either aqueous or ambient atmospheric environments[2,7]. It becomes necessary, therefore, to introduce a protective layer between the GaAs and the cells being cultivated. Ideally, this layer needs to be thick enough to prohibit the corrosion but thin enough so that the cell potentials for bio-detection are not dampened[1].

(3-mercaptopropyl)trimethoxysilane (MPT) has been chosen for this work as it can be deposited into a layer of the necessary thickness, cell cultures can bind to its functionalized surface[8], the thiol group is known to bind very strongly to the GaAs substrate[9,10] and the layer is not conductive[1]. As a protective barrier, MPT prevents diffusion of AsO_3^{3-} species from the GaAs surface into the cell culture. It also prevents oxygen migration to the GaAs surface from the cell culture. This is important because cells are very sensitive to arsenic and will detach from the surface and die if the arsenic concentration exceeds safe levels. Furthermore, upon oxygen exposure, the GaAs surface will form a high concentration of defect states which cause a pinning of the Fermi level near mid-gap[6,7,11].

Reliable sensor operation cannot be initiated if the surface defect state concentration is too high. For this reason it is hoped that we can show in future work that MPT can be used as a passivator for the GaAs surface and provide the necessary physical barrier to corrosion.

2. THE MATERIALS

2.1 GaAs and Its Native Oxide

For GaAs, oxidation begins with the absorption of oxygen on to the surface, which breaks the Ga-As bonds so that As_2O_3, As_2O_5, $GaAsO_4$ and Ga_2O_3 are formed. However the compounds As_2O_5, $GaAsO_4$ and As_2O_3 are not stable near the GaAs substrate and will decompose in the following reactions[2,7,11]

$$As_2O_3 + 2GaAs \rightarrow Ga_2O_3 + 4As \quad (1)$$
$$3As_2O_5 + 10GaAs \rightarrow 5Ga_2O_3 + 16As \quad (2)$$
$$3GaAsO_4 + 5GaAs \rightarrow 4Ga_2O_3 + 8As \quad (3)$$

The GaAs/Oxide interface then becomes arsenic rich due to low diffusion rates of elemental arsenic through the Ga_2O_3 and because of excess arsenic formation.

The oxide thickness and growth rate are largely dependent on temperature since this controls the diffusion rate of gallium through the layer forming Ga_2O_3 at the surface and also how volatile the arsenic oxides are. This means that at room temperature the stoichiometric composition of the oxide favors an amorphous mix of As_2O_3 and Ga_2O_3 and the thickness tends to be about 30-40Å[2]. For higher temperatures even the most stable arsenic oxide, As_2O_3 becomes more volatile and will evaporate throughout the oxide leaving mostly crystalline Ga_2O_3 and a pronounced arsenic rich interface[2].

Oxygen absorption on the GaAs surface usually occurs within seconds but rarely forms a uniform coverage on a GaAs {100}. Instead the formation favors clusters usually about 80×300Å[2] in area. The layer then gradually thickens, depending on temperature and oxygen concentration[2]. In aqueous environments no oxide layer exists owing to continuous etching of the GaAs substrate. The arsenic concentration in the buffer solution then becomes a time-exposure-dependent property.

However, maintaining an oxide free surface is of special difficulty considering the favorable standard molar Gibbs energy of formation ($\Delta_f G°$) for the As_2O_5 and Ga_2O_3 are -782.3 kJmol^{-1} and -998.3 kJmol^{-1}, respectively[12].

The arsenic rich interfacial layer is thought to be responsible for the Fermi level pinning since it causes local lattice rearrangement and considerable reconstruction of the GaAs surface[2,3,7,11]. It has also been shown that when the arsenic rich interfacial layer is removed the system becomes unpinned[2,11,13].

2.2 (3-mercaptopropyl)trimethoxysilane (MPT)

Polymers are an ideal material for GaAs passivation since they offer ease of deposition and low cost, by comparison with more traditional passivation layers like epitaxially grown $Al_xGa_{1-x}As$, SiO_2 and Si_xN_y[7]. There is also a wide choice of molecular structure, functional sites and densities available[14]. Dip coating is an ideal method for depositing layers on GaAs as it is simple, easy and is low in cost. It can also produce Self Assembled Monolayers (SAMS) and thicker overlayers, depending on deposition time[5,15].

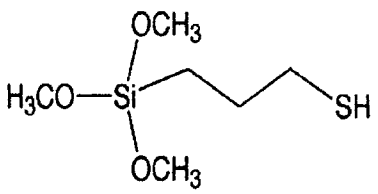

Figure 1. MPT molecule

MPT, in particular, is a functionalized silane comprised of a mercaptan and a trimethoxysilane group at either end of a propyl chain (Figure 1). The molecule is 12Å in length and can cross-link with itself, hence the layer is able to polymerize, increasing its chemical stability and density (Figure 2)[8]. Furthermore, the sulphur in the mercaptan group is known to bond covalently to both gallium and arsenic and hence forms a chemically stable adhesive layer to the GaAs substrate (Figure 2)[6,8,10]. However, the exact mechanism responsible for passivation is unclear since there is some evidence that a preference for As-S bonding will result in surface state defect improvement[15].

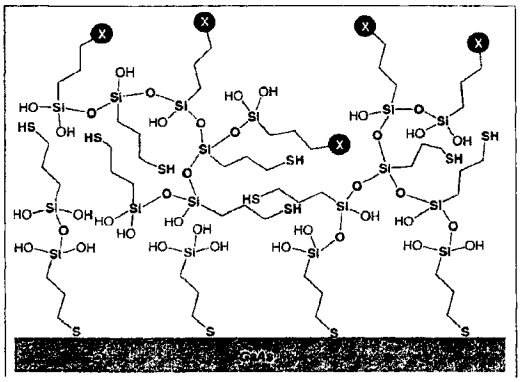

Figure 2. MPT overlayer on GaAs

When sulphur forms As-S, Ga-S, or both, bonding with the electronic vacant states on the surface, these dangling bonds become occupied and are no longer free for extrinsic atomic or molecular interaction. Because the reaction pathways are blocked for arsenic antisite reconstruction, the system maintains an unpinned state[2,3,7,11]. In effect the free elemental arsenic is prevented from pinning the Fermi level since it readily bonds with the sulphur atoms. However, oxidization still commences gradually in the presence of light and oxygen[4] and so a thicker layer, typically a thiol-based silane, is used to make the passivation more permanent and is a requirement in aqueous environments[8].

Polymerization of the overlayer is thought to enhance the passivation effectiveness since it increases the density of the diffusion barrier between the bare semiconductor surface and the ambient environment[8]. There is also some evidence, at least in other polymers similar to MPT, that substrate bonding can be enhanced by monolayer deposition. Therefore, monolayers act as a seed layer for aggregate formation during deposition and polymerization of a given overlayer[16].

2.3 Field Effect Addressable Potentiometric Sensor/ Stimulator (FAPS)

It was discovered that electrical fields from ions could be detected on the semiconductor surface by ion selective field effect transistors (ISFET). FETs and other types of sensors utilize electrically excitable cell potentials to steer the source-drain current of the gate electrode[17]. These sensors have a very bright future for

extra-cellular detection of excited cell potentials on semiconductor surfaces.
However, the sensor contact must be small enough and contain a sufficient number of contacts to allow detection of a single cell on the surface. If the contact is too far from the cell or too large then resolution will be low and device operation not practical. Much additional work has commenced regarding the development of enhanced sensors aimed at reducing many of the limitations of the ISFET approach. One method is to reduce the number of wired contacts required for a given resolution and surface area. For large areas it is not practical to measure cell potentials with high spatial resolution since the number of contacts increases quadratically with resolution and surface area[1].

FAPS has the advantage of a different addressing scheme that can drastically reduce the number of required contacts for a given surface area and resolution. Since a FAPS is derived from a FET, it becomes necessary to explain the FET channel operation. FET contains a thin channel that effectively restricts the flow of electrons through the channel in the x and y directions. A bias voltage from a perpendicular gate electrode applied to a channel can then deplete the region of free electrons and this in turn increases the resistance of the channel nearby the bias region. This region can then be selected owing to its increased sensitivity by measuring the output voltage on the appropriate FET channel. Since it is known which gate electrode has a bias voltage and which FET channels are affected, (x,y) coordinates will be assigned on the surface.

Furthermore, when we increase the resistance of a certain region of the FET channel, it becomes very sensitive to local potentials either on the surface or underneath. A surface cell can then cause a small shift in the applied bias. However, because the number of electrons in the FET channel is already so low (gone into the non-linear region) any further depletion will cause a very large change in the resistance. This can be measured and detected, giving extreme sensitivity to one region along the FET channel with the applied bias.

However, this device is not without its problems. The cells can sometimes become conductive. This means they could provide an avenue for conduction between the FET channel and the electrode in question and nearby channels or electrodes. Worse still, for GaAs the arsenic could be leached from the surface into the solution, killing the cells and damaging the sensors. It becomes necessary to apply a thin, protective, insulating overlayer. It is undesirable for the overlayer to be conductive since this will hamper the ability to apply a potential to only one region of the GaAs surface[1,17].

GaAs has the potential to reduce the noise associated with potentiometric detection of living cells and so makes new sensors such as FAPS more feasible. Current FAPS sensors made from silicon, lack the necessary signal-to-noise ratio required to sense extra-cellular potentials of 100μV or less, which is required for cell detection[17].

Figure 3 features a typical FAPS sensor setup that contains the gate electrode and FET channel. The MPT polymer would form an insulation layer between the cell potential (ΔU) and the FET channel. U_b is a suitable gate bias applied to deplete the FET channel and increase its resistance and sensitivity to ΔU. By driving a constant current I_c and measuring the resultant potential U_c, the ΔU can be measured.

3. EXPERIMENTAL DETAILS

3.1 Sample Preparation

Samples were prepared with the aim of assessing the influences of different preparation procedures on the passivation effectiveness of the overlayer. Samples for which good data were obtained are listed in Table 1. Other samples were not used because the preparation was bad or insufficient time has been available to scan them.

Sample preparation varied according to experiment type. All samples were based on 11x11mm^2, n-GaAs (100) wafers, Te-doped to 2-6x10^{17}cm^{-3}, supplied by Freiberger Compound Materials GmbH, Germany. They were cleaned which involved 5 min ultrasonic treatment in acetone and ethanol and then drying under a stream of N_2 gas. A subscript "E" in the sample designation implies an etch for 1 min in HCl (37%, Merck) followed by rinsing with de-ionized water (millipore) and ethanol (absolute grade, Merck). The subscript "M" implies that a monolayer was deposited on to the surface. Monolayer deposition required 2 hrs in a 11 mM solution of MPT (Gelest) in ethanol at 50°C. "P" designates that the full MPT overlayer has been deposited on to the surface. Polymer deposition required 64 hrs in 11 mM-MPT/250 mM-HCl solution of ethanol.

After polymer deposition, the polymer coated samples where baked for 3 hrs at 120°C in air. The MPT was dissolved into ethanol with HCl acid because it is believed that HCl can induce "in-situ etching". It is thought that HCl can remove the oxide while the MPT layer deposits on to the surface[5].

3.2 X-ray Reflectivity

Grazing incidence x-ray reflectivity has proved to be an invaluable technique as it is non-destructive of sensitive surface features and can give nanometric resolution of overlayer thickness, density and interfacial roughness[18].

For x-rays, materials have refractive indices less than one which produces a totally reflecting regime up to a critical angle, α_c, which varies depending on the photon wavelength and the material electron density[18]. For

angles of incidence above α_c, x-rays penetrate into the material and scatter from any electromagnetic variation which usually corresponds to layers on the surface, as seen in Figure 4. Depending on the "optical path length", relative to the photon wavelength and incident angle, the reflected waves from the various interfaces can interfere constructively or destructively.

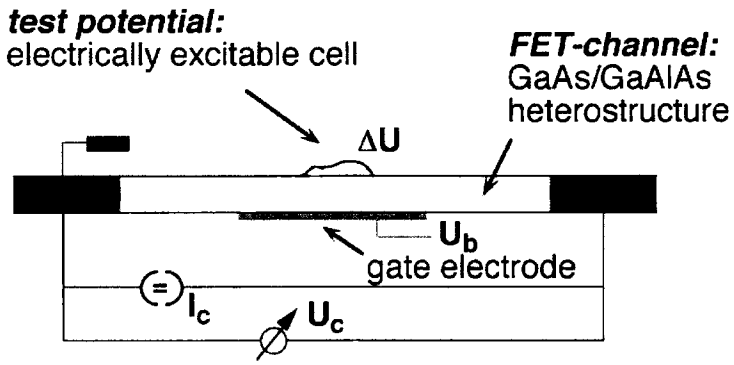

Figure 3. Setup of FAPS GaAs sensor[1]

Table 1. Samples used and preparation

Sample	Etch	Monolayer	MPT	Scan Result, Fit Result, Passivation Result
1				Good Scan, Satisfactory Fit, No Passivation
2_E	X			Good Scan, Satisfactory Fit, No Passivation
3_M		X		Great Scan, Perfect Fit, No Passivation
4_{EM}	X	X		Great Scan, Excellent Fit, No Passivation.
5_P			X	Good Scan, Poor Fit, No Passivation
6_{MP}		X	X	Great Scan, Excellent Fit, Partial Passivation
7_{EP}	X		X	Poor Scan, Poor Fit, No Passivation
8_{EMP}	X	X	X	Great Scan, Excellent Fit, Partial Passivation

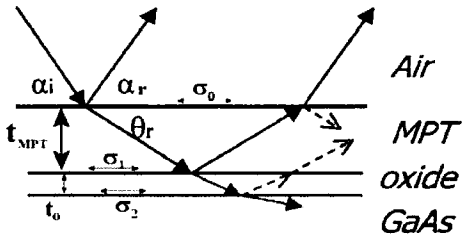

Figure 4. Incident x-ray beam interacting with the sample. $\alpha_i > \theta_r$.

The measured intensity at a given incidence angle then becomes the magnitude squared of the sum of the amplitudes of all the reflected waves seen in Figure 4[19]. The oscillations due to this thin-film interference are called Kiessig fringes and can be seen in Figure 5.

This model assumes that all surfaces are perfectly flat when really they are not. The roughness, however, is unknown and must be approximated for a given region so we use a Gaussian smoothing function, G(z). The deviation from the average height of the surface is called the RMS roughness, σ[18].

$$G(z) = \frac{1}{(2\pi)^{1/2}\sigma} \exp\left(\frac{-z^2}{2\sigma^2}\right) \qquad (4)$$

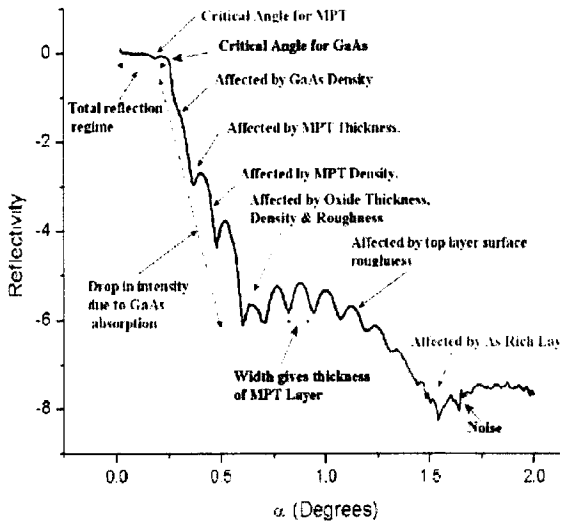

Figure 5. Most dominant effects on X-ray reflectivity curve for MPT, Oxide and As rich layer roughness (σ), density (ρ) and thickness (t) parameters

The Fresnel reflectivity, R_F, from a perfectly smooth interface can then be modified to account for the roughness according to[20]

$$R = R_F \exp(-Q_z Q_z^t \sigma^2) \qquad (5)$$

where the Qs are the moduli of the wave vectors on either side of the interface. Roughness effects for x-rays are extreme because waves are scattered strongly by features whose size is greater than the wavelength, and the wavelength of the x-rays used here, being 1.3 Å, is very small[18]. Generally Kiessig fringes will blur or become washed out and the final curve will loose many orders of intensity.

All experiments were conducted at DESY, Hamburg, Germany, Beamline E2, using 9.5 keV radiation. Two detectors, a photodiode for low α_i and a NaI(Tl) scintillation counter for high α_i, were used to measure the reflected beam from the sample. For intermediate α_i, the scintillation detector was used with Al foil to attenuate the reflected beam. To improve accuracy, the dark current of the photodiode was measured and subtracted from the collected sample data. This removed most of the background noise. The background for the scintillation detector was negligible.

The layered interface electron density is unknown and so modeling of near surface layers was performed by computer simulation. Each layer was treated as a stoichiometric, homogenous region of finite thickness, t, density, ρ, and vertical roughness, σ, on the substrate (Figure 4). Two programs PCTRF[21] and Parrott32[22] were used to fit the reflectivity data.

4. RESULTS AND DISCUSSION

Typical reflectivity curves obtained are reproduced in Figures 6 and 7 along with the best fits and their results listed in Table 2.

All samples examined using x-ray reflectometry showed the presence of an oxide layer and an arsenic rich interfacial layer. This is clear as data fits improved significantly when these additional layers were added. However the inclusion of an additional set of variables for a fitting procedure could improve results artificially. For this reason additional layers are only added if there are independent references that suggest from their results a need to introduce additional layers into the model. If the layers do not drastically improve the fit result, they should be removed since slight improvement always comes about due to increased parameterization of the overlayers.

Table 2. Results of fits obtained for scanned samples.

Sample FIT	σ_0 (Å)	t_{MPT} (Å)	ρ_{MPT} (gcm^{-3})	σ_1 (Å)	t_{oxide} (Å)	ρ_{oxide} (gcm^{-3})	σ_2 (Å)	t_{As} (Å)	ρ_{As} (Å)	σ_3 (Å)	Best Fit (RMS)
1	1.9	-	-	-	16.6	1.97	17.2	8.8	5.97	2.8	0.033
2_E	3.3	-	-	-	25.9	3.186	4.2	0.2	6.02	0.0	0.113
3_M	4.2	16.9	2.432	1.6	24.3	4.153	9.6	6.3	5.39	0.0	0.011
4_{EM}	8.3	20.3	2.284	3.3	35.1	5.044	5.9	1.8	5.6	0.0	0.017
5_P	19.5	269.2	1.38	1.9	23.2	1.991	20.5	0.0	5.52	0.0	0.185
6_{MP}	10.7	271.4	1.384	21.7	12.3	3.923	7.9	12.7	5.47	0.0	0.089
7_{EP}	20.0	239.3	1.325	0.0	37.3	2.079	19.5	-	-	-	0.171
8_{EMP}	10.2	278.2	1.403	21.6	8.0	4.018	4.5	5.7	4.99	0.0	0.101

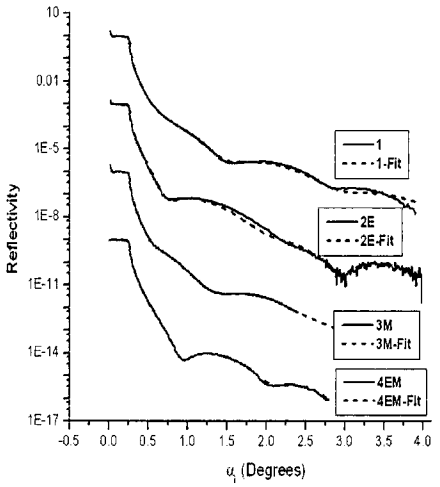

Figure 6. Reflectivity profiles for treatments without polymer on the GaAs surface. With the exception of 1 and 1-Fit all profiles are offset with respect to absolute reflectivity for clarity.

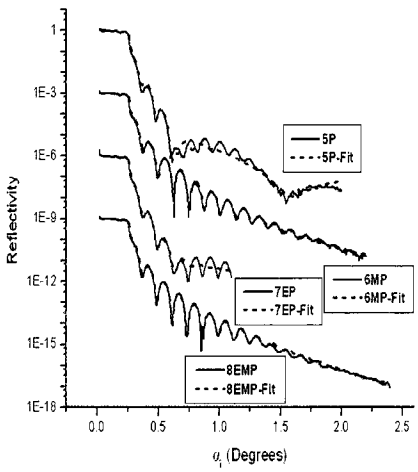

Figure 7. Reflectivity profiles for various treatments including polymer on the GaAs surface. With the exception of 5_P and 5_P-Fit, all profiles are offset with respect to absolute reflectivity for clarity.

4.1 Arsenic Rich Interfacial Layer

Brozel *et al.*[2] indicate that an interfacial arsenic rich layer will form upon oxide growth but that it is temperature dependent. However, Seker *et al.*[6] have shown that etching of the oxide layer by HCl may remove more gallium than arsenic, leading to arsenic rich interfacial layers. Samples here support both conclusions as etched and non-etched samples both received quite large improvements in fit values via the addition of arsenic rich layers. Furthermore, there is some evidence that the excess arsenic on the surface can cause lattice rearrangement and so can be a source of Fermi level pinning[3]. Considering that this perturbs reliable detection of analyte molecules, it seems prudent to undertake further work to investigate possible non-preferential GaAs etchants. Densities ranged from 4.99gcm^{-3} through to 6.02gcm^{-3} for the arsenic layer which is what would be expected considering that solid arsenic has a density of 5.77gcm^{-3} [12].

4.2 Etching

Prior etching of the GaAs substrate before monolayer/MPT deposition had a small effect on the final oxide layer thickness and quality but the results are mixed. For samples 4_{EM} and 7_{EP} etching seemed to have actually thickened the oxide compared to results for samples 3_M and 5_P, in agreement with Crompton *et al.*[23] where it was found that no etching produced the thinnest oxides. For samples 6_{MP} and 8_{EMP} etching has caused a slight reduction in the oxide thickness (Figs. 6 and 7, Table 2). However it is hard to conclude that prior etching of the GaAs substrate before the monolayer or MPT deposition will improve the passivation of the resultant samples.

4.3 Monolayer

The prior addition of a monolayer of MPT was found to produce considerable improvement to the passivation abilities of the MPT overlayer as samples with an applied monolayer, 6_{MP} and 8_{EMP}, had large reductions in the thicknesses of their respective oxide layers compared to samples with no monolayer deposition, as in 5_P and 7_{EP} (Figs. 6 and 7, Table 2). This is most likely on account of a higher coverage of sulphur bond formations between the monolayer and the GaAs substrate.

It was also found that monolayer densities were higher than bulk MPT densities, 2.43gcm^{-3} (sample 3_M) compared to 1.38gcm^{-3} for sample 6_{MP}, suggesting that the monolayer has the potential to increase the density of the MPT overlayer via seeding. However, it wasn't shown that the monolayer actually increased the density of the MPT layer. It is thought that the seeding effect may be too localized and so has not dispersed into the MPT overlayer to have any significant effect on its density.

4.4 Oxide Layer

Oxide was found on all samples. Its density ranged from 1.97gcm^{-3} through to 5.044gcm^{-3}, which suggested a large variation in growth rate and conditions at the time of growth. This can be explained by the facts that room temperature oxides tend to be amorphous and can contain mixed quantities of As_2O_3, α-Ga_2O_3 and β-Ga_2O_3, whose densities are 3.738, 6.44 and 5.88gcm^{-3}, respectively[2,12], depending on oxygen concentration and temperature. The oxide during initial stages of growth can form a loosely packed overlayer if grown very rapidly and so it is possible that the lower density oxide layers will allow further oxidation of the surface[2].

Oxides are known to form graded interface structures from higher to lower density as one proceeds from the GaAs surface. The fitted results would then be an approximation to a graded layer which, depending on how it varied, would be different to the fitted model[20].

When and how the oxide was formed on the surface could help to explain its properties since it is possible that the oxide was etched away in pre-treatments but reformed either due to polymerization of the MPT overlayer or as a result of oxygen diffusion after passivation. Polymerization could form a buried oxide as it is essentially a hydrophilic condensation reaction which is dependent on the available ambient moisture content[24]. Since it uses oxygen to cross-link the polymer, it is safe to assume that some oxygen may have migrated to the surface.

Further investigation of the oxide formation mechanisms would no doubt improve ones ability to passivate the GaAs surface reliably and is a requirement for future sensor work.

5. CONCLUSIONS

Current passivation techniques preclude the immediate use of GaAs material as a biosensor on account of oxide/arsenic layer formation and the release of arsenic species from the surface. For this reason it would be impossible to use GaAs material as a biosensor without further developments to passivation technologies. However, with a continued analysis regarding the pinning mechanism and further work focusing on improved passivation layers and elimination of oxides, progress will be made, resulting in a system that will suit this proposed application.

ACKNOWLEDGMENTS

The authors acknowledge the support of a DESY project grant which provided access to the HASYLAB beamline E2. JDS was grateful for support from Monash University (via Monash Abroad, SPME and the J.L. William Bequest) and for the hospitality of RWTH-Aachen.

REFERENCES

1. Parak, W.J., Gaub, H.E., Bohm, S. and Lorke, A.: *Sensors and Actuators B*, 1999, vol. 58, 497-504.
2. Brozel, M.R. and Stillman, G.E. eds.: *Properties of Gallium Arsenide*, 3rd ed. (INSPEC, London, 1996) 9, 36, 151, 335, 447, 449, 451, 463-157.
3. Trigg, G. L. ed: *Encyclopedia of Applied Physics*, vol. 7, (VCH Publishers, 1993), 43-69.
4. Yang, G.H., Kang, E.T. and Neoh, K.G.: *J. Phys. Chem. B*, 2003, vol. 107, 2780-87.
5. Baum, T. Ye, S. and Uosaki, K.: *Langmuir*, 1999, vol. 15, 8577-9.
6. Seker, F. Meeker, K., Kuech, T.F. and Ellis, A.B.: *Chem. Rev.*, 2000, vol. 100, 2505-36.
7. Green, A.M. and Spicer, W.E.: *J. Vac. Sci. Technol. A.*, 1993, vol. 11, 1061-8.
8. Kirchner, C., George, M., Stein, B., Parak, W.J., Gaub, H.E. and Seitz, M.: *Adv. Funct. Mater.*, 2002, vol. 70, 266-76.
9. Hirsch, G., Kruger, P. and Pollmann, J.: *Surf. Sci.*, 1998, vol. 402-4, 778-81.
10. Ke, Y., Milano, S., Wang, X.W., Tao, N. and Darici, Y.: *Surf. Sci.*, 1998, vol. 415, 29-36.
11. Hou, T., Greenlief, M., Keller, S.W., Nelen, L. and Kauffman, J.F.: *Chem. Mater.*, 1997, vol. 9, 3181-6.
12. Lide, D.R. ed: *CRC Handbook of Chemistry and Physics*, 72nd edn., Chemical Rubber Company Press, Boca Raton, 1991, B69 and B92.
13. Ives, N.A, Stupian, G.W. and Leung, M.S.: *Appl. Phys. Lett.*, 1987, vol. 50, 256-8.
14. Harsanyi, G.: *Polymer Films in Sensor Applications*, Technomic Pub, 1995, xv-xviii.
15. Adlkofer, K. and Tanaka, M.: *Langmuir*, 2001, vol. 17, 4267-73.
16. Daniels, M.W, Sefcik, J., Francis, L.F. and McCormick, A.V.: *J. Colloid Interface Sci.*, 1999, vol. 219, 351-6.
17. Parak, W.J., Domke, J., George, M., Kardinal, A., Radmacher, M., Gaub, H.E., de Roos, A.D.G., Theuvenet, A.P.R., Wiegand, G., Sackmann, E. and Behrends, J.C.: *Biophys. J.*, 1999, vol. 76, 1659-67.
18. Russell, T.P.: *Mater. Sci. Rep.*, 1990, vol. 5, 171-271.
19. Dosch, H.: *Critical Phenomena at Surfaces and Interfaces*, Springer-Verlag, 1992, 1-14.
20. Klemradt, U., Funke, M., Fromm, M., Lengeler, B., Peisl, J. and Forster, A.: *Physica B*, 1996, vol. 221, 27-33.
21. Klemradt, U.: *PCTRF Multiplayer Reflectivity Fitting Program* (available on request).
22. (HMI) H-M-IB. Parratt32 - The Reflectivity Tool. 1.5.2 Build 211 ed, 1999.
23. http://www.hmi.de/bensc/instrumentation/instrumente/v6/refl/parratt_en.htm#top
24. Crompton, K.E., Finlayson, T.R., Kirchner, C., Seitz, M. and Klemradt, U.: *Surf. Rev. Lett.*, 2003, vol. 10, 373-9.
25. Leyden, D.E. and Collins, W.T.: *Silylated Surfaces*, Gordon and Breach Science Publishers, Inc, 1980, 31-4.

K5

„Cytotoxicity of Colloidal CdSe and CdSe/ZnS Nanoparticles“

C. Kirchner, T. Liedl, S. Kudera, T. Pellegrino, A. Munoz-Javier, H.E. Gaub, S. Stölzle, N. Fertig, W.J. Parak, *Nano Letters*, vol. 5/2, pp. 331-338, 2005

NANO LETTERS

2005
Vol. 5, No. 2
331−338

Cytotoxicity of Colloidal CdSe and CdSe/ZnS Nanoparticles

Christian Kirchner,[†] Tim Liedl,[†] Stefan Kudera,[†] Teresa Pellegrino,[†] Almudena Muñoz Javier,[†] Hermann E. Gaub,[†] Sonja Stölzle,[‡] N. Fertig,[‡] and Wolfgang J. Parak*[,†]

Center for Nanoscience, Ludwig Maximilians Universität München, Germany, Nanion Technologies GmbH, Pettenkoferstr. 12, 80336 Munich, Germany

Received December 3, 2004

ABSTRACT

Cytotoxicity of CdSe and CdSe/ZnS nanoparticles has been investigated for different surface modifications such as coating with mercaptopropionic acid, silanization, and polymer coating. For all cases, quantitative values for the onset of cytotoxic effects in serum-free culture media are given. These values are correlated with microscope images in which the uptake of the particles by the cells has been investigated. Our data suggest that in addition to the release of toxic Cd^{2+} ions from the particles also their surface chemistry, in particular their stability toward aggregation, plays an important role for cytotoxic effects. Additional patch clamp experiments investigate effects of the particles on currents through ion channels.

Introduction. Recent progress in nanotechnology allows for the creation of new materials with properties tunable on the nanometer scale. Currently, already first attempts to use the functionality of such "smart" nanomaterials in life sciences are reported. Applications range from using fluorescent nanoparticles as dyes for fluorescence labeling of cells[1−3] and for motility assays[4], using gold nanoparticles for immunostaining[5] and gene delivery[6], to using magnetic nanoparticles as contrast agents for magnetic resonance imaging[7,8] and for hypothermia.[8,9] In addition to working with cell cultures, nanoparticles have been successfully introduced in animal experiments as contrast agents,[10,11] and future use in clinical applications is envisioned.[12] It is evident that for any clinical application biocompatibility of the nanoparticles is crucial. Since nanoparticles are different from their respective bulk material due to their size, it is an obvious question to ask for potential dangers arising from their smallness.[13] We can think of at least three different pathways by which nanoparticles introduced into an organism could interfere with its function and finally lead to impairment. (1) Most evident, introduced nanoparticles can be composed of toxic materials. This is true, for example, for fluorescence CdSe as well as for magnetic Co particles. Upon corrosion inside the organism, toxic ions could be released which finally poison the cells. Cytotoxic effects of Cd^{2+} (refs 14−18) and other metal ions[19] are well-known. Compared to the respective bulk material, partial decomposition and release of ions is more likely for nanoparticles due to their enhanced surface-to-volume ratio. (2) There might be a negative effect of particles in general on cells, regardless of the material of the particles. It is known that particles can stick to the surface of cell membranes,[20,21] and particles are also known to be ingested by cells.[4,21−23] Mantling of the cell membrane and storage of particles inside cells might have impairing effects, even for absolutely inert particles that do not decompose or react. (3) There might be an effect caused by the shape of the (inert) particles. It has been reported for example, that carbon nanotubes can impale cells like needles.[24,25] Particles of the same material but in a different modification can have a different toxic effect on cells in this way: Carbon nanotubes that have reached the lung are significantly more toxic than carbon-black and graphite.[24,25] So far, most cytotoxicity studies on nanomaterials are focused on aerosols[26] and involve particle uptake by the lungs. Such studies are important for many technical devices, for example, regarding the output of platinum nanoparticles from the catalysts of cars which might potentially endanger people who inhale these particles.[27,28] In this study we focus on the toxic effects of colloidal nanoparticles dispersed in aqueous solution on cells. As already mentioned above, many different types of colloidal nanoparticles can be used for a broad variety of applications in life sciences and medicine. In this study we will focus on fluorescent CdSe and CdSe/ZnS nanoparticles.

To our knowledge, so far only two studies exist in which the cytotoxic effects of CdSe and CdSe/ZnS nanoparticles are investigated in detail. Derfus et al. have reported that

* Corresponding author. E-mail: Wolfgang.Parak@physik.uni-muenchen.de.
† Ludwig Maximilians Universität München.
‡ Nanion Technologies GmbH.

10.1021/nl047996m CCC: $30.25
Published on Web 12/31/2004

CdSe particles dissolved in aqueous solution release Cd^{2+} ions[29] and that the concentration of the Cd^{2+} ions directly correlates with cytotoxic effects. The same authors have demonstrated that ion release is enhanced by oxidation, either through exposure to air or UV irradiation, but is repressed by encapsulating the particles with appropriate shells, as with ZnS and an additional organic shell. Shiohara et al. have investigated the cytotoxic effects of CdSe/ZnS particles of different size on three different cell types.[30] The same group claims that for CdSe/ZnS particles the main source of cytotoxicity is not their cadmium content but rather the interaction of the particle surface with the cells.[31] In our work described here we want to extend these studies to investigate the effect of different organic shells on cytotoxicity. Also, quantitative values for the onset of cytotoxic effects are determined.

Materials and Methods. Several cell lines (NRK fibroblasts, MDA-MB-435S breast cancer cells, CHO cells, RBL cells) were grown on standard cell culture substrates (All Materials and Methods can be found in detail in the Supporting Information). Nanocrystals of different materials and different surface coatings dissolved in water were added at different concentrations to adherent cells. In particular, CdSe,[32] CdSe/ZnS,[33] and Au[34] nanocrystals coated with mercaptopropionic acid,[35] embedded in a silica shell[35,36] or embedded in an amphiphilic polymer shell,[37] were investigated. In a first set of experiments, uptake of the nanocrystals by cells was investigated. For this purpose, green and red fluorescent CdSe/ZnS nanocrystals with different surface coatings were added to the cells, and after 18 h incubation the nuclei of the cells were stained with DAPI.[4] Living cells were then imaged with differential interference contrast (DIC) and fluorescence microscopy. In this way the position of the nuclei and the ingested nanocrystals with two different surface coatings could be co-localized by their color of fluorescence (blue, green, red). In a second set of experiments, toxic effects of the ingested particles on the cells were investigated. From previous studies it is known that the adhesion behavior of NRK fibroblast is highly sensitive to toxic metal ions.[38] In the study described here, the proliferation of the adherent cells was blocked by exchanging the culture medium to SATO medium.[39] The number of adherent cells per labeled region on the cell culture substrate was counted and nanocrystals were then added at several concentrations. After 48 h of incubation, the nonadherent cells were removed by rinsing and the number of the adherent cells at the same region was counted. In this way the ratio R of the number of adherent cells after and before incubation with nanocrystals, detected at the identical position, could be derived. The more toxic the effect of the nanocrystals on the cells, the lower this value is expected to be. As control, the constituents of the nanocrystals as Cd^{2+} and Se^{2-} ions and mercaptopropionic acid were added to the cells. In addition, the viability of the adherent cells before and after incubation with the nanocrystals was measured with a commercially available test (L3224, Molecular Probes). As a third set of experiments, nanocrystals were added to cells expressing hERG ion channels, and the effect of the nanocrystals on the ionic currents through these channels was investigated with an automated patch−clamp setup (Nanion[40,41]). This idea is similar to a previous study.[42] Uptake of nanocrystals by the cells was monitored by confocal microscopy.

Results and Discussion. *Uptake of CdSe/ZnS Nanocrystals by MDA-MB-435S Breast Cancer Cells.* In Figure 1 fluorescence and DIC images of MDA-MB-435S breast cancer cells that have been incubated for 18 h in serum-supplemented cell medium containing around c(CdSe/ZnS particles) = 2−10 nM water-soluble CdSe/ZnS nanocrystals are shown. For each experiment red and green fluorescent nanocrystals with different surface coatings were used simultaneously, and experiments were performed for all different combinations. In particular, particles coated with mercaptopropionic acid (MPA), a silica shell bearing phosphonate groups (phos-silane), a silica shell bearing polyethylene groups (PEG-silane), and an amphiphilic polymer (polymer) were used. From the images shown in Figure 1 it is evident that most of the different particles are ingested by the cells. By staining the nucleus with DAPI and manually changing the focus it could be shown that the ingested particles are stored in vesicular structures around the nucleus. For almost all combinations of particles with different surface coating, the ingested particles were stored in similar vesicular structures. Our data indicate that MPA, phos-silane, and polymer-coated particles are ingested by the cells in a very similar way, since these particles were found to co-localize inside the cells. However, different behavior was observed for PEG-silane coated particles. Whereas small green-fluorescent particles (hydrodynamic diameter of ~13 nm, unpublished results) were barely found inside the cells, bigger red-fluorescent particles (hydrodynamic radius of ~24 nm) could be detected inside the cells. These co-localization data demonstrate that water-soluble CdSe/ZnS particles are ingested by MDA-MB-435S cells in a nonspecific way, regardless of their size (in the range between 10 and 24 nm) and surface coating. Only for small PEG-silane coated particles uptake is significantly reduced. Nanocrystal uptake has also been demonstrated for other cell lines, such as NRK fibroblasts (data not shown).

Detachment of NRK Fibroblast from the Cell Culture Substrate upon Incubation with Nanocrystals. Since a previous study suggests that Cd^{2+} ions released from the surface of Cd-containing nanocrystals are the main cause of toxic effects,[29] we converted the concentration of CdSe and CdSe/ZnS particles to the concentration of Cd atoms on the surface of the CdSe core (see Supporting Information). This means that, in the case of a 1 nM concentration of CdSe particles with 100 surface Cd-atoms per particle, the concentration of Cd surface atoms is 100 nM. Analogously, the concentration of Au particles was converted to the concentration of Au atoms on the surface of the Au particles. The study of Shiohara et al. showed that for the same mass concentration (mg/mL) of particles cytotoxic effects are higher for smaller particles.[30] Since for smaller particles the surface-to-volume ratio is higher, these findings support our idea to plot a "concentration parameter" proportional to the

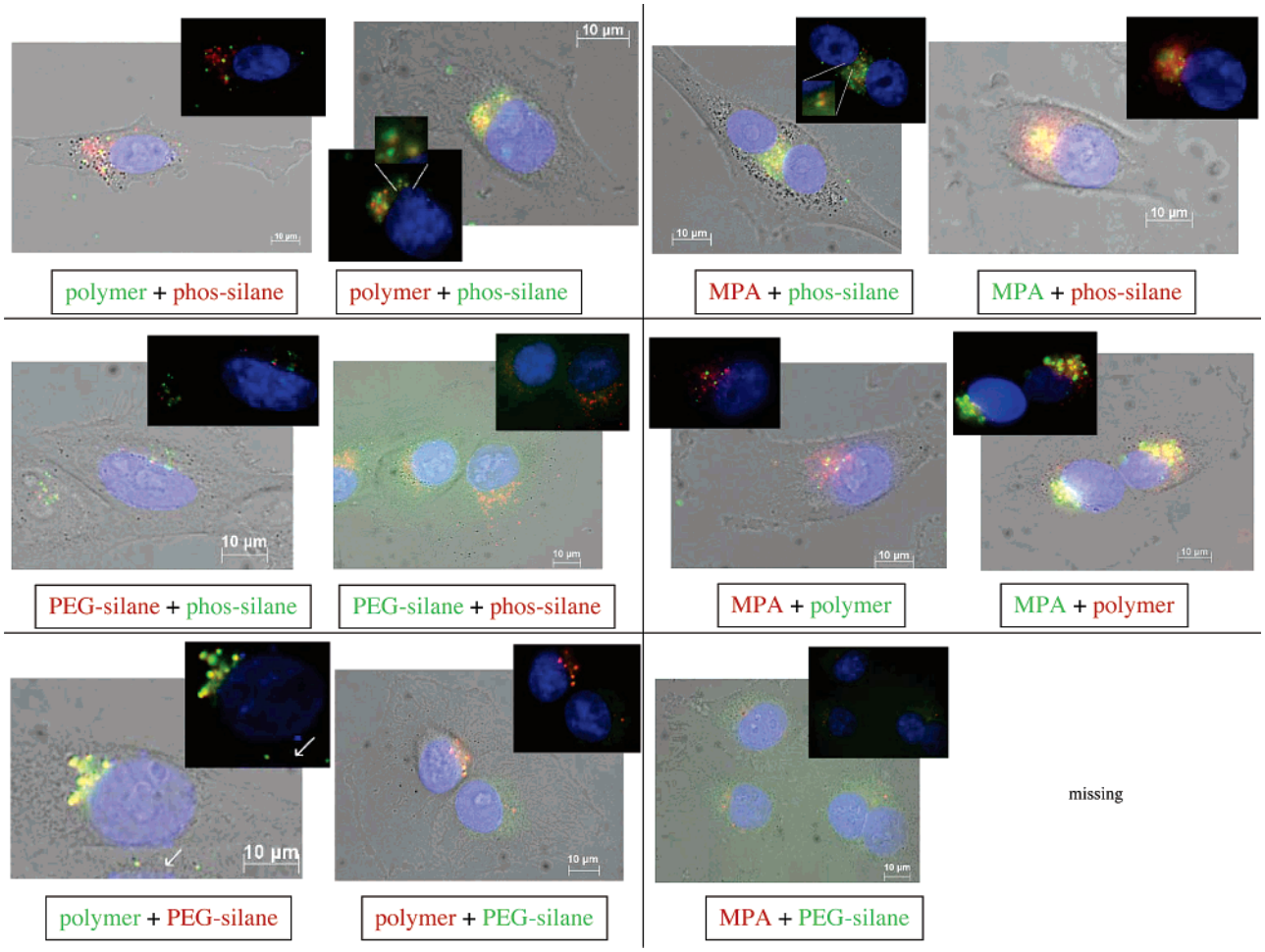

Figure 1. Red and green fluorescent CdSe/ZnS nanocrystals with different surface coatings have been ingested by MDA-MB-453S cells. Images of the cells were recorded with differential interference contrast (DIC) microscopy, and the nanocrystals and the DAPI-stained nuclei were recorded with fluorescence microscopy. For each experiment, always red and green fluorescent nanocrystals with different surface coatings were used so that their position within the cells can be resolved by their color of fluorescence. The DAPI-stained nuclei appear in blue. The big images contain the merged DIC and fluorescence images, the smaller images show only the fluorescence. All scale bars represent 10 μm.

surface and not to the volume of the particles (i.e., to use the surface atom instead of the particle concentration). In Figure 2, the ratio R between the number of adherent cells after and before incubation with nanoparticles is shown. As reference, this ratio is shown also for the case of incubation with Cd salts.

As is seen in Figure 2a, the same characteristic tendency can be observed in Figure 2b. For low Cd concentrations, R adopts a constant value well below 1. With an increased number of Cd (surface) atoms, R first decreases to a minimum value and then increases again to a value that can be close to 1. Thus, we can divide these curves in three different concentration regions. In the first region, the concentration of Cd atoms is very low and cell viability tests showed that all attached cells were alive (see Supporting Information). Exchanging the serum-containing cell culture medium to serum-free SATO medium resulted in the detachment of a significant fraction of cells, i.e., $R < 1$ even for $c(\mathrm{Cd}) = 0$. Therefore, we assume that there are no toxic effects due to Cd in the first region of low Cd concentration and that the value of $R < 1$ can be simply explained by the effect of the SATO medium. In the second concentration region, R drops. This means that more cells are detached due to the increased concentration of Cd (surface) atoms. Viability tests showed that attached cells in this region were still alive. For this reason we assume that in this region the viability of the cells is decreased due to poisoning by Cd^{2+} ions in solution. Poisoned cells detach and therefore are not counted, which results in a decrease in R. We might refer to this effect as apoptosis. Upon further increment of the Cd concentration R raises again, even sometimes to values larger than the value for very low Cd concentrations. Viability tests showed that the attached cells in this region were dead. We therefore assume that the concentration of Cd^{2+} ions in solution was sufficiently high to immediately poison the cells before they could start to detach. We might refer to this effect as necrosis. This differentiation is suggested by the detailed study of López et al., in which apoptosis and necrosis are reported to be the pathway for cell death for low and high cadmium concentrations, respectively.[18] The same authors also have shown that cytotoxic effects of Cd^{2+} ions are more severe in serum-free medium compared to serum-containing medium. Therefore, our experimental conditions of serum-

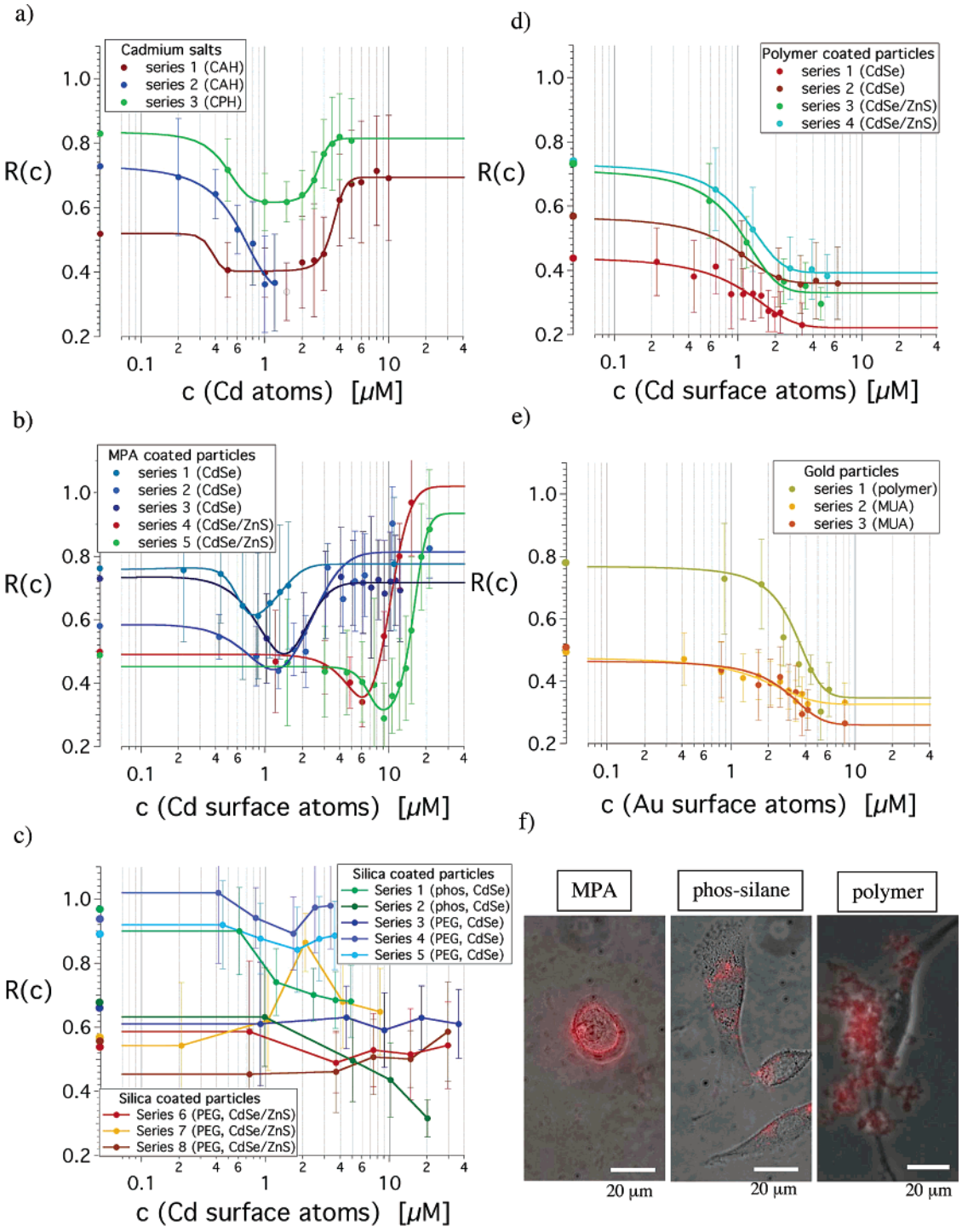

Figure 2. (a−e) Ratio $R(c)$ of adherent cells after/before incubation with Cd salts, CdSe and CdSe/ZnS particles, and Au particles. NRK fibroblasts have been incubated with (a) cadmium acetate hydrate (CAH) and cadmium perchlorate hydrate (CPH), (b) mercaptopropionic acid coated CdSe- and CdSe/ZnS nanocrystals, (c) silica-coated CdSe and CdSe/ZnS nanocrystals, (d) polymer-coated CdSe and CdSe/ZnS nanocrystals, and (e) polymer and mercaptoundecanoic acid (MUA) coated Au nanocrystals. The Cd salts fully dissociate in aqueous solution. Therefore, in (a) the *x*-axis represents the concentration c(Cd atoms) of Cd atoms in solution. In (b−d) the *x*-axis represents the concentration c(Cd surface atoms) of all the Cd atoms that are on the surface of the nanoparticles (see the Supporting Information; there also the scaling factor between c(Cd surface atoms) and c(CdSe particles) is given), and in (e) the *x*-axis represents the concentration c(Au surface atoms) of all the Au atoms that are on the surface of the nanoparticles. In each case results are shown for at least three separate series. For each data point within each series around 20000 cells were analyzed. For practical reasons in each series only a limited number of data points could be recorded (due to the limited number of cells that could be analyzed under the same conditions). For this reason not all series span the whole concentration range. Therefore, to compare the separate series for similar tendencies, the data points of each series were fitted with a double sigmoidal curve: $R(c) = a_1 - a_2/(1 + \exp((a_3 - c)/a_4)) + a_5/(1 + \exp(a_6 - c)/a_7))$ with seven fit parameters a_1−a_7. The derived parameters for the respective series are enlisted in the table shown below. The value $R(c = 0)$ represents the control sample to which no Cd, or CdSe or CdSe/ZnS nanoparticles have been added, but in which cell growth has been affected by changing the serum-containing medium to SATO medium. Due to a limited amount of nanocrystals, the accessible concentration range was limited. In

(a) and (b) clearly the double sigmoidal behavior of $R(c)$ can be seen. As indicator for the concentration limit of the onset of cytotoxic effects we use the a_3 parameter from the fits (a) $<a_3> = <0.35, 0.60, 0.48> \mu M = 0.48 \pm 0.13 \mu M$, (b) $<a_3> = <0.58, 0.58, 0.79> \mu M = 0.65 \pm 0.12 \mu M$ for CdSe and (c) $<a_3> = <4.9, 6.8> \mu M = 5.9 \pm 1.3 \mu M$ for CdSe/ZnS particles. In (c) no general tendency of $R(c)$ can be seen for PEG-silica coated nanoparticles and $R(c)$ seems to remain constant over the investigated concentration range. On the other hand, $R(c)$ decreases for increased concentrations of phosphonate-silica coated nanoparticles. In (d) and (e) the shape of $R(c)$ can be approximated with a sigmoidal curve with the a_3 parameter from the fits as indicator for the concentration limit of the onset of cytotoxic effects: (d) $<a_3> = <0.83, 0.77> = 0.80 \pm 0.04 \mu M$ for CdSe and $<a_3> = <0.93, 1.0> \mu M = 0.98 \pm 0.07 \mu M$ for CdSe/ZnS particles, (e) $<a_3> = 3.2 \mu M$ for polymer and $<a_3> = <1.2, 2.7> \mu M = 2.0 \pm 1.1 \mu M$ for MUA-coated Au particles. In the case of CdSe and CdSe/ZnS particles λ_{core} denotes the wavelength of the first exciton peak of the CdSe core. In the case of Au and CdSe particles d_{core} denotes the diameter of the particles, and in the case of CdSe/ZnS particles d_{core} denotes the diameter of the CdSe core underneath the ZnS shell. The number of surface atoms per core in the case of CdSe, Au, and CdSe/ZnS particles is the number of Cd, Au, and Cd atoms on the surface of each CdSe particle, Au particle, and CdSe core underneath the ZnS shell, respectively. The terms a_1, a_2, a_3, a_4, a_5, a_6, and a_7 are the resulting fit parameters for the function $R(c) = a_1 - a_2/(1 + \exp((a_3 - c)/a_4)) + a_5/(1 + \exp(a_6 - c)/a_7))$. $R(c)$ describes a double sigmoidal curve. Sigmoid curves are typically used in toxicology to describe dose−response functions. All values of one sigmoidal curve are between two asymptotes, determined by a_1 and a_1+a_2. The parameter $a_2/(4a_4)$ controls the slope in terms of a rate at the inflection point a_3, which is the response halfway between the baseline and the maximum, also called EC_{50}. A double sigmoidal curve is the superposition of two single sigmoidal curves. (f) Overlay of phase-contrast and fluorescence image for NRK cells incubated for 48 h with CdSe/ZnS nanocrystals. The images of these cells correspond to the high concentration range shown in (b), (c), and (d). For MPA-coated CdSe/ZnS particles, cells incubated at high particle concentrations are dead, while the cell debris remains on the substrate. For silane coated particles no effect of the particles on the cells can be observed; even for high particle concentrations, the particles are ingested and stored around the nucleus and cells remain adherent. Polymer-coated particles at high concentrations tend to precipitate on the cell surface. Most cells detach from the surface, while the few still adherent cells are alive. Clearly different behavior dependent on the particle surface compared to the low concentration regime shown in Figure 1 can be seen.

fig.	series	salt/type of nanopart.	λ_{core} [nm]	d_{core} [nm]	number of surface atoms per core	a_1	a_2	a_3 [μM]	a_4	a_5	a_6 [μM]	a_7
a	1	CAH	-	-	-	0.52	0.12	0.35	0.042	0.29	3.6	0.43
a	2	CAH	-	-	-	0.76	0.42	0.60	0.22	0	-	-
a	3	CPH	-	-	-	0.61	−0.22	0.48	−0.11	0.20	2.7	0.31
b	1	CdSe	560	3.3	110	0.75	0.22	0.58	0.083	0.25	1.1	0.37
b	2	CdSe	599	4.5	213	−0.049	0.88	0.58	0.37	1.7	0.22	1.1
b	3	CdSe	599	4.5	213	0.52	1.6	0.79	0.39	1.8	0.80	0.63
b	4	CdSe/ZnS	508	2.4	61	0.47	0.60	4.9	1.4	1.2	8.5	2.4
b	5	CdSe/ZnS	508	2.4	61	0.45	0.18	6.8	0.88	0.66	16	2.1
c	1	CdSe (phos)	560	3.3	110	-	-	-	-	-	-	-
c	2	CdSe (phos)	560	3.3	110	-	-	-	-	-	-	-
c	3	CdSe (PEG)	560	3.3	110	-	-	-	-	-	-	-
c	4	CdSe (PEG)	560	3.3	110	-	-	-	-	-	-	-
c	5	CdSe (PEG)	560	3.3	110	-	-	-	-	-	-	-
c	6	CdSe/ZnS (PEG)	560	3.3	110	-	-	-	-	-	-	-
c	7	CdSe/ZnS (PEG)	510	2.4	62	-	-	-	-	-	-	-
c	8	CdSe/ZnS (PEG)	510	2.4	62	-	-	-	-	-	-	-
d	1	CdSe	560	3.3	110	0.51	−0.29	0.83	0.73	0	-	-
d	2	CdSe	599	4.5	213	0.61	−0.25	0.77	0.51	0	-	-
d	3	CdSe/ZnS	599	4.5	213	0.76	−0.43	0.93	0.45	0	-	-
d	4	CdSe/ZnS	510	2.4	62	0.77	−0.38	1.0	0.48	0	-	-
e	1	Au (polymer)	-	4.6	831	0.78	−0.43	3.22	0.93	0	-	-
e	2	Au (MUA)	-	4.6	831	0.53	−0.20	1.2	1.2	0	-	-
e	3	Au (MUA)	-	4.6	831	0.48	−0.22	2.7	1.1	0	-	-

free culture should allow for a very sensitive detection of cytotoxic effects.

In Figure 2a the concentration of Cd atoms is equal to the concentration of free Cd^{2+} ions in solution because Cd was administered as salt. In Figure 2b the concentration of Cd is given as the concentration of Cd atoms on the surface of CdSe particles or on the surface of the CdSe core below the ZnS shell of CdSe/ZnS particles. Taking into account the findings of Derfus et al.,[29] who have shown by inductively coupled plasma optical emission spectroscopy (ICP/OES) measurements that free Cd^{2+} ions are released by CdSe particles, we can assume that a part of the Cd surface atoms is released to solution as Cd^{2+} ions, which are, according to this study, primarily responsible for cytotoxic effects. Our data suggest that, for our conditions (serum-free medium, 48 h incubation time, NRK cells), toxic effects of Cd^{2+} ions start at concentrations of about c(Cd atoms) $= 0.48 \pm 0.13$ μM (see Figure 2a). For CdSe and CdSe/ZnS particles, toxic effects start at concentrations of about c(Cd surface atoms) $= 0.65 \pm 0.12$ μM and 5.9 ± 1.3 μM Cd surface atoms (see Figure 2b). Within the hypothesis that Cd^{2+} ions released into solution are the main source for cytotoxic effects, a comparison of these values suggests that a significant amount of the Cd atoms on the surface of CdSe particles is released

as Cd^{2+} ions into solution ($\approx$0.48 μM/0.65 μM $\approx$ 75% as a very rough estimate), but that the mantling of CdSe with a ZnS shell drastically reduces this value to a rough estimate of 0.48 μM/5.9 μM $\approx$ 8%. Here we want to point out again that both the CdSe and the CdSe/ZnS particles had the same surface chemistry, a ligand shell of mercaptopropionic acid. Therefore, this direct comparison is another indicator that in this case indeed the release of Cd^{2+} and not eventual effects of the surface chemistry is responsible for the cytotoxic effects.

We also tested the other constituent of mercaptocarbonic acid coated CdSe and CdSe/ZnS nanoparticles for cytotoxic effects. No cytotoxic effects of Se^{2-} (selenious acid) and Zn^{2+} (zinc chloride) ions could be observed up to concentrations of 40 μM (we were not able to investigate higher ion concentrations). The ligands used to stabilize the particles in water, mercaptopropionic acid (MPA), led to cell detachment at concentrations between 1 and 10 mM (the same value was found for an alternative ligand, mercaptoacetic acid). Compared to the onset of cytotoxic effect of Cd^{2+} ions at concentrations of about 0.48 μM, this suggests that cadmium is the main source of cytotoxic effects of mercaptopropionic acid stabilized CdSe and CdSe/ZnS nanocrystals (at most, one MPA molecule can be attached per Cd surface atom).

Instead of coating the nanocrystals with a monolayer ligand shell of mercaptopropionic acid, more stable coatings are also possible. First, we investigated the effect of embedding nanocrystals in a silica shell, which comprises many layers of cross-linked silane molecules. From Figure 2c it can be seen that a PEG-silica shell basically prevented toxic effects of particles on cells in the investigated concentration range. Even for PEG-silica coated CdSe nanoparticles, no clear toxic effects up to Cd surface atom concentrations of 30 μM were found. On the other hand, $R(c)$ decreased upon increasing the concentration of phosphonate-silica coated CdSe nanoparticles. Microscopy images showed reduced particle uptake for PEG-silica coated particles, whereas phosphonate-silica coated particles were ingested by the cells and stored around the nucleus even for high Cd concentrations (Figures 1 and 2f). Viability tests showed that as well for PEG-silica as for phosphonate-silica coated particles within the whole concentration region, all adherent cells were living. For phosphonate-silica coated CdSe particle $R(c)$ started to decrease only at higher Cd surface atom concentrations than MPA coated CdSe particles. Therefore, we conclude that the cross-linked silica shell around the particles in general is a good barrier against the release of Cd^{2+} ions from the particle surface. In addition, embedding PEG-groups in the silica shell reduced the uptake of the particles (see microcopy images Figure 1), which resulted in reduced cytotoxicity (see the $R(c)$ curves shown in Figures 2b and 2c). Since silica shells embedding PEG and phosphonate groups should prevent the release of Cd^{2+} ions, in the same way we can further conclude that not only is the absolute concentration of Cd^{2+} ions responsible for cytotoxic effects but also the location where the Cd^{2+} ions are released is very important. If particles are ingested by cells, Cd^{2+} can be released directly inside cells (e.g., for phos-silica coating), which seems to cause more severe cytotoxic effects than release of Cd^{2+} outside cells (e.g., for PEG-silica coating).

For polymer-coated CdSe and CdSe/ZnS nanocrystals, a gradual decrease of R upon increased Cd concentration was observed (Figure 2d). Viability tests showed that all adherent cells were living for all Cd surface atom concentrations, although there were basically no adherent cells left in the case of high Cd concentrations (right part of the curve in Figure 2d). Phase contrast and fluorescence microscopy analysis showed that, in the case of high concentrations, clouds of nanoparticles precipitated on the surface of the cells and on the cell culture substrate (Figure 2f). In the case of low concentrations no precipitation effects were observed, and it is important to point out that under these conditions polymer-coated particles were ingested by cells similar to silanized and mercaptopropionic acid coated ones (Figure 1). Reduction in the number of adherent cells already started at Cd surface atom concentrations of 0.80 $\pm$ 0.04 μM for CdSe and 0.98 $\pm$ 0.07 μM for CdSe/ZnS particles.

Most striking, for inert polymer-coated Au nanoparticles the same effects were observed as for polymer-coated CdSe and CdSe/ZnS nanoparticles (Figure 2e). This excludes the effect of Cd^{2+} ion release as the only source for poisoning of the cells in the case of polymer-coated particles. We therefore conclude that in the case of our polymer-coated particles the precipitation of the particles on the cells and not the release of Cd^{2+} atoms is the major factor for cell impairment. Again, we have to recall that for low particle concentration regular particle uptake by the cells has been observed and that therefore our polymer-coated particles are still useful for cellular labeling. Recently, other groups have reported a modified polymer coating procedure in which polyethylene groups are incorporated in the polymer shell,[10] which should make these particles more stable against precipitation. Also, for other systems such as C_{60} fullerenes, it has been observed that cytotoxicity correlates with water solubility and thus with the surface chemistry of the particles.[43]

Impairment of Currents through Ion Channels upon Incubation of Cells with Nanocrystals. Two cell lines (RBL and CHO) were investigated regarding changes in their morphology and their electrophysiological properties upon incubation with nanocrystals. The CHO cell line was stably transfected to express the hERG channel, and the used RBL cell line endogenously expressed an inward rectifying potassium channel. For CdSe/ZnS particle concentrations in the nM range and incubation times of up to 2 days in serum-containing medium, no morphological changes of the cells were identified using high magnification light microscopy (see Supporting Information), although uptake of the nanocrystals by the cells was clearly verified by fluorescence microscopy (Figure 3a). Patch-clamp recordings under identical experimental circumstances of untreated and incubated cells revealed no changes of ion channel function and characteristic electrophysiological properties of the cells. In Figures 3b and 3c, currents through the ion channels of RBL and CHO cells before and after incubation with nanocrystals are displayed. As ion channels play an important role in the

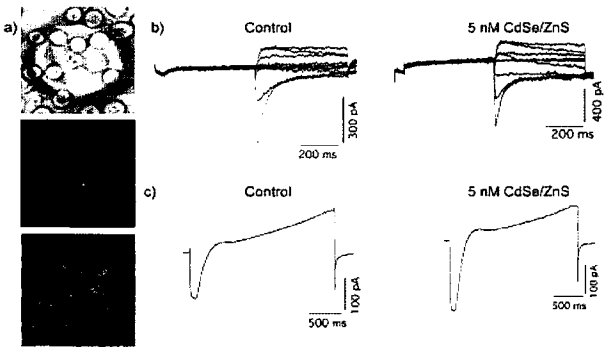

Figure 3. (a) RBL cells after 4 h incubation with *c*(CdSe/ZnS particles) = 10 nM MPA-coated CdSe/ZnS particles on the patch-clamp chip (wavelength of the absorption peak of the CdSe core λ = 508 nm, corresponding to a CdSe core diameter of d = 2.4 nm; 61 Cd surface atoms per nanoparticle). The bright field and fluorescence image as well as the overlay of both of them are shown. (b) hERG currents as obtained from one nontreated CHO cell and from one cell incubated 3 h in 5 nM MPA-coated CdSe/ZnS nanocrystals (wavelength of the absorption peak of the CdSe core λ = 508 nm, corresponding to a CdSe core diameter of d = 2.4 nm; 61 Cd surface atoms per nanoparticle). (c) Endogenous K^+ inward rectifier currents of RBL cells without treatment and 3 h after incubation in 5 nM MPA-coated CdSe/ZnS nanocrystals (wavelength of the absorption peak of the CdSe core λ = 508 nm, corresponding to a CdSe core diameter of d = 2.4 nm; 61 Cd surface atoms per nanoparticle).

cells vitality and function, their characteristics and functionality are a subtle indicator of the condition and viability of the cells. We suggest that for our experimental conditions for concentrations sufficient for CdSe/ZnS fluorescence labeling of cells no impairment of the ion channels of the investigated cells is observable.

Conclusions. In addition to a previous study,[29] we have determined the concentration limits of mercaptopropionic acid coated CdSe and CdSe/ZnS nanocrystals in a more detailed and absolute way. Poisoning of NRK cells due to the release of Cd^{2+} ions starts at concentrations of 0.65 ± 0.12 μM and 5.9 ± 1.3 μM of surface Cd atoms for mercaptopropionic acid coated CdSe and CdSe/ZnS particles, respectively (Figure 2b). In agreement with previous studies[29] our data show that coating of CdSe particles with a ZnS shells increases the critical concentration up to which no toxic effects can be observed by almost a factor of 10. Since a ligand shell of mercaptopropionic acid around the particles is not very stable, such a shell cannot prevent the release of Cd^{2+} ions from the particle surface. On the other hand, embedding the particles in a stable ligand shell of cross-linked silica molecules dramatically reduces the release of Cd^{2+} ions. In the case of PEG-silica coated CdSe and CdSe/ZnS particles we could not observe any toxic effect up to concentrations of 30 μM Cd surface atoms (Figure 2c). We ascribe this to the fact of reduced uptake of these particles by cells. For polymer-coated nanocrystals, an additional pathway of poisoning was observed. For polymer-coated CdSe and CdSe/ZnS nanocrystals, cytotoxic effects started at concentrations of approximately 0.80 ± 0.04 μM and 0.98 ± 0.07 μM Cd surface atoms, respectively. These values seem to be independent of an optional ZnS shell around the CdSe particles. Cytotoxic effects for polymer-coated particles start at slightly higher concentrations than for MPA-coated CdSe, but already at significantly lower concentrations than for MPA-coated CdSe/ZnS particles. These data suggest that the polymer shell rather than an MPA shell is a better diffusion barrier against the release of Cd^{2+} ions from CdSe surfaces. On the other hand, if Cd^{2+} is drastically hindered by a ZnS shell around the CdSe particles, cytotoxic effects are more severe for polymer- than for MPA-coated particles. This effect could be attributed to a precipitation of the polymer-coated particles on the cell surface (Figure 2f).

We conclude that, in addition to the release of Cd^{2+} ions from the surface of CdSe or CdSe/ZnS nanoparticles, cells can also be impaired if nanoparticles precipitate on the cell surface. Furthermore, cytotoxic effects are different in the case that particles are ingested by the cells compared to the case that particles are just present in the medium surrounding the cells. From this point of view it is important to correlate any study on the cytotoxicity of particles with a detailed microscopy analysis about the pathway of particle uptake. In accordance with another study,[31] our data indicate a massive influence of the surface chemistry of the particles on their cytotoxic behavior in addition to the release of toxic molecules. Certainly many aspects of particle cytotoxicity still have to be investigated, since effects strongly depend on many parameters such as surface chemistry, type of the cell line, incubation time, serum-containing/free medium, etc. Cleary, Cd-containing nanoparticles cannot be considered as 100% biocompatible, but depending on the experimental situation conditions can be found under which no cytotoxic effects occur.

Acknowledgment. This work was supported in part by the Emmy Noether Program of the Deutsche Forschungsgemeinschaft DFG (W.J.P.), the Volkswagen Stiftung (W.J.P.), the Sonderforschungsbereich SFB 486 of the DFG (H.E.G.), and the Excellence Network NanoBioTechnology ENNaB (W.J.P., N.F.). The authors are grateful to Michael George, Andrea Brüggemann, and Thomas Nicolaus for excellent technical support, and to Dr. Liberato Manna for helpful discussions.

Supporting Information Available: Details of Materials and Methods used in the study. This material is available free of charge via the Internet at http://pubs.acs.org.

References

(1) Wu, M. X.; Liu, H.; Liu, J.; Haley, K. N.; Treadway, J. A.; Larson, J. P.; Ge, N.; Peale, F.; Bruchez, M. P. *Nature Biotechnol.* **2003**, *21*, 41−46.
(2) Dahan, M.; Levi, S.; Luccardini, C.; Rostaing, P.; Riveau, B.; Triller, A. *Science* **2003**, *302*, 442−445.
(3) Lidke, D. S.; Nagy, P.; Heintzmann, R.; Arndt-Jovin, D. J.; Post, J. N.; Grecco, H. E.; Jares-Erijman, E. A.; Jovin, T. M. *Nature Biotechnol.* **2004**, *22*, 198−203.
(4) Parak, W. J.; Boudreau, R.; Gros, M. L.; Gerion, D.; Zanchet, D.; Micheel, C. M.; Williams, S. C.; Alivisatos, A. P.; Larabell, C. A. *Adv. Mater.* **2002**, *14*, 882−885.
(5) Roth, J. *Histochem. Cell Biol.* **1996**, *106*, 1−8.
(6) Sanford, J. C.; Smith, F. D.; Russell, J. A. *Methods Enzymol.* **1993**, *217*, 483−509.
(7) Schulze, E.; Ferrucci, J. T.; Poss, K.; Lapointe, L.; Bogdanova, A.; Weissleder, R. *Invest. Radiol.* **1995**, *30*, 604−610.

(8) Pankhurst, Q. A.; Connolly, J.; Jones, S. K.; Dobson, J. *J. Phys. D* **2003**, *36*, R167−R181.
(9) Jordan, A.; Scholz, R.; Wust, P.; Fahling, H.; Felix, R. *J. Magn. Magn. Mater.* **1999**, *201*, 413−419.
(10) Ballou, B.; Lagerholm, B. C.; Ernst, L. A.; Bruchez, M. P.; Waggoner, A. S. *Bioconjugate Chem.* **2004**, *15*, 79−86.
(11) Kim, S.; Lim, Y. T.; Soltesz, E. G.; Grand, A. M. D.; Lee, J.; Nakayama, A.; Parker, J. A.; Mihaljevic, T.; Laurence, R. G.; Dor, D. M.; Cohn, L. H.; Bawendi, M. G.; Frangioni, J. V. *Nature Biotechnol.* **2004**, *22*, 93−97.
(12) Alivisatos, A. P. *Sci. Am.* **2001**, *285*(September), 59−65.
(13) Service, R. F. *Science* **2000**, *290*, 1526−1527.
(14) Kondoh, M.; Araragi, S.; Sato, K.; Higashimoto, M.; Takiguchi, M.; Sato, M. *Toxicol.* **2002**, *170*, 111−117.
(15) Limaye, D. A.; Shaikh, Z. A. *Toxicol. Appl. Pharmacol.* **1999**, *154*, 59−66.
(16) Rikans, L. E.; Yamano, T. *J. Biochem. Molec. Toxicol.* **2000**, *14*, 110−117.
(17) Santone, K. S.; Acosta, D.; Bruckner, J. V. *J. Toxicol. Environ. Health* **1982**, *10*, 169−177.
(18) López, E.; Figueroa, S.; Oset-Gasque, M. J.; Gonzalez, M. P. *Br. J. Pharmacol.* **2003**, *138*, 901−911.
(19) Goyer, R. A. *Am. J. Clin. Nutr.* **1995**, *61*, 646s−650s.
(20) Ghitescu, L.; Fixman, A. *J. Cell Biol.* **1984**, *99*, 639−647.
(21) Jordan, A.; Scholz, R.; Wust, P.; Schirra, H.; Schiestel, T.; Schmidt, H.; Felix, R. *J. Magn. Magn. Mater.* **1999**, *194*, 185−196.
(22) Wilhelm, C.; Billotey, C.; Roger, Pons, J. N.; Bacri, J.-C.; Gazeau, F. *Biomat.* **2003**, *24*, 1001−1011.
(23) Kloepfer, J. A.; Mielke, R. E.; Wong, M. S.; Nealson, K. H.; Stucky, G.; Nedeau, J. L. *Appl. Environ. Microbiol.* **2003**, *69*, 4205−4213.
(24) Lam, C.-W.; James, J. T.; McCluskey, R.; Hunter, R. L. *Toxicol. Sci.* **2004**, *77*, 126−134.
(25) Warheit, D. B.; Laurence, B. R.; Reed, K. L.; Roach, D. H.; Reynolds, G. A. M.; Webb, T. R. *Toxicol. Sci.* **2004**, *77*, 117−125.
(26) Videira, M. A.; Botelho, M. F.; Santos, A. C.; Gouveia, L. F.; Lima, J. J. P. d.; Almeida, A. J. *J. Drug. Target.* **2002**, *10*, 607−613.
(27) Artelt, S.; Creutzenberg, O.; Kock, H.; Levsen, K.; Nachtigall, D.; Heinrich, U.; Ruhle, T.; Schlogl, R. *SCIENCE OF THE TOTAL ENVIRONMENT* **1999**, *228*, 219−242.
(28) Kanitsar, K.; Koellensperger, G.; Hann, S.; Limbeck, A.; Puxbaum, H.; Stingeder, G. *J. Anal. Atomic Spectrom.* **2003**, *18*, 239−246.
(29) Derfus, A. M.; Chan, W. C. W.; Bhatia, S. N. *Nano Lett.* **2004**, *4*, 11−18.
(30) Shiohara, A.; Hoshino, A.; Hanaki, K.; Suzuki, K.; Yamamoto, K. *Microbiol. Immunol.* **2004**, *48*, 669−675.
(31) Hoshino, A.; Fujioka, K.; Oku, T.; Suga, M.; Sasaki, Y. F.; Ohta, T.; Yasuhara, M.; Suzuki, K.; Yamamoto, K. *Nano Lett.* **2004**, *4*, 2163−2169.
(32) Reiss, P.; Bleuse, J.; Pron, A. *Nano Lett.* **2002**, *2*, 781−784.
(33) Dabbousi, B. O.; Rodriguez-Viejo, J.; Mikulec, F. V.; Heine, J. R.; Mattoussi, H.; Ober, R.; Jensen, K. F.; Bawendi, M. G. *J. Phys. Chem. B* **1997**, *101*, 9463−9475.
(34) Fink, J.; Kiely, C. J.; Bethell, D.; Schiffrin, D. J. *Chem. Mater.* **1998**, *10*, 922−926.
(35) Gerion, D.; Pinaud, F.; Williams, S. C.; Parak, W. J.; Zanchet, D.; Weiss, S.; Alivisatos, A. P. *J. Phys. Chem. B* **2001**, *105*, 8861−8871.
(36) Parak, W. J.; Gerion, D.; Zanchet, D.; Woerz, A. S.; Pellegrino, T.; Micheel, C.; Williams, S. C.; Seitz, M.; Bruehl, R. E.; Bryant, Z.; Bustamante, C.; Bertozzi, C. R.; Alivisatos, A. P. *Chem. Mater.* **2002**, *14*, 2113−2119.
(37) Pellegrino, T.; Manna, L.; Kudera, S.; Liedl, T.; Koktysh, D.; Rogach, A. L.; Keller, S.; Rädler, J.; Natile, G.; Parak, W. J. *Nano Lett.* **2004**, *4*, 703−707.
(38) Kirchner, C.; George, M.; Stein, B.; Parak, W. J.; Gaub, H. E.; Seitz, M. *Adv. Funct. Mater.* **2002**, *12*, 266−276.
(39) Barnes, D.; Sato, G. *Anal. Biochem.* **1980**, *102*, 255−270.
(40) Fertig, N.; Blick, R. H.; Behrends, J. C. *Biophys. J.* **2002**, *82*, 3056−3062.
(41) Brueggemann, A.; George, M.; Klau, M.; Beckler, M.; Steindl, J.; Behrends, J. C.; Fertig, N. *Curr. Drug Discovery Technol.* **2004**, *1*, 91−96.
(42) Rosenthal, S. J.; Tomlinson, I.; Adkins, E. M.; Schroeter, S.; Adams, S.; Swafford, L.; McBride, J.; Wang, Y.; DeFelice, L. J.; Blakely, R. D. *J. Am. Chem. Soc.* **2002**, *124*, 4586−4594.
(43) Sayes, C. M.; Fortner, J. D.; Guo, W.; Lyon, D.; Boyd, A. M.; Ausman, K. D.; Tao, Y. J.; Sitharaman, B.; Wilson, L. J.; Hughes, J. B.; West, J. L.; Colvin, V. L. *Nano Lett.* **2004**, *4*, 1881−1887.

NL047996M

A
42

Supplementary Information

Cytotoxicity of colloidal CdSe and CdSe/ZnS nanoparticles

Christian Kirchner[1], Tim Liedl[1], Stefan Kudera[1], Teresa Pellegrino[1], Almudena Muñoz Javier[1], Hermann E. Gaub[1], Sonja Stölzle[2], N. Fertig[2], Wolfgang J. Parak[1,*]

[1] Center for Nanoscience, Ludwig Maximilians Universität München, Germany
[2] Nanion Technologies GmbH, Pettenkoferstr. 12, 80336 Munich, Germany

*To whom correspondence should be addressed:
Dr. Wolfgang J. Parak
Center for Nanoscience
Amalienstrasse 54
80799 München
Germany
Wolfgang.Parak@physik.uni-muenchen.de

(I) Synthesis of the nanoparticles

The synthesis of hydrophobic CdSe, CdSe/ZnS, and Au nanoparticles is described in detail in the supporting information of a previous paper [1]. We have followed these protocols without change. The hydrophobic particles were transferred to aqueous solution using three different protocols.

1) The silanization of CdSe/ZnS particles with phosphonate silane has been described by Gerion et al. [2,3] and the silanization of CdSe/ZnS particles with PEG silane has been performed as reported by Parak et al. [3].

2) The polymer coating of Au and CdSe/ZnS particles has been described in detail by Pellegrino et al. [1]. We have followed these protocols without change. The same protocol was applied for the polymer coating of CdSe particles.

3) We have changed our previous protocol in which the transfer of particles to aqueous solution by ligand exchange with mercaptocarbonic acids is described [2].

The protocols for ligand exchange with mercaptocarbonic acids as used in this study are reported below:

Coating of CdSe and CdSe/ZnS particles with mercaptopropionic acid

First, CdSe or CdSe/ZnS particles (as prepared in organic solvent as described above) were washed one time by precipitating them with methanol and redissolving them in chloroform. The particles were then precipitated by the addition of methanol and the sample was centrifuged and the supernatant discarded. The ligand exchange on the semiconductor particles was carried out by taking the wet precipitate (approximately 10 nmol of red fluorescent particles, or 40 nmol of green fluorescent particles) and adding 2 ml of anhydrous DMF (N,N-Dimethylformamide, purchased from Sigma, #22,705-6). A homogeneous distribution of the particles, which did not dissolve, was established by vortexing the sample. Then, equal molar amounts of mercaptopropionic acid (200 µl, purchased from Sigma, #M580-1) and 2-mercaptoethanol (160 µl, purchased from Sigma, #56,867-2) were added. After vortexing the solution turned transparent in the case of CdSe/ZnS particles. The CdSe cores did not produce a clear solution. This product was stored in the dark at room temperature until actual experiments with the particles were scheduled. Then, the particles were precipitated by adding 2 ml of deionized water and centrifugation. The particles were resuspended in deionized water. The addition of 50-100 µl Base (TMAH dissolved in methanol in a ratio of 1:3, tetramethylammonium hydroxide pentahydrate from Sigma, #T7505) yielded a clear solution with a pH of 10. The solution was then run through two NAP 25 gel columns (purchased from Amersham Biosciences, #17-0852-02) loaded with deionized water in order to neutralize the pH and to clean the product of remaining reactants.

Coating of Au particles with mercaptoundecanoic acid

Tetraoctylammonium bromide stabilized Au particles dissolved in toluene have been prepared according to standard protocols [4-7]. We have followed the detailed description of the gold synthesis reported by Pellegrino et al. [1]. In this report the tetraoctylammonium bromide ligands were then replaced by dodecanethiol ligands and the particles remained hydrophobic. Here we performed a ligand exchange to mercaptoundecanoic acid, which resulted in hydrophilic and thus water-soluble particles. For the ligand exchange with mercaptoundecanoic acid we followed the protocol of Mayya et al. [8].

100 ml of tetraoctylammonium bromide stabilized Au particles dissolved in toluene as prepared by Pellegrino et al. [1] were heated to 65°C. A hot solution (65°C) of 5.8 g mercaptoundecanoic acid (MUA, Sigma #45.056-1) dissolved in 10 ml toluene was added. This corresponds to a thirty-fold molar excess of MUA over the initial amount of gold. The solution was kept at 65°C for 1 hour. Then it was stirred overnight at room temperature. The day after a precipitate had formed. The solution was then centrifuged, and the translucent supernatant was discarded. The precipitate was dissolved in 0.1M TRIS buffer and sonicated to obtain a homogeneous, clear, violet solution of mercaptoundecanoic acid stabilized water-soluble Au-particles.

(II) Calculation of the number of surface atoms per nanoparticle and of the nanoparticle / surface atom concentrations

1) Calculation of the number of Cd surface atoms per CdSe particle

Given a certain radius of the particles, the number of surface atoms could be calculated by comparing the spherical particles with a small, faceted nanorod with the same surface. We assume, that we find the same number of atoms on a rod as we would find on a spherical particle. A rod has six lateral and two basal facets, see Figure S1a. On the lateral (non-polar) facets of the rods one finds one Cd-Atom per 30Å^2. This can be understood by looking at a unit cell of a wurtzite structure, see Figure S1b. The unit cell has the same shape as the rod; especially it also has the six lateral facets. Each of these facets contains one Cd-Atom. The area of one of these facets is a•c, with a and c being the lattice constants of the CdSe-wurtzite structure. With a = 4.28 Å and c = 7.01 Å, one obtains 30.00 Å^2 for the area occupied by one Cd-atom on the lateral facets. A rod can be constructed by adding an adequate number of layers of atoms onto one core unit cell.

On the hexagonal basal facets of the unit cell there are three atoms. This facet can be split into six equivalent triangles, each of them with an area of $1/2 \bullet 3^{1/2}/2 \bullet a^2$. So the total area per atom on this facet can be calculated to 15.86 Å^2. However, due to the intrinsic asymmetry of the wurtzite structure, and due to the growth mechanism, the (0001)-facet is only occupied by Cd atoms, whereas the opposing (000-1)-facet is composed exclusively of Se-atoms [9], so that the overall density of atoms of one species on the basal facets, is one per 31,72 Å^2, which is roughly the same as on the lateral facets.

As the lateral facets mainly constitute the surface of the rod, a density of 1 atom per 30 Å^2 surface area is a good approximation. Overall the number of Cd-atoms on the surface of a CdSe particle can be calculated as $N = 4 \pi r^2/30Å^2$, whereby r is the radius of the CdSe particle.

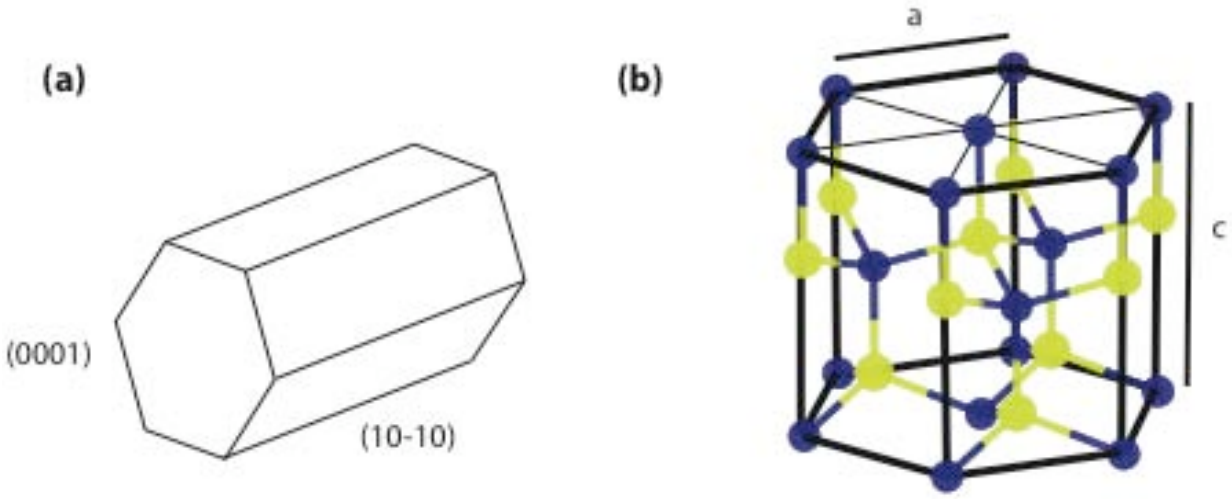

Figure S1: a) A schematic drawing of a rod. b) A unit cell of the wurtzite structure. Cd atoms are drawn in blue, Se atom in yellow. In each of the lateral facets there is one cadmium atom and one Selenium atom. Inner atoms are screened by atoms of the other species. From this picture one can also understand the difference between the two basal facets (0001) and (000-1). In this figure the Cd atoms have three bonds upwards, the selenium atoms only one. In the other direction the situation is contrary. From this derives the chemical difference of the two facets.

2) Calculation of the number of Cd atoms on the surface of the CdSe core of CdSe/ZnS particles

Since we identified Cd as the main source for cytotoxic effects, the ZnS shell around the CdSe cores rather has to be considered as a protection shell preventing the release of Cd atoms from the CdSe core than as an additional source of contamination. For this reason we consider the Cd atoms on the surface of the CdSe particle core as surface atoms, which are shielded by the ZnS shell. Thus, the number of Cd surface atoms for one CdSe/ZnS particle is $N = 4 \pi r^2/30Å^2$ (analogues to CdSe particles), whereby r is the radius of the CdSe core and not of the whole CdSe/ZnS particle.

3) Calculation of the number of Au atoms on the surface of Au particles

To estimate the number of atoms on the surface of Au particles a method similar to that used for the estimation of surface atoms of the CdSe particles is employed. First, we calculate a mean surface area A_{Au} per atom on a particle, then we calculate the number of atoms on the surface of a particle with given radius r as $N = 4 \pi r^2 / A_{Au}$. In the case of the gold particles we have to consider that gold grows in fcc-structure. We assume that the particles' surface is mainly constituted by (111) and (100) facets. They have a close packing, and therefore are very stable. On the (100) facet of the unit cell there are two atoms, so with a lattice constant of a = 4.08 Å we find a density of one atom per 8.3 $Å^2$. On the (111) facet we find one atom per 7.21 $Å^2$. This can be understood by looking at a cross section of the fcc unit cell perpendicular to the [111] axis as marked in figure S2b. We find a triangle with three atoms on each side. The side length is $2^{1/2} \bullet a$. One of these triangles contains 2 atoms. So we find a density of one atom per 7.21 $Å^2$ on the (111) facet. Looking at the model systems Au_{55} and Au_{147} (see Figure S2a and b), which have closed shells, one can easily see that their surface is mainly constituted by (100) facets. Therefore, as an approximation, we used the value of $A_{Au} = 8 Å^2$ surface area per atom. Overall the number of Au atoms on the surface of an Au particle can be then calculated as $N = 4 \pi r^2 / 8 Å^2$, whereby r is the radius of the Au particle.

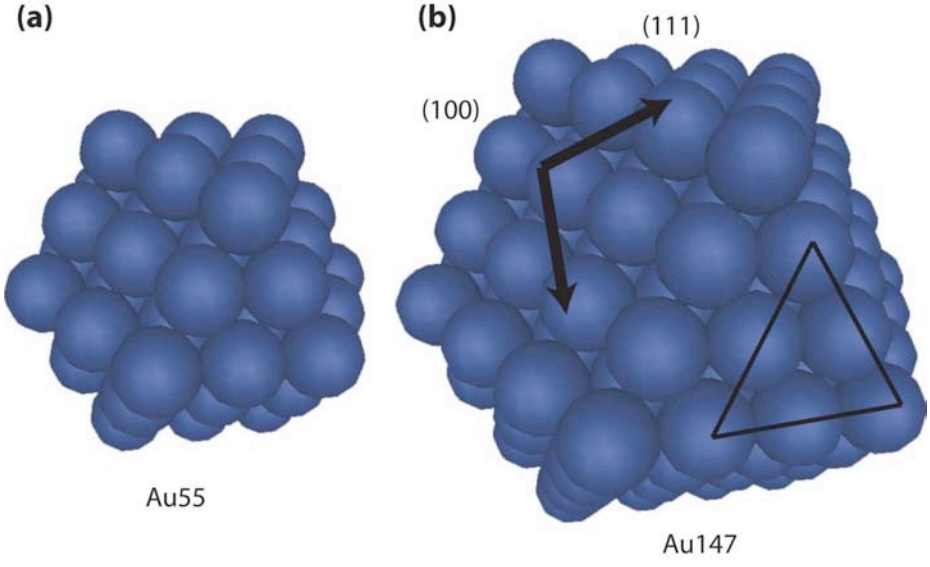

Figure S2: a) A model of Au_{55}. This cluster is obtained by covering one single Au atom with two closed layers of atoms. b) A model of Au_{147}. Marked with arrows on the (100) plane is one face of the cubic unit cell. On the (111) plane the triangle marks six atoms that can be assigned to one cubic unit cell.

4) Determination of the concentration of CdSe particles and Cd surface atoms

Measurement of the CdSe particle concentration c(CdSe particles):

The concentration of the CdSe nanocrystals is evaluated according to Yu et al. [10]. Here, absorption spectra of the cores in the range of 200-800 nm were measured with an UV/visible spectrophotometer (BIOCHROM Ultraspec 3100 pro). The absorption A at first exciton peak at wavelength λ_0 is related to the particle concentration of the sample c_P = c(CdSe particles) by $A = \frac{c_P \times l \times \varepsilon(\lambda_0)}{d}$, where $\varepsilon(\lambda_0)$ is size-dependent the extinction coefficient [10], l the pathlength of the cuvette, and d the dilution factor. Thus the particle concentration can be obtained from the absorption spectra.

Calculation of the concentration of cadmium atoms c(Cd surface atoms) of the CdSe core surface in solution:

For the estimation of the number N_{Cd} of cadmium atoms on the surface of a CdSe core we calculate $N_{Cd} = \frac{A_{core}(\lambda_0)}{A_{Cd}}$, where $A_{Cd} = 30$ Å^2 (see II.1) is the average area of one Cd atom and $A_{core}(\lambda_0)$ the core surface area. The latter value is calculated by $A_{core}(\lambda_0) = 4r(\lambda_0)^2_{core}\pi$, where $r_{core}(\lambda_0)$ is taken from Yu et al. [10], in dependence of the wavelength λ_0 of the first exciton peak. Thus the particle concentration c_P = c(CdSe particles) can be converted to a cadmium surface atom concentration c_N = c(Cd surface atoms) according to $c_N = c_P \times N_{Cd}$.

Calculation of the mass concentration of CdSe nanocrystals in solution:

The mass m_{NC} of one CdSe particle was calculated according to $m_{NC} = m_{core} = d_{CdSe} \times V_{core}$, using the particle volume $V_{core} = \frac{4}{3} r^3_{core}\pi$ and the mass density of CdSe $d_{CdSe} = 5.810 \frac{g}{cm^3}$ and ignoring the mass contribution of organic surface ligands. The mass concentration is $c_m = c_P \times m_{NC} \times N_A$, where $N_A = 6.022 \times 10^{23} mol^{-1}$ is the Avogadro constant.

5) Determination of the concentration of CdSe/ZnS particles and Cd surface atoms

Measurement of the CdSe particle concentration:

In the case of CdSe cores with ZnS shell we assume the same extinction coefficient as for CdSe particles without shell to get the particle concentration. The extinction coefficient is taken from the data publishes by Yu et al. [10]. We neglect the fact that upon growing a ZnS shell the first exciton peak of CdSe/ZnS particles is shifted to higher wavelength by 5 to 15 nm compared to CdSe cores.

Calculation of the concentration of cadmium atoms c(Cd surface atoms) of the CdSe core surface of CdSe/ZnS particles in solution:

For CdSe/ZnS particles we calculate the number of Cd surface atoms as the number of Cd atoms that lie on the surface of the CdSe core. For this purpose the first exciton peak of the CdSe cores has to be determined before growing the ZnS shell around them. From the wavelength of the first exciton peak the diameter of the CdSe core and thus the number of Cd atoms on the surface can be derived as described above for CdSe particles.

Calculation of the mass concentration of CdSe/ZnS nanocrystals in solution:

The mass $m_{NC} = m_{core}$ of a CdSe particle without ZnS shell was calculated according to $m_{NC} = m_{core} = d_{CdSe} \times V_{core}$, using $V_{core} = \frac{4}{3} r_{core}^3 \pi$ and the mass density of CdSe $d_{CdSe} = 5.810 \frac{g}{cm^3}$ by ignoring the mass contribution of organic surface ligands. In the case of an additional ZnS shell around the CdSe particles the mass $m_{ZnS} = d_{ZnS} \times \frac{4}{3}\pi((r_{core} + \Delta r_{shell})^3 - r_{core}^3)$ of the ZnS shell was added to the core mass m_{core} to get $m_{NC} = m_{core} + m_{ZnS}$, where $d_{ZnS} = 4.090 \frac{g}{cm^3}$ is the mass density of ZnS and $\Delta r_{shell} = 0.75nm$ is an average empirical value for the thickness of a ZnS shell, derived from TEM measurements reported by Gerion et al. [2]. The mass concentration is $c_m = c_P \times m_{NC} \times N_A$, where $N_A = 6.022 \times 10^{23} mol^{-1}$ is the Avogadro constant and c_P the concentration of CdSe/ZnS particles in M.

6) Determination of the concentration of Au particles and Au surface atoms

Measurement of the Au particle concentration:

As in the case of CdSe particles absorption spectra of the Au particles in the range of 200-800 nm were measured with an UV/visible spectrophotometer (BIOCHROM Ultraspec 3100 pro). The absorption A at the wavelength of the plasmon peak is $A = \frac{c_P \times l \times \varepsilon(r_P)}{d}$, where $\varepsilon(r_P) = 1.29\ 10^7\ M^{-1}cm^{-1}$ is assumed as extinction coefficient for our gold particle with a radius of $r_P = 2.3$ nm, l the pathlength of the cuvette, d the dilution factor, and c_P = c(Au particles) the concentration of Au particles in the sample.

Calculation of the concentration of Au atoms located on the Au particle surface:

As in the case of CdSe particles, for the estimation of the number N_{Au} of Au atoms on the surface of an Au particle we use $N_{Au} = \frac{A_P(r_P)}{A_{Au}}$, where $A_{Au} = 8$ Å^2 (see II.3.) is the average area of an Au atom and $A_P(r_P)$ is the surface area of a particle with radius r_P. The latter value is calculated by $A_P(r_P) = 4r_P^2\pi$, where all the Au particles used in this study had a radius of $r_P = 2.3$ nm as determined by TEM. Thus the particle concentration c_P = c(Au particles) was converted to an Au surface atom concentration c_N = c(Au surface atoms) according to $c_N = c_P \times N_{Au}$.

7) Table of the used CdSe, CdSe/ZnS, and Au samples

In order to compare our results with the observations of other groups we give here a table in which the conversion between different ways of quantifying nanocrystal concentrations is given.

CdSe nanocrystals

λ [nm]	c(CdSe particles) [nM]	c(Cd surface atoms) [μM]	c(CdSe particles) [μg/ml]
560	10	1.1	0.63
599	10	2.1	1.7

λ [nm] = wavelength of the first exciton peak in the absorption spectrum of the CdSe core particle

c(CdSe particles) [nM] = concentration of CdSe particles

c(Cd surface atoms) [µM] = concentration of Cd atoms which are located on the surface of the CdSe particles

c(CdSe particles) [µg/ml] = mass concentration of CdSe particles

CdSe/ZnS nanocrystals

λ [nm]	c(CdSe/ZnS particles) [nM]	c(Cd surface atoms) [µM]	c(CdSe/ZnS particles) [µg/ml]
508	10	0.61	0.86
510	10	0.62	0.87
560	10	1.1	1.6
599	10	2.1	3.3

λ [nm] = wavelength of the first exciton peak in the absorption spectrum of the CdSe core of the CdSe/ZnS particle (must have been determined before the growth of the ZnS shell)

c(CdSe/ZnS particles) [nM] = concentration of CdSe/ZnS core/shell particles

c(Cd surface atoms) [µM] = concentration of Cd atoms which are located on the surface of the CdSe core of the CdSe/ZnS particles

c(CdSe/ZnS particles) [µg/ml] = mass concentration of CdSe/ZnS particles

Au nanocrystals

c(Au particles) [nM]	c(Au surface atoms) [µM]	c(Au particles) [µg/ml]
10	8.31	5.92

c(Au particles) [nM] = concentration of Au particles

c(Au surface atoms) [µM] = concentration of Au atoms which are located on the surface of the Au particles with a diameter of 4.6 nm

c(Au particles) [µg/ml] = mass concentration of Au particles with a diameter of 4.6 nm

(III) Uptake of CdSe/ZnS nanocrystals by MDA-MB-435S breast cancer cells

MDA-MB-435S breast cancer cells were purchased from American Type Cell Culture (ATCC) and cultivated at 37°C and 5% CO_2 in the media proposed by ATCC. For uptake-experiments the adherent cells were rinsed twice with PBS without Ca^{++} and Mg^{++} (PBS, 9,55g/l, Biochrom AG, Germany) in order to reduce the concentration of adhesion-promoting Ca^{++} and Mg^{++} -ions inside the cells. The cells were then covered with Trypsin-EDTA-solution (Biochrom AG, Germany) and incubated at 37°C for 5 minutes. After incubation the now detached cells were diluted in PBS, filled into test tubes and centrifuged (5 min, 300g). The Trypsin-EDTA containing supernatant was removed and the cells were resuspended in media. The cells were diluted to a concentration of 7 * 10^4 cells/ml. For all uptake-experiments 1 ml of cell-suspension was filled into a nunc-chamber® (Nalge, U.S.). To each chamber 10 µl of 2-10 µM solution of two types of different coated nanocrystals, fluorescing in red and green, respectively, were added. The final concentration of each type of nanocrystals in the serum-supplemented media was 2-10 nM. After 18 h of incubation at 37°C and 5% CO_2 the cells were rinsed twice with PBS and fresh medium was added. The cells were then incubated for additional 4 h to allow the cells to ingest the nanocrystals.

Before visualizing the cells their nucleus was stained with DAPI (Molecular Probes, U.S.) following the providers protocol for adherent cells. For visualizing the cells the nunc-chambers® were mounted onto a fluorescence microscope (Axiovert 200, Zeiss, Germany) using a 100x oil-immersion objective. For every image one channel in differential interference contrast mode (bw) and three individual channels in the fluorescence mode were recorded using the following filters: blue channel (DAPI): excitation: G 365, beamsplitter: FT 395, emission: BP 445/50; green channel (green nanocrystals): excitation: BP 450, beamsplitter: FT 480, emission: BP 535; red channel (red nanocrystals): excitation: BP 546, beamsplitter: FT 580, emission: LP 590. For excitation a 100 Watt Mercury lamp (HBO 100, Osram) was used at half power. The acquisition times varied between 100 and 500 ms for the different types of nanocrystals, as they have different quantum yields. Images were recorded with a Zeiss AxioCam CCD camera. The recorded channels were overlaid using the microscope software (Axiovision 4.1).

(IV) Detachment of NRK fibroblast from the cell culture substrate upon incubation with nanocrystals

Chemicals

Ultrapure water (MilliQ-grade) was used in all experiments. Octadecyltrichlorosilane (OTS) was obtained from ABCR, Karlsruhe, Germany. Hexadecane, hexane, chloroform, mercaptopropionic acid (MPA), cadmium acetate hydrate (CAH), cadmium perchlorate hydrate (CPH), selenious acid (SA), zincchloride (ZC) PBS (phosphate buffer saline), Penstrep solution (containing 10,000 units/ml Penicillin and 10 mg/ml streptomycin-sulfate, and 0.9% NaCl), Liquid Media Supplement (ITS) as well as trypsin were purchased from Sigma-Aldrich. Dulbecco's Modified Eagle Medium (DMEM, FG 0435), HAM'S F-12 Medium (FG 0815) and fetal bovine serum (FBS, S0115) were from Biochrom KG (Berlin, Germany). All chemicals were used as received.

Cell culture

Normal Rat Kidney (NRK)-fibroblasts (CRL-6509) were obtained from ATCC, Manassas, USA. As cell culture medium DMEM with 10% FBS (fetal bovine serum) and 1% Penstrep solution was used. During incubation with nanocrystals cells were cultivated in serum free SATO medium (HAMS F12 with 1% serum supplement ITS), which stopped cell proliferation. Measurements had to be performed in serum free medium since for our applied automated counting procedure (see below) it is important that cell do not proliferate and migrate too much. Otherwise it would be impossible to verify for each individual cell whether it is still adherent at the same place of whether it has detached from the surface.

NRK-fibroblasts were seeded in 6-wellplates (TPP, Switzerland; polyethylene, tissue culture treated) to a concentration of 3600 cells / cm^2. Special care was taken to achieve a cell population of separated single cells, in order to get optimal conditions for the optical counting procedure. Adhesion of the cells was observed after 5 to 24 hours. After cell adhesion, the cell layer was gently rinsed three times with PBS buffer, and the adherent cells were counted in PBS buffer within 20 min. The buffer then was replaced by the incubation medium (SATO and the toxin, i.e. Cd salts or nanocrystals, in a target concentration). SATO treatment always caused a certain loss of cells by detachment, even without toxin. After 48 hours of incubation, cells were rinsed three times with PBS buffer, removing detached cells, while the residual adherent cells were counted again in PBS buffer within 20 min.

Automated procedure to count adherent cells

A computer based optical counting method was used to sensibly detect the effects of very low toxin concentrations to the adhesion behavior of living cells. Cells were counted on images recorded with a phase contrast microscope before and after incubation with the toxin, and the ratio R(c) of cells adherent to the surface after / before incubation versus the toxin concentration c is plotted. For this purpose for each individual cell which was adherent before incubation with the toxin, it was tested if the same cell is still adherent after incubation with the toxin. Therefore, the position of each cell within the wellplate had to be registered before incubation with the toxin and had to be found again after 48 hours incubation with the toxin. While the motorized xy-stage of the microscope allowed for a very precise repositioning of the wellplate holder, placing the wellplates led to an overall repositioning error of approx. 100 µm. This contributes to the relative error of about 10% for the measured average ratios R. While a ratio R close to zero indicates the complete detachment of the cells from the surface, a ratio of R = 1 means that statistically every cell is found after the incubation time where it was seeded. The reference value R(c = 0) never is found to be = 1, because of the SATO medium. Changing the serum-containing medium to serum free SATO medium alone results in a detachment of some cells, even when no toxin is added (i.e. c = 0). Moreover, R(c) never

is found to be = 0 since always a certain amount of dirt, dust particles, or cell debris is counted wrongfully as adherent cells. In the worst case this background noise in R(c) due to cell debris and other impurities could be as high as R(c) = 0.34. In the case of the polymer coated nanocrystals for high particle concentrations there are basically no adherent cells left and the constant R(c) > 0 background level is due to impurities wrongfully counted as adherent cells. Therefore, for the interpretation of our data it is important to correlate the R(c) curve with microscopy images. Another important information additional to the R(c) curves is result of the viability tests performed for different concentrations. These data indicate whether the counted adherent cells are alive or dead.

In practice, for each toxin concentration approximately 20000 cells were monitored in 94 pictures taken from two wellplate chambers. This was done with an inverted optical microscope (Axiovert 200, Carl Zeiss, Jena) in phasecontrast mode with a 4x Achroplan objective. Hydrophobic circular glass cover slides (preparation see below) were placed to float on the buffer surface to avoid light scattering through the meniscus of the liquid at the chamber walls, which would result in a brightness gradient in the pictures. The pictures, taken with a Zeiss AxioCam HRm CCD camera, showed a surface area of 2.6 mm × 3.5 mm as a black background with the light spots of adherent cells (and dirt), see Figure S3. This high contrast and the low brightness variations of the background allowed for a computer based particle analysis with the data evaluation software Igor Pro 4.1, running on a Dual 2.0 GHz Macintosh PowerPC. Using the subroutine package of Igor Pro for image processing, it was possible to automate the cell counting. For particle analysis, a threshold in the grayscale was used for the particle detection based on the average brightness of a picture. The threshold and a minimum value for the spot size were the necessary parameters for a reliable counting of surface adherent particles.

a)

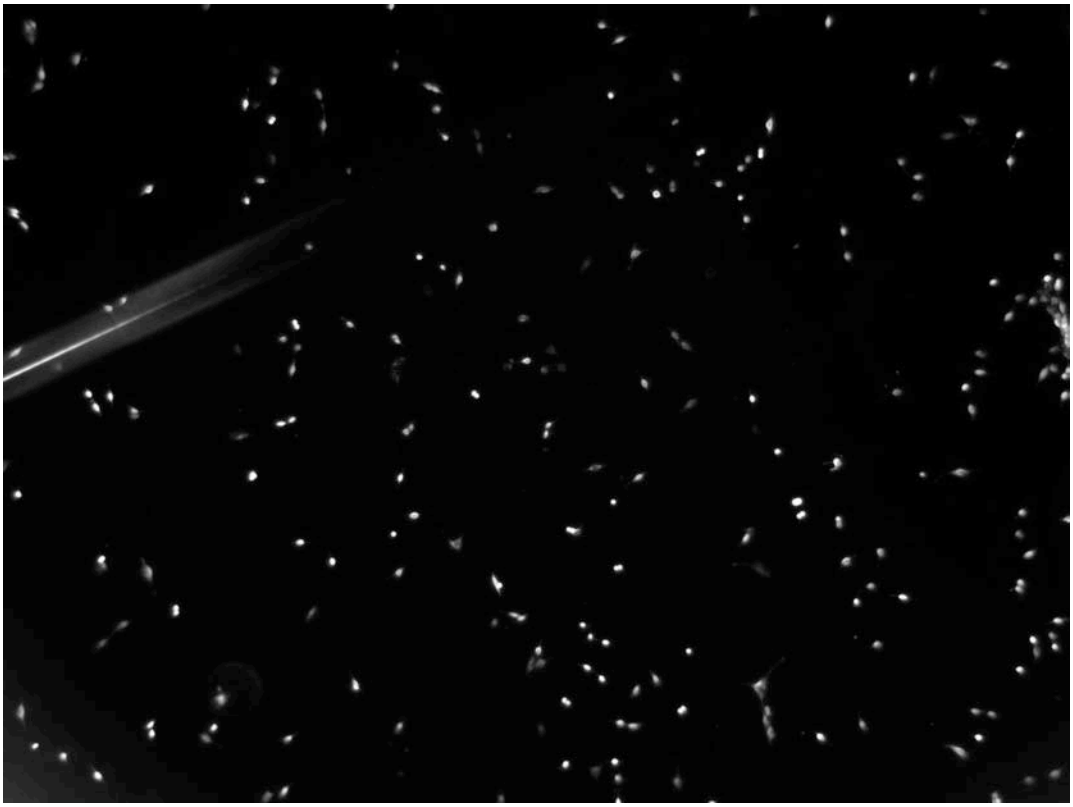

b)

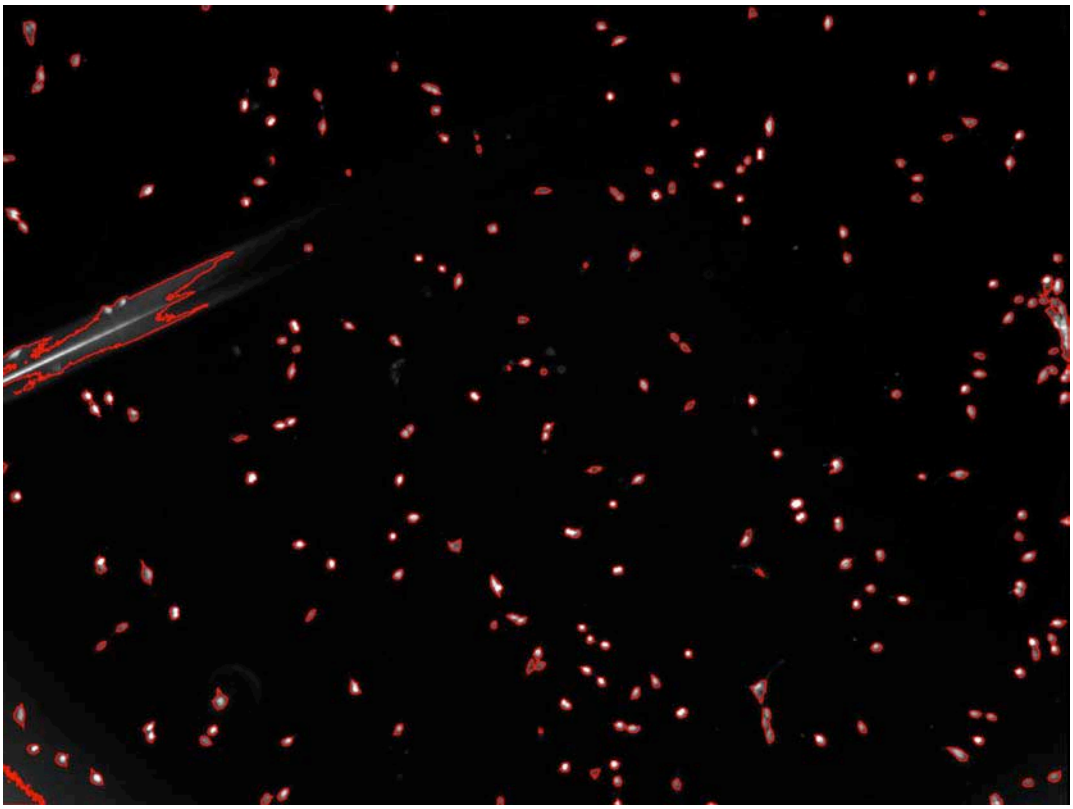

c)

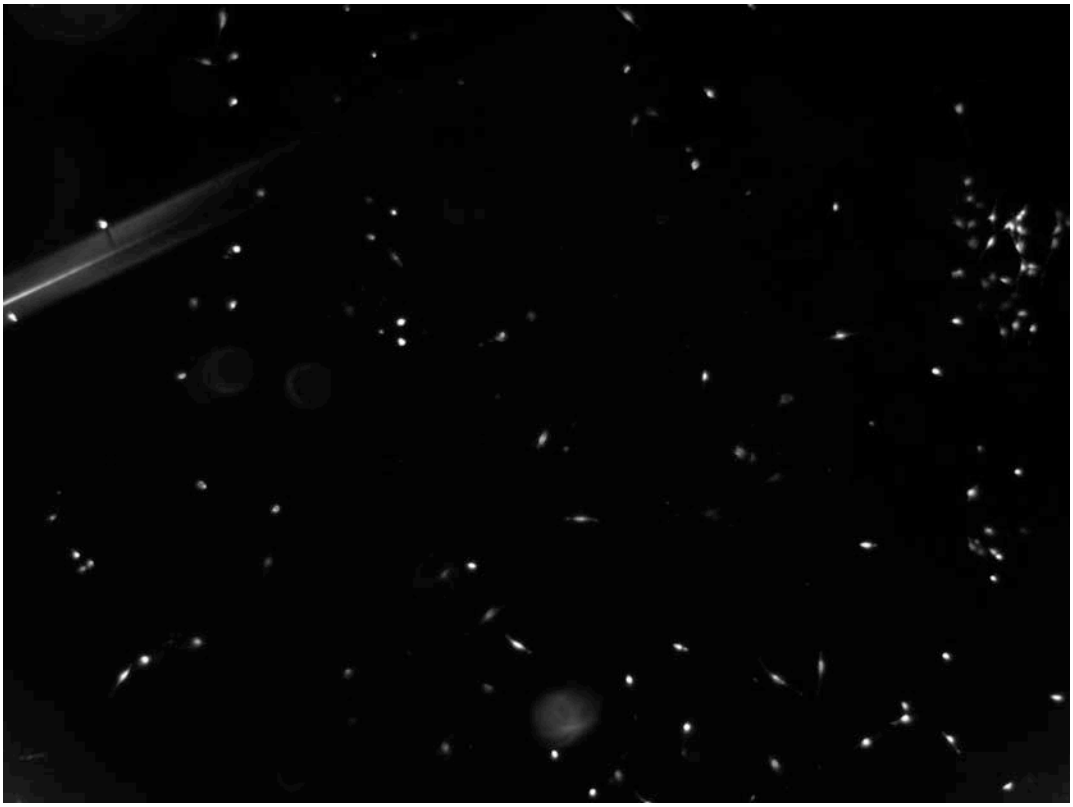

d)

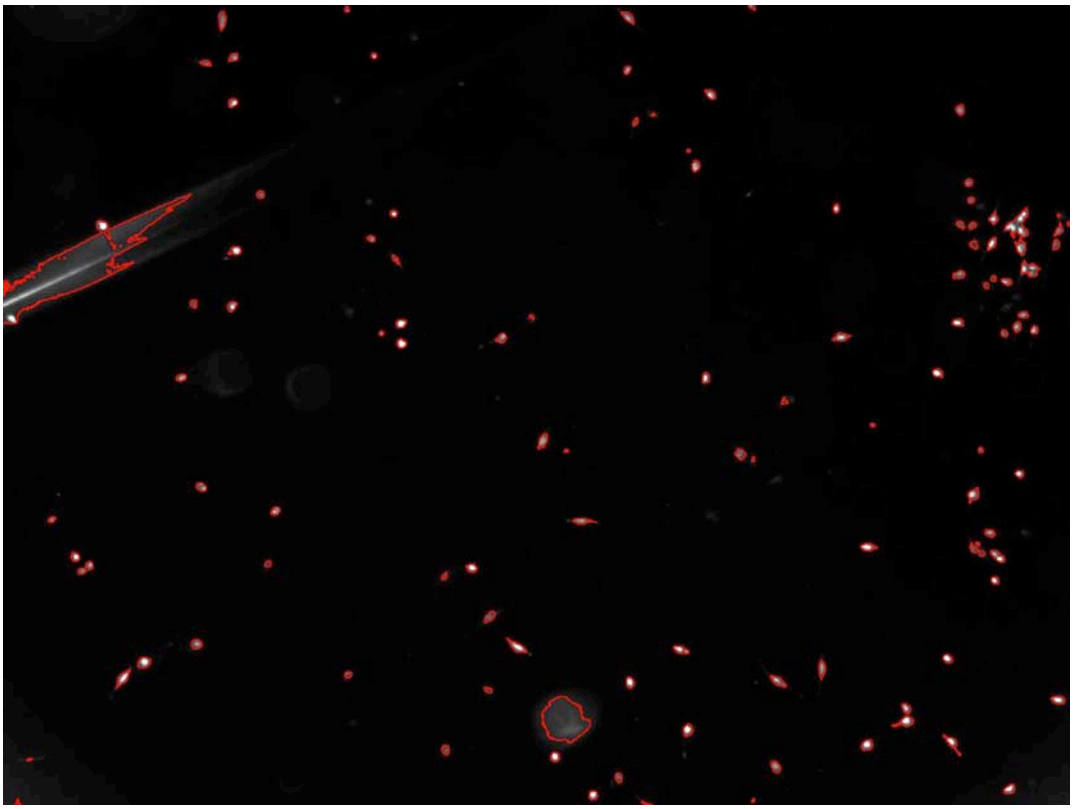

e)

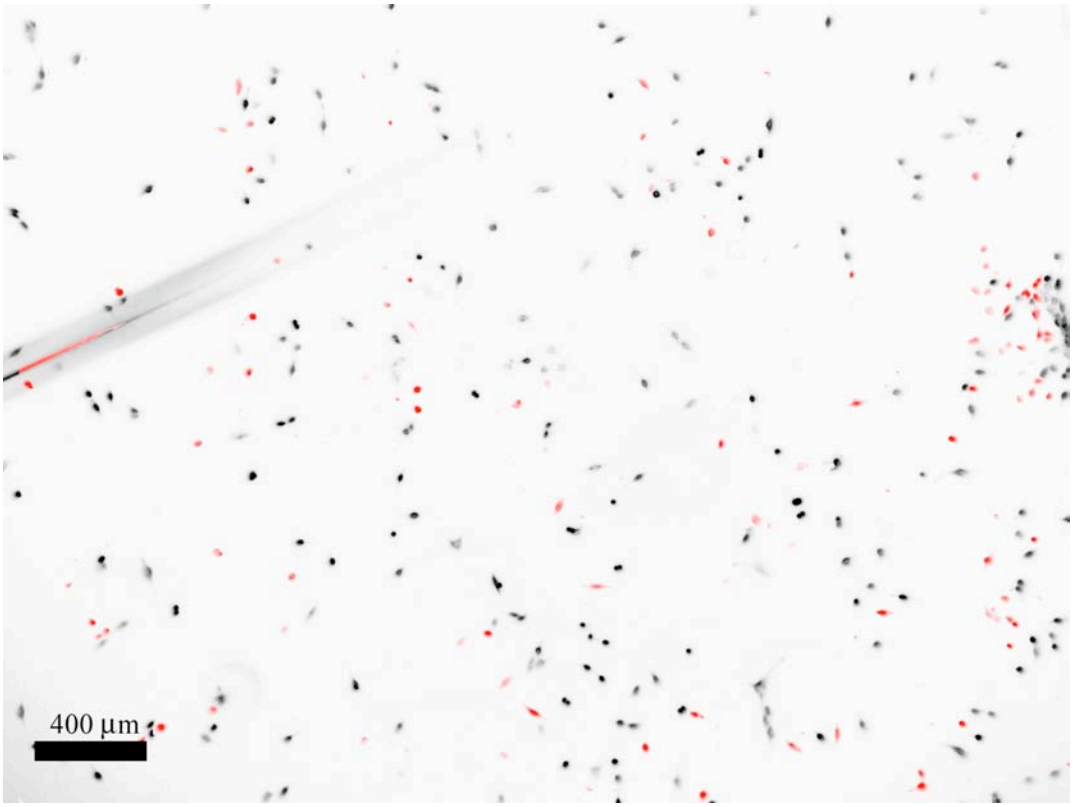

Figure S3.1: a) Phase contrast image of NRK fibroblasts in SATO medium, cultured for 24 hours, before the addition of nanocrystals. b) Same image with the N_A=198 counted cells (marked in the image) that have been detected by the image analysis software. c) Phase contrast image of NRK fibroblasts after 48 hours of incubation in 50 nM MPA coated CdSe/ZnS nanocrystals wavelength of the absorption peak of the CdSe core □ = 508 nm, corresponding to a CdSe core diameter of d = 2.4 nm; 61 Cd surface atoms per nanoparticle) in SATO medium. This image shows the same area of the cell culture substrate as shown in a) and b). The area could be identified by the scratch in the surface. d) Same image with N_B=108 cells counted by the image analysis software (marked in the image). e) Overlay of image a) (black) and c) (red). This image compares the adherent cells before (a) and after (c) incubation with the nanocrystals. Note that a lot of cells detached from the surface upon incubation with the nanocrystals, while the still adherent cells moved during the 48 hours incubation time in SATO medium. They show a spindle-like shape and viability tests indicate that these cells are alive. The situation is typical for the intoxication of the NRK fibroblasts in serum free medium and for a low concentration of cadmium. The value $R = \frac{N_B}{N_A}$ is taken for the same concentration from in total 94 positions (pictures). The averaged value is plotted in the diagrams R vs. concentration as one data point including the standard deviation of R as error bar.

a)

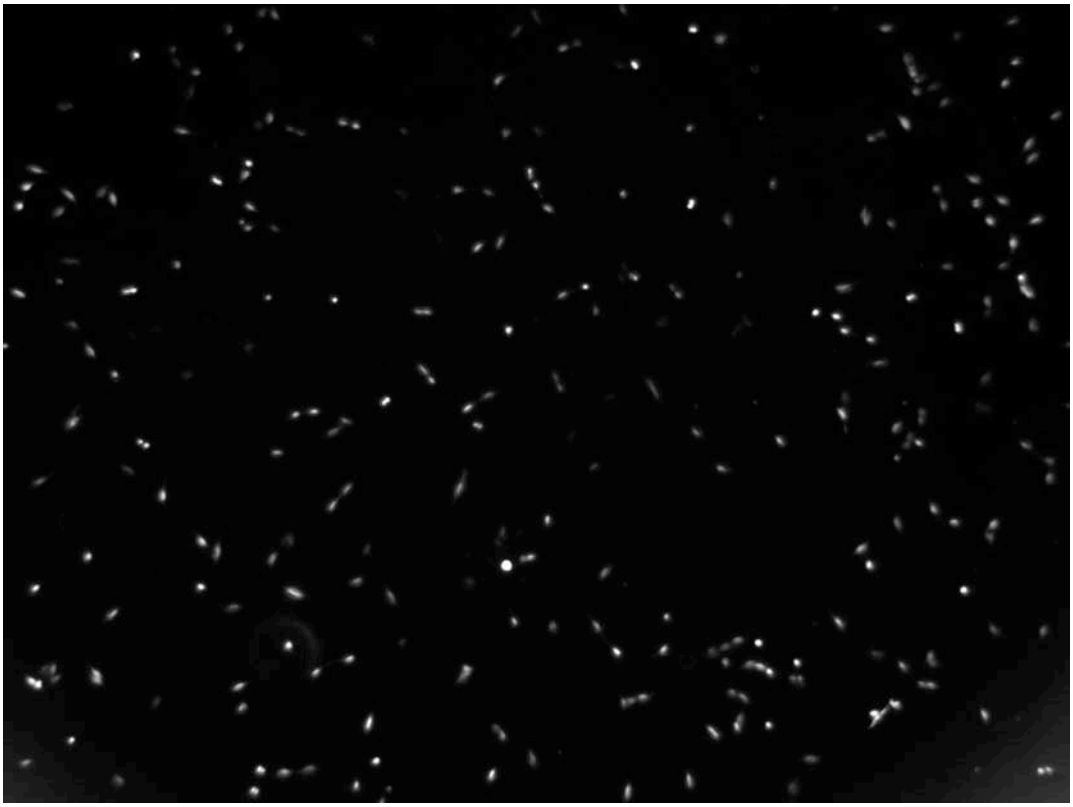

b)

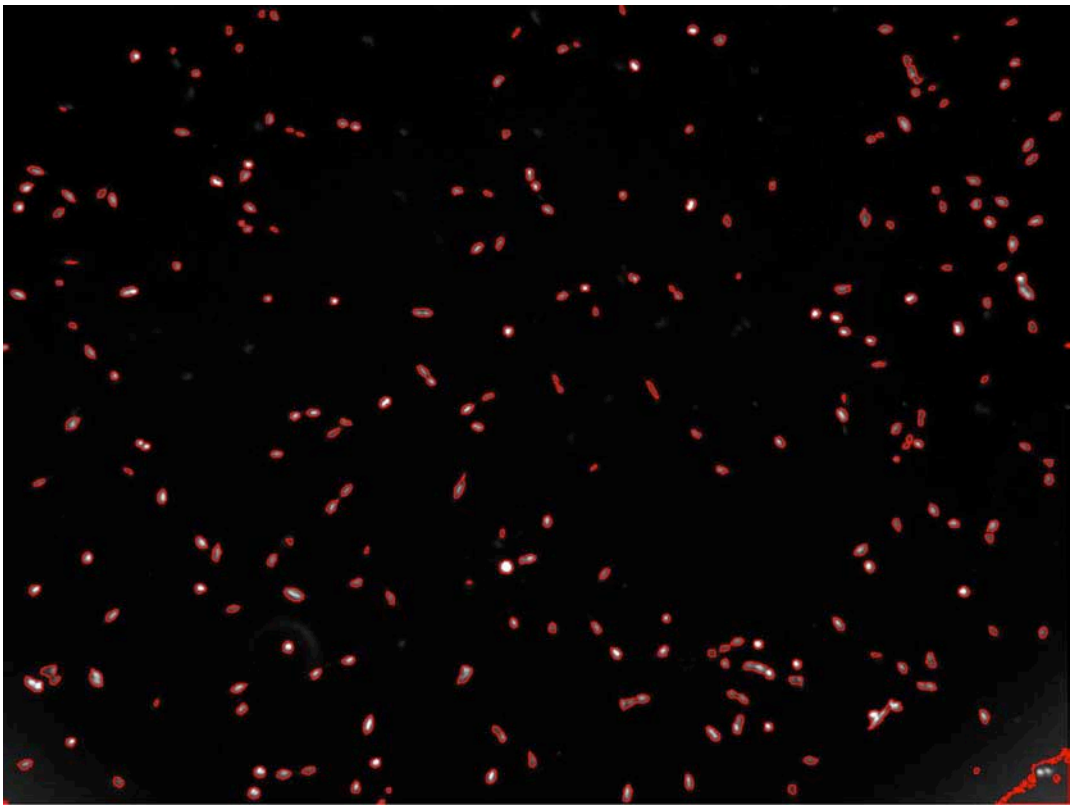

c)

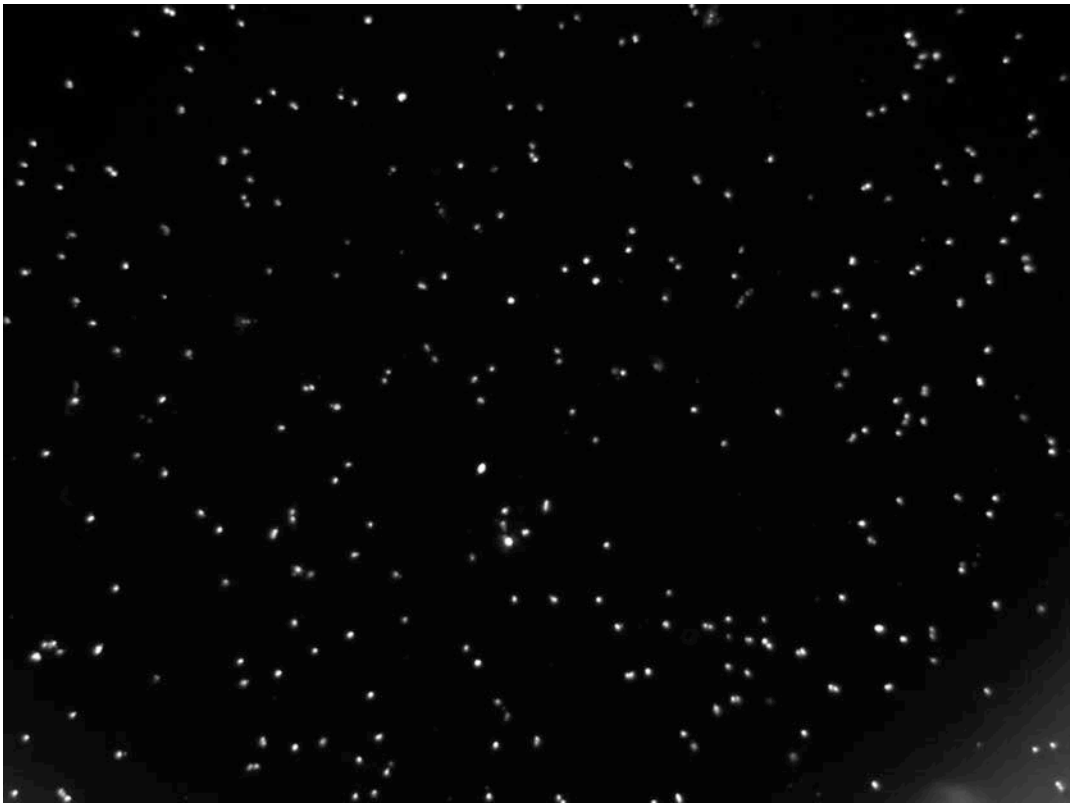

d)

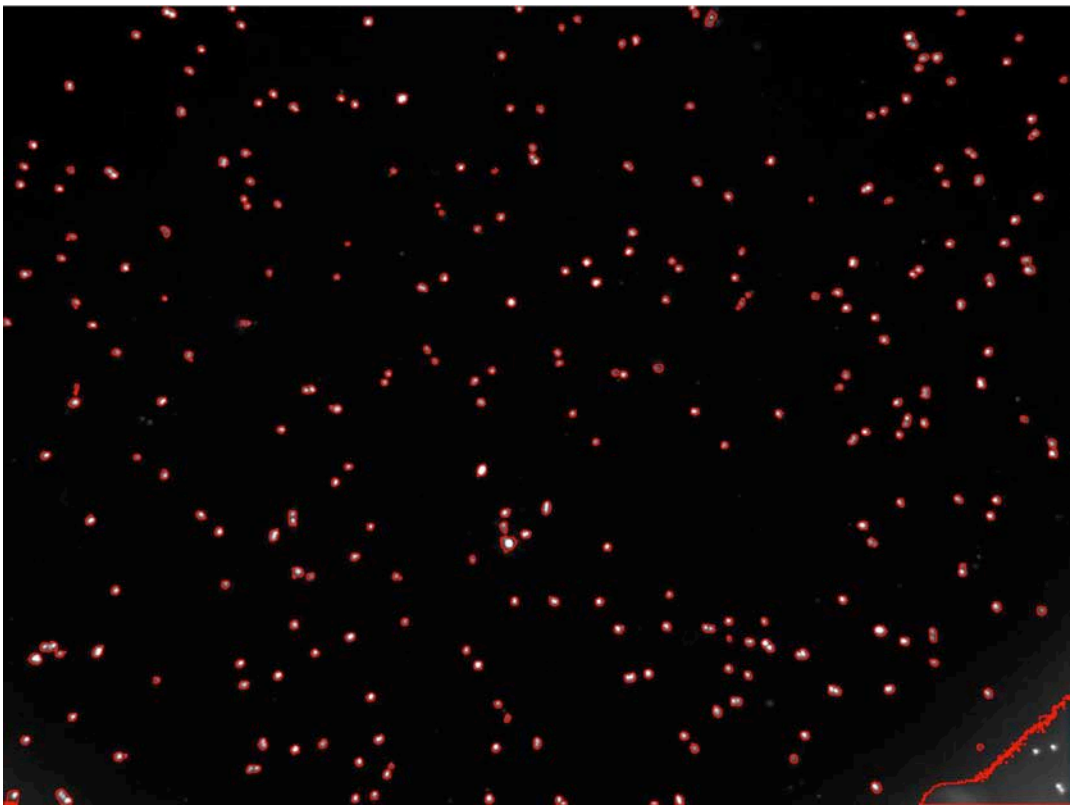

e)

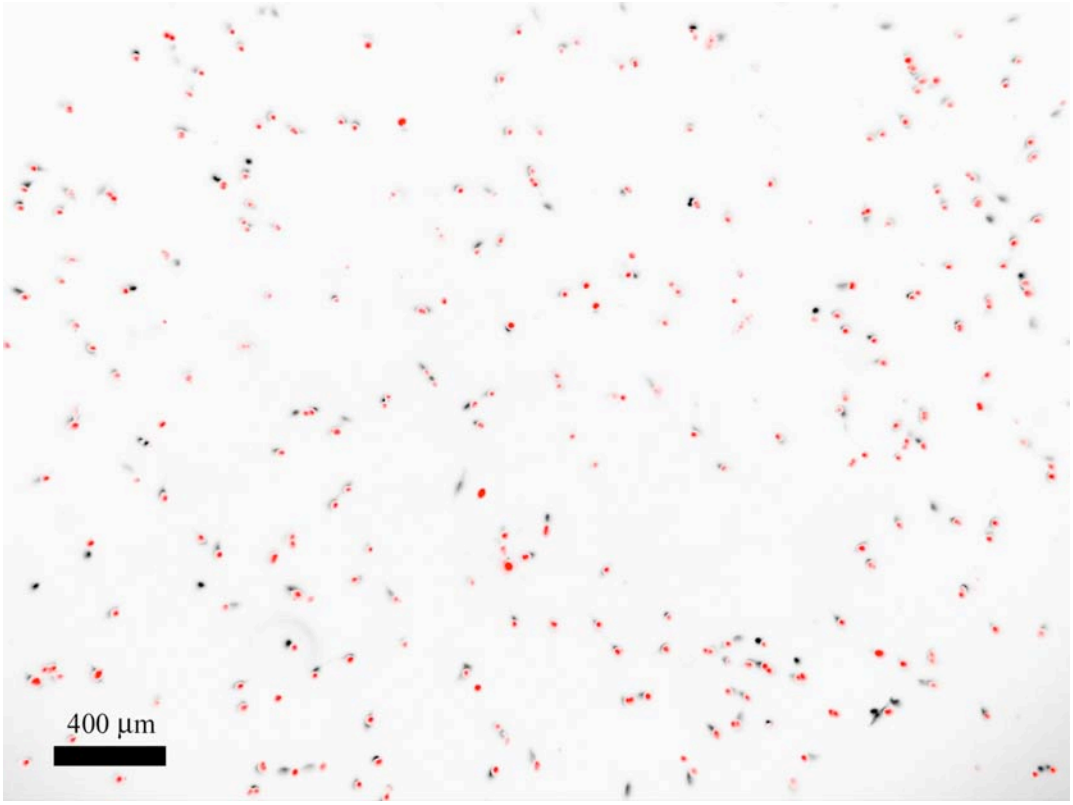

Figure S3.2: a) Phase contrast image of NRK fibroblasts in SATO medium, cultured for 24 hours, before the addition of nanocrystals. b) Same image with the N_A=228 counted cells (marked in the image) that have been detected by the image analysis software. c) Phase contrast image of NRK fibroblasts after 48 hours of incubation in 325 nM MPA coated CdSe/ZnS nanocrystals wavelength of the absorption peak of the CdSe core □ = 508 nm, corresponding to a CdSe core diameter of d = 2.4 nm; 61 Cd surface atoms per nanoparticle) in SATO medium. This image shows the same area of the cell culture substrate as shown in a) and b). d) Same image with N_B=225 cells counted by the image analysis software (marked in the image). e) Overlay of image a) (black) and c) (red). This image compares the adherent cells before (a) and after (c) incubation with the nanocrystals. Note that almost no cells detached from the surface upon incubation with nanocrystals. Adherent cells did not move on the substrate during the 48 hours incubation in the SATO medium. They show a sphere-like shape and viability tests indicate that the cells are dead. The situation is typical for intoxication of the NRK fibroblasts in serum free medium at high concentration of cadmium. In general, non-adherent cells and dirt were suppressed by rinsing with PBS buffer prior to image capturing. The value $R = \frac{N_B}{N_A}$ is taken for the same concentration from in total 94 positions (pictures). The averaged value is plotted in the diagrams R vs. concentration as one data point including the standard deviation of R as error bar.

Hydrophobic glass cover slides

A solution of 10 mM octadecyltrichlorosilane (OTS) in hexadecane was used to functionalize the surface of glass cover slides by dip coating for one hour. Finally the slides were rinsed with hexadecane, hexane and chloroform. The resulting surface showed advancing contact angles of approx. 92° for water.

Fluorescence microscopy to image the nanocrystals ingested by individual cells

Fluorescence microscopy was performed on an inverted microscope (Axiovert 200 from Carl Zeiss) with a Carl Zeiss FluoArc system, using a mercury lamp HBO 100. The filters for the fluorescence detection of the nanocrystals were the Q-dot TM 500 LP from AHF, Germany, as well as the filter sets 15 and 49 from Carl Zeiss.

Viability test

The Viability Kit L3224 from Molecular Probes was applied to distinguish between living and dead cells. Esterase activity of living cells converts non-fluorescent calcein-AM to intensely green fluorescent calcein. The second agent of this kit, Ethidium homodimer-1, enters defect cell membranes of dead cells and shows a 40-fold enhanced red fluorescence when it binds to nucleic acids of the cytoplasm. Following the manufacturers instructions for this test, cells were rinsed thoroughly with PBS buffer and a 4 µM solution of the agents was applied for 45 min. The filter set 00 from Carl Zeiss was used to watch the red fluorescence, while a 31001 filter from Chroma was used for the green fluorescence. In Figure S4 an example of this viability test is shown.

Similar viability tests have been used by other groups to determine cytotoxic effects of Cd ions, and CdSe and CdSe/ZnS particles [11-13]. These tests are based on measuring metabolic activity of cells or on the staining of dead cells, and are from this point conceptually different from our experiments in which cell survival was measured in terms of cell adherence.

a)

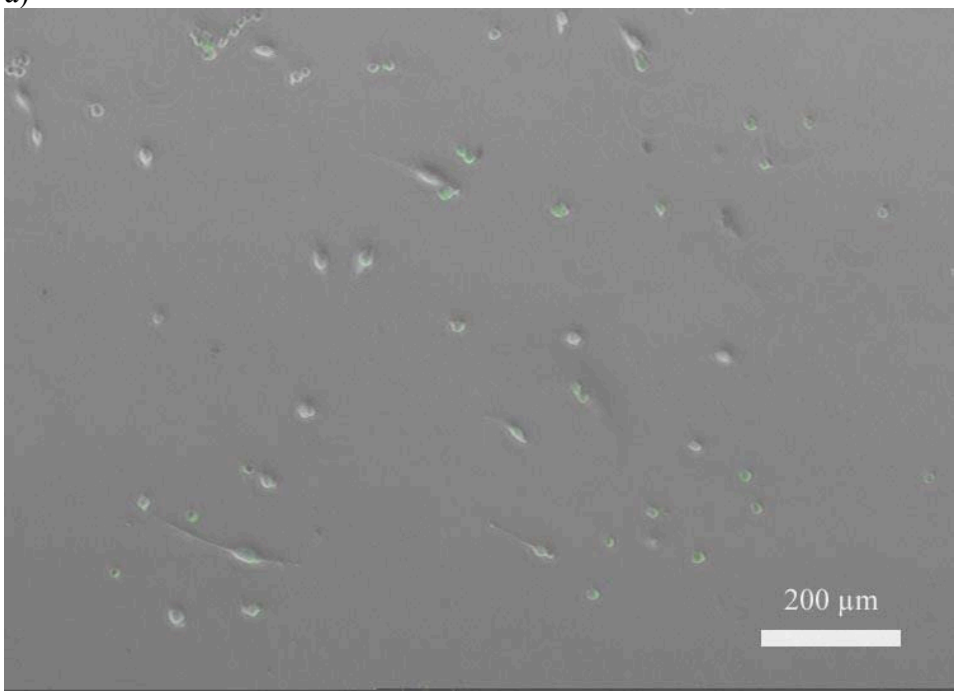

b)

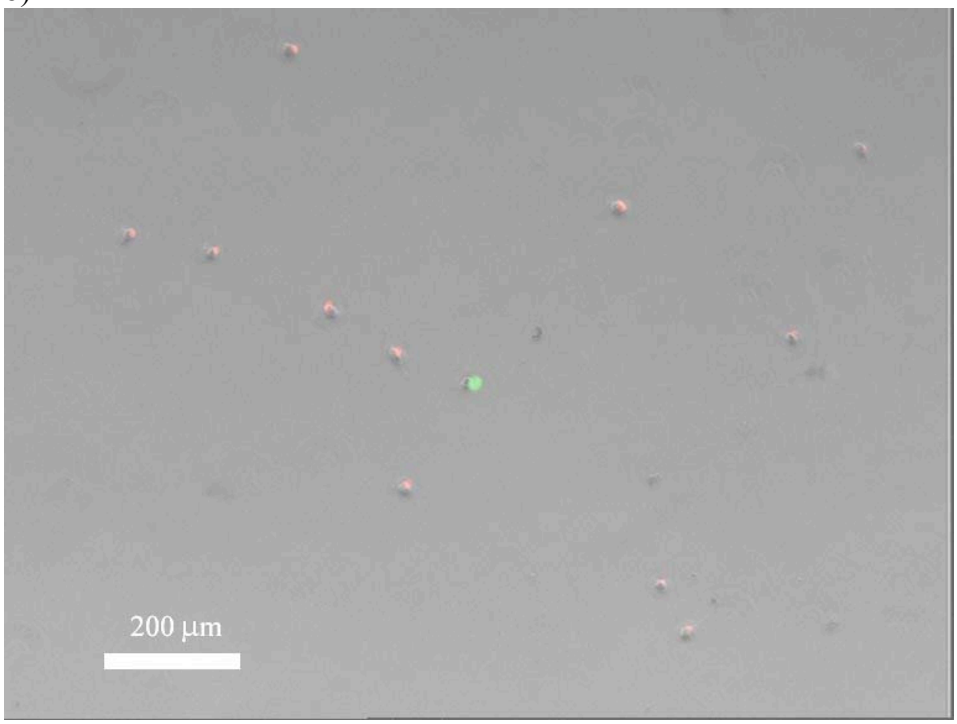

Figure S4: NRK fibroblasts were cultivated for 24 hours in DMEM cell medium with serum. After this incubation they were rinsed with PBS buffer. Further culture was performed in serum free SATO medium containing cadmium perchlorate hydrate as cadmium source. The viability test was applied. Pictures show an overlay of the phase contrast image and the images of green and red fluorescence. a) NRK fibroblasts after incubation in 0.1 □M cadmium perchlorate hydrate. All adherent cells are marked as living (green color) and show a spindle like shape. b) NRK fibroblasts after incubation in 5 □M of cadmium perchlorate hydrate. Almost all adherent cells are marked as dead (red color) and show a spherical shape.

(V) Patch clamp experiments

To further evaluate the biocompatibility of nanocrystals we conducted electrophysiological studies of cells incubated with nanocrystals using the planar patch clamp technique [14]. Two cell lines (RBL and CHO) were investigated in regard to changes in their morphology and their electrophysiological properties upon incubation with nanocrystals. The CHO cell line was stably transfected to express the hERG channel and the RBL cell line used endogenously expresses an inward rectifying potassium channel.

All cells were grown to 60-80% confluence in their standard serum-supplemented medium as described in the ATCC catalogue. The cells were incubated with nanocrystals at the desired concentration in their normal growth medium at 37 degrees Celsius and 5% CO_2 (several hours up to 2 days). After the incubation period, cells were isolated with a brief trypsin treatment. The resulting cell suspension was centrifuged twice at 1000 U/min for 2 minutes and the supernatant was pipetted off to remove cell fragments and debris. For resuspension the electrophysiological recording solutions were used. The cleaned cell suspension had a cell concentration of about one million cells per milliliter. Cells were examined with a confocal laser microscope to validate the quantum dot uptake by fluorescence measurements.

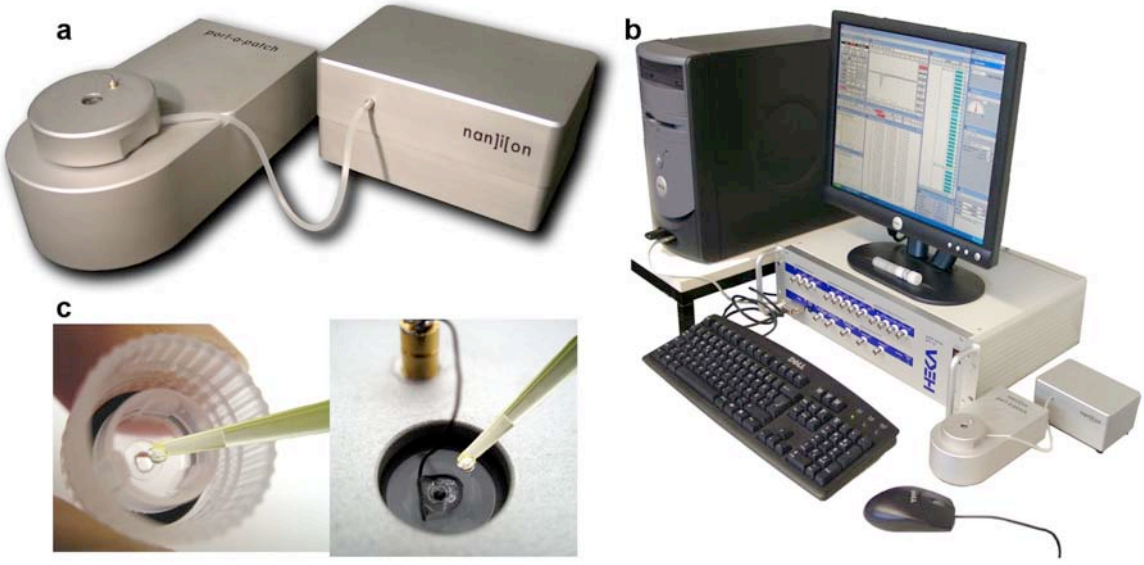

Figure S5: The Port-a-Patch electrophysiology workstation. In a) the chip mounting station and the software steered suction control unit are shown. The full Port-a-Patch system including amplifier and PC is depicted in b) and c) displays the micro structured borosilicate glass chips, which are glued onto small twist caps. The caps contain an O-ring and are screwed onto the holder in the chip mounting station to obtain an airtight arrangement for suction application. Electrolyte solutions and cell suspension is pipetted onto the backside and top of the chip with standard pipettes as shown. The solutions are electrically contacted via Ag/AgCl electrodes, which are implemented in the system.

Electrophysiological characterization and evaluation of cell function/viability of the cells ion channels were performed by whole cell recordings [15]. All measurement have been performed with the chip-based patch clamp technique [14] using the Port-a-Patch system by Nanion Technologies (www.nanion.de) [16]. The system uses micro structured borosilicate glass chips for whole cell patch clamp assays in an automated format. The Port-a-Patch was used in conjunction with an EPC-10 patch clamp amplifier (HEKA, Lambrecht, Germany) and is shown in Figure S5.

Cells were positioned and sealed on a micron-sized aperture in the glass chips by feedback controlled suction application. Brief suction pulses were applied to rupture the cells membrane across the aperture to obtain access to the cells interior, e.g. getting into the whole cell configuration. In the whole cell configuration, the current through the complete ensemble of all ion channels in the cell membrane is recorded, allowing the investigation of the ionic current conducted by the entire cell.

The chips for the recordings had an open aperture resistance of 2-3 MΩ. The recorded data were filtered at 3 kHz and sampled at 10 kHz. The electrophysiological recording solutions had the following ionic compositions (mM): extracellular (top of chip): NaCl (140), KCl (3), $MgCl_2$ (1), $CaCl_2$ (1), HEPES (10), pH = 7.4, 270 mOsm; intracellular (underside of chip): for RBL cells: K-Aspartate (120), EGTA (10), HEPES (10), NaCl (10), pH=7.2; for CHO cells: KCl (120), NaCl (10), EGTA (10), Hepes (10), pH = 7,2. About 5 µl of cell suspension were pipetted onto the chip and standard suction protocols of the Port-a-Patch system were applied for cell positioning and achieving tight seal whole cell configurations. Standard voltage protocols were applied for the recordings of ionic currents.

After the electrophysiological characterization, the patch clamped cell on the aperture was examined with the confocal microscope to evaluate the fluorescence of nanocrystals inside the cell. In Figure S6, images of patch clamped cells on the chip are displayed, showing the fluorescence of the quantum dots inside the cell. Below the cell is the micron-sized aperture in the chip, which can be perceived as a small dot. The larger circle around aperture in the centre corresponds to the 3-D-microstructure in the chip. On the chip surface are more cells in the vicinity of the patch clamped cell and all show the characteristic fluorescence. By this procedure it was guaranteed, that all cells investigated had incorporated the nanocrystals.

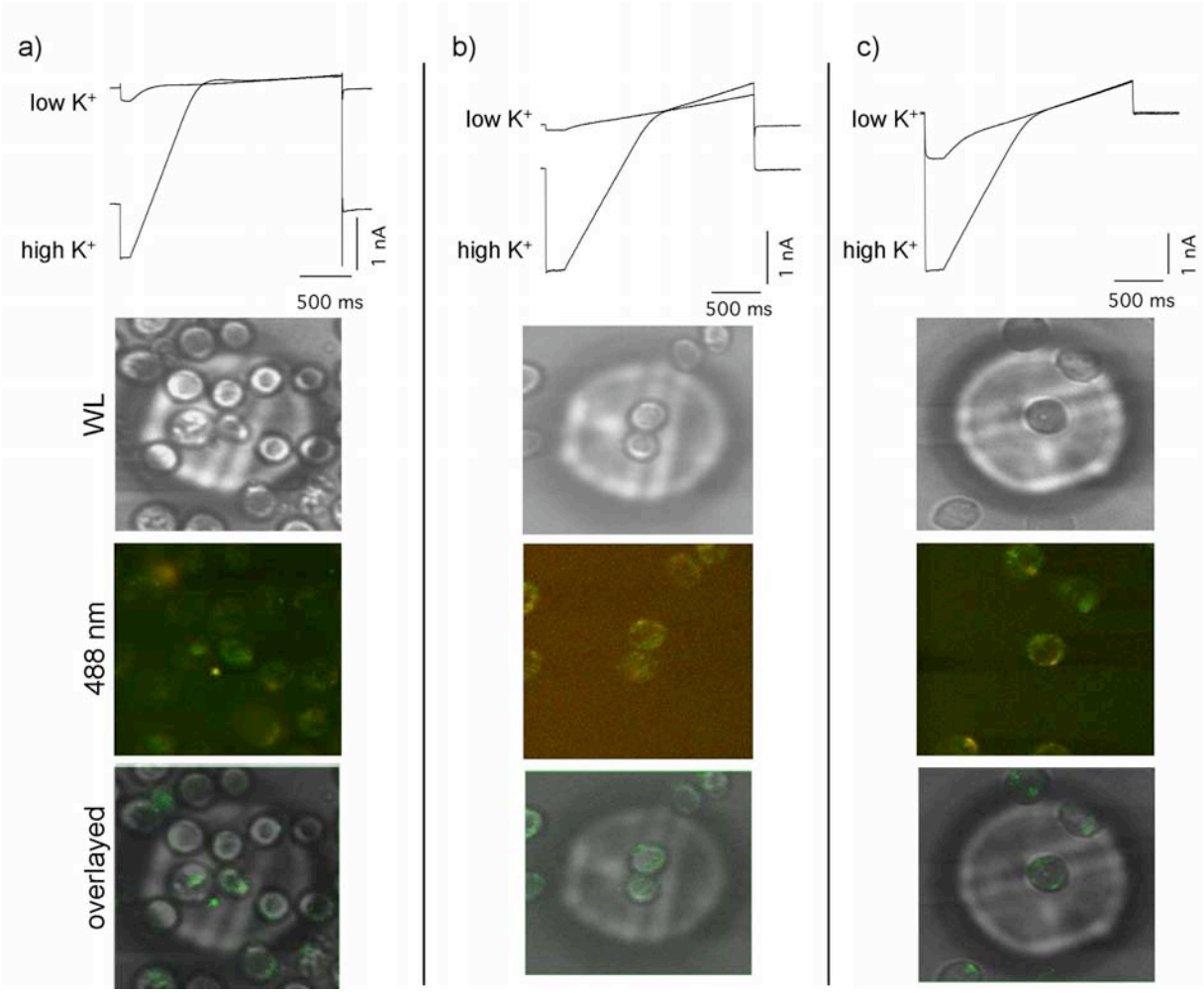

Figure S6: Electrical properties of RBL cells after 4 h incubation with MPA-coated CdSe/ZnS nanocrystals (wavelength of the absorption peak of the CdSe core = 508 nm, corresponding to a CdSe core diameter of d = 2.4 nm; 61 Cd surface atoms per nanoparticle). Top*:* Currents as obtained after incubation in 10 nM, 50 nM, and 100 nM CdSe/ZnS particles. Measurements were performed in two different external K^+ concentrations showing the characteristic inward rectifying current of the fully functional potassium channels. The current at the higher potassium concentration is larger due to the abundance of permeating ions. Bottom: Each picture shows a cell positioned on the hole in the glass chip as seen under white light (WL, bright field) and as fluorescence while excitation with 488 nm laser light. The images at the bottom show an overlay of the bright field and fluorescence pictures.

In addition the cell morphology before and after incubation of the cells was investigated by optical microscopy (Figures S7, S8). No changes in cell morphology could be detected at the used concentrations and incubation time. Incubation with nanocrystals was performed for 4 hours in serum-supplemented medium.

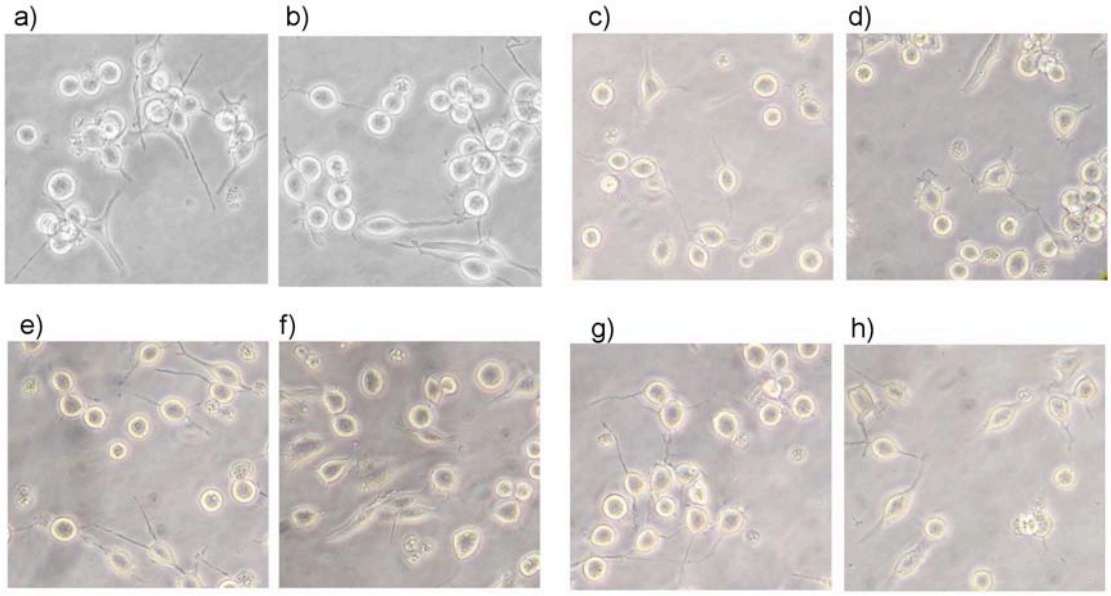

Figure S7: RBL cells before and after 3-4 h incubation with MPA-coated CdSe/ZnS nanocrystals (wavelength of the absorption peak of the CdSe core = 508 nm, corresponding to a CdSe core diameter of d = 2.4 nm; 61 Cd surface atoms per nanoparticle). The images show RBL cells before (a) and 3 h after (b) incubation in 5 nM CdSe/ZnS particles; RBL cells before (c) and 4 h after (d) incubation in 10 nM; before (e) and 4 h after (f) incubation in 50 nM; before (g) and 4 h after (h) incubation in 100 nM CdSe/ZnS particles.

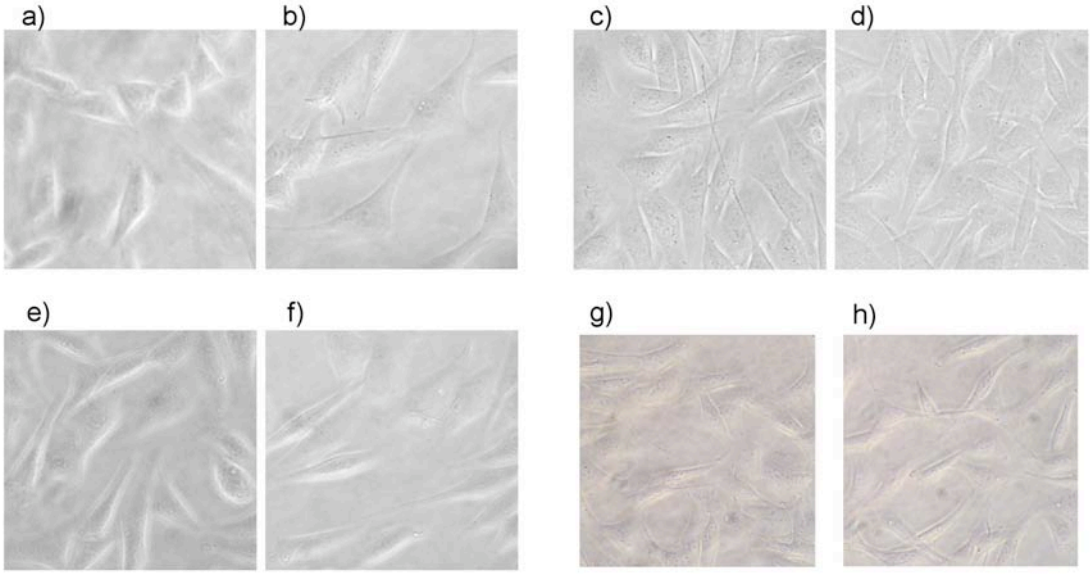

Figure S8: CHO cells expressing hERG before and after incubation with MPA-coated CdSe/ZnS nanocrystals. The images show cells before (a) and 3 h after (b) incubation in 5 nM nanocrystals (wavelength of the absorption peak of the CdSe core = 508 nm, corresponding to a CdSe core diameter of d = 2.4 nm; 61 Cd surface atoms per nanoparticle); before (c) and 3 h after (d) incubation in 5 nM nanocrystals (wavelength of the absorption peak of the CdSe core = 547 nm, corresponding to a CdSe core diameter of d = 3.0 nm; 92 Cd surface atoms per nanoparticle); before (e) and 3 h after (f) incubation in 200 nM nanocrystals (wavelength of the absorption peak of the CdSe core = 547 nm, corresponding to a CdSe core diameter of d = 3.0 nm; 92 Cd surface atoms per nanoparticle); before (g) and 10 h after (h) incubation in 200 nM (wavelength of the absorption peak of the CdSe core = 547 nm, corresponding to a CdSe core diameter of d = 3.0 nm; 92 Cd surface atoms per nanoparticle).

(VI) References

(1) Pellegrino, T.; Manna, L.; Kudera, S.; Liedl, T.; Koktysh, D.; Rogach, A. L.; Keller, S.; Rädler, J.; Natile, G.; Parak, W. J. *Nanoletters* **2004**, *4*, 703-707.
(2) Gerion, D.; Pinaud, F.; Williams, S. C.; Parak, W. J.; Zanchet, D.; Weiss, S.; Alivisatos, A. P. *J. Phys. Chem. B* **2001**, *105*, 8861-8871.
(3) Parak, W. J.; Gerion, D.; Zanchet, D.; Woerz, A. S.; Pellegrino, T.; Micheel, C.; Williams, S. C.; Seitz, M.; Bruehl, R. E.; Bryant, Z.; Bustamante, C.; Bertozzi, C. R.; Alivisatos, A. P. *Chem. Mat.* **2002**, *14*, 2113-2119.
(4) Fink, J.; Kiely, C. J.; Bethell, D.; Schiffrin, D. J. *Chem. Mat.* **1998**, *10*, 922-926.
(5) Kiely, C. J.; Fink, J.; Zheng, J. G.; Brust, M.; Bethell, D.; Schiffrin, D. J. *Adv. Mater.* **2000**, *12*, 640-643.
(6) Templeton, A. C.; Wuelfing, W. P.; Murray, R. W. *Accounts Chem. Res.* **2000**, *33*, 27-36.
(7) Leff, D. V.; O'Hara, P. C.; Heath, J. R.; Gelbart, W. M. *The Journal of Physical Chemistry* **1995**, *99*, 7036-7041.
(8) Mayya, K. S.; Caruso, F. *Langmuir* **2003**, *19*, 6987-6993.
(9) Scher, E. C.; Manna, L.; Alivisatos, A. P. *Phil. Trans. R. Soc. Lond. A* **2002**, *361*, 241-257.
(10) Yu, W. W.; Qu, L.; Guo, W.; Peng, X. *Chem. Mat.* **2003**, *15*, 2854-2860.
(11) López, E.; Figueroa, S.; Oset-Gasque, M. J.; Gonzalez, M. P. *Br. J. Pharmacol.* **2003**, *138*, 901-911.
(12) Derfus, A. M.; Chan, W. C. W.; Bhatia, S. N. *NanoLetters* **2004**, *4*, 11-18.
(13) Shiohara, A.; Hoshino, A.; Hanaki, K.; Suzuki, K.; Yamamoto, K. *MICROBIOLOGY AND IMMUNOLOGY* **2004**, *48*, 669-675.
(14) Fertig, N.; Blick, R. H.; Behrends, J. C. *Biophys. J.* **2002**, *82*, 3056-3062.
(15) Hamill, O. P.; Marty, A.; Neher, E.; Sakman, B.; Sigworth, F. J. *Pflügers Arch.* **1981**, *391*, 85 - 100.
(16) Brueggemann, A.; George, M.; Klau, M.; Beckler, M.; Steindl, J.; Behrends, J. C.; Fertig, N. *Current Drug Discovery Technologies* **2004**, *1*, 91-96.

K6

„Cytotoxicity of nanoparticle-loaded polymer hollow-capsules“

C.Kirchner, A. Munoz-Javier, A.S. Susha, A.L. Rogaj, O. Kreft, G.B. Sukhorukov, W.J. Parak, *Talanta*, vol. 67, Issue 3, pp. 486-491, 2005

Cytotoxicity of nanoparticle-loaded polymer hollow-capsules

C. Kirchner[1], Almudena Muñoz Javier[1], A. S. Susha[1], A. L. Rogach[1], O. Kreft[2], G. B. Sukhorukov[2], W. J. Parak[1,*]

[1]Physics Department and Center for Nanoscience (CeNS), Ludwig-Maximilians-Universität München, Amalienstrasse 54, 80799 München, Germany
[2]Max Planck Institute of Colloids and Interfaces, 14424 Potsdam/Golm, Germany

[*]To whom correspondence should be addressed: Dr. Wolfgang J. Parak
Email: Wolfgang.Parak@physik.uni-muenchen.de

Abstract

Cytotoxic effects of micrometer-sized polymer hollow capsules composed out of alternating layers of polystyrenesulfonate and polyallylamine hydrochloride on a fibroblast cell line are investigated with an adhesion assay. No cytotoxic effects are visible up to concentrations of 100 capsules per µl. For the purpose of visualization with fluorescence nanometer-sized CdTe nanoparticles have been embedded in the shells of the capsules. Similar to free mercaptoacetic acid stabilized CdTe nanoparticles also for capsules loaded with CdTe nanoparticles toxic Cd-ions are released from the CdTe particles. For the CdTe nanoparticle-loaded capsules cytotoxic effects are clearly visible at concentrations of 60 capsules per µl. By comparing this value with the critical concentration of 5.5 nM at which cytotoxic effects of free mercaptoacetic acid stabilized CdTe nanoparticles with 3 nm diameter start, we conclude that each of the capsules loaded with CdTe nanoparticles has $5.5 \cdot 10^7$ CdTe nanoparticles embedded in its shell.

Introduction

The aim of targeted drug delivery is to selectively deliver drugs to desired parts of a tissue and to release them locally at the target in a way that only the target tissue but not the surrounding tissue is affected by the effect of the drugs [1-3]. Many different drug carrier systems have already been developed and investigated. One of such concepts is to load drugs into the interior of hollow carriers such as lipid vesicles [4] or polymer hollow capsules [3,5]. In this way the drug is protected inside the carrier against degradation. Furthermore, the encapsulation of the drug inside a carrier prevents any effect of the drug outside the target tissue. Once the carrier system has reached the target tissue the carrier has to open and the drug is released. Recently we have suggested a concept for the practical realization of such a carrier system based on polymer hollow capsules [6].

Polymer hollow capsules can be formed by layer-by-layer assembly of charged polymers [7-9]. If for example a positively charged template sphere is introduced into a solution of negatively charged polymers the polymers will be electrostatically adsorbed onto the template surface. After removal of unbound excess polymer the now negatively charged sphere is dipped into a solution of positively charged polymers, which will be electrostatically adsorbed to the surface and thus give the sphere a positive charge. By iterating this process, i.e. successive dipping of the sphere in solutions with negatively and positively charged polymers, an onion-

like polyelectrolyte multilayer shell can be grown around the template sphere. The individual layers are glued together by electrostatic interaction. In this way also molecules others than polymers, as for example nanoparticles, can be introduced in the shell of the capsules. Nanoparticles of different materials with negative and positive charge can be adsorbed onto positively and negatively charged polymer layers, respectively [10-12]. By adsorption of additional layers of polymer the shell can be grown further, so that the nanoparticles are inside the shell. With the same procedure also charged biological molecules as proteins can be incorporated in the shell or on their surface [13]. In a final step the template sphere can be dissolved which results in a hollow polymer capsule [14]. The individual polymer layers of the capsule shell form a network whose pores can be expanded and shrunken by changing the pH of the surrounding medium [15-18]. In this way a drug can be loaded into the interior of the capsule by first expanding and then after addition of the drug shrinking the pores.

In particular, we have proposed a multifunctional system comprising polyelectrolyte multilayer hollow capsules in whose shells fluorescent, magnetic, and metallic nanoparticles are embedded, on whose surface proteins are adsorbed, and whose interior is loaded with drugs [6]. In our concept such loaded polymer capsules are administered by injecting them in the blood stream. A magnetic field gradient is then focused on the target tissue. Due to the magnetic particles incorporated in the capsule shells the capsules will be accumulated in the target tissue by trapping them in the magnetic field. Focusing of magnetic particles in magnetic field gradients has already been successfully demonstrated in animal experiments for so-called ferrofluids [19-25]. The proteins adsorbed to the capsule surface are chosen in a way that they specifically recognize receptors on the cell membranes of the target tissue [1,2,26,27], which results in specific receptor-ligand mediated uptake of the capsules by the cells. The whole process of the capsule uptake by the cells of the target tissue can be followed by the fluorescence of the fluorescent nanoparticles that are incorporated in the capsule shell. Once inside the cells the capsules are irradiated in the infrared at a wavelength that is barely adsorbed by the tissue, but which is adsorbed by the metallic particles embedded in the capsule shell. By adsorption of the infrared light the metallic particles are heated. We now can envisage two different strategies. By heating the metallic particles to a high degree the temperature increase will result in a burst of the capsules and finally to a destruction of the cell by heat [28,29]. This strategy is know as hyperthermia and has already been demonstrated by several groups [30-35]. On the other hand, by moderately heating of the capsules their shells could be ruptured in a controlled way, resulting in holes through which the drug loaded inside the capsules could be released [36]. We have to point out that the individual ideas are not new, but the novelty of our concept is the combination of several mechanisms in one single carrier system.

Of course the practical realization of our concept as a whole is still science fiction, although parts of it have already been successfully demonstrated. Fluorescent, magnetic, and metallic nanoparticles have been embedded in the shells of polymer hollow capsules [12], the interior of the capsules has been loaded with biological molecules [37], biological molecules adsorbed to the capsule surface have allowed for specific receptor-ligand interactions with surfaces [38], uptake of polymer capsules by living cells has been demonstrated [6], and the shells of capsules with embedded metal particles have been open upon irradiation in the infrared [6,36]. So far one important aspect has been neglected. If capsules are to be introduced as drug carrier systems into animals or human beings, first their biocompatibility has to be proven.

Capsules can be assembled out of most polyelectrolytes and therefore it is no problem to compose capsules out of biocompatible materials. Living cells can for example be embedded in shells of such polyelectrolytes [39,40]. However, although capsules can be composed out of

biocompatible and biodegenerable materials cells still might be affected by their uptake. In addition, the biocompatibility of nanoparticles incorporated in the capsules shells in order to render them functional can be problematic. Iron oxide based magnetic particles can be highly biocompatible [41], because iron oxide particles that have been incorporated by cells are eventually degraded to iron and oxygen, with are both natural compounds. However, cytotoxic effects of other magnetic particles have been observed [42]. Commonly used fluorescent nanoparticles are based on cadmium-containing materials as CdTe or CdSe. It has been reported that upon corrosion highly toxic cadmium ions are released from these particles, although embedding the particles in appropriate shells can hinder corrosion [43]. Another group has pointed out the influence of the surface chemistry of such particles on the cytotoxicity [44,45]. Even inert gold particles can be cytotoxic under certain conditions [46].

Recently we have developed a standard assay to investigate cytotoxic effects of nanoparticles on cell cultures [47]. In this report we applied this assay to investigate the cytotoxicity of polymer hollow capsules and of polymer hollow capsules loaded with fluorescent CdTe particles. As reference also the cytotoxicity of plain CdTe was investigated.

Materials and Methods

Mercaptoacetic acid stabilized fluorescent CdTe nanoparticles have been synthesized in aqueous solution following standard protocols [48]. In this work we used particles with an absorption wavelength of the first exciton at 530 nm. From this wavelength the mean diameter of the CdTe particles can be deduced to be 2.98 nm [49] and each CdTe particle exposes around 80 Cd atoms on its surface. Polymer hollow capsules of about 5 μm diameter have been composed out of about 10 alternating layers of polystyrenesulfonate (PSS) and polyallylamine hydrochloride (PAH) [12]. In part of the capsules fluorescent CdTe nanoparticles were incorporated [6,12]. CdTe nanoparticles, plain capsules and CdTe-labeled capsules were added to NRK normal rat kidney cells [6,47] and cytotoxic effect on the cells were detected using an adhesion assay [47]. For this assay cells were seeded on a glass substrate, imaged with an automated optical microscope, and the number of adherent cells was counted using an image processing software. After the counting procedure cells were kept in serum-free SATO medium and CdTe nanoparticles, plain capsules, or CdTe-labeled capsules were added at different concentrations. After 48 hours of incubation nonadherent cells were removed by rinsing and adherent cell were again imaged and counted by optical microscopy. An automated xy-stage of the microscope allowed for finding the same positions on the cell culture substrate, so that the number of adherent cells before and after incubation with particles could be counted at exactly the same region [47]. As result the ratio R(c) of adherent cells after and before incubation with particles with a concentration c was obtained. In addition, the viability of adherent cells before and after incubation with particles was measured with a commercial kit (L3224, Molecular Probes) [47].

Results and Discussion

As well CdTe nanoparticles, as plain and CdTe-labeled capsules were ingested by the cells (Figure 1). The uptake of mercaptoacetic acid coated CdTe nanoparticles was found to be identical to the reported uptake of mercaptopropionic acid coated CdSe nanoparticles [47]. The uptake of the polymer capsules, although by another cell line, has already been reported previously [6].

In Figure 2 the results for the adherence assay of CdTe particles are shown. The curves show the same behavior as has been previously reported for CdSe particles. For low particle concentrations the R(c) value is constant, decreases and increases again at higher particle concentrations to finally reach a constant value for high concentrations [47]. The commercial viability test showed that all adherent cells at low particle concentrations were alive, whereas all adherent cells at very high particle concentrations were dead. This can be interpreted in the following way [47]. Even without addition of CdTe particles R(c=0) is smaller than 1, because culture in serum-free medium impairs the cellular development and after 48 hours culture in serum-free medium less adherent cells are present than before. However, serum-free medium had to be used in order to hinder cell proliferation so that the number of cells after and before incubation with particles could be directly compared. For low CdTe concentrations no additional effect besides the effect of the serum-free culture medium was observable and R(c) stayed constant. Upon further increasing the CdTe concentration R(c) decreased, i.e. the number of adherent cells decreased. CdTe particles release toxic Cd-ions [43], which lead to an impairment of parts of the cells within this concentration region. Poisoned cells slowly lost contact to the cell culture substrate, detached, and the number of adherent cells decreased. Cell adhesion is an active process and for this reason slow poisoning of the cells results in detachment from the surface. We have to point out that the commercial viability test showed that all adherent, and thus counted cells, were alive under these conditions. Further increase in the CdTe concentration resulted in an increase of R(c) until a final saturation. The commercial viability test showed that under these conditions all adherent cells were dead. This suggests that at high CdTe concentrations the number of released Cd-ions is sufficient enough to kill the cells very fast. Instead of slowly poisoning the cells, which leads to a slow detachment of the cells, at such high Cd concentrations cells are instantaneously killed and their debris remains on the cell culture substrate surface. These dead cells (= cell debris) are counted as adherent cells and therefore R(c) is increasing again. R(c) is even higher for very high CdTe particle concentrations compared to very low particle concentrations. At very high concentrations cells are instantaneously killed and most of them remain as fragments on the substrate, resulting in a high R(c) value. At low concentrations within 48 hours of incubation more and more cells get impaired by the effect of the serum-free culture medium (and the CdTe particles) resulting in a lower R(c) value. As reported previously, we have fitted the R(c) curves with a bi-sigmoidal function $R(c) = a_1 - a_2/(1 + \exp((a_3-c)/a_4)) + a_5/(1 + \exp(a_6-c)/a_7))$ with 7 fit parameters a_1 - a_7 [47]. The a_3 parameter of the function is a measure for onset of the decrease in the R(c) function and thus for the beginning of cytotoxic effects of the CdTe particles on the cells. In our study we found a_3 (CdTe particles) = 5.5 ± 0.6 nM, and thus this concentration of CdTe particles can be considered as critical concentration for the onset of cytotoxic effects. The use of the fitting procedure thus allows us to extract a quantitative threshold for the onset of cytotoxic effects from our data. Since for these particles cytotoxic effects are caused by the release of Cd-ions from the CdTe particle surface [43] we have converted the concentration of CdTe particles to the concentration of Cd-atoms lying on the surface of the CdTe particles [47]. For the CdTe particles af about 3 nm core diamter used here each particle had 80 Cd atoms on its surface. This results in a critical concentration of a_3 (Cd surface atoms) = 440 ± 50 nM. This is in good agreement with the value a_3 (Cd surface atoms) = 650 ± 120 nM found for CdSe particles in a previous study. We have to point out that the CdTe particles used in this study have been directly synthesized under the presence of mercaptoacetic acid in aqueous solution [48], whereas the CdSe particles used in the previous study [47] have been synthesized in organic solution and then have been transferred to aqueous solution by a ligand exchange procedure in which the original TOPO ligands were replaced by mercaptopropionic acid. This independence from the actual synthesis procedure suggests that for these particles the release of Cd-ions via corrosion of the particles and not any effect connected to the surface chemistry of the particles is relevant for the cytotoxic effects.

For plain polymer capsules the experimentally obtained R(c) curve has a completely different shape (Figure 3). R(c) is constant for low capsule concentrations c and starts to slightly decrease at higher concentrations. Viability assays using the commercial kit showed that for all concentrations all adherent cells were alive. For concentrations up to 100 capsules per µl no effects of the capsules on the cells are visible (Figure 3). Higher capsule concentrations yield to a slow impairment of the cell viability, which eventually results in cell detachment. Microscopy images showed a massive precipitation or sedimentation of capsules on the cell surface and on the cell culture substrate (Figure 4). It is likely that this sedimentation of capsules on the cells is responsible for the impairment of the cells. A similar effect has been observed for sedimentation of polymer-coated nanoparticles on cell surfaces in a previous study [47].

The embedding of CdTe particles in the shell of the polymer capsules lead to a R(c) curve similar to that of free CdTe particles (Figure 3). Application of the commercial viability test showed that adherent cells were alive for low capsule concentrations (before the dip in the R(c) curve) and dead for high capsule concentrations (after the dip in the R(c) curve), similar to the case of incubation of cells with free CdTe nanoparticles (Figure 2). These findings suggest that in the case of CdTe-loaded polymer capsules the release of Cd-ions from the CdTe particles is responsible for cytotoxic effects. The shell of the capsules in which the CdTe nanoparticles are embedded is permeable for ions and thus does not offer protection again the release of Cd-ions from the surface of the CdTe nanoparticles into solution. However, the CdTe particles are embedded inside the shell in a way that they cannot be released from there as a whole. We do not know how many CdTe nanoparticles are embedded in each capsules, but by comparing the critical concentrations a_3 for the cases of free CdTe particles and CdTe-labeled capsules we can derive an estimate for this number. Cytotoxic effects for CdTe-labeled capsules started at a_3 = 60 capsules per µl (Figure 3). This corresponds to a critical capsule concentration of $a_3 = 60$ capsules$\cdot\mu l^{-1}$ / $6\cdot10^{23}$ capsules$\cdot mol^{-1}$ = $1\cdot10^{-16}$ M. For free CdTe nanoparticles a critical particle concentration of $a_3 = 5.5\cdot10^{-9}$ M was found (Figure 2). Thus we can estimate that $5.5\cdot10^{-9}$ M / $1\cdot10^{-16}$ M = $5.5\cdot10^{7}$ CdTe nanoparticles (with a core diameter of 3 nm) are embedded in the shell of each capsule (with a diameter of 5 µm), assuming that the pathway of cytotoxic effects is the same in both cases.

In summary we have shown that polystyrenesulfonate / polyallylamine hydrochloride multilayer hollow capsules are relatively biocompatible. However, at high concentrations bigger than 100 capsules per µl the capsules start to sediment on top of the cells and thus impair cell viability. Nanoparticles of different materials can be embedded in the capsule shells to provide functionality. Since the capsule shells form a porous network of polyelectrolyte layers they are permeable for ions. Therefore, any toxic ions released due to corrosion from the nanoparticles embedded in the capsule shells can diffuse out of the capsules. For this reason the cytotoxicity of these nanoparticles has to be considered. For the simplest system of fluorescent nanoparticles, mercaptoacetic acid coated CdTe nanocrystals, cytotoxic effects are visible above a critical particle concentration of 5.5 nM. In this way capsules comprising CdTe nanoparticles exhibit higher toxic effects than plain capsules. For this reason the nanoparticle systems, which are to be embedded into the capsules, have to be chosen very carefully. Instead of mercaptoacetic acid-coated CdTe particles for example silica-coated CdSe/ZnS nanoparticles could be used, which are far less cytotoxic [47].

Acknowledgements

This project has been founded by the Volkswagen Foundation (ALR, GBS, WJP) and by the Emmy Noether program of the German Research Foundation DFG (WJP) and by the Fonds der Chemischen Industrie (WJP).

Figures

Figure 1: Overlay of phases contrast and fluorescence image of NRK normal rat kidney fibroblast cells with internalized capsules. Ingested capsules (fluorescence labeled with colloidal CdTe nanoparticles) are stored around the nuclei inside the cells. The used capsules have a polyelectrolyte polymer shell that is terminated with a positively charged polymer layer and then coated with negatively charged fluorescent CdTe nanocrystals. The capsule diameter is 5 μm. All experimental details can be found in a previous report [6].

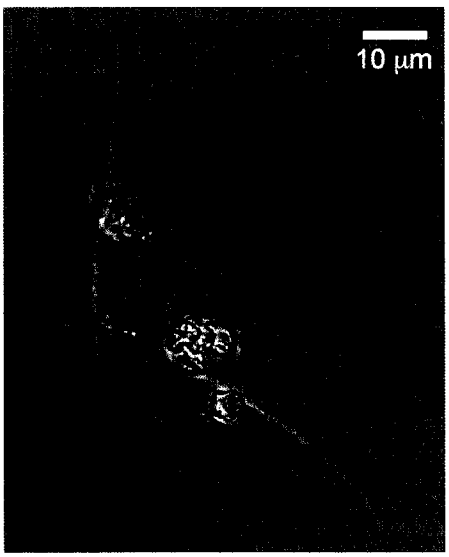

Figure 2: Ratio R(c) of adherent cells after and before incubation of NRK fibroblasts with mercaptoacetic acid stabilized CdTe particles dependent on the particle concentration c. Values are shown for 2 independent series of measurements. All experimental details have been published previously [47]. The data points of each series were fitted with the function $R(c) = a_1 - a_2/(1 + \exp((a_3-c)/a_4)) + a_5/(1 + \exp(a_6-c)/a_7))$. The a_3 parameter yielded from the fit described the onset of the decay in the R(c) curve and thus the critical concentration for the beginning of cytotoxic effects. The a_3 parameter of both fits were found to be 6.0 nM and 5.1 nM, which results in a mean value for the critical concentration of 5.5 ± 0.6 nM.

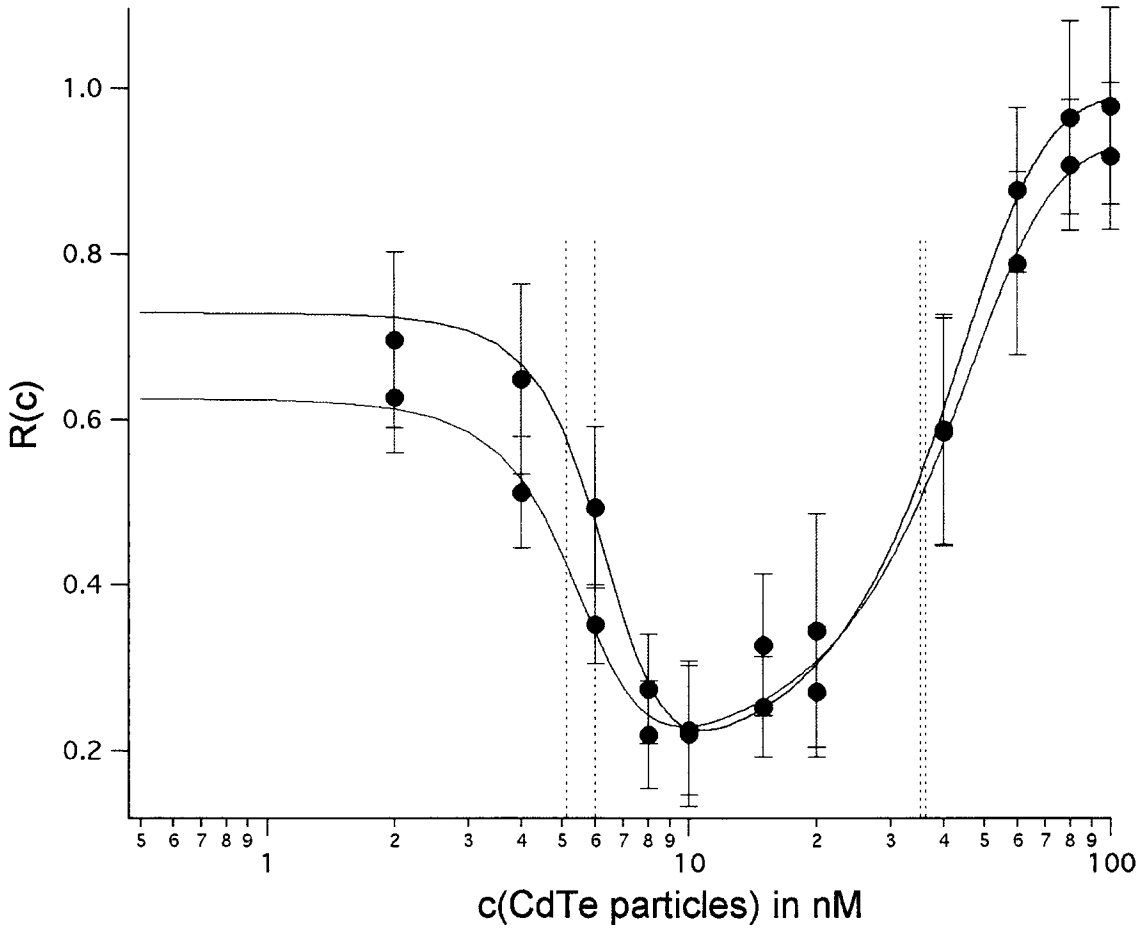

Figure 3: Ratio R(c) of adherent cells after and before incubation of NRK fibroblasts with plain (shown in blue) and CdTe-loaded (shown in red) polymer hollow capsules of 5 μm diameter in dependence of the capsule concentration c. The data points of the series using CdTe-loaded capsules were fitted with the function $R(c) = a_1 - a_2/(1 + \exp((a_3-c)/a_4)) + a_5/(1 + \exp(a_6-c)/a_7))$. The a_3 parameter of the fit was found to be $a_3 = 60$ capsules per μl. At this capsule concentration clear cytotoxic effect for the CdTe-labeled capsules can be seen, whereas for plain capsules no decrease in R(c) can seen at least until concentrations of 100 capsules per μl.

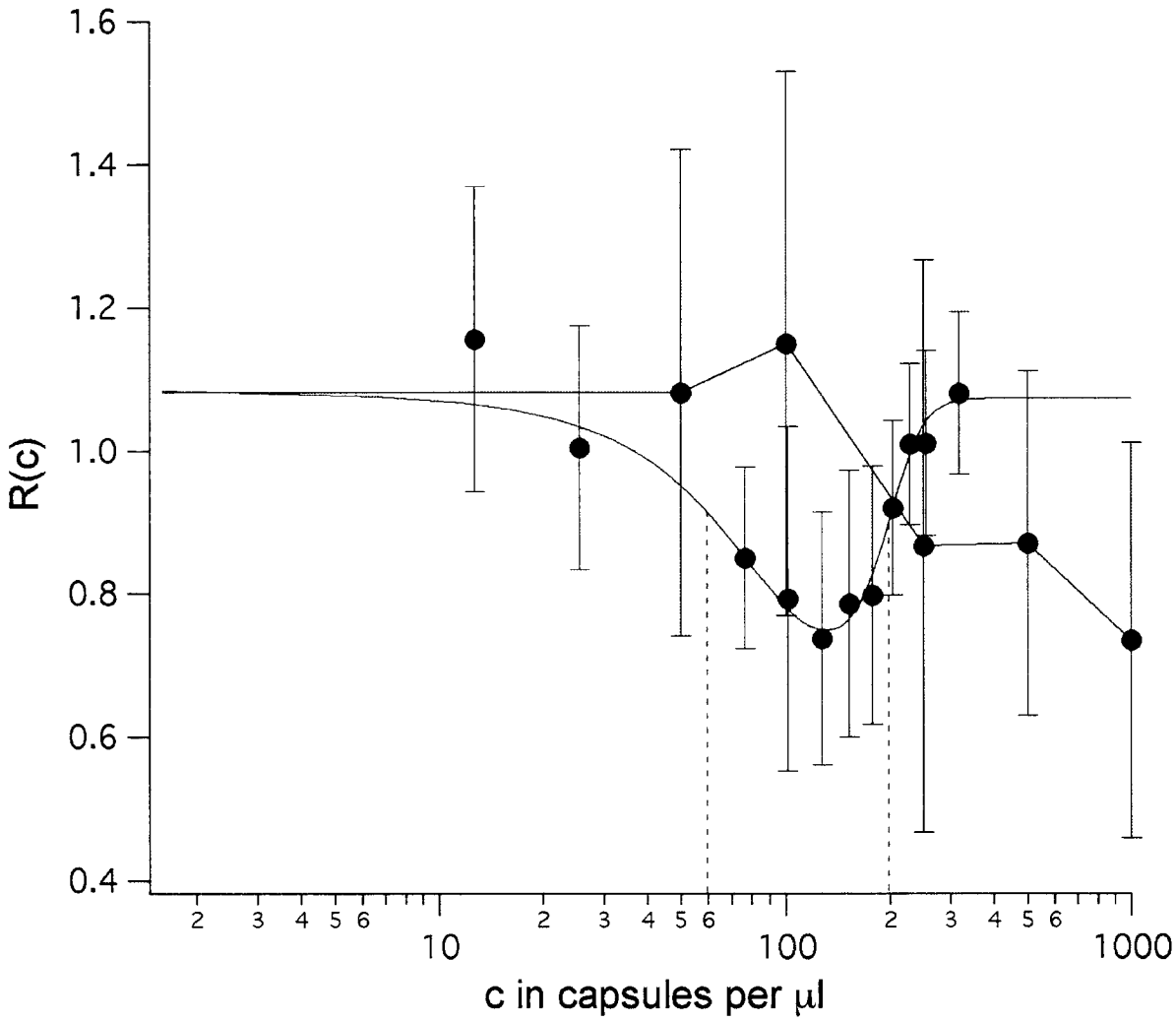

Figure 4: Phase contrast microscopy image of adherent NRK fibroblast to which plain 5 μm diameter polymer hollow capsules have been added at concentrations of 50 and 1000 capsules per μl. For high capsule concentrations massive sedimentation of capsules on the surface of the cells and the cell culture substrate is visible.

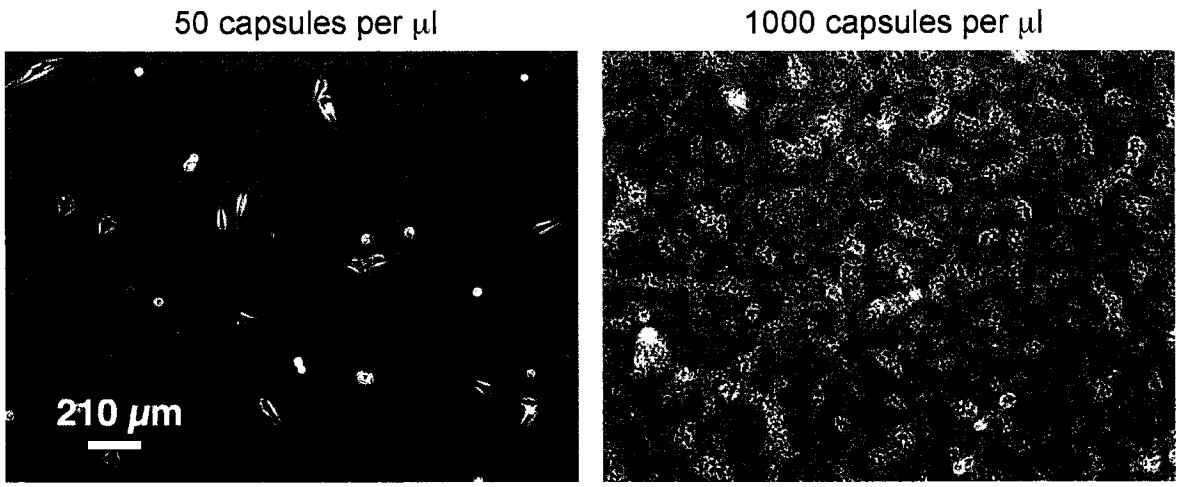

References

(1) Garnett, M. C. *Advanced Drug Delivery Reviews* **2001**, *53*, 171-216.
(2) Allen, T. M.; Cullis, P. R. *Science* **2004**, *303*, 1818-1822.
(3) Tu, R. S.; Tirrell, M. *Advanced Drug Delivery Reviews* **2004**, *56*, 1537-1563.
(4) Lukyanov, A. N.; Torchilin, V. P. *Advanced Drug Delivery Reviews* **2004**, *56*, 1273-1289.
(5) Lavasanifar, A.; Samuel, J.; Kwon, G. S. *Advanced Drug Delivery Reviews* **2002**, *54*, 169-190.
(6) Sukhorukov, G. B.; Rogach, A. L.; Zebli, B.; Liedl, T.; Skirtach, A. G.; Köhler, K.; Antipov, A. A.; Gaponik, N.; Susha, A. S.; Winterhalter, M.; Parak, W. J. *Small* **2005**, *in press*.
(7) Donath, E.; Sukhorukov, G. B.; Caruso, F.; Davis, S. A.; Möhwald, H. *Angewandte Chemie International Edition* **1998**, *37*, 2201-2205.
(8) Sukhorukov, G. B.; Donath, E.; Davis, S.; Lichtenfeld, H.; Caruso, F.; Popov, V. I.; Möhwald, H. *Polymers for Advanced Technologies* **1998**, *9*, 759-767.
(9) Shchukin, D. G.; Sukhorukov, G. B.; Möhwald, H. *Angew. Chem.-Int. Edit.* **2003**, *42*, 4472-4475.
(10) Shchukin, D. G.; Radtchenko, I. L.; Sukhorukov, G. B. *MATERIALS LETTERS* **2003**, *57*, 1743-1747.
(11) Gaponik, N.; Radtchenko, I. L.; Gerstenberger, M. R.; Fedutik, Y. A.; Sukhorukov, G. B.; Rogach, A. L. *Nano Letters* **2003**, *3*, 369-372.
(12) Gaponik, N.; Radtchenko, I. L.; Sukhorukov, G. B.; Rogach, A. L. *Langmuir* **2004**, *20*, 1449-1452.
(13) Volodkin, D. V.; Petrov, A. I.; Prevot, M.; Sukhorukov, G. B. *Langmuir* **2004**, *20*, 3398-3406.
(14) Antipov, A. A.; Shchukin, D.; Fedutik, Y.; Petrov, A. I.; Sukhorukov, G. B.; Möhwald, H. *Colloid Surf. A-Physicochem. Eng. Asp.* **2003**, *224*, 175-183.
(15) Antipov, A. A.; Sukhorukov, G. B.; Leporatti, S.; Radtchenko, I. L.; Donath, E.; Möhwald, H. *Colloid Surf. A-Physicochem. Eng. Asp.* **2002**, *198*, 535-541.
(16) Dejugnat, C.; Sukhorukov, G. B. *Langmuir* **2004**, *20*, 7265-7269.
(17) Sukhorukov, G. B.; Fery, A.; Brumen, M.; Möhwald, H. *PCCP Phys. Chem. Chem. Phys.* **2004**, *6*, 4078-4089.
(18) Mauser, T.; Dejugnat, C.; Sukhorukov, G. B. *MACROMOLECULAR RAPID COMMUNICATIONS* **2004**, *25*, 1781-1785.
(19) Häfeli, U. O. *INTERNATIONAL JOURNAL OF PHARMACEUTICS* **2004**, *277*, 19-24.
(20) Alexiou, C.; Arnold, W.; Klein, R. J.; Parak, F. G.; Hulin, P.; Bergemann, C.; Erhardt, W.; Wagenpfeil, S.; Lübbe, A. S. *Cancer Research* **2000**, *60*, 6641-6648.
(21) Alexiou, C.; Arnold, W.; Hulin, P.; Klein, R. J.; Renz, H.; Parak, F. G.; Bergemann, C.; Lübbe, A. S. *Journal of Magnetism and Magnetic Materials* **2001**, *225*, 187-193.
(22) Alexiou, C.; Jurgons, R.; Schmid, R. J.; Bergemann, C.; Henke, J.; Erhardt, W.; Huenges, E.; Parak, F. *JOURNAL OF DRUG TARGETING* **2003**, *11*, 139-149.
(23) Lübbe, A. S.; Alexiou, C.; Bergemann, C. *Journal of Surgical Research* **2001**, *95*, 200-206.

(24) Lübbe, A. S.; Bergemann, C.; Brock, J.; McClure, D. J. *Journal of Magnetism and Magnetic Materials* **1999**, *194*, 149-155.
(25) Babincova, M.; Altanerova, V.; Lampert, M.; Altaner, C.; Machova, E.; Sramka, M.; Babinec, P. *Zeitschrift fuer Naturforschung C* **2000**, *55*, 278-281.
(26) Hilt, J. Z.; Byrne, M. E. *ADVANCED DRUG DELIVERY REVIEWS* **2004**, *56*, 1599-1620.
(27) Chung, N. S.; Wasan, K. M. *ADVANCED DRUG DELIVERY REVIEWS* **2004**, *56*, 1315-1334.
(28) Hirsch, L. R.; Stafford, R. J.; Bankson, J. A.; Sershen, S. R.; Rivera, B.; Price, R. E.; Hazle, J. D.; Halas, N. J.; West, J. L. *PROCEEDINGS OF THE NATIONAL ACADEMY OF SCIENCES OF THE UNITED STATES OF AMERICA* **2003**, *100*, 13549-13554.
(29) O'Neal, D. P.; Hirsch, L. R.; Halas, N. J.; Payne, J. D.; West, J. L. *CANCER LETTERS* **2004**, *209*, 171-176.
(30) Hiergeist, R.; Andrä, W.; Buske, N.; Hergt, R.; Hilger, I.; Richter, U.; Kaiser, W. *Journal of Magnetism and Magnetic Materials* **1999**, *201*, 420-422.
(31) Chan, D. C. F.; Kirpotin, D. B.; Bunn_Jr., P. A. *J. Magn. Magn. Mater.* **1993**, *122*, 374-378.
(32) Jordan, A.; Scholz, R.; Wust, P.; Schirra, H.; Schiestel, T.; Schmidt, H.; Felix, R. *JOURNAL OF MAGNETISM AND MAGNETIC MATERIALS* **1999**, *194*, 185-196.
(33) Jordan, A.; Scholz, R.; Wust, P.; Fahling, H.; Felix, R. *J. Magn. Magn. Mater.* **1999**, *201*, 413-419.
(34) Mornet, S.; Vasseur, S.; Grasset, F.; Duguet, E. *J. Mater. Chem.* **2004**, *14*, 2161-2175.
(35) Pankhurst, Q. A.; Connolly, J.; Jones, S. K.; Dobson, J. *J. Phys. D* **2003**, *36*, R167-R181.
(36) Skirtach, A. G.; Antipov, A. A.; Shchukin, D. G.; Sukhorukov, G. B. *Langmuir* **2004**, *20*, 6988-6992.
(37) Volodkin, D. V.; Larionova, N. I.; Sukhorukov, G. B. *BIOMACROMOLECULES* **2004**, *5*, 1962-1972.
(38) Heuberger, R.; Sukhorukov, G. B.; Vörös, J.; Textor, M.; Möhwald, H. *Adv. Funct. Mater.* **2005**, *in press*.
(39) Diaspro, A.; Silvano, D.; Krol, S.; Cavalleri, O.; Gliozzi, A. *Langmuir* **2002**, *18*, 5047-5050.
(40) Krol, S.; Diaspro, A.; Magrassi, R.; Ballario, P.; Grimaldi, B.; Filetici, P.; Ornaghi, P.; Ramoino, P.; Gliozzi, A. *IEEE TRANSACTIONS ON NANOBIOSCIENCE* **2004**, *3*, 32-38.
(41) Weissleder, R.; Stark, D.; Engelstad, B. L.; Bacon, B. R.; Compton, C. C.; White, D. L.; Jacobs, P.; Lewis, J. *American Journal of Roentgenology* **1989**, *152*, 167-173.
(42) Lacava, Z. G. M.; Azevedo, R. B.; Martins, E. V.; Lacava, L. M.; Freitas, M. L. L.; Garcia, V. A. P.; Rébula, C. A.; Lemos, A. P. C.; Sousa, M. H.; Tourinho, F. A.; Silva, M. F. D.; Morais, P. C. *Journal of Magnetism and Magnetic Materials* **1999**, *201*, 431-434.
(43) Derfus, A. M.; Chan, W. C. W.; Bhatia, S. N. *NanoLetters* **2004**, *4*, 11-18.
(44) Shiohara, A.; Hoshino, A.; Hanaki, K.; Suzuki, K.; Yamamoto, K. *MICROBIOLOGY AND IMMUNOLOGY* **2004**, *48*, 669-675.
(45) Hoshino, A.; Fujioka, K.; Oku, T.; Suga, M.; Sasaki, Y. F.; Ohta, T.; Yasuhara, M.; Suzuki, K.; Yamamoto, K. *Nano Letters* **2004**.
(46) Bhattacharya, R.; Mukherjee, P.; Xiong, Z.; Atala, A.; Soker, S.; Mukhopadhyay, D. *Nano Letters* **2004**, *4*, 2479-2481.

(47) Kirchner, C.; Liedl, T.; Kudera, S.; Pellegrino, T.; Javier, A. M.; Gaub, H. E.; Stölzle, S.; Fertig, N.; Parak, W. J. *Nanoletters* **2005**, *in press*.
(48) Gaponik, N.; Talapin, D. V.; Rogach, A. L.; Hoppe, K.; Shevchenko, E. V.; Kornowski, A.; Eychmüller, A.; Weller, H. *J. Phys. Chem. B* **2002**, *106*, 7177-7185.
(49) Yu, W. W.; Qu, L.; Guo, W.; Peng, X. *Chem. Mat.* **2003**, *15*, 2854-2860.

Danksagung

An dieser Stelle meiner Promotionsarbeit möchte ich den Menschen danken, die mich in den Jahren meiner Promotion unterstützt haben. Besonders herzlich danke ich Prof. H.E. Gaub, der mir die Möglichkeit zur Promotion an seinem Lehrstuhl für Angewandte Physik gab. Allen Mitgliedern des Instituts sage ich Dank für die stets fantastische Stimmung, in deren guten Geist meine Arbeit entstanden ist. Um ein paar Leute zu nennen:

Dr. Markus Seitz, für die konsequente und stets motivierende Betreuung meiner Forschungsarbeit, das Publikations- und Patent-Schreiben, die Konferenzbesuche, Rückenprophylaxe, kurz- die ganze Vielzahl unserer gemeinsamen Projekte.

Dr. Wolfgang Parak für unser Projekt „Nano Safety“ , die wertvollen Diskussionen, und dass er so eine nette Arbeitsgruppe gesammelt hat, mit internationalen Kooperationen, Pasta und Salsa.

Dank an Prof. Uwe Klemradt, RWTH Aachen, für die produktive Kooperation und die genialen Fits zu den X-Ray Messungen, ebenso an Prof. Finlayson von der Monash University in Australien, seine brilliante Mitarbeiterin Kylie Crompton und Justin Smith sowie John Sutter vom HASYLAB, DESY in Hamburg.

A. S. Susha, A. L. Rogach, LS für Photonik und Optoelektronik Prof. J. Feldmann, LMU, für das gemeinsame Projekt „Drug delivery via Polyelectrolyt-capsules“.

Dr. Petra Denk (ehemals LMU), für die Arbeit am SFB486 Workshop auf Schloss Ringberg und sonstige Unterstützung. A. Cavanna am Laboratoire de Photonique et de Nanostructure (LPN) und H. Riechelt von Infineon Corporate Research für das Bereitstellen der GaAs-Heterostrukturen.

Dr. B. Helmreich und Dr. C. Greio am Institut für Wassergüte und Abfallwirtschaft
der TU München für die Durchführung der Atom-Absorptions-Spektroskopie Messungen.

Dr. Jan Krauss und Dr. Udo Beierlein, LS für Festkörperphysik Prof. J.P. Kotthaus, LMU, für die Photoluminiszenz- bzw. FTIR-Messungen an GaAs-Substraten.

A. Kriele und PD. Dr. B. Lorenz für die Unterstützung bei den Arbeiten im Reinraum.

Dr. Liberato Manna, NNLI Lecce, Italien, für seine Unterstützung beim Paper und seine nette Gesellschaft.

Teresa Pellegrino für die wissenschaftlichen Diskussionen und Synthesen, für zu sein ein Schatz von Mensch und wahrer Freund: das ist eine schönen Kooperationen! (have you seen)

Stefan Kudera ebenso, danke für die unendliche Synthese von Millionen und Abermillionen von Nanopartikeln, um sie zu „wasten“.

Tim Liedl für die Synthesen sowie unsere Arbeit rund um das Paper und dass er in München geblieben ist.

Almudena Munoz, Ralph Sperling, Alicia Piera, Marco Zanella, Bernd Zebli, Jimmy, James, die ganze bunte Truppe des Arbeitskreis Parak, für ein ausgefülltes Arbeits- und Institutsleben.

Bernhard Stein –mein Vorbild- und Michael George für die gemeinsame Arbeit am Sensorprojekt und ihre stete Hilfsbereitschaft. Angelika Wehle weil sie die Universal-Informationsquelle war, Rainer Matzke für Bioskop-Messungen, Hilde Rinja für AFM-Imaging, und allen für die schöne gemeinsame Zeit.

Angelika Kardinal, für die wertvolle Hilfe in Labor- und Zelllabor und Ihr goldenes Gemüt. Martin Benoit, der hilfreichste Mensch auf Gambis Erden.

Thomas Nikolaus und Agnes Mühlfeldner für die Hilfe im Zellabor und ihre stets gute Laune.

Hermann Gumpp, ein Vergelts Gott!, dass er mich als Computeradmin ablöst, dabei auch all denen, die mich früher beim EDV-Geschäft unterstützt haben.

Danke an meine Eltern und meine Familie für ihre Unterstützung.

Erklärung

Hiermit erkläre ich, Christian Kirchner, dass ich die vorliegende Dissertationsarbeit selbstständig und ohne die Benutzung anderer als den von mir angegeben Quellen angefertigt habe und die den benutzten Werken wörtlich und inhaltlich entnommenen Stellen als solche kenntlich gemacht habe.

München, den 06.10.2005 _____

DIPL.-PHYS. CHRISTIAN KIRCHNER

LEBENSLAUF

2000 - 2005	Wissenschaftlicher Angestellter am Lehrstuhl für Angewandte Physik, Biophysik und molekulare Materialien, Prof. Gaub, und Center for Nanoscience der Ludwig-Maximilians Universität München Promotionsabschluss voraussichtlich Herbst 2005
1991 - 2000	Physik Studium an der Ludwig-Maximilians Universität München Abschluss: Physik-Diplom Note: Sehr gut
1990	Auslandsaufenthalt in Venezuela, Kolumbien, Ecuador, Peru, Chile, Sprach- und Bildungsreise
1988 - 1989	Wehrdienst an der Pionierschule München
1979 - 1988	Pestalozzi-Gymnasium München Abschluss: Abitur, Note: 1,9
1975 - 1979	Grundschule in der Sambergerstrasse, München
19. August 1969	geboren in Köln